STATE OF THE CLIMATE IN 2021

GLOBAL CLIMATE

R. J. H. Dunn, F. Aldred, N. Gobron, J. B Miller, and K. M. Willett, Eds.

Special Online Supplement to the *Bulletin of the American Meteorological Society*, Vol. 103, No. 8, August 2022

doi:10.1175/BAMS-D-22-0092.1

Corresponding author: Robert Dunn / robert.dunn@metoffice.gov.uk

STATE OF THE CLIMATE IN 2021
Global Climate

Editors

Jessica Blunden
Tim Boyer

Chapter Editors

Freya Aldred
Peter Bissolli
Kyle R. Clem
Howard J. Diamond
Matthew L. Druckenmiller
Robert J. H. Dunn
Catherine Ganter
Nadine Gobron
Gregory C. Johnson
Rick Lumpkin
Ademe Mekonnen
John B. Miller
Twila A. Moon
Marilyn N. Raphael
Ahira Sánchez-Lugo
Carl J. Schreck III
Richard L. Thoman
Kate M. Willett
Zhiwei Zhu

Technical Editor

Laura Ohlmann

BAMS Special Editor for Climate

Michael A. Alexander

American Meteorological Society

Cover credit:
Caption: Lightning discharges appear in various colours depending on the scatter of light inside the thundercloud and in the atmosphere. The intracloud lightning discharges in the centre of the thundercloud appear to be white with a bluish tint, and the cloud-to-ground discharge below appears to be orange. The right hand side of the thundercloud exhibits a green tint that is attributed to the unique composition of hydrometeors inside the thundercloud.

The photo was taken in the late evening of 10 September 2013, near Tarragona in northeastern Spain.

Global Climate is one chapter from the State of the Climate in 2021 annual report and is available from https://doi.org/10.1175/BAMS-D-22-0092.1. Compiled by NOAA's National Centers for Environmental Information, *State of the Climate in 2021* is based on contributions from scientists from around the world. It provides a detailed update on global climate indicators, notable weather events, and other data collected by environmental monitoring stations and instruments located on land, water, ice, and in space.
The full report is available from https://doi.org/10.1175/2022BAMSStateoftheClimate.1

How to cite this document:

Citing the complete report:
Blunden, J. and T. Boyer, Eds., 2022: "State of the Climate in 2021". *Bull. Amer. Meteor. Soc.*, **103** (8), Si–S465 https://doi.org/10.1175/2022BAMSStateoftheClimate.1

Citing this chapter:
Dunn, R. J. H., F. Aldred, N. Gobron, J. B Miller, and K. M. Willett, Eds., 2022: Global Climate [in "State of the Climate in 2021"]. *Bull. Amer. Meteor. Soc.*, **103** (8), S11–S142, https://doi.org/10.1175/BAMS-D-22-0092.1.

Citing a section (example):
Cornes, R. C., T. Cropper, R. Junod, and E. C. Kent, 2022: Night marine air temperature [in "State of the Climate in 2021"]. *Bull. Amer. Meteor. Soc.*, **103** (8), S31–S33, https://doi.org/10.1175/BAMS-D-22-0092.1.

Editor and Author Affiliations (alphabetical by name)

Ades, Melanie, European Centre for Medium-Range Weather Forecasts, Reading, United Kingdom
Adler, Robert, CMNS-Earth System Science Interdisciplinary Center, University of Maryland, College Park, Maryland
Aldred, Freya, Met Office Hadley Centre, Exeter, United Kingdom
Allan, R. P., Department of Meteorology and National Centre for Earth Observation, University of Reading, Reading, United Kingdom
Anderson, John, Department of Atmospheric and Planetary Science, Hampton University, Hampton, Virginia
Anneville, Orlane, National Research Institute for Agriculture, Food and Environment (INRAE), CARRTEL, Université Savoie Mont Blanc, Thonon les Bains, France
Aono, Yasuyuki, Graduate School of Life and Environmental Sciences, Osaka Prefecture University, Sakai, Osaka, Japan
Argüez, Anthony, NOAA/NESDIS National Centers for Environmental Information, Asheville, North Carolina
Arosio, Carlo, University of Bremen, Bremen, Germany
Augustine, John A., NOAA Global Monitoring Laboratory, Boulder, Colorado
Azorin-Molina, Cesar, Centro de Investigaciones sobre Desertificación, Spanish National Research Council (CIDE, CSIC-UV-Generalitat Valenciana), Climate, Atmosphere and Ocean Laboratory (Climatoc-Lab), Moncada, Valencia, Spain
Barichivich, Jonathan, Instituto de Geografía, Pontificia Universidad Católica de Valparaíso, Valparaíso, Chile and Climatic Research Unit, School of Environmental Sciences, University of East Anglia, Norwich, United Kingdom
Basu, Aman, York University, Toronto, Canada
Beck, Hylke E., Joint Research Centre of the European Commission, Ispra, Italy and GloH2O, Almere, the Netherlands
Bellouin, Nicolas, University of Reading, Reading, United Kingdom
Benedetti, Angela, European Centre for Medium-Range Weather Forecasts, Reading, United Kingdom
Blagrave, Kevin, York University, Toronto, Canada
Blenkinsop, Stephen, School of Engineering, Newcastle University, Newcastle-upon-Tyne, United Kingdom
Bock, Olivier, Université de Paris Cité, Institut de physique du globe de Paris, CNRS, IGN, F-7500 Paris, France
Bodin, Xavier, Laboratoire EDYTEM, CNRS/Université Savoie Mont-Blanc, Le Bourget-du-Lac, France
Bosilovich, Michael G., Global Modeling and Assimilation Office, NASA Goddard Space Flight Center, Greenbelt, Maryland
Boucher, Olivier, Sorbonne Université, Paris, France
Bove, Gerald, University of the Virgin Islands, St. Thomas, U.S. Virgin Islands
Buechler, Dennis, University of Huntsville Alabama, Huntsville, Alabama
Buehler, Stefan A., Meteorologisches Institut, Centrum für Erdsystem- und Nachhaltigkeitsforschung (CEN), Fachbereich Erdsystemwissenschaften, Universität Hamburg, Hamburg, Germany
Carrea, Laura, Department of Meteorology, University of Reading, Reading, United Kingdom
Chang, Kai-Lan, Cooperative Institute for Research in Environmental Sciences, University of Colorado Boulder; and NOAA Chemical Sciences Laboratory, Boulder, Colorado
Christiansen, Hanne H., Geology Department, University Centre in Svalbard, Longyearbyen, Norway
Christy, John R., The University of Alabama in Huntsville, Huntsville, Alabama
Chung, Eui-Seok, IBS Center for Climate Physics, South Korea
Ciasto, Laura M., NOAA Climate Prediction Center, College Park, Maryland
Coldewey-Egbers, Melanie, DLR (German Aerospace Center) Oberpfaffenhofen, Wessling, Germany
Cooper, Owen R., Cooperative Institute for Research in Environmental Sciences, University of Colorado, Boulder, Colorado; and NOAA Chemical Sciences Laboratory, Boulder, Colorado
Cornes, Richard C., National Oceanography Centre, Southampton, United Kingdom
Covey, Curt, Lawrence Livermore National Laboratory, Livermore California
Cropper, Thomas, National Oceanography Centre, Southampton, United Kingdom
Crotwell, Molly, Cooperative Institute for Research in Environmental Sciences, University of Colorado, Boulder, Colorado; and NOAA Global Monitoring Laboratory, Boulder, Colorado
Cusicanqui, Diego, Université Grenoble Alpes, Institut de Géosciences de l'Environnement (IGE), Grenoble, France
Davis, Sean M., NOAA Chemical Sciences Laboratory, Boulder, Colorado
de Jeu, Richard A. M., Planet Labs, Haarlem, The Netherlands
Degenstein, Doug, University of Saskatchewan, Saskatoon, Saskatchewan, Canada
Delaloye, Reynald, Department of Geosciences, University of Fribourg, Fribourg, Switzerland
Donat, Markus G., Barcelona Supercomputing Centre, Barcelona, Spain and Catalan Institution for Research and Advanced Studies (ICREA), Barcelona, Spain
Dorigo, Wouter A., TU Wien, Vienna, Austria
Dunn, Robert J. H., Met Office Hadley Centre, Exeter, United Kingdom
Durre, Imke, NOAA/NESDIS National Centers for Environmental Information, Asheville, North Carolina
Dutton, Geoff S., Cooperative Institute for Research in Environmental Sciences, University of Colorado, Boulder, Colorado; and NOAA Global Monitoring Laboratory, Boulder, Colorado
Duveiller, Gregory, Max Planck Institute for Biogeochemistry, Jena , Germany
Elkins, James W., NOAA Global Monitoring Laboratory, Boulder, Colorado
Estilow, Thomas W., Rutgers University, Piscataway, New Jersey
Fedaeff, Nava, National Institute of Water and Atmospheric Research (NIWA), New Zealand
Fereday, David, Met Office Hadley Centre, Exeter, United Kingdom
Fioletov, Vitali E., Environment and Climate Change Canada, Toronto, Canada
Flemming, Johannes, Copernicus Department, European Centre for Medium-Range Weather Forecasts, Reading, United Kingdom
Foster, Michael J., Cooperative Institute for Meteorological Satellite Studies, Space Science and Engineering Center, University of Wisconsin-Madison, Madison, Wisconsin
Frith, Stacey M., Science Systems and Applications, Inc., Lanham, Maryland; and NASA Goddard Space Flight Center, Greenbelt, Maryland
Froidevaux, Lucien, Jet Propulsion Laboratory, California Institute of Technology, Pasadena, California
Füllekrug, Martin, University of Bath, Bath, United Kingdom
Garforth, Judith, Woodland Trust, Grantham, United Kingdom
Garg, Jay, SSAI, Hampton, Virginia
Gentry, Matthew, Cooperative Institute for Research in Environmental Sciences, University of Colorado, Boulder, Colorado; and NOAA Global Monitoring Laboratory, Boulder, Colorado
Gobron, Nadine, European Commission Joint Research Centre, Ispra, Italy
Goodman, Steven, Thunderbolt Global Analytics, Huntsville, Alabama
Gou, Qiqi, Hydro-Climate Extremes Lab (H-CEL), Ghent University, Ghent, Belgium
Granin, Nikolay, Siberian Branch of Russian Academy of Sciences, Irkutsk, Russia
Guglielmin, Mauro, Department of Theoretical and Applied Science, Insubria University, Italy
Hahn, Sebastian, TU Wien, Vienna, Austria
Haimberger, Leopold, Department of Meteorology and Geophysics, University of Vienna, Vienna, Austria

Hall, Brad D., NOAA Global Monitoring Laboratory, Boulder, Colorado
Harris, Ian, National Centre for Atmospheric Science (NCAS), University of East Anglia, Norwich, United Kingdom; and Climatic Research Unit, School of Environmental Sciences, University of East Anglia, Norwich, United Kingdom
Hemming, Debbie L., Met Office Hadley Centre, Exeter, United Kingdom; and Birmingham Institute of Forest Research, Birmingham University, Birmingham, United Kingdom
Hirschi, Martin, ETH Zürich, Zürich, Switzerland
Ho, Shu-pen (Ben), Center for Satellite Applications and Research, NOAA, College Park, Maryland
Holzworth, Robert, University of Washington, Seattle, Washington
Hrbáček, Filip, Department of Geography, Masaryk University, Brno, Czech Republic
Hubert, Daan, Royal Belgian Institute for Space Aeronomy (BIRA-IASB), Brussels, Belgium
Hulsman, Petra, Hydro-Climate Extremes Lab (H-CEL), Ghent University, Ghent, Belgium
Hurst, Dale F., Cooperative Institute for Research in Environmental Sciences, University of Colorado Boulder, Boulder, Colorado; NOAA Global Monitoring Laboratory, Boulder, Colorado
Inness, Antje, European Centre for Medium-Range Weather Forecasts, Reading, United Kingdom
Isaksen, Ketil, Norwegian Meteorological Institute, Oslo, Norway
John, Viju O., EUMETSAT, Darmstadt, Germany
Jones, Philip D., Climatic Research Unit, School of Environmental Sciences, University of East Anglia, Norwich, United Kingdom
Junod, Robert, Earth System Science Center (ESSC), University of Alabama in Huntsville, Huntsville, Alabama
Kääb, Andreas, Department of Geosciences, University of Oslo, Norway
Kaiser, Johannes W., Centre for Agrometeorological Research (ZAMF), German Meteorological Service (DWD), Braunschweig, Germany
Kaufmann, Viktor, Institute of Geodesy, Working Group Remote Sensing and Photogrammetry, Graz University of Technology, Graz, Austria
Kellerer-Pirklbauer, Andreas, Institute of Geography and Regional Science, Cascade – The Mountain Processes and Mountain Hazards Group, University of Graz, Graz, Austria
Kent, Elizabeth C., National Oceanography Centre, Southampton, United Kingdom
Kidd, Richard, Earth Observation Data Centre (EODC), Vienna, Austria
Kim, Hyungiun, Moon Soul Graduate School of Future Strategy and Department of Civil and Environmental Engineering, Korea Advanced Institute of Science and Technology, Daejeon, Korea
Kipling, Zak, European Centre for Medium-Range Weather Forecasts, Reading, United Kingdom
Koppa, Akash, Hydro-Climate Extremes Lab (H-CEL), Ghent University, Ghent, Belgium
L'Abée-Lund, Jan Henning, Norwegian Water Resources and Energy Directorate, Oslo, Norway
Lan, Xin, Cooperative Institute for Research in Environmental Sciences, University of Colorado, Boulder, Colorado; NOAA Global Monitoring Laboratory, Boulder, Colorado
Lantz, Kathleen O., NOAA Global Monitoring Laboratory, Boulder, Colorado
Lavers, David, European Centre for Medium-Range Weather Forecasts, Reading, United Kingdom
Loeb, Norman G., NASA Langley Research Center, Hampton, Virginia
Loyola, Diego, DLR (German Aerospace Center) Oberpfaffenhofen, Wessling, Germany
Madelon, Remi, CESBIO (Université Toulouse 3, CNES, CNRS, INRAE, IRD), Toulouse, France
Malmquist, Hilmar J., Icelandic Museum of Natural History, Reykjavík, Iceland
Marszelewski, Wlodzimierz, Nicolaus Copernicus University in Toruń, Toruń, Poland
Mayer, Michael, University of Vienna, Vienna, Austria; and European Centre for Medium-Range Weather Forecasts, Reading, United Kingdom
McCabe, Matthew F., Division of Biological and Environmental Sciences and Engineering, King Abdullah University of Science and Technology, Thuwal, Saudi Arabia
McVicar, Tim R., CSIRO Land and Water, Canberra, Australian Capital Territory; and Australian Research Council Centre of Excellence for Climate Extremes, Sydney, New South Wales, Australia
Mears, Carl A., Remote Sensing Systems, Santa Rosa, California
Menzel, Annette, TUM School of Life Sciences, Technical University of Munich, Freising, Germany; and Institute for Advanced Study, Technical University of Munich, Garching, Germany
Merchant, Christopher J., Department of Meteorology, University of Reading, Reading, United Kingdom
Miller, John B., NOAA Global Monitoring Laboratory, Boulder, Colorado
Miralles, Diego G., Hydro-Climate Extremes Lab (H-CEL), Ghent University, Ghent, Belgium
Montzka, Stephen A., NOAA Global Monitoring Laboratory, Boulder, Colorado
Morice, Colin, Met Office Hadley Centre, Exeter, United Kingdom
Mösinger, Leander, TU Wien, Vienna, Austria
Mühle, Jens, Scripps Institution of Oceanography, University of California, San Diego, La Jolla, California
Nicolas, Julien P., European Centre for Medium-Range Weather Forecasts, Reading, United Kingdom
Noetzli, Jeannette, WSL Institute for Snow and Avalanche Research SLF, Davos-Dorf, Switzerland and Climate Change, Extremes and Natural Hazards in Alpine Regions Research Center CERC, Davos Dorf, Switzerland
Nõges, Tiina, Estonian University of Life Sciences, Tartu, Estonia
Noll, Ben, National Institute of Water and Atmospheric Research (NIWA), New Zealand
O'Keefe, John, The Harvard Forest, Harvard University, Petersham, Massachusetts
Osborn, Tim J., Climatic Research Unit, School of Environmental Sciences, University of East Anglia, Norwich, United Kingdom
Park, Taejin, NASA Ames Research Center, Moffett Field, California; Bay Area Environmental Research Institute, Moffett Field, California
Pellet, Cecile, Department of Geosciences, University of Fribourg, Fribourg, Switzerland
Pelto, Maury S., Nichols College, Dudley, Massachusetts
Perkins-Kirkpatrick, Sarah E., University of New South Wales, Canberra, Australia
Phillips, Coda, Cooperative Institute for Meteorological Satellite Studies, Space Science and Engineering Center, University of Wisconsin-Madison, Madison, Wisconsin
Po-Chedley, Stephen, Program for Climate Model Diagnosis and Intercomparison, Lawrence Livermore National Laboratory, Livermore, California
Polvani, Lorenzo, Columbia University, New York, New York
Preimesberger, Wolfgang, TU Wien, Vienna, Austria
Price, Colin, Tel Aviv University, Tel Aviv, Israel
Pulkkanen, Merja, Finnish Environment Institute SYKE, Helsinki, Finland
Rains, Dominik G., Hydro-Climate Extremes Lab (H-CEL), Ghent University, Ghent, Belgium
Randel, William J., National Center for Atmospheric Research (NCAR), Boulder, Colorado

Editor and Author Affiliations (alphabetical by name)

Rémy, Samuel, HYGEOS, Lille, France
Ricciardulli, Lucrezia, Remote Sensing Systems, Santa Rosa, California
Richardson, Andrew D., School of Informatics, Computing, and Cyber Systems and Center for Ecosystem Science and Society, Northern Arizona University, Flagstaff, Arizona
Robinson, David A., Rutgers University, Piscataway, New Jersey
Rodell, Matthew, Earth Sciences Division, NASA Goddard Space Flight Center, Greenbelt, Maryland
Rodríguez-Fernández, Nemesio J., CESBIO, Université Toulouse 3, CNES, CNRS, INRAE, IRD, Toulouse, France
Rosenlof, Karen H., NOAA Chemical Sciences Laboratory, Boulder, Colorado
Roth, Chris, University of Saskatchewan, Saskatoon, Canada
Rozanov, Alexei, University of Bremen, Bremen, Germany
Rutishäuser, This, Swiss Academy of Sciences (SCNAT), Bern, Switzerland
Sánchez-Lugo, Ahira, NOAA/NESDIS National Centers for Environmental Information, Asheville, North Carolina
Sawaengphokhai, Parnchai, Science Systems and Applications, Inc. (SSAI), Hampton, Virginia
Schenzinger, Verena, Medical University of Innsbruck, Innsbruck, Austria
Schlegel, Robert W., Sorbonne Université, CNRS, Villefranche-sur-mer, France
Schneider, Udo, Global Precipitation Climatology Centre, Deutscher Wetterdienst, Offenbach, Germany
Sharma, Sapna, York University, Toronto, Ontario, Canada
Shi, Lei, NOAA/NESDIS National Centers for Environmental Information, Asheville, North Carolina
Simmons, Adrian J., European Centre for Medium-Range Weather Forecasts, Reading, United Kingdom
Siso, Carolina, Cooperative Institute for Research in Environmental Sciences, University of Colorado, Boulder CO USA, and NOAA Global Monitoring Laboratory, Boulder, Colorado
Smith, Sharon L., Geological Survey of Canada, Natural Resources Canada, Ottawa, Canada
Soden, Brian J., University of Miami Rosenstiel School of Marine and Atmospheric Science (RSMAS), Key Biscayne, Florida
Sofieva, Viktoria, Finnish Meteorological Institute (FMI), Helsinki, Finland
Sparks, Tim H., Poznań University of Life Sciences, Poznań, Poland
Stackhouse, Jr., Paul W., NASA Langley Research Center, Hampton, Virginia
Stauffer, Ryan, NASA Goddard Space Flight Center, Greenbelt, Maryland
Steinbrecht, Wolfgang, German Weather Service (DWD), Hohenpeissenberg, Germany
Steiner, Andrea K., Wegener Center for Climate and Global Change, University of Graz, Graz, Austria
Stewart, Kenton, State University of New York at Buffalo, Buffalo, New York
Stradiotti, Pietro, TU Wien, Vienna, Austria
Streletskiy, Dimitri A., George Washington University, Washington, D.C.
Telg, Hagen, Cooperative Institute for Research in the Environmental Sciences, University of Colorado, Boulder, Colorado
Thackeray, Stephen J., Centre for Ecology and Hydrology, Lancaster, United Kingdom
Thibert, Emmanuel, Université Grenoble Alpes, INRAE, UR ETGR, Grenoble, France
Todt, Michael, Cooperative Institute for Research in the Environmental Sciences, University of Colorado, Boulder
Tokuda, Daisuke, Institute of Industrial Science, The University of Tokyo, Tokyo, Japan
Tourpali, Kleareti, Aristotle University, Thessaloniki, Greece
Tye, Mari R., National Center for Atmospheric Research, Boulder, Colorado
van der A, Ronald, Royal Netherlands Meteorological Institute (KNMI), DeBilt, The Netherlands
van der Schalie, Robin, Planet Labs, Haarlem, The Netherlands
van der Schrier, Gerard, Royal Netherlands Meteorological Institute, De Bilt, The Netherlands
van der Vliet, Mendy, Planet Labs, Haarlem, The Netherlands
van der Werf, Guido R., Faculty of Science, Vrije Universiteit Amsterdam, Amsterdam, Netherlands
van Vliet, Arnold., Environmental Systems Analysis Group, Wageningen University & Research, the Netherlands
Vernier, Jean-Paul, National Institute of Aerospace/NASA Langley Research Center, Hampton, Virginia
Vimont, Isaac J., Cooperative Institute for Research in Environmental Sciences, University of Colorado Boulder; and NOAA Global Monitoring Laboratory, Boulder, Colorado
Virts, Katrina, University of Huntsville, Huntsville, Alabama
Vivero, Sebastiàn, Department of Geosciences, University of Fribourg, Fribourg, Switzerland
Vömel, Holger, Earth Observing Laboratory, National Center for Atmospheric Research, Boulder, Colorado
Vose, Russell S., NOAA National Centers for Environmental Information, Asheville, North Carolina
Wang, Ray H. J., Georgia Institute of Technology, Atlanta, Georgia
Weber, Markus, University of Bremen, Bremen, Germany
Wiese, David, Jet Propulsion Laboratory, California Institute of Technology, Pasadena, California
Wild, Jeanette D., ESSIC/University of Maryland, College Park, Maryland; and NOAA Climate Prediction Center, College Park, Maryland
Willett, Kate M., Met Office Hadley Centre, Exeter, United Kingdom
Williams, Earle, Massachusetts Institute of Technology, Cambridge, Massachusetts
Wong, Takmeng, NASA Langley Research Center, Hampton, Virginia
Woolway, R. I., School of Ocean Sciences, Bangor University, Menai Bridge, Anglesey, Wales
Yin, Xungang, NOAA National Centers for Environmental Information, Asheville, North Carolina
Yuan, Ye, TUM School of Life Sciences, Technical University of Munich, Freising, Germany
Zhao, Lin, School of Geographical Sciences, Nanjing University of Information Science and Technology, Nanjing, China
Zhou, Xinjia, Center for Satellite Applications and Research, NOAA, College Park, Maryland
Ziemke, Jerry R., Goddard Earth Sciences Technology and Research, Morgan State University, Baltimore, Maryland; and NASA Goddard Space Flight Center, Greenbelt, Maryland
Ziese, Markus, Global Precipitation Climatology Centre, Deutscher Wetterdienst, Offenbach am Main, Germany
Zotta, Ruxandra M., TU Wien, Vienna, Austria

Editorial and Production Team

Allen, Jessicca, Graphics Support, Cooperative Institute for Satellite Earth System Studies, North Carolina State University, Asheville, North Carolina

Camper, Amy, Graphics Support, Innovative Consulting and Management Services, LLC, NOAA/NESDIS National Centers for Environmental Information, Asheville, North Carolina

Hammer, Gregory, Content Team Lead, Communications and Outreach, NOAA/NESDIS National Centers for Environmental Information, Asheville, North Carolina

Love-Brotak, S. Elizabeth, Lead Graphics Production, NOAA/NESDIS National Centers for Environmental Information, Asheville, North Carolina

Misch, Deborah J., Graphics Support, Innovative Consulting and Management Services, LLC, NOAA/NESDIS National Centers for Environmental Information, Asheville, North Carolina

Ohlmann, Laura, Technical Editor, Innovative Consulting and Management Services, LLC, NOAA/NESDIS National Centers for Environmental Information, Asheville, North Carolina

Riddle, Deborah B., Graphics Support, NOAA/NESDIS National Centers for Environmental Information, Asheville, North Carolina

Veasey, Sara W., Visual Communications Team Lead, Communications and Outreach, NOAA/NESDIS National Centers for Environmental Information, Asheville, North Carolina

2. Table of Contents

2. Table of Contents

*Please refer to Chapter 8 (Relevant datasets and sources) for a list of all climate variables and datasets used in this chapter for analyses, along with their websites for more information and access to the data.

2. GLOBAL CLIMATE

R. J. H. Dunn, F. Aldred, N. Gobron, J. B. Miller, and K. M. Willett, Eds.

a. Introduction—R. J. H. Dunn, F. Aldred, N. Gobron, J. B Miller, and K. M. Willett

In 2021, both social and economic activities began to return towards the levels preceding the COVID-19 pandemic for some parts of the globe, with others still experiencing restrictions. Meanwhile, the climate has continued to respond to the ongoing increase in greenhouse gases and resulting warming. La Niña, a phenomenon which tends to depress global temperatures while changing rainfall patterns in many regions, prevailed for all but two months of the year. Despite this, 2021 was one of the six-warmest years on record as measured by global mean surface temperature with an anomaly of between +0.21° and +0.28°C above the 1991–2020 climatology.

Lake surface temperatures were their highest on record during 2021. The number of warm days over land also reached a new record high. Exceptional heat waves struck the Pacific Coast of North America, leading to a new Canadian maximum temperature of 49.6°C at Lytton, British Columbia, on 29 June, breaking the previous national record by over 4°C. In Death Valley, California, the peak temperature reached 54.4°C on 9 July, equaling the temperature measured in 2020, and the highest temperature recorded anywhere on the globe since at least the 1930s. Over the Mediterranean, a provisional new European record of 48.8°C was set in Sicily on 11 August. In the atmosphere, the annual mean tropospheric temperature was among the 10 highest on record, while the stratosphere continued to cool.

While La Niña was present except for June and July, likely influencing Australia's coolest year since 2012 and wettest since 2016, other modes of variability played important roles. A negative Indian Ocean dipole event became established during July, associated with a warmer east and cooler west Indian Ocean. Northern Hemisphere winters were affected by a negative phase of the North Atlantic Oscillation at both the beginning and end of 2021. In the Southern Hemisphere, a very strong positive Southern Annular Mode (also known as the Antarctic Oscillation) contributed to New Zealand's record warm year and to very cold temperatures over Antarctica. Land surface winds continued a slow reversal from the multi-decadal stilling, and over the ocean wind speeds were at their highest in almost a decade.

La Niña conditions had a clear influence on the regional patterns of many hydrological variables. Surface specific humidity and total column water vapor over land and ocean were higher than average in almost all datasets. Relative humidity over land reached record or near-record low saturation depending on the dataset, but with mixed signals over the ocean. Satellite measurements showed that 2021 was the third cloudiest in the 19-year record. The story for precipitation was mixed, with just below-average mean precipitation falling over land and below-average mean precipitation falling over the ocean, while extreme precipitation was generally more frequent, but less intense, than average. Differences between means and extremes can be due to several factors, including using different indices, observing periods, climatological base reference periods, and levels of spatial completeness. The sharp increase in global drought area that began in mid-2019 continued in 2021, reaching a peak in August with 32% of global land area experiencing moderate or worse drought, and declining slightly thereafter.

Arctic permafrost temperatures continued to rise, reaching record values at many sites, and the thickness of the layer which seasonally thaws and freezes also increased over 2020 values

in a number of regions. It was the 34th-consecutive year of mass balance loss for alpine glaciers in mountainous regions, with glaciers on average 25 m thinner than in the late 1970s. And the duration of lake ice in the Northern Hemisphere was the fourth lowest in situ record dating back to 1991.

The atmospheric concentrations of the major long-lived greenhouse gases, CO_2, CH_4, and N_2O, all reached levels not seen in at least the last million years and grew at near-record rates in 2021. La Niña conditions did not appear to have any appreciable impact on their growth rates. The growth rate for CH_4, of 17 ppb yr^{-1}, was similar to that for 2020 and set yet another record, although the causes for this post-2019 acceleration are unknown presently. Overall, CO_2 growth continues to dominate the increase in global radiative forcing, which increased from 3.19 to 3.23 W m^{-2} (watts per square meter) during the year. In 2021, stratospheric ozone did not exhibit large negative anomalies, especially near the poles, unlike 2020, where large ozone depletions appeared, mainly from dynamical effects. The positive impact of reductions in emissions of ozone depleting substances can be seen most clearly in the upper stratosphere, where such dynamical effects are less pronounced.

It was the fourth-lowest fire year since global records began in 2003, though extreme regional fire activity was again seen in North America and also in Siberia; as in 2020, the effects of wildfires in these two regions led to locally large regional positive anomalies in tropospheric aerosol and carbon monoxide abundance.

Vegetation is responding to the higher global mean temperatures, with the satellite-derived measures for the Northern Hemisphere for 2021 rated among the earliest starts of the growing season and the latest end of the season on record. The first bloom date for cherry trees in Kyoto, Japan, broke a 600-year record set in 1409.

This year we welcome a sidebar on the global distribution of lightning, which has been recently declared an essential climate variable (ECV) by the Global Climate Observing System (GCOS).

Time series and anomaly maps from many of the variables described in this chapter can be found in Plates 1.1 and 2.1. As with other chapters, many of the sections have moved from the previous 1981–2010 to the new 1991–2020 climatological reference period, in line with WMO recommendations (see Chapter 1). This is not possible for all datasets, as it is dependent on their length of record or legacy processing methods. While anomalies from the new climatology period are not so easily comparable with previous editions of this report, they more clearly highlight deviations from more recent conditions.

(a) Surface Temperature

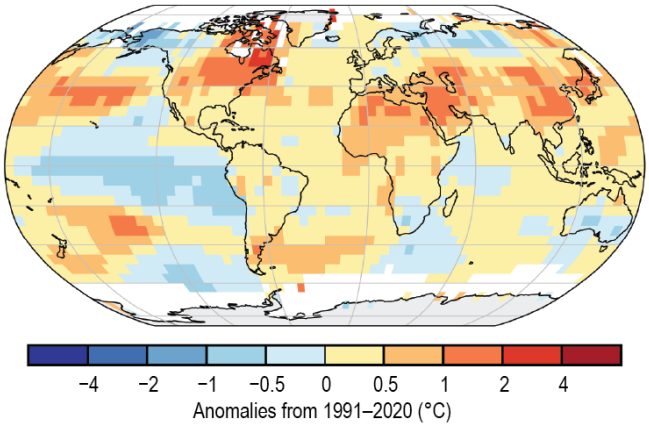

(b) Lake Temperature

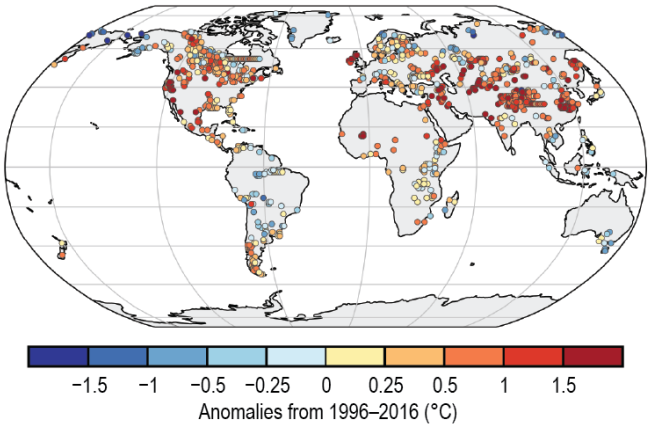

(c) Night Marine Air Temperature

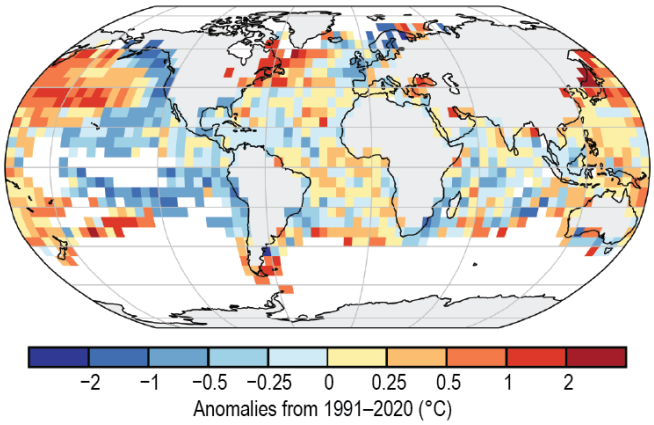

(d) Warm Days

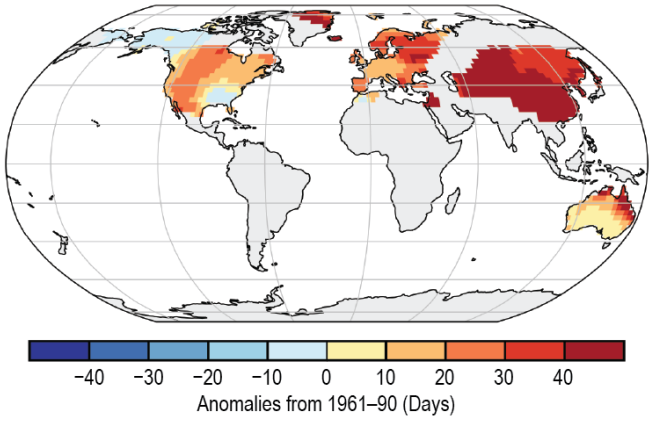

(e) Cool Nights

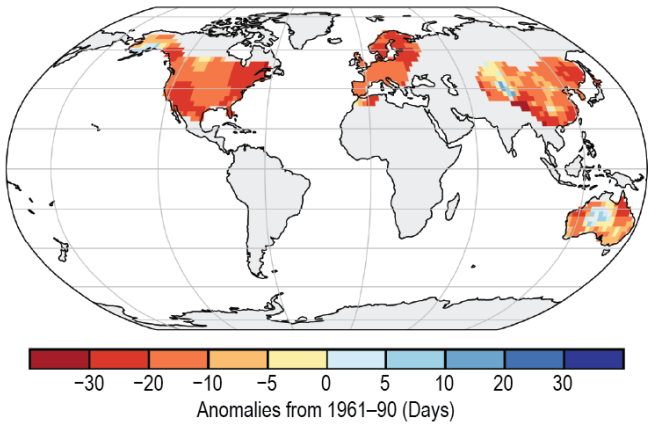

(f) Lower Tropospheric Temperature

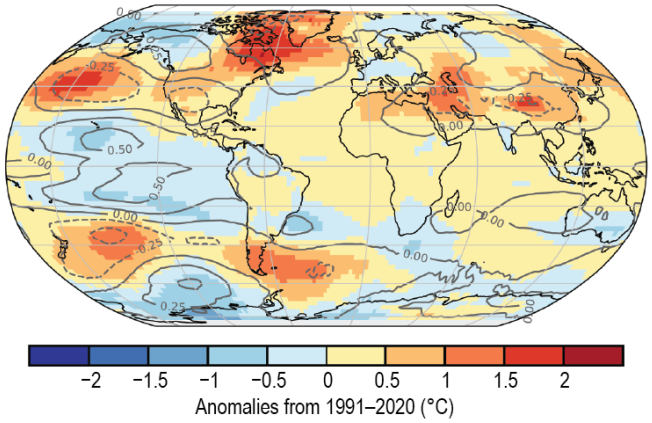

(g) Surface Specific Humidity

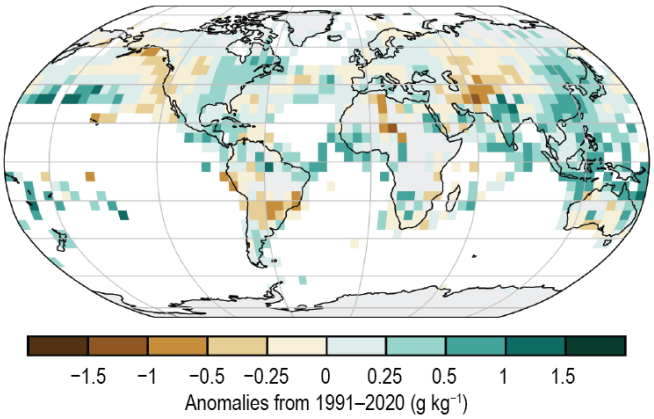

Plate 2.1. (a) NOAA NCEI Global land and ocean surface annual temperature anomalies (°C); (b) Satellite-derived warm season lake surface water temperature anomalies (°C); (c) CLASSnmat night marine air temperature annual average anomalies (°C); (d) GHCNDEX warm day threshold exceedance (TX90p); (e) GHCNDEX cool night threshold exceedance (TN10p); (f) Average of RSS and UAH lower tropospheric temperature anomalies (°C). Gray contours represent the value of the linear regression between the monthly Niño 3.4 index and the monthly local lower tropospheric temperature anomaly over 1979–2019; (g) HadISDH surface specific humidity anomalies (g kg^{-1});

(h) Surface Relative Humidity

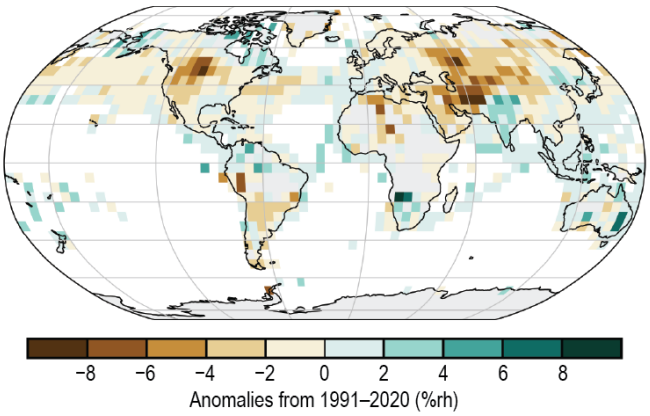

(i) Total Column Water Vapor

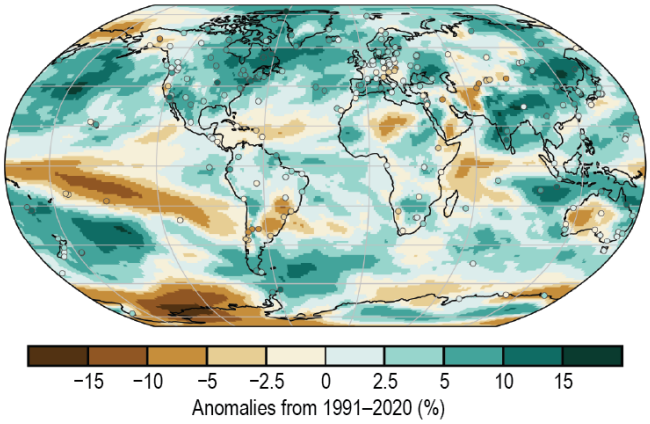

(j) Upper Tropospheric Humidity

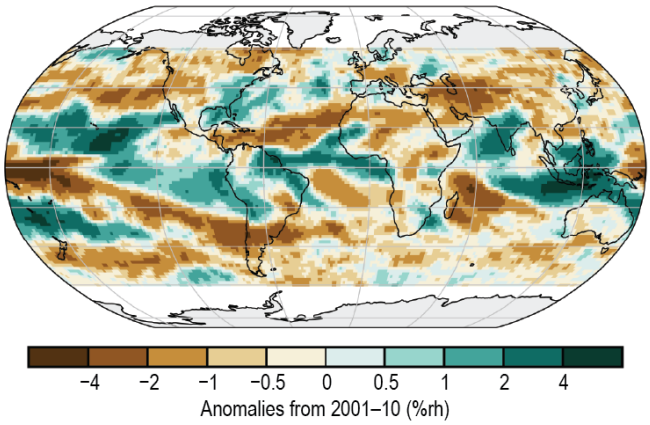

(k) Precipitation

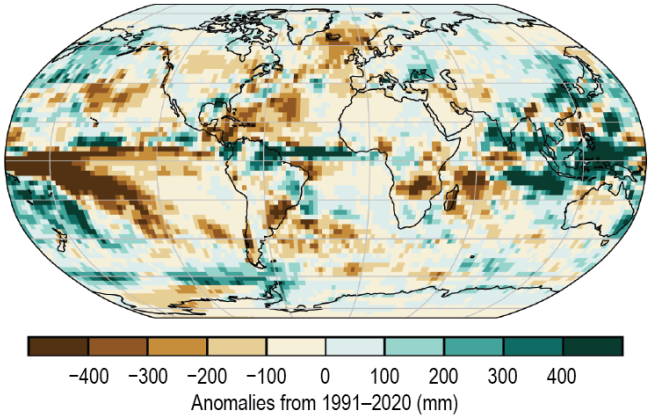

(l) Rx1day Anomalies

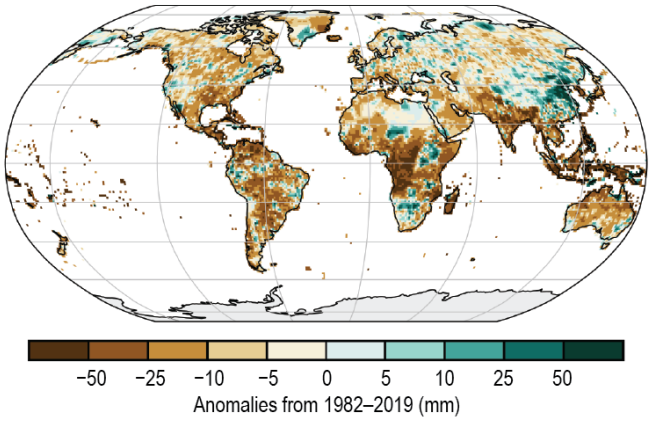

(m) Cloudiness

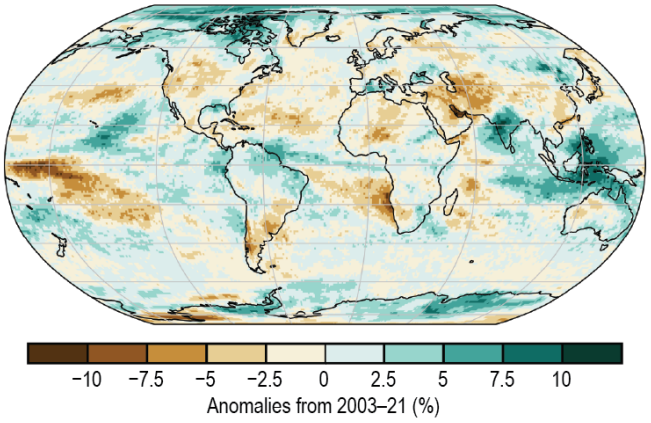

(n) Runoff

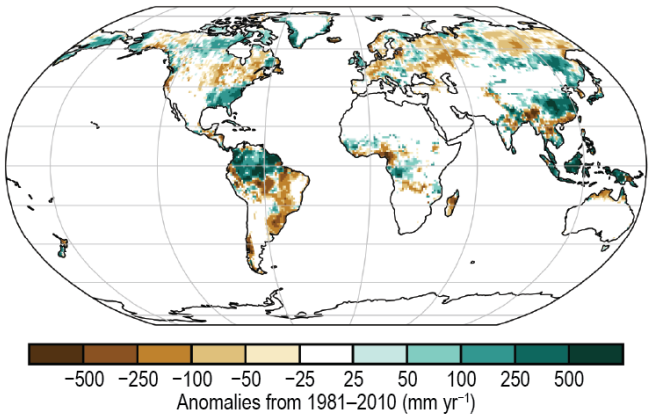

Plate 2.1. (cont.) (h) HadISDH surface relative humidity anomalies (%rh); (i) MERRA2 TCWV anomalies (%). Data from GNSS stations are plotted as filled circles; (j) "All sky" microwave-based UTH anomalies (%rh); (k) GPCP v2.3 annual mean precipitation anomalies (mm yr^{-1}); (l) GPCC maximum 1-day (Rx1day) annual precipitation anomalies (mm); (m) MODIS Aqua C6.1 cloud fraction annual anomalies (%); (n) ELSE (Ensemble Land State Estimator) global distribution of runoff anomalies (mm yr^{-1});

(o) River Discharge

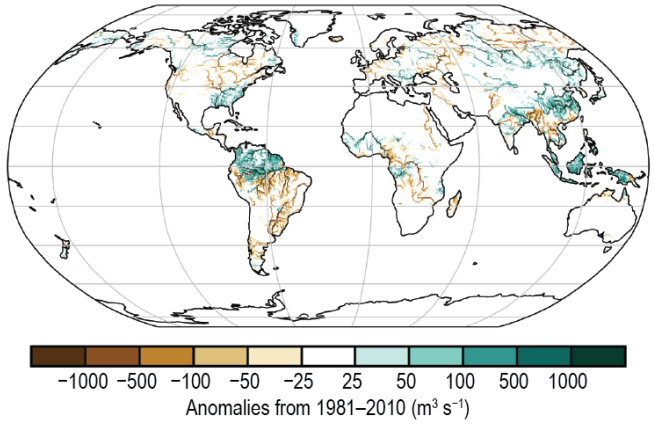

(p) Terrestrial Water Storage

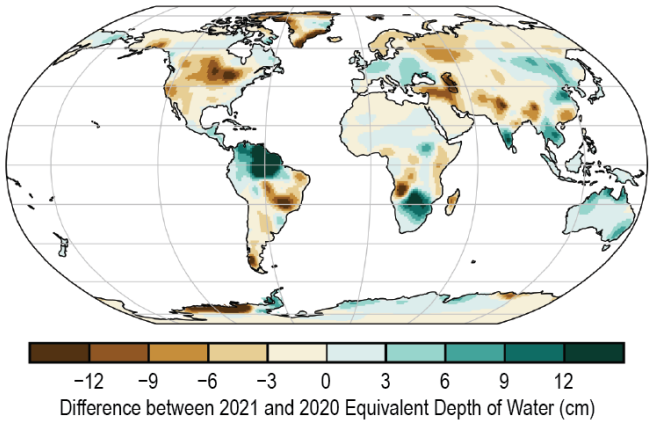

(q) Soil Moisture

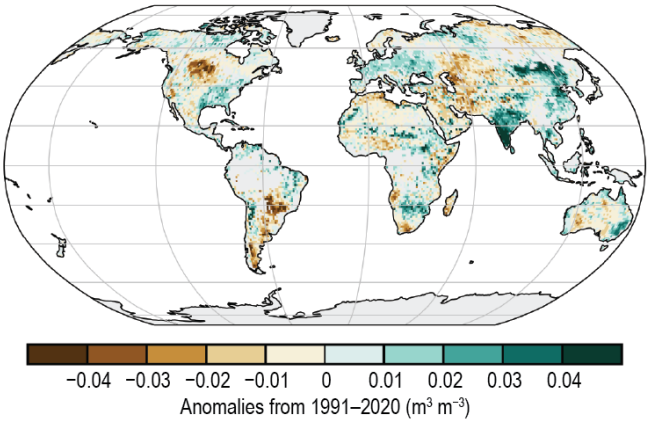

(r) Drought

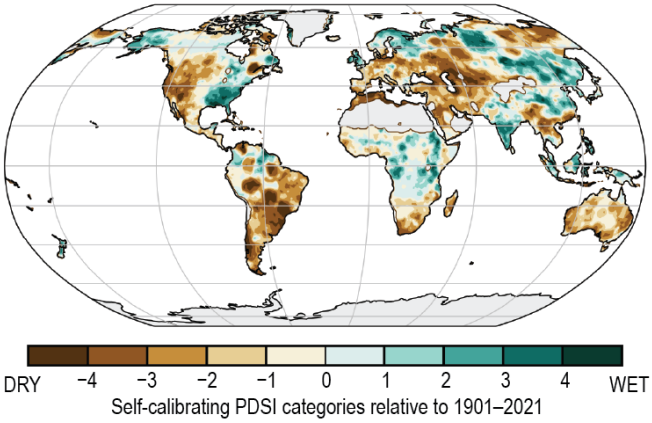

(s) Land Evaporation

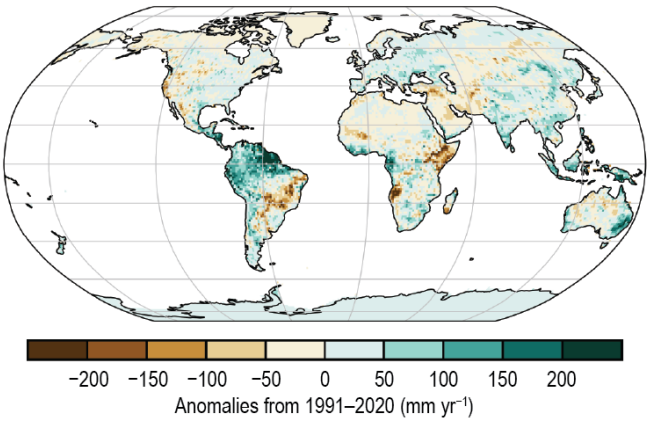

(t) Sea Level Pressure

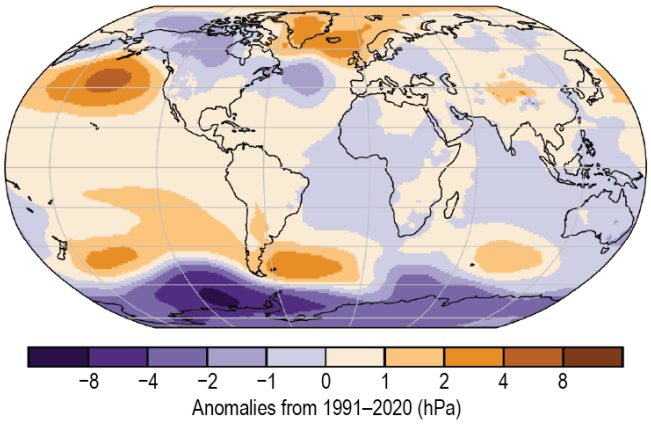

Plate 2.1. (cont.) (o) ELSE global distribution of river discharge anomalies ($m^3 s^{-1}$); (p) GRACE and GRACE-FO difference in annual-mean terrestrial water storage between 2021 and 2020 (cm); (q) ESA CCI average surface soil moisture anomalies ($m^3 m^{-3}$); (r) Mean scPDSI for 2021. Droughts are indicated by negative values (brown), wet episodes by positive values (green); (s) GLEAM land evaporation anomalies (mm yr^{-1}); (t) ERA5 sea level pressure anomalies (hPa);

(u) Surface Winds

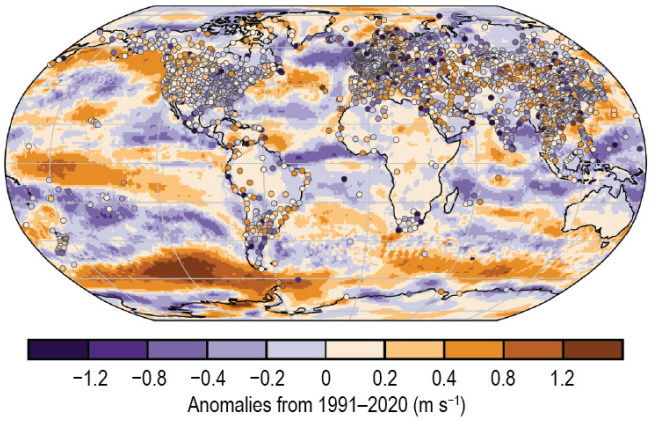

(v) Upper Air (850-hPa) Eastward Winds

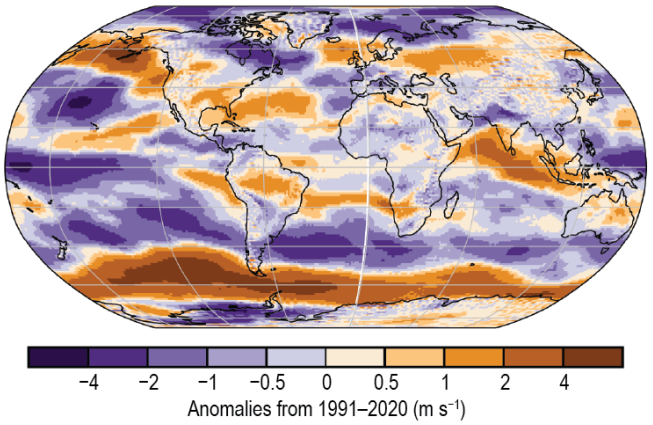

(w) Total Aerosol

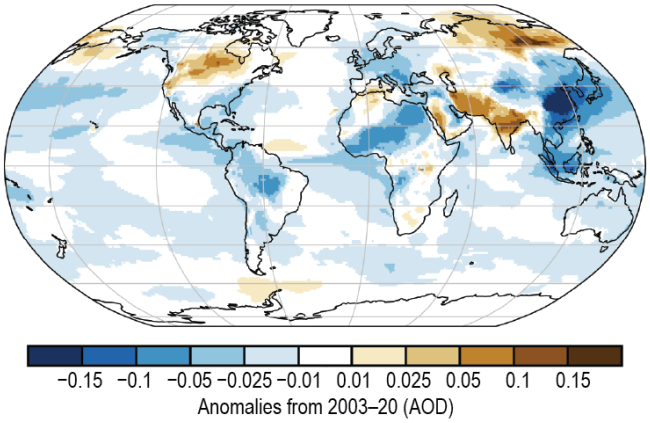

(x) AOD Ratio

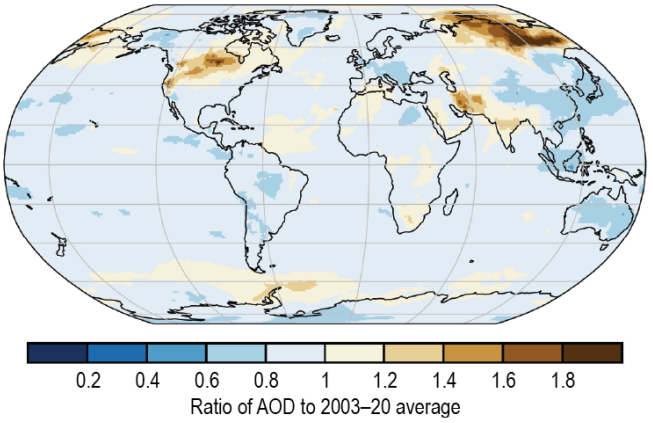

(y) Extreme Aerosol Days

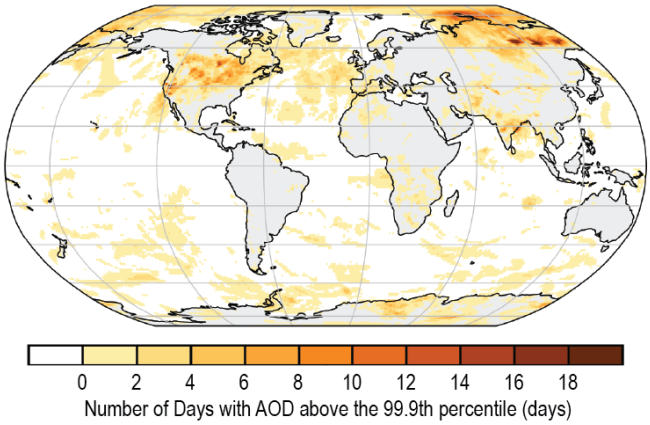

(z) Stratospheric (Total Column) Ozone

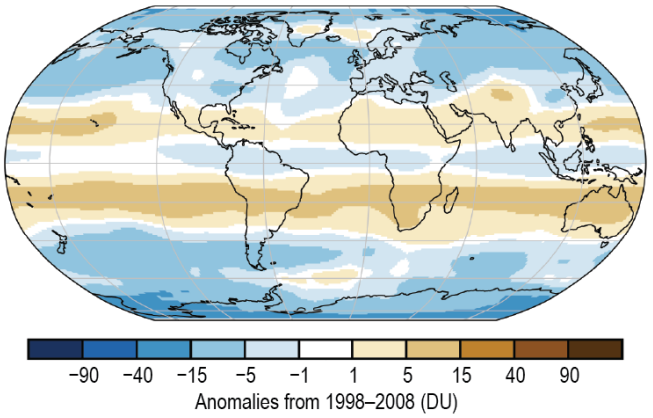

(aa) OMI/MLS Tropospheric Column Ozone

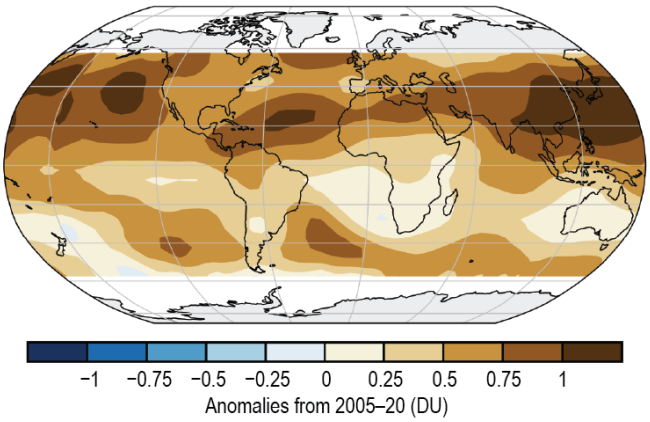

Plate 2.1. (cont.) (u) Surface wind speed anomalies (m s^{-1}) from the observational HadISD3 dataset (land, circles), the ERA5 reanalysis output (land, shaded areas), and RSS satellite observations (ocean, shaded areas); (v) ERA5 850-hPa eastward wind speed anomalies (m s^{-1}); (w) Total aerosol optical depth (AOD) anomalies at 550 nm; (x) Ratio of total AOD at 550 nm in 2021 relative to 2003–20; (y) Number of days with AOD above the 99.9th percentile. Areas with zero days appear as the white/gray background; (z) GOME-2C total column ozone anomalies relative to the 1998–2008 mean from GSG merged dataset (DU); (aa) OMI/MLS tropospheric ozone column anomalies for 60°S–60°N (DU);

(ab) Carbon Monoxide

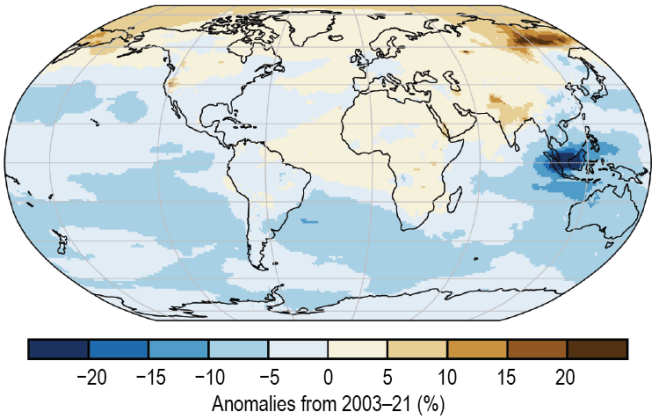

(ac) Land Surface Albedo in the Visible

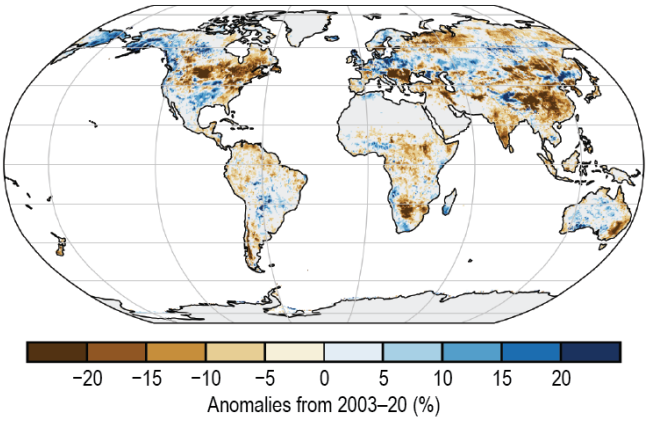

(ad) Land Surface Albedo in the Near-Infrared

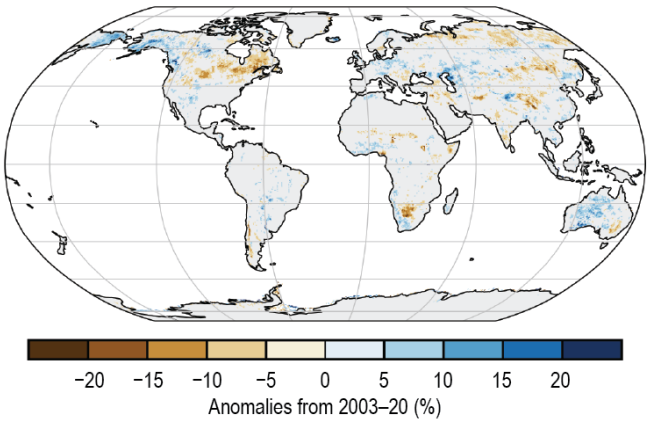

(ae) Fraction of Absorbed Photosynthetically Active Radiation

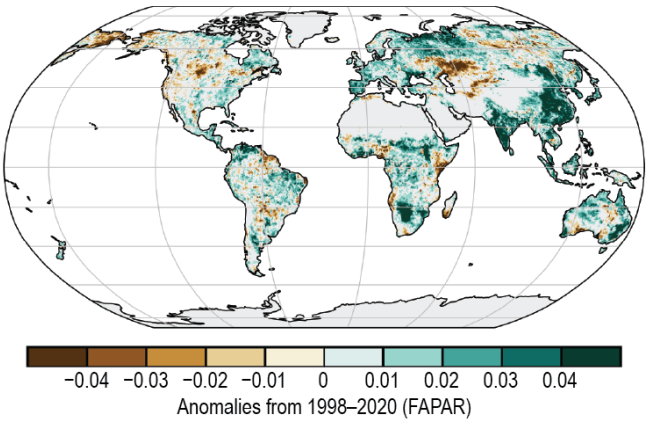

(af) Carbon Emissions from Biomass Burning

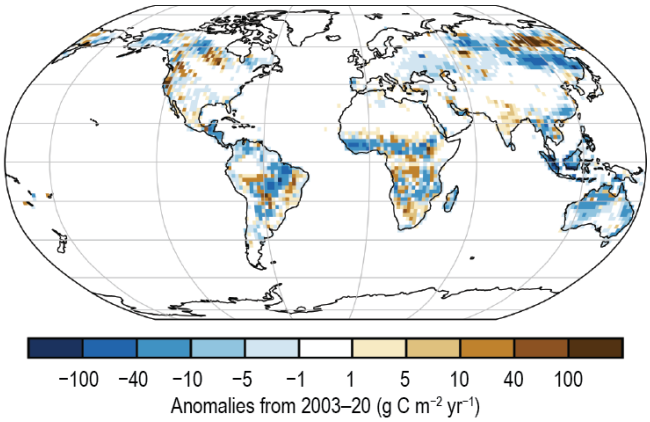

(ag) Vegetation Optical Depth

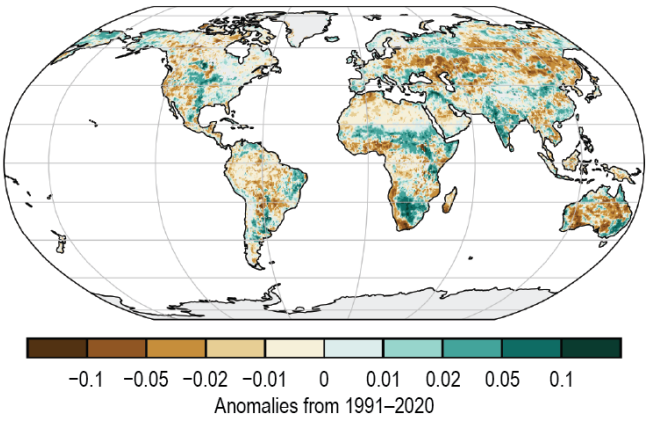

Plate 2.1. (cont.) (ab) CAMS reanalysis total column CO anomalies (%); (ac) Land surface visible broadband albedo anomalies (%); (ad) Land surface near-infrared albedo anomalies (%); (ae) FAPAR anomalies; (af) GFASv1.4 carbonaceous emission anomalies (g C m^{-2} yr^{-1}) from biomass burning; (ag) VODCA Ku-band VOD anomalies.

b. Temperature

1. GLOBAL SURFACE TEMPERATURE—A. Sánchez-Lugo, C. Morice, J. P. Nicolas, and A. Argüez

The year 2021 was among the seven warmest years since global records began in the mid-to-late 1800s, with a temperature departure between +0.21° and +0.28°C, according to six global temperature datasets (Table 2.1). Depending on the dataset, 2021 was either the fifth, sixth, or equal with 2018 as sixth-warmest year on record (Fig. 2.1). These datasets consist of four independent global in situ surface temperature analyses (NASA-GISS, Lenssen et al. 2019; HadCRUT5, Morice et al. 2021; NOAAGlobalTemp, Zhang et al. 2019; Berkeley Earth, Rhode and Hausfather 2020) and two global atmospheric reanalyses (ERA5, Hersbach et al. 2020, Bell et al. 2021; JRA-55, Kobayashi et al. 2015).

Table 2.1. Temperature anomalies (°C) and uncertainties (where available) for 2021 (1991–2020 base period). Where uncertainty ranges are provided, the temperature anomalies correspond to the central values of a range of possible estimates. Uncertainty ranges represent a 95% confidence interval. Note that for the HadCRUT5 column, land values were computed using the CRUTEM.5.0.1.0 dataset (Osborn et al. 2021), ocean values were computed using the HadSST.4.0.1.0 dataset (Kennedy et al. 2019) and global land and ocean values used the HadCRUT.5.0.1.0 dataset.

Global	NASA-GISS	HadCRUT5	NOAA GlobalTemp	Berkley Earth	ERA5	JRA-55
Land	+0.40	+0.32 ± 0.11	+0.41 ± 0.14	+0.35 ± 0.03	+0.41	+0.33
Ocean	+0.14	+0.19 ± 0.06	+0.15 ± 0.16	—	+0.22	+0.16
Land and Ocean	+0.24 ± 0.05	+0.22 ± 0.03	+0.22 ± 0.15	+0.24 ± 0.03	+0.28	+0.21

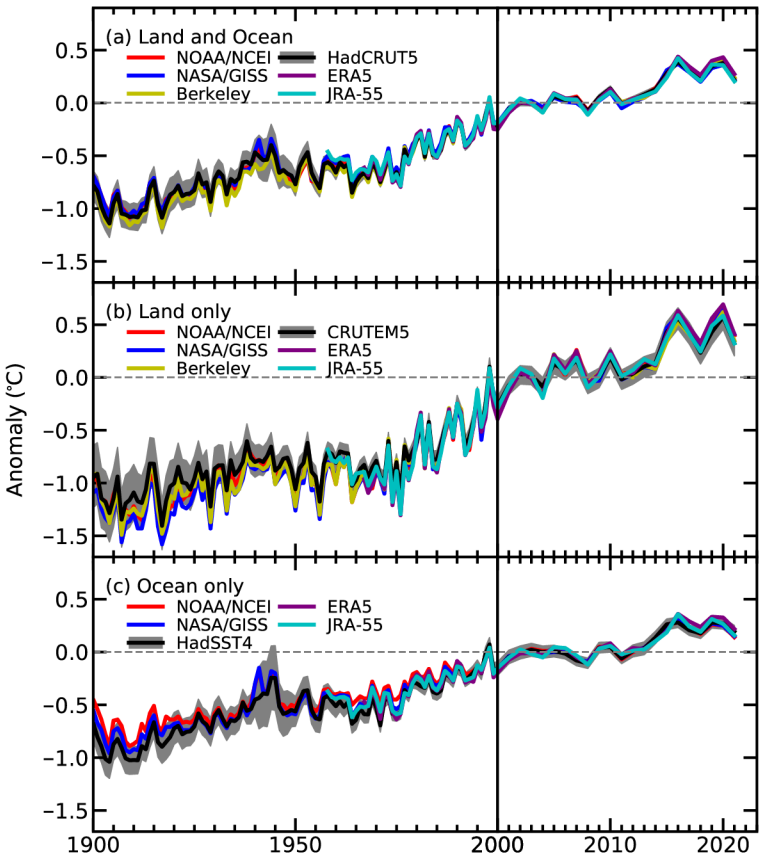

Fig. 2.1. Global average surface air temperature anomalies (°C; 1991–2020 base period). In situ estimates are shown for NOAA/NCEI (Zhang et al. 2019), NASA-GISS (Lenssen et al. 2019), Berkeley Earth (Rhode and Hausfather 2020), HadCRUT5 (Morice et al. 2021), CRUTEM5 (Osborn et al. 2021), and HadSST4 (Kennedy et al. 2019). Reanalysis estimates are shown from ERA5 (Hersbach et al. 2020), including from the preliminary ERA5 back-extension (Bell et al. 2021) for 1967–2021, and JRA-55 (Kobayashi et al. 2015). Please note change in x-axis scale pre/post 2000.

The six datasets all agree that the last seven years (2015–21) were the seven warmest years on record. Similarly, the datasets agree that the global average surface temperature has increased at an average rate of 0.08°–0.09°C decade^{-1} since 1880 and at a rate more than twice as high since 1981 (0.18°–0.20°C decade^{-1}, depending on the dataset).

The year began with a cold phase of the El Niño-Southern Oscillation (ENSO; see section 4b), also known as La Niña, across the eastern and central tropical Pacific Ocean, helping cool global temperatures slightly. The month of February had the smallest temperature anomaly of the year for the globe and was the coldest February since 2014, with global temperatures close to the 1991–2020 base period. La Niña dissipated by June, but re-emerged in August. With the exception of February, each month during 2021 had a global temperature that was above the 1991–2020 average.

While it is common, and arguably expected, for each newly completed year to rank as a top 10 warmest year (see Arguez et al. 2020), the global annual temperature for 2021 was considerably lower than we would expect due to the secular upward trend alone, with trend-adjusted anomalies registering between the 10th and 40th percentiles (depending on the dataset) following the Arguez et al. (2020) approach. These relatively cool conditions observed in 2021 are generally consistent with the typical cooling influence of La Niña. Moreover, trend-adjusted anomalies for 2021 are similar to the values recorded over the relatively cool years from 2011 to 2014, a period that also predominantly exhibited cooler-than-normal ENSO index values.

The year 2021 was characterized by above-average temperatures across much of the globe (Plate 2.1a; Appendix Figs. A2.1–A2.4), in particular across a large swath of North America (from the western United States to far northeastern Canada), as well as a region spanning northern Africa, western and central Asia, and into eastern Asia. Average to below-average temperatures prevailed across the central and eastern tropical Pacific Ocean and across parts of northwestern North America, Scandinavia, northern Russia, southern Africa, southern Australia, and parts of the southern oceans. Averaged as a whole, the global land-only surface air temperature for 2021 ranked among the sixth highest in the six datasets with a temperature departure of +0.32° to +0.41°C. The globally averaged SST was either sixth or seventh highest on record at +0.14° to +0.22°C, depending on the dataset.

Even though each dataset might differ slightly on the annual rankings and anomalies, it is worth noting that these differences are small and that, overall, temperature anomalies for each dataset are in close agreement (for more details see Simmons et al. 2017, 2021; Morice et al. 2021). Global atmospheric reanalyses use a weather prediction model to combine information from a range of satellite, radiosonde, aircraft, and other in situ observations to reconstruct historical weather and climate across the whole globe. While reanalyses may show regional differences from in situ surface temperature analyses because of regional model biases and changes in the observation network, they have been shown to agree well in well-observed regions (Simmons et al. 2017, 2021). Here, the data from ERA5 and JRA-55 are processed as described in Sanchez-Lugo et al. (2021).

2. LAKE SURFACE WATER TEMPERATURE—L. Carrea, C. J. Merchant, and R. I. Woolway

In 2021, the worldwide averaged satellite-derived lake surface water temperature (LSWT) warm-season anomaly was +0.60°C with respect to the 1996–2016 baseline, the highest since the beginning of the record in 1995, comparable with 2016. The mean LSWT trend during 1995–2021 is +0.24° ± 0.01°C decade^{-1} (Fig. 2.2a), broadly consistent with previous analyses (Woolway et al. 2017, 2018; Carrea et al, 2019, 2020, 2021). The warm-season anomalies for each lake are shown in Plate 2.1b, with 78% having positive (i.e., above-average temperature) and 22% negative (i.e., below-average) anomalies.

Globally, distinct regions of coherent above- and below-average LSWT anomaly can be seen. Almost half (45%) of the observed lakes show LSWT anomalies exceeding +0.5°C, with 3% having anomalies higher than +3°C. The highest positive anomalies were located across the Tibetan Plateau, in the northwest United States, and in the Middle East and Pakistan. Negative anomalies

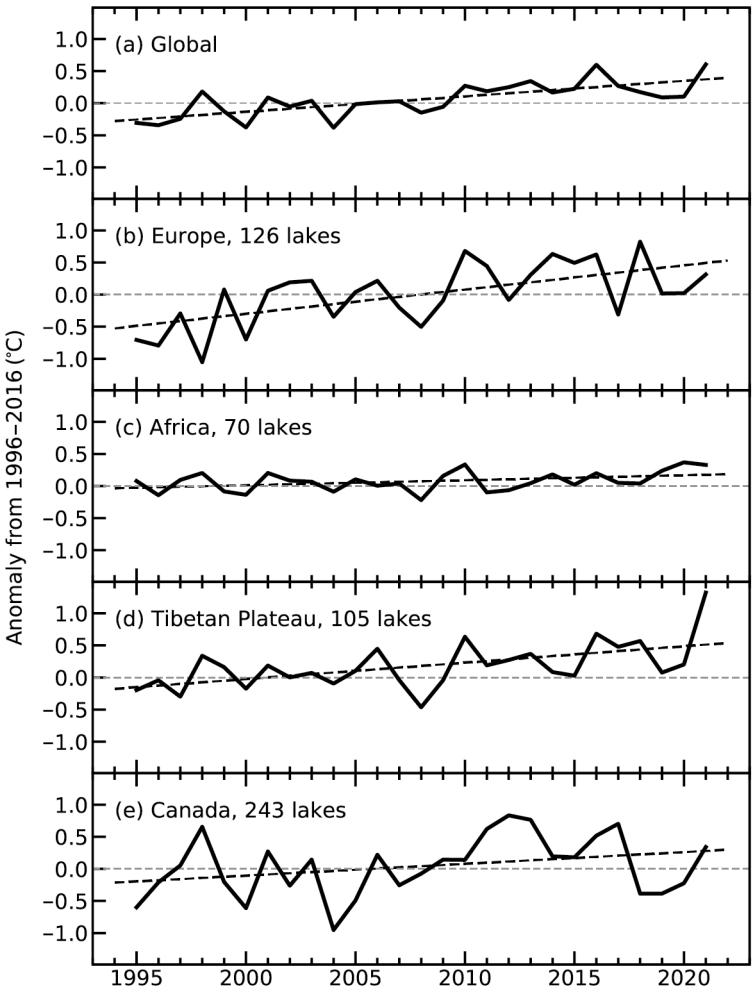

Fig. 2.2. Annual time series of satellite-derived warm-season lake surface water temperature anomalies (°C; 1996–2016 base period) from 1995 to 2021 for (a) more than 900 lakes distributed globally, (b) Europe, (c) Africa, (d) Tibet, and (e) Canada.

were mostly in South America (except Patagonia), Australia, and in high northern latitudes, including Alaska, Greenland, and eastern Russia (Plate 2.1b). Two lakes in the latter region had the most negative anomalies (below –3°C).

Four regions are considered in more detail: Canada, Europe, Tibet, and Africa (Fig. 2.3). The warm-season (July–September) LSWT anomalies calculated from the satellite data are consistent with the averaged surface air temperature (SAT) anomalies and show a warming tendency (from 1995) of +0.38° ± 0.03°C decade^{-1} in Europe and +0.18° ± 0.03°C decade^{-1} in Canada (Figs. 2.2b,e). In Africa, the tendency is closer to neutral (+0.08° ± 0.01°C decade^{-1}), while in Tibet the warming tendency has increased with respect to the previous years due to the exceptionally positive 2021 anomaly (Figs. 2.2c,d). In the Tibetan area, all but two lakes had positive anomalies in 2021, with an average of +1.3°C. This is exceptionally high for the region, being 3.8 times the standard deviation of the average anomalies (1996–2016) and the highest on record. In Europe, below-average anomalies in northern Europe (29 lakes) are less prevalent than above-average anomalies (97 lakes), with an average anomaly of +0.31°C. In Africa, 74% of the 70 lakes recorded positive anomalies. Several of the highest anomalies occurred north of the equator, contributing to an average continental anomaly of +0.33°C. In Canada, 80% of the lakes had positive anomalies, with an average LSWT anomaly of +0.34°C. The 2021 warm-season anomalies for Lakes Superior, Michigan, and Huron were computed using both in situ measurements and satellite data. The 2021 in situ anomalies were +3.36°C, +1.47°C, and +1.00°C, and the satellite were +2.49°C (the highest on record), +0.85°C, and +0.99°C, respectively. The differences are mostly because the in situ measurements are taken at only some sites on the lake while the satellite observations

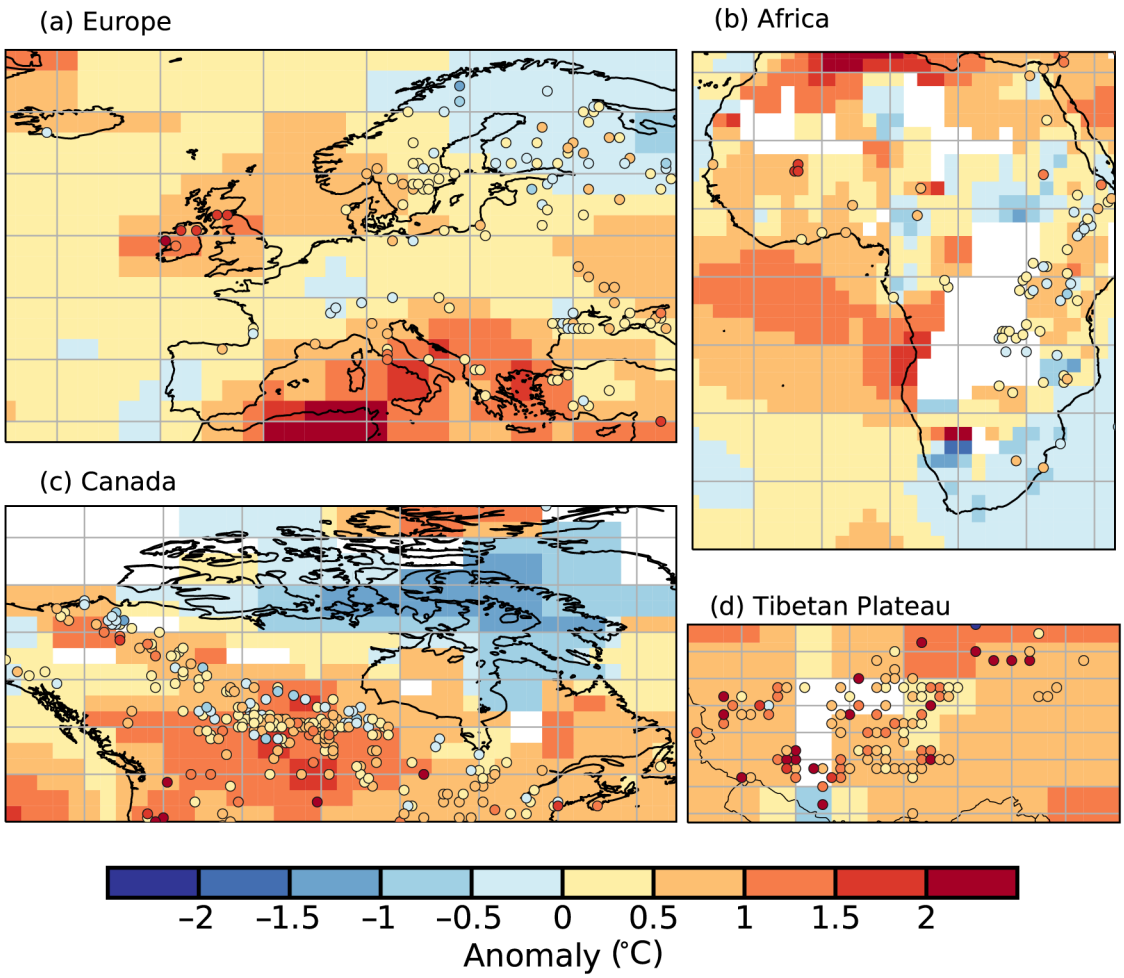

Fig. 2.3. Individual lake temperature anomalies (°C, colored dots) and 2-m air temperature anomalies (°C) in 2021 in (a) Europe, (b) Africa, (c) Canada, and (d) Tibet. These values were calculated for the warm season (Jul–Sep in the extratropical NH; Jan–Mar in the extratropical SH; Jan–Dec in the tropics) with reference to the 1996–2016 base period.

cover the whole lake. The spatial distribution of 2021 anomalies for these lakes (Appendix Fig. A2.5) all have positive values, but with strong variation across each of the lakes. The LSWT warm-season averages for midlatitude lakes are computed for summers, (July–September [JAS] in the extratropical Northern Hemisphere and January–March [JFM] in the extratropical Southern Hemisphere) and whole-year averages (January–December) are presented for tropical lakes (within 23.5° of the equator). LSWT time series were derived from satellite observations from the series of Along Track Scanning Radiometers (ATSRs), the Advanced Very High Resolution Radiometers (AVHRRs) on MetOp A and B (1996–2019), and the Sea and Land Surface Temperature Radiometers (SLSTRs) on Sentinel3A and 3B (2019–2021). The retrieval method of MacCallum and Merchant (2012) was applied on image pixels filled with water according to both the inland water dataset of Carrea et al. (2015) and a reflectance-based water detection scheme. The satellite-derived LSWT data are spatial averages for each of a total of 963 lakes, for which high quality temperature records were available in 2021. The satellite-derived LSWT data were validated with in situ measurements with a good agreement (average satellite minus in situ temperature difference less than 0.5°C). Lake-wide average surface temperatures have been shown to give a more representative picture of LSWT responses to climate change than single-point measurements (Woolway and Merchant 2018). The averaged surface air temperature was calculated from the GHCN v4 (250-km smoothing radius) data of the NASA GISS surface temperature analysis (Hansen et al. 2010; GISTEMP Team 2022). The in situ data for the Great Lakes were collected by the NOAA National Data Buoy Center.

3. NIGHT MARINE AIR TEMPERATURE—R. C. Cornes, T. Cropper, R. Junod, and E. C. Kent

Globally gridded datasets of night marine air temperature (NMAT) provide a useful and independent comparison against sea surface temperature (SST) data. Air temperature values have been recorded onboard vessels for centuries and continue to the present through the Voluntary Observing Ship (VOS) network. These observations can be used to construct global datasets of marine air temperature back to at least 1900. While temperature values are recorded throughout the day and night on these ships, only the nighttime observations are currently used to construct the gridded values due to the heating bias that arises in the daytime data, as a result of the superstructure of the ship.

Global mean temperature anomalies calculated from the two gridded NMAT datasets (CLASSnmat, Cornes et al. 2020 and UAHNMAT, Junod and Christy 2020) show a marked cooling in 2021 compared to 2020 but also relative to values over the last decade (Fig. 2.4). For CLASSnmat, the average global temperature anomaly (relative to the 1961–90 average) during 2021 was +0.38°C, a value comparable to that recorded in 2006. As such, 2021 was only the 13th highest in the series, which dates back to 1880. For UAHNMAT, the global mean anomaly value was +0.33°C in 2021; this is also the 13th highest annual mean temperature in its 1900–2021 record. These values contrast with the HadSST4 sea surface temperature dataset (Kennedy et al. 2019), which shows that 2021 was the fifth highest in the 1850–2021 period, with a global average anomaly of

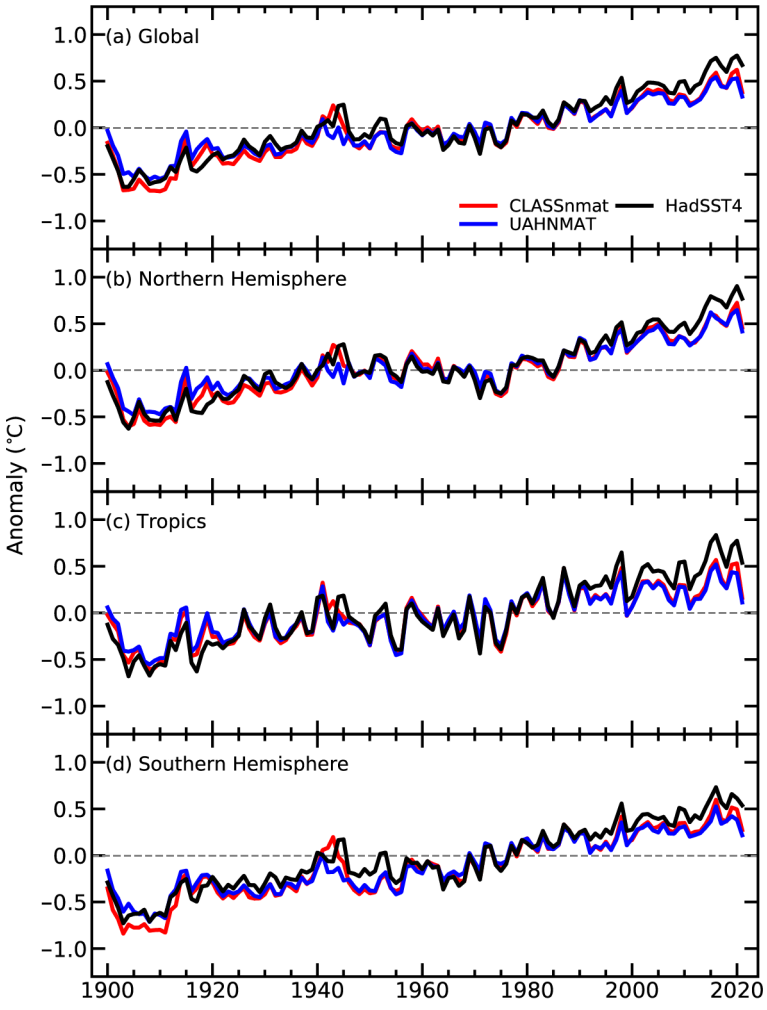

Fig. 2.4. Annual mean temperature anomalies (°C; 1961–90 base period) calculated from the CLASSnmat, UAHNMAT, and HadSST4 datasets averaged over four domains. The tropics is defined as the latitude range 20°S–20°N and the Northern (Southern) Hemisphere is defined as north (south) of 0°. The averages only include values that are common to all three datasets for a given year, and since UAHNMAT are only available after 1900, only values for the period 1900–2021 are plotted.

Table 2.2. Annual average temperature anomalies (°C) across four regions for 2021 for the CLASSnmat, UAHNMAT, and HadSST4 datasets (1961–90 base period). The values in parentheses indicate the ranking (1 = highest) of these values over the period 1900–2021.

	Global	Northern Hemisphere	Southern Hemisphere	Tropics
CLASSnmat2.1	+0.38 (13)	+0.46 (11)	+0.27 (17)	+0.16 (31)
UAHNMAT	+0.33 (13)	+0.42 (11)	+0.22 (25)	+0.11 (38)
HadSST4	+0.67 (5)	+0.77 (4)	+0.54 (7)	+0.54 (10)

+0.67°C. A similar difference of about −0.3°C in the 2021 NMAT averages, relative to HadSST4, is seen across other large-scale regions (Table 2.2). In this comparison of the three datasets, co-located gridded data are used to avoid any complication to the analysis from differing global coverage. In particular, the NMAT datasets have poor coverage south of 40°S.

The principal reason for the lower temperature anomalies during 2021, compared to recent years, is the extended La Niña conditions that were present during the year (see section 4b). Historically, the NMAT data show a clear response to La Niña conditions, with a pattern across the Pacific that is similar in form and magnitude to that observed in the SST data (Figs. 2.5a–c). However, differences are apparent in the NMAT data compared to SST beyond the typical La Niña pattern and is the reason for the lower global average anomalies in the two NMAT datasets for 2021 compared to 2020 (Figs. 2.5d–f). The negative temperature anomalies in the central Pacific are more widespread in NMAT compared to SST, and the two nodes of positive anomalies in the North and southwestern Pacific are not clearly defined in either NMAT dataset. In addition, while positive anomalies for 2021 are evident in most grid cells in the SST data across the Atlantic and Indian Oceans, these are much weaker in the NMAT datasets, and there are many more grid cells in these regions with negative anomalies. Some of these regional differences can be explained by different data availability in the SST and NMAT datasets. Most notably, across the southern Pacific there is greater uncertainty in the NMAT values because there are few ship observations in the region; this is mitigated in the SST through the use of drifting buoy measurements in the grid cell averages. However, this does not fully explain the differences seen in these results as there is relatively good observational coverage in the NMAT datasets across the North Atlantic.

The data used in Fig. 2.5 were detrended, prior to averaging, in order to remove the long-term trend from the data by calculating the residuals from a linear regression fit to the data per grid cell. This detrending allows the response of the SST and NMAT data to La Niña conditions to be compared more directly. Over approximately the last 50 years, global mean NMAT has increased at a slower rate than SST (Fig. 2.4; Cornes et al. 2021); this accounts for the difference in rankings in the NMAT datasets compared to HadSST4. The reasons for this trend-differential are not well understood, and work is ongoing to determine if this is a true feature of the data or an artifact in the NMAT and/or SST datasets. It is also not clear if the interannual variability, and notably the relatively cool conditions observed during 2021, is related to this difference in long-term trends since taking into account this trend differential, the −0.3°C offset between NMAT and SST in 2021 was unusually large.

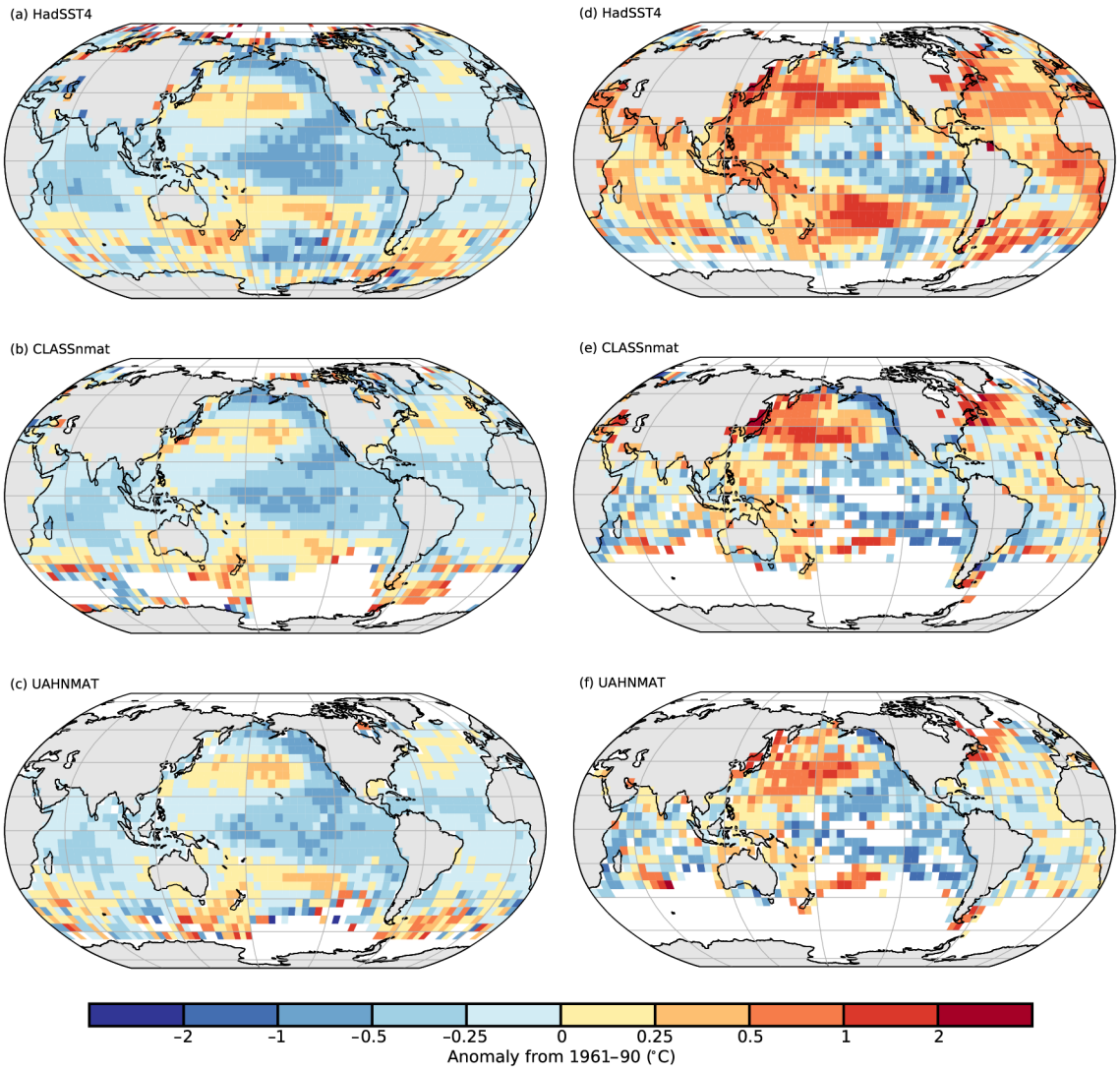

Fig. 2.5. Average detrended temperature anomalies (°C) in the HadSST4, CLASSnmat, and UAHNMAT datasets calculated as (a–c) the mean of nine years between 1955 and 2000 in the year following a La Niña event and (d–f) for the year 2021. The years used in (a–c) are 1955, 1956, 1965, 1971, 1974, 1976, 1989, 1999, and 2000. Grid-cell values are marked missing if there are fewer than five months complete per year. In (a–c), grid-cells are marked as missing if there are fewer than five of the nine years complete.

4. LAND AND SURFACE MARINE TEMPERATURE EXTREMES—R. J. H. Dunn, M. G. Donat, R. W. Schlegel, and S. E. Perkins-Kirkpatrick

The average number of warm days (TX90p, Table 2.3) over land was the second most on record, according to the observational dataset GHCNDEX (Donat et al. 2013; Fig. 2.6, using the 1961–90 reference period), with 68 days, though we note the incomplete spatial coverage. The average number of cool nights (TN10p) was 22, which was 14 fewer than the expected average, but not at record values. The expected values for these two indices are 36.5 days over the reference period, which is used in their calculation. The average values of the spatially complete reanalysis dataset ERA5 (Hersbach et al. 2020, using the 1981–2010 reference period) over land are similar to those from GHCNDEX, and TX90p was at its third highest value at 65.6 days, after 2016 and 2020 (Fig. 2.6). The spatial patterns of these indices (Plates 2.1d,e; Appendix Fig. A2.6) show especially high numbers of warm days over Africa and Asia and relatively low numbers over Australia, which also had high numbers of cool nights in 2021. Below we describe some of the low and high temperature events of 2021 in more detail (see also WMO 2022), primarily from the global north where these details were more readily available.

Table 2.3. WMO Extremes indices from the Expert Team for Climate Change Detection and Indices (ETCCDI) used in this section and their definitions (Zhang et al. 2011). In GHCNDEX, these indices are calculated using 1961–90 as the reference period, and thus these anomalies use the same period. As a result of their construction, comparison, or conversion to other base periods is not simple (Dunn and Morice 2022).

Index	Name	Definition
TX90p	Number of warm days	Number of days in a year where the daily maximum temperature was above the 90th percentile of the 1961–90 values.
TN10p	Number of cool nights	Number of days in a year where the daily minimum temperature was below the 10th percentile of the 1961–90 values.

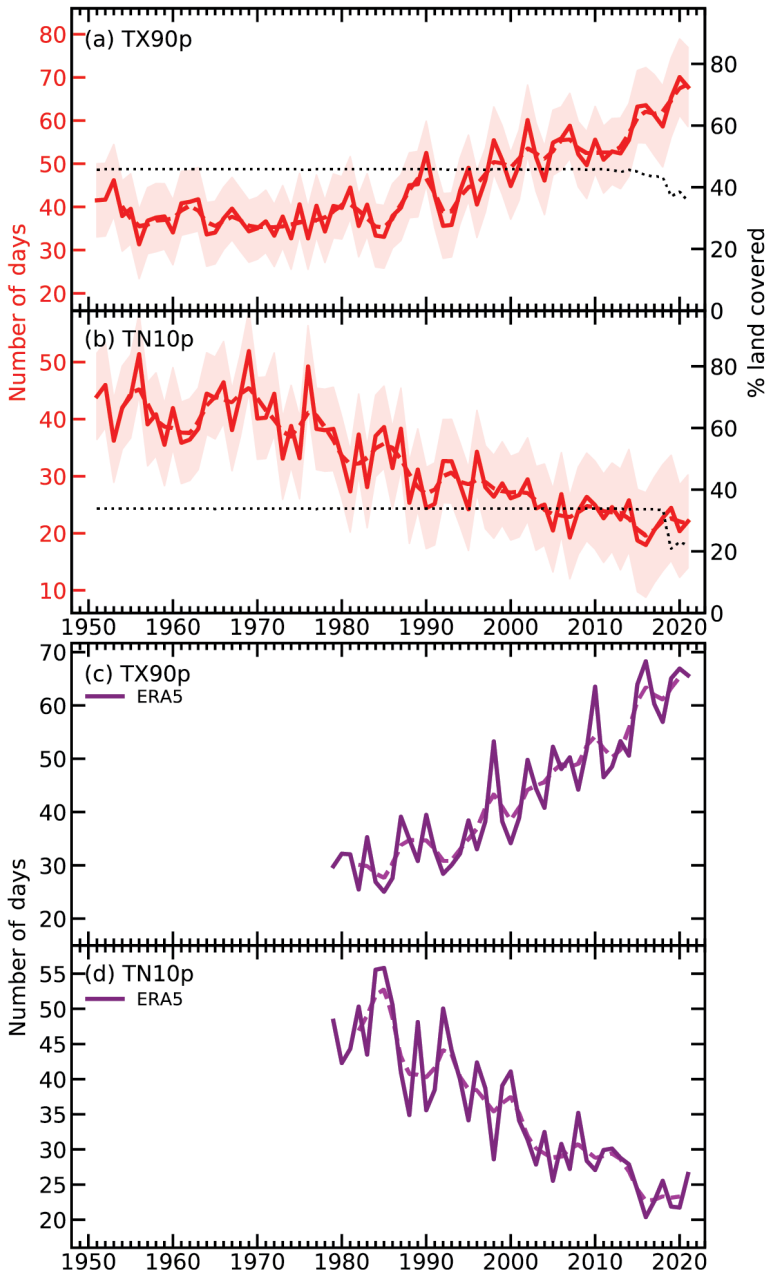

Fig. 2.6. Timeseries of (a),(c) number of warm days (TX90p) and (b),(d) number of cool nights (TN10p) from GHCNDEX (a),(b) and ERA5 (c),(d). The dashed lines show the smoothed behavior from a binomial filter, and the coverage uncertainty (following Brohan et al. 2006) is shown by the shading in (a) and (c). The dotted black lines in (a),(b) show the percentage of land grid boxes with sufficient temporal coverage over the record which have data in each year.

During 2021 there were a number of notable cold periods, starting with the after effects of a major storm on the Iberian Peninsula in January, with widespread temperatures below –20°C in northeast Spain, and a new national record of –34.1°C set on 6 January at Clot del Tuc de la Llança (Appendix Table 2.1). In February, North America was affected by two major winter storms, leading to the coldest event across the continental United States in more than 30 years, reaching as far south as northern Mexico. Heating demand placed strain on the electrical power grid in Texas, resulting in up to 10 million people without power, and there were over 200 direct and indirect deaths related to this event (see section 7b2 for details).

Following a warm end to March, Europe had an abnormally cold April, with record low minimum temperatures for the month (Appendix Table 2.1). Western North America experienced exceptional heat waves during June and July. Temperatures of above 40°C occurred over a large area in June, with maximum temperatures more than 15°C above average. Lytton (British Columbia, Canada) reached 49.6°C on 29 June, a new Canadian national record 4.6°C above the previous record (Appendix Fig. A2.7; see Sidebar 7.1 for details). On 9 July, Death Valley (California) recorded 54.4°C, equaling the temperature measured in 2020 as the highest temperature on Earth since at least the 1930s. Many other stations reported new maximum records from these two events.

The Mediterranean region experienced a number of record-setting heatwaves in July and August, and a station near Syracuse, Sicily (Italy), recorded a provisional new European maximum temperature record of 48.8°C on 11 August (Appendix Table 2.1). On 5 July, Lapland (Finland) recorded 33.6°C in Kevo, the hottest day in the region for over a century; it was the second warmest summer (JJA) average in the 120-year Finnish national record (see section 7f for details). Around the Arabian Gulf, a high temperature of 50.4°C was recorded at Dammam, Saudi Arabia, on 31 July. Also, during July, and coinciding with the delayed 2020 Olympic Games, a heatwave over Japan broke all-time records at numerous stations (see Sidebar 7.4 for details). In the Southern Hemisphere, New Zealand recorded its warmest year on record, which included its warmest June on record, 2°C higher than the 1981–2010 average (see Sidebar 7.5 for details).

Analyzing data from NOAA OISST v2.1 (Huang et al. 2021), 57% of the surface of the ocean experienced at least one marine heatwave (MHW, Hobday et al. 2016) in 2021 (Fig. 2.7b), and 25% experienced at least one marine cold-spell (MCS, Fig. 2.7d). Category 2 Strong MHWs (Hobday et al. 2018) were the most common (28%) for the eighth consecutive year, whereas Category 1 Moderate MCSs have remained the most common (20%) since 1985. The ocean experienced a global average of 49 MHW days (13 MCS days), which is fewer than the 2020 average of 58 days (14 days) and the 2016 record of 61 days (1982 record of 27 days, Figs. 2.7a,c). This daily average equates to 13% (4%) of the surface of the ocean experiencing a MHW (MCS) on any given day (Figs. 2.7a,c). The equatorial Pacific and Southern Oceans showed a noticeable lack of MHWs in 2021 while experiencing nearly complete MCS coverage. Heat anomalies in the equatorial Pacific Ocean are tightly linked with ENSO, which was in a La Niña state most of the year (see section 2e1), a continuation from 2020. The relationship between extreme events in the Southern Ocean and broad climate indices is complex and still poorly understood, making this an opportune avenue of future research. Note that with the Hobday et al. (2016) MHW definition the long-term trend is not removed before detecting events. This means that warming (cooling) areas will generally experience more (fewer) MHWs in the present than in the past, with the inverse observed for MCSs.

GHCNDEX (Donat et al. 2013) is based on the daily GHCND dataset (Menne et al. 2012). The extremes indices developed by the former ETCCDI (WMO Expert Team in Climate Change Detection and Indices, Zhang et al. 2011) are calculated for each station and then interpolated onto a regular 2.5° grid. Reduced spatial coverage in the most recent years (Fig. 2.6) arises because of late arriving data; hence for complete global land coverage we also use the ERA5 reanalysis (Hersbach et al. 2020), not including the preliminary release of the 1950–78 data. The shorter temporal coverage means a different reference period needs to be used (1981–2010), which can lead to differences when comparing recent trends (Dunn et al. 2020; Yosef et al. 2021; Dunn and Morice 2022).

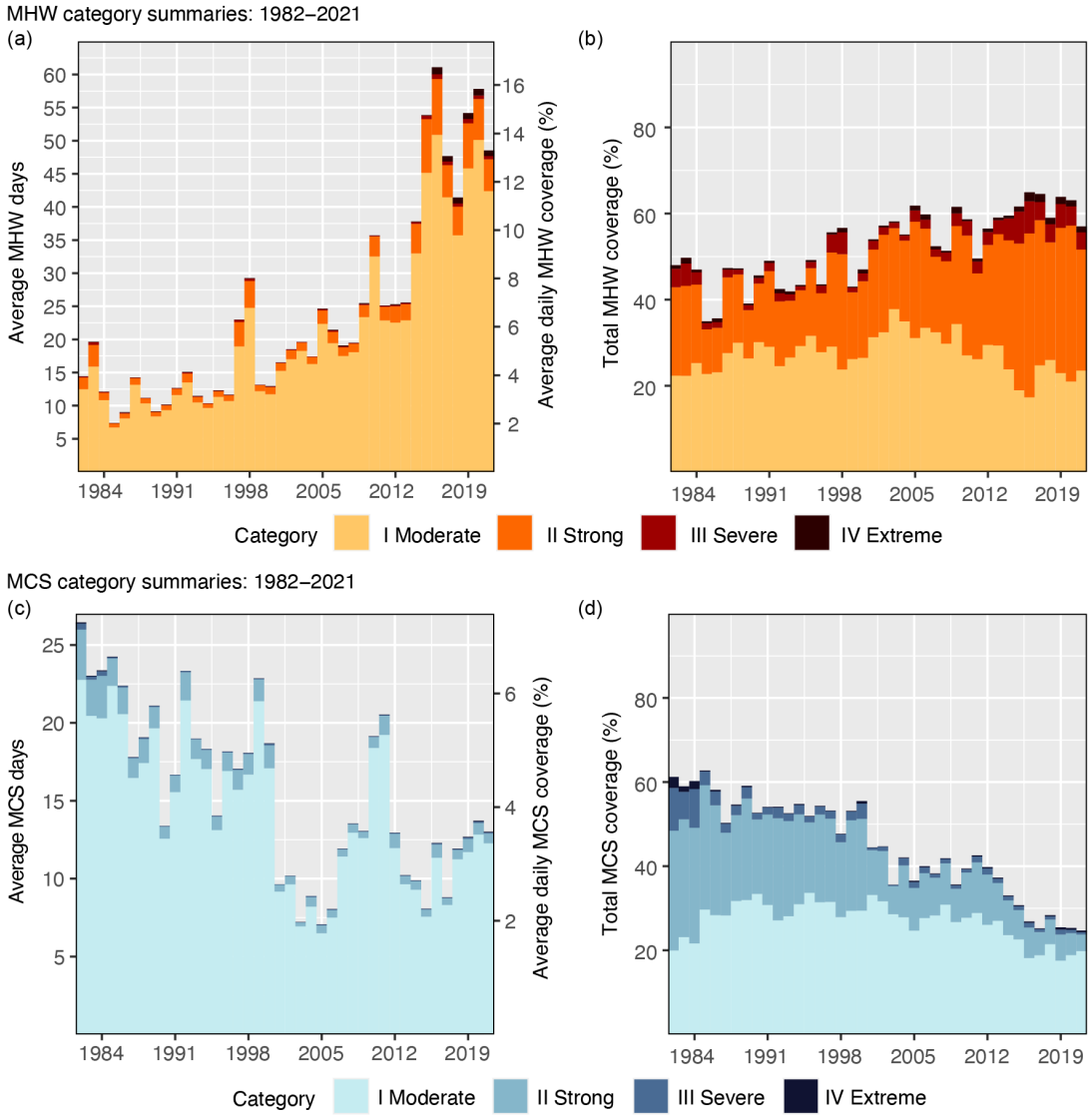

Fig. 2.7. Annual global marine heatwave (MHW; a,b) and marine cold-spell (MCS; c,d) occurrence from NOAA OISST using a climatology base period of 1982–2011. (a),(c) The average count of MHW/MCS days experienced over the surface of the ocean in 2021 (left y-axis), also expressed as the percent of the surface of the ocean experiencing a MHW/MCS on any given day (right y-axis). (b),(d) Total percent of the surface area of the ocean that experienced an MHW/MCS at some point during the year. The values shown are for the highest category of MHW/MCS experienced at any point.

5. TROPOSPHERIC TEMPERATURE—S. Po-Chedley, J. R. Christy, L. Haimberger, and C. A. Mears

The 2021 global lower-tropospheric temperature (LTT) was approximately 0.25°C higher (0.14°–0.34°C, depending on dataset) than the long-term climatological (1991–2020) average. This places 2021 among the 10 warmest years on record (since 1958) despite La Niña conditions during most of 2021, which typically reduce the temperature of the troposphere.

Earth's tropospheric temperature is influenced by several natural factors such as volcanic eruptions, solar variability, and internal climate variability. Anthropogenic emissions of greenhouse gases and aerosols also affect LTT and collectively contribute to long-term warming of the global troposphere (Table 2.4). Since August of 2020, the El Niño-Southern Oscillation (ENSO) has largely been in a La Niña state (Fig. 2.8; see section 4b), which corresponds to below-average central and eastern tropical Pacific Ocean SSTs and reduced tropical and global average tropospheric temperatures. The background warming trend and La Niña conditions combined in 2021 to create a global LTT that was higher-than-average, but not record-breaking (Fig. 2.9).

Table 2.4. Temperature trends (°C decade^{-1}) for global lower tropospheric temperature (LTT) and tropical tropospheric temperature (TTT) over the period 1958–2021 and 1979–2021, respectively. NASA MERRA-2 data begins in 1980. UW (Po-Chedley et al. 2015) and NOAA STAR (Zou and Wang 2011) data do not produce LTT products.

		LTT (90°S–90°N)		TTT (20°S–20°N)	
Start Year		**1958**	**1979**	**1958**	**1979**
Radiosonde	NOAA/RATPACvA2	0.18	0.22	0.17	0.19
	RAOBCOREv1.9	0.168	0.18	0.14	0.16
	RICHv1.9	0.18	0.20	0.18	020
Satellite	UAHv6.0	—	0.13*	—	0.13
	RSS v4.0	—	0.21	—	0.17
	UWv1.0	—	—	—	0.17
	NOAA STAR v4.1	—	—	—	0.23
Reanalyses	ERA5	—	0.18	—	0.16
	JRA-55	0.17	0.18	0.16	0.15
	NASA/MERRA-2	—	0.19	—	0.18
	Median	**0.18**	**0.19**	**0.17**	**0.17**

*The vertical sampling in UAH LTT is slightly different from other datasets and results in temperature trends that are approximately 0.01°C decade^{-1} smaller than other datasets.

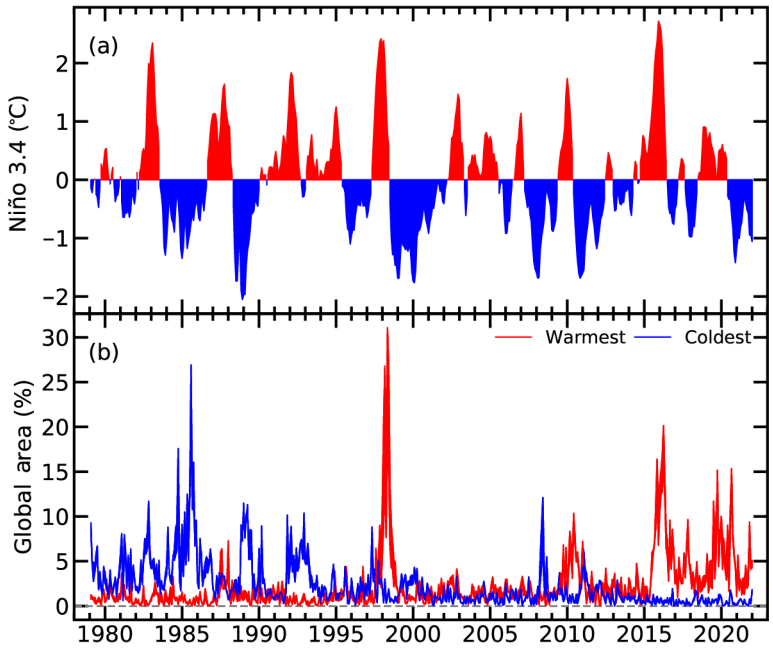

Fig. 2.8. (a) Sea surface temperature anomalies (°C, 1991–2020 base period) in the Niño 3.4 region in the central equatorial Pacific. Prolonged positive anomalies in red are associated with El Niño events; the reverse is true for La Niña events (in blue). (b) Fraction of Earth (%) with record high (red) and low (blue) monthly LTT values. The width of the line represents the difference between the UAH and RSS datasets.

The LTT anomaly pattern in 2021 is typical of La Niña conditions (Plate 2.1f; Yulaeva and Wallace 1994). Although La Niña events tend to reduce globally averaged LTT, some regions are associated with above-average LTT (Plate 2.1f), and approximately 5% of the planet experienced its highest annual mean LTT since 1979 (Fig. 2.8). Regions of record low annual mean LTT were sparse and represented less than 1% of global area (Fig. 2.8). Areas experiencing record high temperatures included the Pacific Ocean midlatitudes, the southwest Atlantic Ocean, the Middle East,

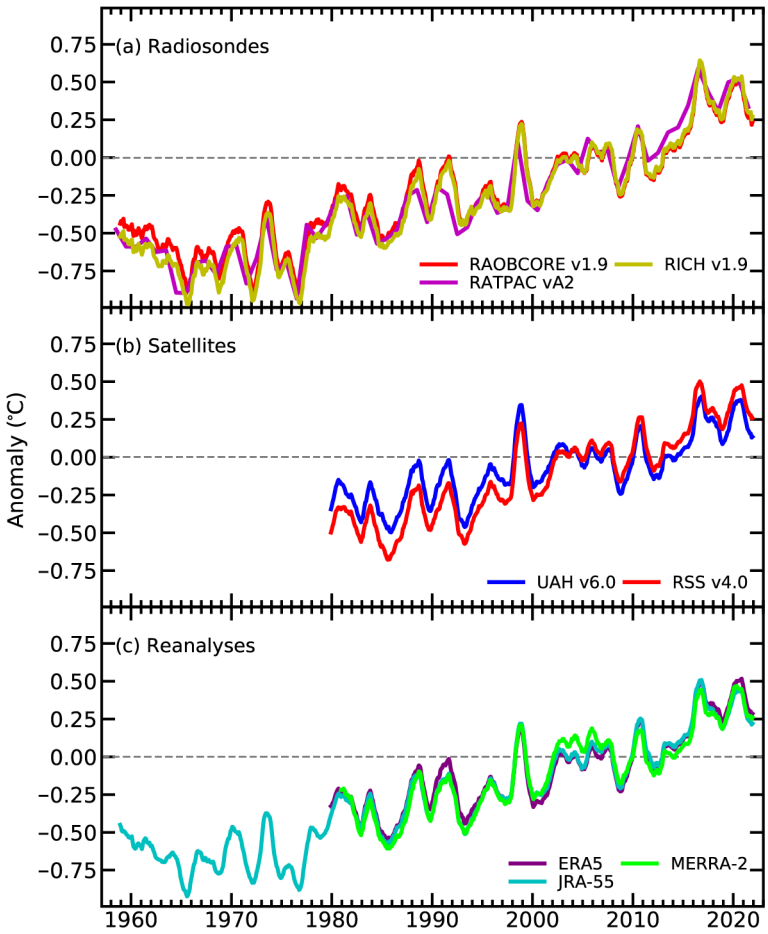

Fig. 2.9. Monthly average LTT anomalies (°C) for (a) radiosonde, (b) satellite, and (c) reanalysis datasets. Time series are smoothed using a 12-month running average. Annual averages are displayed for the RATPAC dataset. Anomalies are with respect to a 1991–2020 base period.

southwest China, and northeastern Canada. In contrast, the tropical eastern Pacific Ocean, regions along the West Antarctic coastline, and northwest Canada and Alaska exhibited below-average tropospheric temperatures in 2021.

Datasets of atmospheric temperature change are derived from balloon-based radiosonde measurements (RATPAC vA2, RICH v1.9, and RAOBCORE v1.9), satellite-based microwave sounding observations (RSS v4, UAH v6, UW v1, and NOAA STAR v4.1), and atmospheric reanalysis products (MERRA-2, ERA5, and JRA-55). Each dataset is constructed with different strategies to remove biases, resulting in slightly different time series. In the ERA5 and MERRA-2 reanalysis datasets, 2021 was the fifth-warmest year on record for global LTT (Hersbach et al. 2020; Gelaro et al. 2017). 2021 was the sixth-warmest year in the RATPAC, RICH, and RSS datasets (Free et al. 2005; Mears and Wentz 2016; Haimberger et al. 2012) and eighth in the JRA-55, RAOBCORE, and UAH datasets (Kobayashi et al. 2015; Spencer et al. 2017). In general, observations of the global LTT (Fig. 2.9) and tropical tropospheric temperature (TTT) have similar interannual variations, but exhibit non-negligible structural uncertainty for long-term trends, which range from 0.13° to 0.23°C decade^{-1} since 1979 (Table 2.4). The estimated trend uncertainty for individual satellite datasets is approximately 0.04°C decade^{-1} and the uncertainty in converting level temperatures to synthetic satellite brightness temperatures is approximately 0.02°C decade^{-1} (Po-Chedley et al. 2021).

Efforts to intercompare and understand differences across tropospheric temperature datasets is ongoing (Steiner et al. 2020). For example, Christy et al. (2018) compares radiosonde and satellite-based measurements of tropospheric temperature and concludes that satellite datasets likely have spurious warming over the 1990s. On the other hand, this analysis also documents unexplained

cooling in satellite datasets over the early 2000s. This latter finding is consistent with recent work by Zou et al. (2021), who note that existing satellite datasets underestimate tropospheric temperature trends relative to a new post-2002 dataset, which relies on observations from the most recent generation of microwave sounding instruments and/or satellites in stable sun-synchronous orbits. Consistent with physical expectations, recent research shows that climate models exhibit a close coupling between atmospheric moistening and warming in the tropics. If model simulations are sufficiently accurate, relationships between distinct geophysical fields (e.g., water vapor and sea surface temperature observations) may be used to investigate potential observational biases in tropospheric temperature datasets (Santer et al. 2021). As a result of collective efforts to better understand and intercompare existing observational datasets, records of tropospheric warming are continually evolving and improving.

6. STRATOSPHERIC TEMPERATURE—W. J. Randel, C. Covey, L. Polvani, and A. K. Steiner

Global mean temperatures in the lower, middle, and upper stratosphere for 2021 were similar to 2020. The long-term trend, however, is multi-decadal cooling of the upper stratosphere and warming of the troposphere due to anthropogenic CO_2 increases. Shorter-term climate variations from both natural and anthropogenic sources (e.g., Australian bushfires in 2020) are also evident in the record but were not prominent in 2021. The Antarctic stratospheric polar vortex was strong and persistent in 2021, while the Arctic was disturbed by a major stratospheric warming event early in the year. The stratospheric quasi-biennial oscillation (QBO) progressed normally in 2021, in contrast to disruptions in 2016 and 2020.

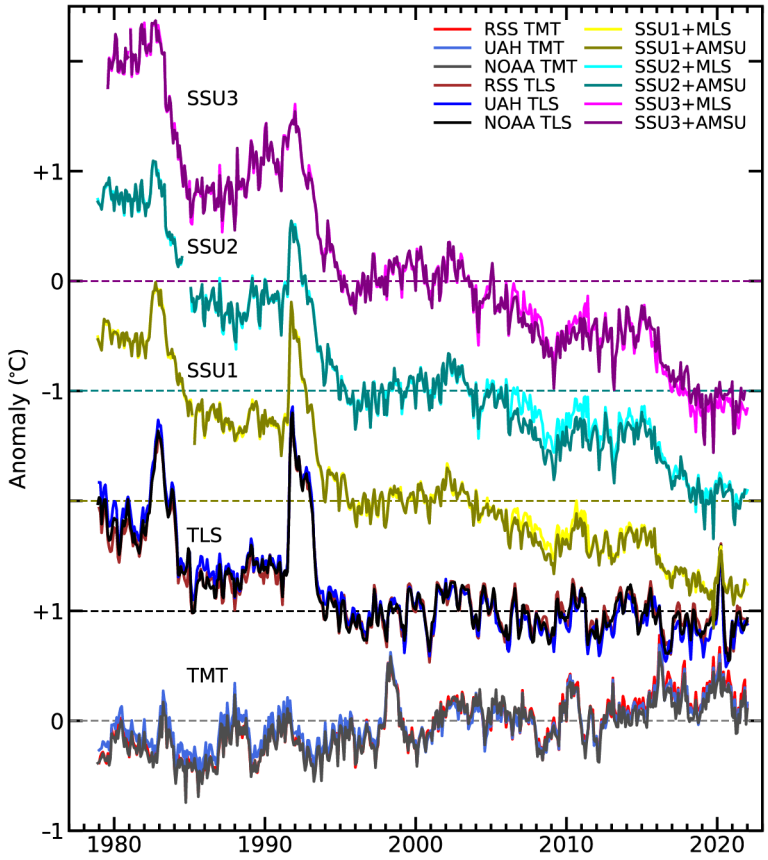

Fig. 2.10. Monthly global temperature anomalies (°C) from the middle troposphere to upper stratosphere (bottom to top). Middle and upper stratosphere data are from the Stratospheric Sounding Unit (SSU), representing thick-layer averages centered near 30, 38, and 45 km (SSU1, SSU2 and SSU3, respectively). Lower stratosphere temperatures (TLS) are ~13–22-km layer averages from satellite microwave measurements. Middle troposphere (TMT) data are ~0–10-km layer averages, and are included for comparison. Each time series has been normalized to zero for the period 1995–2005, and curves are offset for clarity.

Time series of global monthly temperature anomalies from the middle troposphere to the upper stratosphere based on satellite measurements are shown in Fig. 2.10. As discussed in Steiner et al. (2020), the middle and upper stratosphere data are merged products combining infrared emission measurements (Stratospheric Sounding Unit [SSU] 1, 2, 3 from 1979 to 2006) with more recent satellite data from microwave and infrared limb sounders for a continuous record. Merged datasets from microwave emission measurements provide layer-averaged temperatures for the lower stratosphere (TLS) and for the middle troposphere (TMT). In addition to long-term stratospheric cooling (due to CO_2 increase and stratospheric ozone changes) and tropospheric warming due to greenhouse gas increases (section 2b5), transient variations arise from a variety of causes including ENSO (e.g., large El Niño events in 1997 and 2016) and large volcanic eruptions (e.g., in 1982 and 1991). Transient warming in the lower stratosphere (TLS) in early 2020 was caused by stratospheric aerosol injections from the large Australian bushfires (Yu et al. 2021; Rieger et al. 2021; Stocker et al. 2021). However, no such events are apparent in the global average time series for 2021.

Independent measurements of temperatures between altitudes of ~10–30 km are available from occultations of GPS radio signals since 2002 (Steiner et al. 2020; Gulev et al. 2021). Figure 2.11 shows the resulting temperature trends for the period 2002–21 as a function of latitude and altitude. The results clearly differentiate warming in the troposphere from weak cooling over much of the lower to middle stratosphere. A more complicated situation occurs in the Southern Hemisphere subtropics, where warming extends across the tropopause into the lower stratosphere.

The long-term stratospheric cooling caused by rising greenhouse gas concentrations has led to a substantial contraction of the stratosphere over the last decades (Pisoft et al. 2021). Moreover, an increase of the tropopause height by about 50 m decade^{-1} was observed over the Northern Hemisphere with radiosonde data, confirmed with GPS radio occultation (Meng et al. 2021). The increase is found to be due to tropospheric warming and stratospheric cooling over the period 1980–2000, while the continuous rise after 2000 results primarily from enhanced tropospheric warming.

Unlike 2020, when the stratospheric winter polar vortices were unusually strong and undisturbed in both hemispheres, the Arctic polar vortex was disrupted by a major sudden stratospheric warming early in 2021 (Lee 2021). The Antarctic polar vortex was relatively cold and persistent in

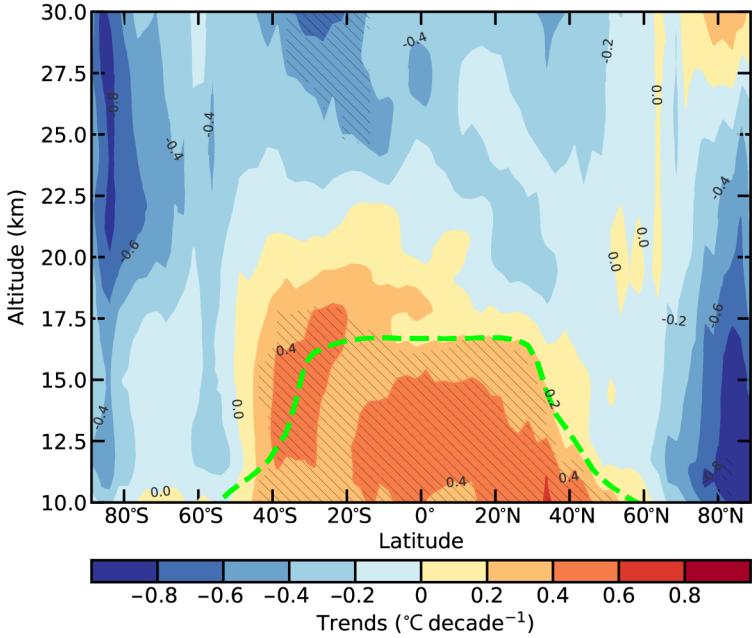

Fig. 2.11. Latitude–height section of temperature trends (°C decade^{-1}) derived from GPS radio occultation measurements over the period 2002–21 (updated from Steiner et al. 2020). Thick dashed line denotes the time average tropopause. Hatching denotes trends that are significant at 2-sigma uncertainty.

2021, coinciding with a large ozone hole persisting until December (sections 2g4, 6h). The equatorial stratosphere's quasi-biennial oscillation progressed in 2021 as it usually has for more than half a century: downward-propagating easterly and westerly wind regimes and accompanying temperature variations, with a mean periodicity of somewhat more than two years. This regular downward propagation from the upper to lower stratosphere was interrupted in both 2016 and 2020, but more regular evolution appeared to resume at the end of 2020 with an easterly phase propagating downward from the middle stratosphere (https://acd-ext.gsfc.nasa.gov/Data_services/met/qbo/qbo.html).

c. Cryosphere

1. PERMAFROST TEMPERATURE AND ACTIVE LAYER THICKNESS—J. Noetzli, H. H. Christiansen, M. Guglielmin, F. Hrbáček, K. Isaksen, S. L. Smith, L. Zhao, and D. A. Streletskiy

Permafrost—ground material remaining at or below 0°C for at least two consecutive years—is a key component of the cryosphere in high-latitude and high-altitude regions. Global permafrost temperatures have increased for several decades, with regional variability in magnitude and shorter-term fluctuations related to meteorological variations (Biskaborn et al. 2019; Etzelmueller et al. 2020; Haberkorn et al. 2021). Observed warming rates close to the depth of the zero annual amplitude (DZAA)—where annual temperature fluctuations become negligible—were in the range of a few tenths °C decade^{-1} (Smith et al. 2022). They were largest (0.3°–0.8°C decade^{-1}) at sites in continuous permafrost or at highest elevations with low permafrost temperatures. Warmer and ice-rich permafrost warms more slowly due to latent heat uptake during ice melt (< 0.3°C decade^{-1}). Changes in active layer thickness (ALT)—the thickness of the layer above the permafrost that freezes and thaws annually—relate to annual atmospheric and snow conditions. ALT was greater in 2021 than in 2020 in some polar regions and generally above average of available records for all observed permafrost regions.

Permafrost temperatures in 2021 across the Arctic regions were the highest on record at many sites (see section 5h); however, at some Arctic sites (e.g., northwestern North America, Nordic region, and northern Russia) lower permafrost temperatures than in the previous years were observed, related to lower air temperatures. ALT could not be fully reported for some Arctic regions due to continued COVID-related travel restrictions. In northern Alaska, ALT was below the 2009–18 average, while it was among the largest values on record in Alaska Interior and on average more than 30 cm greater than in 1995. Greenland also reported its greatest ALT since 1995. Northern European Russia and western and eastern Siberia had lower ALT compared to 2020, but was greater than average, while in central Siberia it was greater than 2020.

On James Ross Island, northeastern Antarctic Peninsula, permafrost temperatures in 2021 were the second highest (–5.0°C) since the record began in 2011. The ground temperature at 75 cm increased by 0.9°C over the period 2011–21 (Hrbáček et al. 2021). ALT has increased here by 12 cm decade^{-1} reaching 66 cm in 2021, which was 6 cm above average. At Rothera Point, permafrost temperature below the DZAA has remained stable since 2009.

Mountain permafrost accounts for approximately one-third of the global area underlain by permafrost (Hock et al. 2019). Data are primarily available from the European Alps, the Nordic region, and the Qinghai-Tibetan Plateau (QTP). Ranges of permafrost temperature and warming rates are similar to those observed in the Arctic, but with high spatial variability due to the complex topography. Significant ALT increase by meters were documented at sites in the European Alps over the past two decades (Etzelmueller et al. 2020; Haberkorn et al. 2021; PERMOS 2022), with considerable loss of ground ice (Mollaret et al. 2019). Ground temperatures close to the surface were lower in 2021 than 2020 in the European Alps (PERMOS 2022; Pogliotti et al. 2015; Magnin et al. 2015) due to a long period of snow cover and lower atmospheric temperatures (e.g., MeteoSwiss 2022). This resulted in ALT that were often lower in 2020 and a general decrease in rock glacier velocity (section 2c2). For many sites, permafrost temperatures at 20-m depth—where they react

to longer term trends—continued to increase in 2021 and reached record levels (Fig. 2.12). This is also true for the Nordic mainland; on Juvvasshøe in southern Norway, 2021 was the eighth consecutive year (since 2014) with record permafrost temperatures (Noetzli et al. 2021a; Etzelmüller et al. 2020). ALT at sites in the Nordic countries in 2021 were greater than or close to the maximum of 2020. In Svalbard, however, permafrost temperatures at 10-m depth continued to decrease due to cold winters in 2019–21 (Christiansen et al. 2021), but were still above the long-term average (Fig. 2.12). Permafrost temperatures in the QTP in central Asia increased at six sites from 2005 to 2020: 0.45°C decade^{-1} at 10-m depth and 0.24°C decade^{-1} at 20-m depth (Fig. 2.13; Zhao et al. 2020, 2021). Along the Qinghai-Tibet Highway (Kunlun mountain pass), an ALT increase was observed with a mean of 19.4 cm decade^{-1} for the period 1981–2020 (Fig. 2.14).

Long-term observation of permafrost relies on field observations of ALT, permafrost temperatures, and, since 2021, on rock glacier velocity (Streletskiy et al. 2021; Pellet et al. 2021). International data are collected by the Global Terrestrial Network for Permafrost (GTN-P) as part of the Global Climate Observing System (GCOS). Permafrost temperatures are logged in boreholes reaching at least the DZAA, with a measurement accuracy assumed to be 0.1°C (Biskaborn et al. 2019; Noetzli et al. 2021b; Streletskiy et al. 2021). ALT is determined by mechanical probing where possible (accuracy of ~1 cm) and otherwise interpolated from borehole temperature measurements. The global coverage of permafrost monitoring sites is sparse and particularly limited in regions such as Siberia, central Canada, Antarctica, and the Himalayan and Andes Mountains.

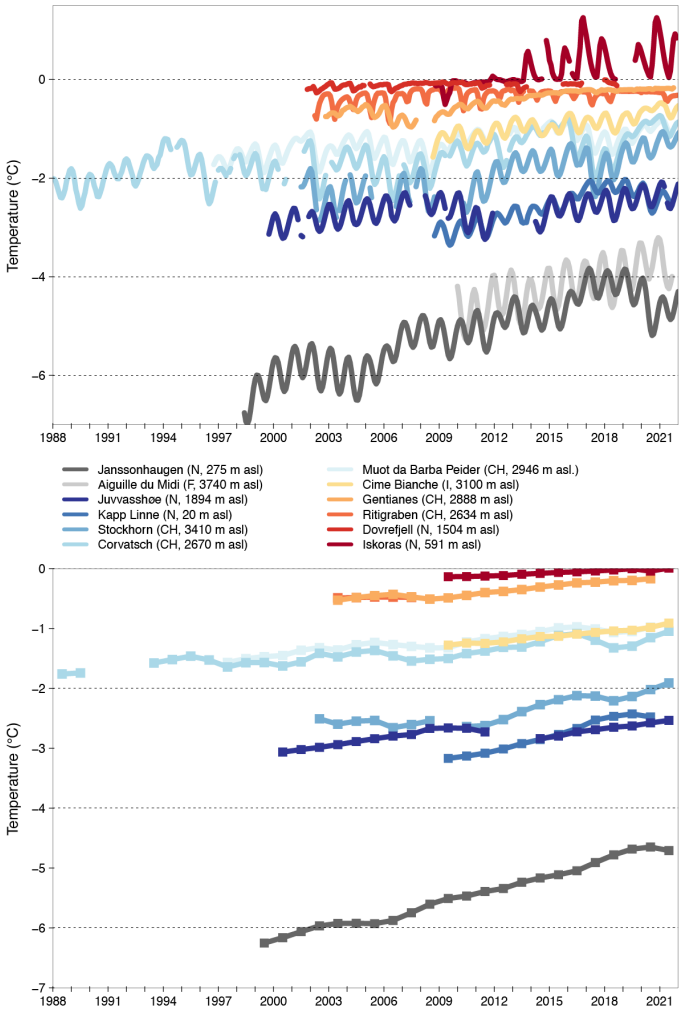

Fig. 2.12. Permafrost temperature (°C) measured in boreholes in the European Alps and the Nordic countries at a depth of (a) ca. 10 m (monthly means) and (b) 20 m (annual means). (Data sources: Switzerland: Swiss Permafrost Monitoring Network PERMOS; Norway: Norwegian Meteorological Institute and the Norwegian Permafrost Database NORPERM; France: updated from Magnin et al. 2015; Italy: updated from Pogliotti et al. 2015.)

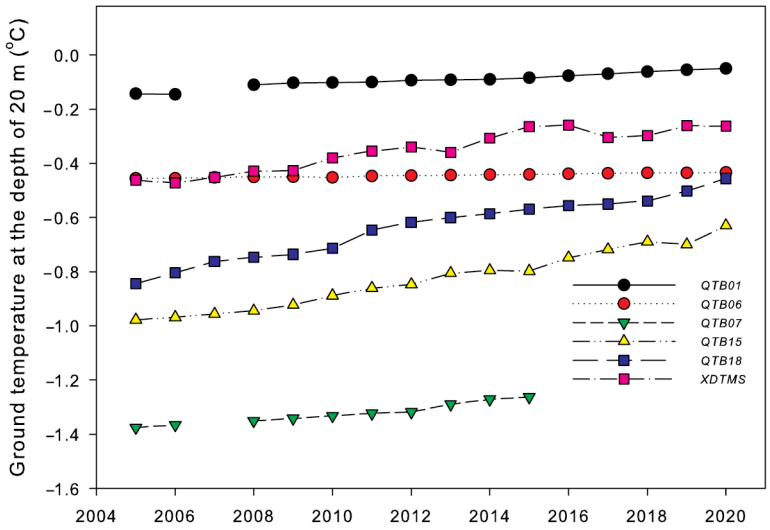

Fig. 2.13. Permafrost temperature (°C) measured in boreholes along the Qinghai-Xizang Highway on the Tibetan Plateau at 2-m depth for the period 2005–20. (Source: Cryosphere Research Station on Qinghai-Xizang Plateau, CAS.)

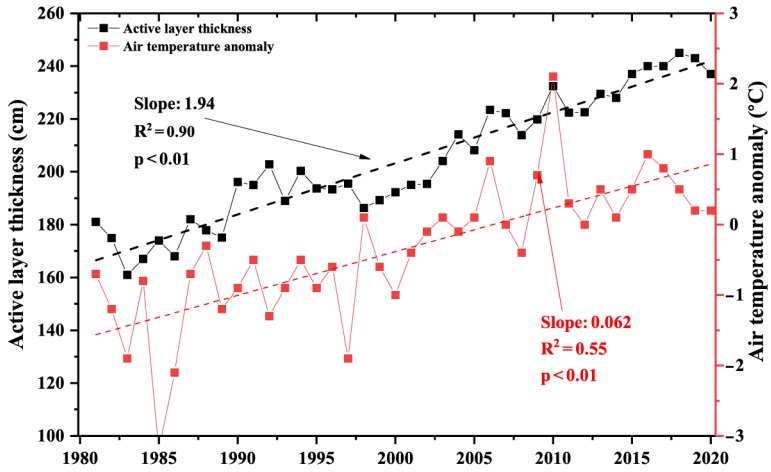

Fig. 2.14. The active layer thickness (cm) and air temperature anomalies (°C) in the permafrost zone along the Qinghai-Tibet Highway during the period 1981–2020. The air temperature anomaly is estimated relative to the base period 1981–2010. (Source: Cryosphere Research Station on Qinghai-Xizang Plateau, CAS.)

2. ROCK GLACIER VELOCITY—C. Pellet, X. Bodin, D. Cusicanqui, R. Delaloye, A. Kääb, V. Kaufmann, J. Noetzli, E. Thibert, S. Vivero, and A. Kellerer-Pirklbauer

Rock glaciers are debris landforms generated by the creep of frozen ground (permafrost) found in most mountain ranges worldwide (RGIK 2021). Changes in their velocities are mostly related to the evolution of ground temperature and liquid water content between the permafrost table and the shearing horizon at depth: the closer to 0°C, the faster the rock glacier is able to move (Cicoira et al. 2019; Frauenfelder et al. 2003; Staub et al. 2016). In 2021, the variable rock glacier velocity (RGV) was adopted as a new associated product to the essential climate variable (ECV) permafrost by GCOS and the Global Terrestrial Network for Permafrost (GTN-P, Streletskiy et al. 2021), given the global occurrence of active rock glaciers and their sensitivity to changes in ground temperature.

RGVs, observed in several mountain ranges across the globe, have been increasing since the 1950s, with regional variability in magnitude and marked interannual variability. Observed rates of increase are largest since 2010 and record high velocities have been recorded since 2015. These changes are consistent with interannual variations of permafrost temperatures (cf. section 2c1), to which rock glacier velocities have been shown to respond synchronously (Cusicanqui et al. 2021; Kääb et al. 2007; Kellerer-Pirklbauer and Kaufmann 2012; Staub et al. 2016; Vivero et al.

2021). Regionally, RGVs follow the same interannual behavior despite variable size, morphology, and velocity range (e.g., Delaloye et al. 2010; Kääb et al. 2021; Kellerer-Pirklbauer et al. 2018; PERMOS 2019).

RGVs in the European Alps have increased by a factor of between 2 and 10 from the 1980s to 2021 (Fig. 2.15b). This acceleration was temporarily interrupted at most sites during 2004–06 and 2016–18, coinciding with a decrease in permafrost temperatures, mainly resulting from snow-poor winters, which enabled more efficient ground cooling due to the later onset of an insulating snow cover (Noetzli et al. 2018; PERMOS 2019). Compared to 2020, RGVs decreased in 2021, e.g., at Gemmi/Furggentälti (Switzerland, –26%), Grosses Gufer (Switzerland, –24%), and Laurichard (France, –4%), whereas RGVs increased at Dösen (Austria, +19%) and Hinteres Langtalkar (Austria, +35%) to record values (Fig. 2.15b). The velocity decrease at Swiss and French sites is consistent with lower air temperatures compared to 2020 (Fig. 2.15a) as well as a long-lasting snow cover in spring and a relatively late thickening of the snow cover in autumn, which led to lower ground temperatures (cf. section 2c1). Different behaviors of the rock glaciers between the Western and Eastern Alps in 2021 might be related to differences in precipitation and temperature, particularly in December 2020 (warmer east), January 2021 (drier east), and July 2021 (warmer and less humid east), in addition to the influence of local topo-climatic factors.

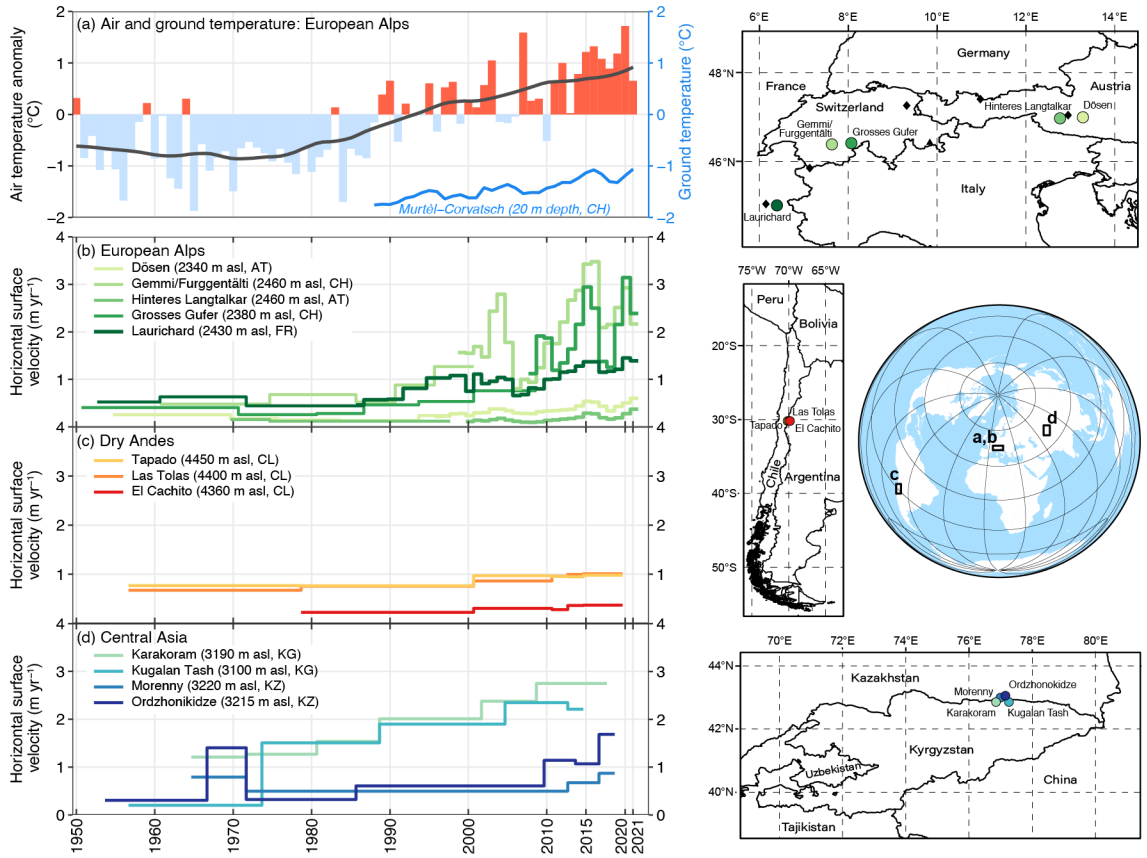

Fig. 2.15. (a) Rock glacier velocity and climate: air and ground temperature (°C) in the European Alps. Rock glacier velocities (m yr^{-1}) at selected sites in (b) the European Alps, (c) the Dry Andes (adapted from Vivero et al. 2021), and (d) central Asia (adapted from Kääb et al. 2021). Rock glacier velocities based on in situ geodetic surveys or photogrammetry in the context of long-term monitoring. In-situ permafrost temperature measured at 20-m depth (blue line) at Murtèl Corvatsch (black triangle on Europe map) and air temperature: composite anomaly to the 1981–2010 average (bars) and composite 20-year running mean (solid line) at Besse (FR), Grand Saint-Bernard (CH), Saentis (CH), Sonnblick (AT), and Zugspitze (D, black diamonds on Europe map). (Data sources: Météo France, Deutscher Wetterdienst [DWD], MeteoSwiss, Zentralanstalt für Meteorologie und Geodynamik [ZAMG], Swiss Permafrost Monitoring Network [PERMOS], University of Fribourg, University of Graz, Graz University of Technology, Université Grenoble Alpes [INRAE], University of Oslo.)

There are few long-term in situ measurements of RGVs outside of the European Alps. However, an increasing number of studies exploit the potential of archival aerial photographs and high-resolution satellite data to reconstruct RGVs (e.g., Cusicanqui et al. 2021; Eriksen et al. 2018). The velocities of three rock glaciers observed in the Dry Andes in South America showed slow velocities from 1950 to 2000, followed by a steady acceleration since the 2000s (Fig. 2.15c), consistent with the climatic conditions observed in the region (Vivero et al. 2021).

RGVs observed in Central Asia since the 1950s do not show a uniform picture (Fig. 2.15d; Kääb et al. 2021). The Karakoram and Kugalan Tash (Kyrgyzstan) RGVs steadily increased since the 1960s, whereas at Ordzhonikidze and Morenny (Kazakhstan) high velocities were observed during the second half of the 1960s, then low velocities until 2010, and increasing velocities in recent years. All RGVs have increased since the start of the observations and accelerated since 2010, which is consistent with increasing air temperatures and with the acceleration reported in the European Alps and Dry Andes.

Long-term RGV time series are reconstructed using multi-temporal aerial or optical satellite images. Horizontal displacements are computed based on feature tracking, 2D ortho-image matching algorithms or digital elevation model matching. The resulting accuracy strongly depends on the spatial resolution of the aerial images and on the image quality. Surface displacements are averaged for a cluster of points selected within areas, representative of the flow field and indicative of the downslope movement of the rock glacier (RGIK 2022). Annual rock glacier velocities are measured using terrestrial geodetic surveys performed each year at the same time (usually at the end of summer). The positions are measured for a number of selected boulders (10–100 per landform) with an average accuracy in the range of mm to cm (Delaloye et al. 2008; PERMOS 2019).

3. ALPINE GLACIERS—M. Pelto

In the hydrological year 2020/21, observed World Glacier Monitoring Service (WGMS) reference glaciers experienced a mass balance loss of –900 mm water equivalent (mm w.e.), compared to –700 mm w.e. in 2019/20. From 1970 to 2021 the eight most negative mass balance years were all recorded after 2010. A value of –1000 mm w.e. per year represents a mass loss of 1000 kg m^{-2} of ice, or an annual glacier-wide thickness loss of about 1100 mm yr^{-1}.

Figure 2.16 illustrates glacier mass balance for the WGMS global reference glaciers with more than 30 years of data for the period 1970 to 2020. Global values are calculated using a single value (averaged) for each of 19 mountain regions in order to avoid a bias to well observed regions. In 2021, a negative annual mass balance was reported from 31 of the 32 reference glaciers reported to the WGMS as of 1 June 2022. The mean annual mass balance of the 32 reference glaciers reporting

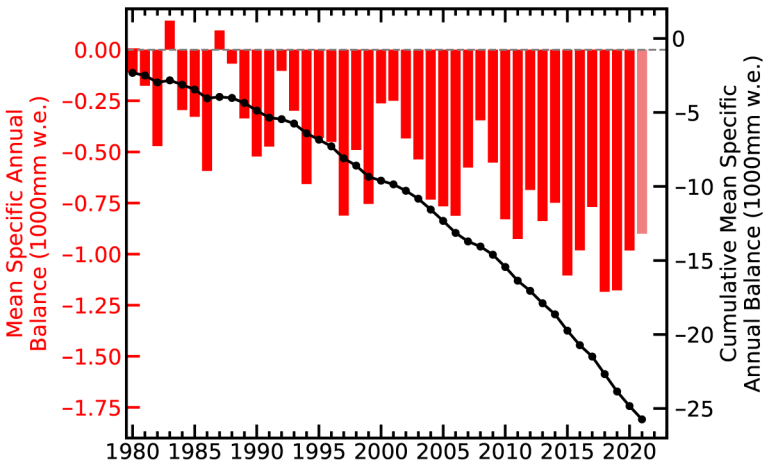

Fig. 2.16. Global annual glacier mass balance of WGMS reference glacier network in mm water equivalent (w.e.), with annual values (red bars, left axis) and cumulative amounts since 1979 (black dots, right axis). Lighter shading for 2021 is used as the final values for that year were not yet available at time of publication.

is −900 mm w.e., which includes data from 12 nations on four continents (not final regionally-averaged global value; there are 42 reference glaciers in total). This will make 2021 the 34th consecutive year with a global alpine mass balance loss and the 13th consecutive year with a mean global mass balance below −500 mm w.e.

The rate of thinning increased from −527 mm yr^{-1} for 2000–09 to −896 mm yr^{-1} for 2010–19 (WGMS 2021). This agrees well with the satellite survey of 200,000 alpine glaciers by Huggonet et al. (2021) who identified a thinning rate excluding ice sheet peripheral glaciers of 360 ± 210 mm yr^{-1} in 2000 to 690 ± 150 mm yr^{-1} in 2019. Alpine glaciers lost a mass of 267 ± 16 Gt yr^{-1} from 2000 to 2019, equivalent to 21 ± 3% of the observed global sea level rise (Huggonet et al. 2021). More frequent and intense heat waves continue to take a toll on alpine glaciers (Pelto et al. 2021, 2022).

All 17 reporting glaciers in the Alps had a negative mass balance averaging −682 mm in 2021. In Austria in 2020, of the 92 glaciers with annual terminus observations, 85 (93.4%) withdrew and seven remained stationary (Lieb and Kellerer-Pirklbauer 2021). This retreat trend continued in 2021, with another year of mass balance loss. In Norway, the six reporting glaciers all had a negative mass balance, yielding an average mass balance of −671 mm in 2021. On Svalbard, the mean loss of the four reporting glaciers was −227 mm. Iceland completed surveys of nine glaciers; all nine had negative balances, with a mean mass balance of −1160 mm.

In western Canada and Washington (United States) all 14 glaciers observed in 2021 had a negative mass balance averaging −1635 mm. The exceptional heat wave during late June and early July in western North America (section 2b4; Sidebar 7.1) set the stage for the large glacier mass loss (Pelto et al. 2022; Fig. 2.17). In Alaska, three of the four glaciers measured had a negative mass balance, with a mean annual balance of −528 mm. In South America, 2021 mass balance data were reported from three glaciers in Argentina, two glaciers in Chile, and one in Colombia; all were negative with a mean of −861 mm. This is greater than the 2000–18 average loss observed in the Andes of −720 ± 220 mm yr^{-1} (Dussaillant et al. 2019). In High Mountain Asia, 15 of 18 glaciers reported negative balances in 2021. The average mass balance was −468 mm. Early winter of 2021 was warm and dry across the Himalayan region. This was capped off by record warmth in the Mount Everest region, leading to the snow line on glaciers rising and snow-free glaciers up to 6000 m (Pelto et al. 2021), illustrating that the ablation season no longer always ends when winter begins. The importance of winter conditions was further noted by Potocki et al. (2022) who reported on an ice core drilled on South Col Glacier, on Mount Everest at 8020 m a.s.l., revealing a contemporary sublimation driven thinning of ~2000 mm yr^{-1}.

Fig. 2.17. Easton Glacier in Washington state in August 2021, with less than 10% snowcover and one month left in the ablation season.

4. LAKE ICE—S. Sharma, R. I. Woolway, A. Basu, K. Blagrave, G. Bove, N. Granin, J. H. L'Abée-Lund, H. J. Malmquist, W. Marszelewski, T. Nõges, M. Pulkkanen, and K. Stewart

In the 2020/21 winter, lake ice phenology (timing of ice-on and ice-off) across the Northern Hemisphere (NH, calculated from Copernicus Climate Change Service [C3S] ERA5 [Hersbach et al. 2020]) continued to exhibit later ice-on dates, earlier ice-off dates, and shorter seasonal ice cover, thus continuing the pattern observed in recent decades (Sharma and Woolway 2021). Relative to the 1991–2020 base period, NH lakes froze, on average, 3.8 days later, thawed 3.5 days earlier, and ice duration was over 7 days shorter (Figs. 2.18, 2.19). The regional variations in ice duration were consistent with NH winter air temperature anomalies. Most notably, some regions in North America, such as western Canada, experienced below-average air temperatures, which resulted in longer-than-average ice duration. Conversely, eastern Canada and many regions in Eurasia experienced warmer-than-average conditions that resulted in shorter-than-average ice duration (Fig. 2.18d).

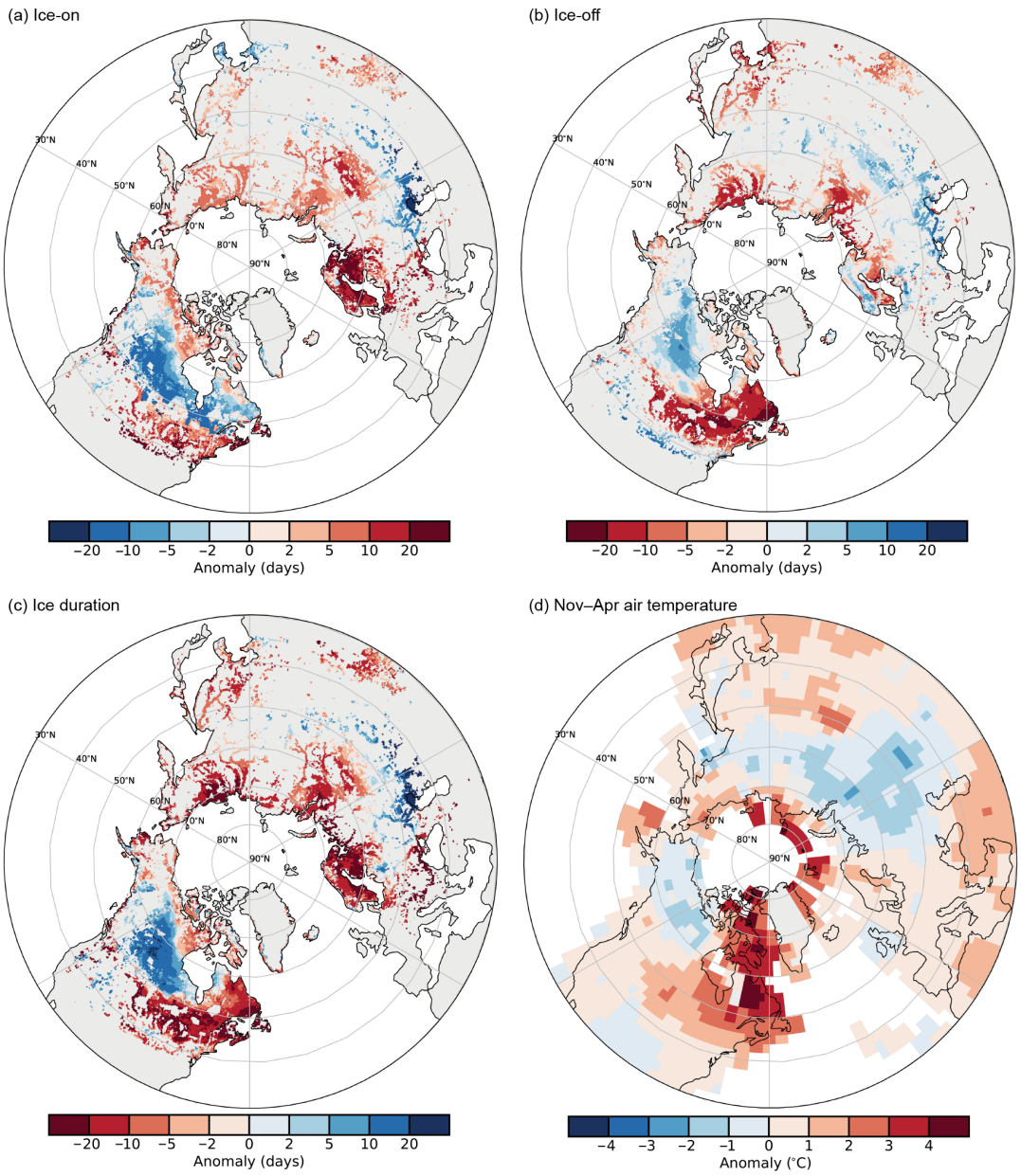

Fig. 2.18. Anomalies (days) in 2021 in (a) ice-on (positive = later), (b) ice-off (negative = earlier), and (c) ice duration for lakes across the NH (negative = shorter), and (d) surface air temperature anomalies (°C) for the NH cold season (Nov–Apr average), the time of year in which lakes typically freeze. The base period is 1991–2020. (Sources: ERA5, GISTEMP.) The winter season for 2021 generally refers to the time between the end of autumn 2020 and the start of spring 2021.

Based on in situ ice phenological records from 110 lakes in North America (NA), Europe, and Asia, ice-on was 11 days later, ice-off was 7.5 days earlier, and there were 19 fewer days of ice cover over the 2020/21 winter season, on average, relative to 1991–2020 (Fig. 2.19). For NA lakes, ice-on averaged 5 days later and ice-off was 11 days earlier. For European lakes, ice-on was 17 days later, ice-off was 3 days earlier, totaling 20 days less ice cover in the winter of 2021 relative to the 1991–2020 base period. Lake Erken, in Sweden, lost the most ice cover during the 2021 winter, with 61 days less ice cover compared to the 1991–2020 normal in response to an anomalously warm winter in 2021 in the region. Analysis of ice phenology trends during 1991–2021 suggest that ice-on date is 4.1 days later per decade, ice-off date is 2.2 days earlier per decade, and ice duration

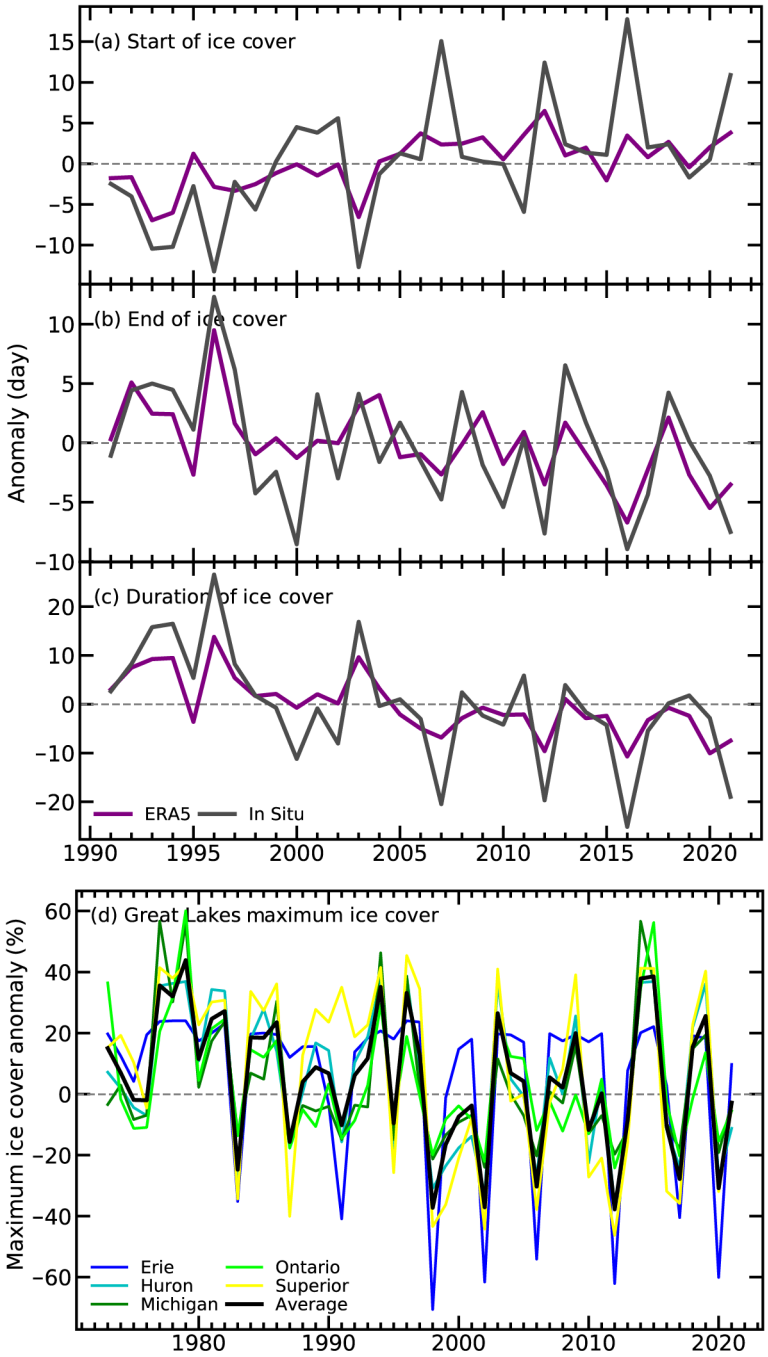

Fig. 2.19. (a) Lake ice-on, (b) ice-off, and (c) ice duration anomalies from 1980 to 2021 derived from in situ observations and ERA5 reanalysis. (d) Anomalies in Great Lakes maximum ice cover extent (%) for 1973–2021. The black line shows the average anomaly for all of the Great Lakes, whereas the lines in color show individual lakes (Erie, Michigan, Superior, Ontario, Huron). Base period is 1991–2020. The winter season for 2021 generally refers to the time between the end of autumn 2020 and the start of spring 2021.

is 6.8 shorter per decade on average for these 110 lakes. In 2021, the Laurentian Great Lakes had 2.9% less maximal ice coverage relative to 1991–2020. The deeper and most northern lakes all had less maximal ice coverage, of which Lake Huron was the most anomalous with 11.6% less ice coverage in 2021. Lake Erie, the shallowest lake, was the exception, with 9.7% more ice coverage in 2021 (Fig. 2.19d). Since 1973, the Laurentian Great Lakes have been losing on average 4.3% (95% confidence interval: 0.5, −9.1) of ice coverage per decade. Lake Superior is losing the most ice coverage per decade of all the Great Lakes (7.0% per decade). In fact, Lake Superior is one of the world's fastest warming lakes (O'Reilly et al. 2015; Sharma et al. 2021) and has lost over 60 days of ice cover since 1857 (Sharma et al. 2021; Wang et al. 2021).

To estimate the timing of ice-on and ice-off and, ultimately, the duration of winter ice cover across NH lakes, ice simulations from the ERA5 reanalysis product (Hersbach et al. 2020) were analyzed following the methods of Grant et al. (2021). We obtained in situ ice phenology for 110 lakes: Canada (5), United States (53), Estonia (2), Finland (27), Iceland (1), Norway (18), Poland (1), Sweden (1), Russia (1), and Japan (1). In addition, we obtained annual maximum ice cover (%) data for each of the Laurentian Great Lakes from 1973 to 2020 (https://www.glerl.noaa.gov/data/ice/). Surface air temperature data for the NH cold season (November–April average) were downloaded from the NASA GISS surface temperature analysis (Lenssen et al. 2019; GISTEMP Team 2022). To create the time series figure, the ERA5 data were averaged across all 0.25° grids and consisted of a much larger sample size relative to the in situ data where the anomalies were averaged across 110 lakes.

5. NORTHERN HEMISPHERE CONTINENTAL SNOW COVER EXTENT—D. A. Robinson and T. W. Estilow

Annual snow cover extent (SCE) over Northern Hemisphere (NH) lands averaged 24.3 million km^2 in 2021. This is 0.6 million km^2 less than the 1991–2020 mean and 0.8 million km^2 below the mean over a 52-year period of record (Fig. 2.20; Table 2.5), marking the seventh least extensive cover on record. Monthly SCE in 2021 ranged from a maximum of 46.8 million km^2 in January to a minimum of 2.5 million km^2 in August.

The year began with NH SCE ranking in the middle tercile of the 55-year record, although North America (NA) SCE was fourth most extensive on record in February. NA quickly lost SCE in March, falling to 47th most extensive, while Eurasia (EUR) remained well below average. These conditions persisted throughout spring, with May having the 52nd most extensive SCE on record and June 47th most extensive.

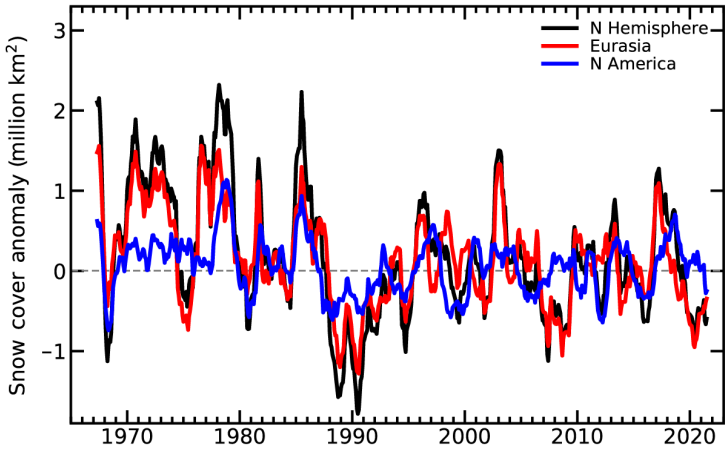

Fig. 2.20. 12-month running anomalies (million km^2) of monthly SCE over NH lands as a whole (black) and EUR (red), and NA (blue) separately, plotted on the seventh month using values from Nov 1966 to Dec 2021. Anomalies are calculated from NOAA snow maps. Mean NH SCE is 25.1 million km^2 for the full period of record. Monthly means for the period of record are used for nine missing months during 1968, 1969, and 1971 in order to create a continuous series of running means. Missing months fall between Jun and Oct. Data from Estilow et al. (2015).

Table 2.5. Monthly and annual climatological information on NH, EUR, and NA SCE between Nov 1966 and Dec 2021. Included are the numbers of years with data used in the calculations, NH means, standard deviations, 2021 values, and rankings. Units: million km^2. 1968, 1969, and 1971 have one, five, and three missing months respectively, thus are not included in the annual (Ann) calculations. NA includes Greenland. Ranks are from most to least extensive.

	Years of data	NH Mean	Std. Dev.	2021	2021 NH rank	2021 Eurasia rank	2021 N Am. rank
Jan	55	47.1	1.5	46.8	32	36	28
Feb	55	46.0	1.8	46.1	22	42	4
Mar	55	40.4	1.9	38.6	44	42	47
Apr	55	30.5	1.7	28.8	45	40	46
May	55	19.1	2.0	16.2	53	51	45
Jun	54	9.4	2.5	6.2	46	52	42
Jul	52	3.9	1.2	2.8	43	44	39
Aug	53	3.0	0.7	2.5	40	42	30
Sep	53	5.4	0.9	5.6	22	30	13
Oct	54	18.6	2.7	18.1	28	22	46
Nov	56	34.3	2.1	35.4	18	9	44
Dec	56	43.7	1.8	44.5	17	13	26
Ann	**52**	**25.1**	**0.8**	**24.3**	**46**	**44**	**41**

NA picked up some early autumn snow, contributing to its 13th most extensive September cover. This ranking fell to 46th most extensive in October, when EUR and the NH ranked in the middle tercile. NH November and December SCE fell near the boundary of the highest and middle tercile, mainly due to above-average SCE in EUR where November ranked ninth most extensive and December 13th most extensive. Following an average snow cover in January, SCE over the contiguous United States was fifth most extensive in February and below-average every other month thereafter in 2021.

SCE is calculated at the Rutgers Global Snow Lab (GSL) from daily SCE maps produced by meteorologists at the U.S. National Ice Center, who rely primarily on visible satellite imagery to construct the maps. Maps depicting daily, weekly, and monthly conditions, anomalies, and climatologies may be viewed at the GSL website (https://snowcover.org).

d. Hydrological cycle

1. SURFACE HUMIDITY—K. M. Willett, D. A. Lavers, M. Bosilovich, and A.J. Simmons

Global mean specific humidity (q) in 2021 was lower compared to 2020, although remaining well above the 1991–2020 average in all datasets (+0.07 to +0.18 g kg^{-1} for q_{land}, +0.07 to +0.20 g kg^{-1} for q_{ocean}) except for ERA5, which placed global q_{land} just below average at −0.01 g kg^{-1} (Figs. 2.21a–d). For global mean relative humidity (RH), 2021 was less saturated than 2020 in all datasets over land (–1.32 to −0.70 %rh) (Figs. 2.21e,f). Both JRA-55 and ERA5 show a large difference between 2020 and 2021, placing 2021 as the least saturated year on record (since 1958 and 1967, respectively) by a large margin (−0.23 %rh and −0.45 %rh, respectively). It was the second driest year on record after 2019 in HadISDH. Over oceans, RH remained mixed with HadISDH and JRA-55 behaving similarly, placing 2021 RH_{ocean} at +0.20 and +0.16 %rh above the 1991–2020 average, respectively, which is slightly above 2020, while ERA5 dropped below average at −0.09 %rh, continuing a short drying trajectory since 2019.

Spatially, missing data regions of HadISDH (Plate 2.1g) over much of northwestern, central, and eastern Africa are regions that showed strong negative q anomalies in ERA5, indicating that the water vapor content was lower than average (Appendix Fig. A2.8). This might explain the discrepancy in global land averages between ERA5 and HadISDH. Central Africa is a key region for differences between the reanalyses, with MERRA-2 (Appendix Fig. A2.9) showing strong high water vapor content anomalies there and more expansive high water vapor content anomalies generally, likely contributing to the MERRA-2 high 2021 q_{land} anomaly. Other discrepancies are notable over western Australia where HadISDH shows an isolated suspect highwater vapor content anomaly, and over northern Colombia and Venezuela where MERRA-2 shows strong low water vapor content anomalies. Over the ocean, MERRA-2 and ERA5 are in good agreement. The HadISDH higher global mean q_{ocean} anomaly for 2021 is missing many of the low water vapor content anomaly regions of the central eastern Pacific and Southern Hemisphere more generally, the former being associated with the La Niña conditions. Positive and negative anomalies are broadly

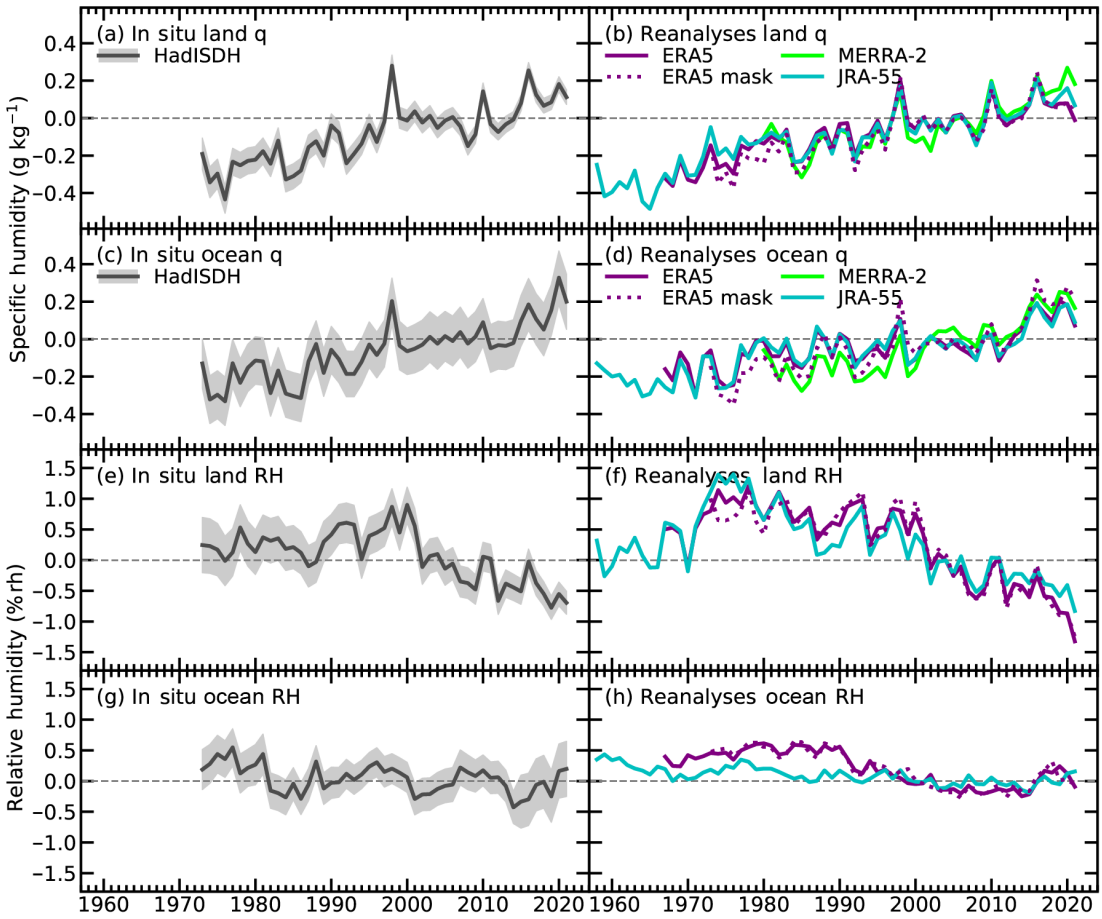

Fig. 2.21. Global average surface humidity annual anomalies (1991–2020 base period). For the in-situ datasets 2-m surface humidity is used over land and ~10-m over the oceans. For the reanalysis 2-m humidity is used over the whole globe. For ERA5 ocean series-only points over open sea are selected. ERA5 mask is a version of ERA5 that spatially matches the coverage of HadISDH. 2-sigma uncertainty is shown for HadISDH capturing the observation, gridbox sampling and spatial coverage uncertainty. (Sources: HadISDH [Willett et al. 2013, 2014, 2020]; ERA5 [Hersbach et al. 2020]; JRA-55 [Kobayashi et al. 2015]; MERRA-2 [Gelaro et al. 2017].)

similar between RH (Plate 2.1h; Appendix Figs. A2.10, A2.11) and q but with the central Eurasian and western North American anomalies more expansive for RH_{land}, and RH_{ocean} anomalies more muted than those for q_{ocean}, q_{land}, and RH_{land} generally.

In terms of long-term trends (Table 2.6), all datasets continue to show long-term increasing water vapor over land and ocean (+0.04 to +0.10 g kg^{-1} decade^{-1}), while the air over land has become less saturated (−0.23 to −0.45 %rh decade^{-1}). This means that the water vapor content of the air has increased more slowly than the water vapor carrying capacity of the air, which increases exponentially with temperature. The trend magnitudes for q are similar over land and ocean for each dataset. HadISDH and MERRA-2 show similar larger trends in q (+0.09 to +0.10 g kg^{-1} decade^{-1},

Table 2.6. Global average decadal trends for the period 1979–2021 fitted using ordinary least squares regression. The 90th percentile confidence intervals are shown in parentheses, fitted using AR(1) correction following Santer et al. (2008). Trends shown in bold are considered significantly different from a zero trend, in which the confidence intervals do not cross the zero line. Units are g kg^{-1} decade^{-1} for q and %rh decade^{-1} for RH.

Variable	HadISDH	ERA5	ERA5 masked to HadISDH	MERRA-2 (1980–2020)	JRA-55
Land q	**0.09 (0.02)**	**0.05 (0.01)**	**0.07 (0.01)**	**0.09 (0.02)**	**0.06 (0.01)**
Land RH	**−0.23 (0.08)**	**−0.45 (0.06)**	**−0.44 (0.08)**	NA	**−0.33 (0.04)**
Ocean q	**0.09 (0.01)**	**0.04 (0.02)**	**0.08 (0.02)**	**0.10 (0.02)**	**0.04 (0.01)**
Ocean RH	−0.03 (0.04)	**−0.18 (0.08)**	**−0.18 (0.07)**	NA	**−0.04 (0.02)**

respectively), while ERA5 and JRA-55 show more moderate trends (+0.04 to +0.06 g kg^{-1} $decade^{-1}$, respectively). While all datasets show a negative trend for RH_{ocean}, these trends are small, relatively widespread (−0.03 to −0.18 %rh $decade^{-1}$), and not considered to be significant for HadISDH. We conclude that there is large uncertainty in whether there is any real change in RH_{ocean}.

Agreement between the monitoring products in terms of both long-term trajectories and year-to-year variability is generally good (Fig. 2.21), with the exception of RH_{ocean}. Greater discrepancy over ocean is expected given the sparse observing network available from the Voluntary Observing Ships (VOS; https://www.vos.noaa.gov/vos_scheme.shtml) that make up the HadISDH record and the difference in methodological approaches between datasets. For example, ERA5 does not incorporate any in situ near-surface temperature or dew point temperature measurements over ocean, whereas HadISDH, MERRA-2, and JRA-55 do. The uncertainty range estimated for HadISDH is larger over ocean than over land, reflecting both the larger observational uncertainty since 2015, when digitized ship metadata provision ended, and larger spatial coverage uncertainty compared to over land. For RH_{land}, ERA5 is consistent with JRA-55 whereas for RH_{ocean} it is not.

Despite the good agreement generally over land, the reanalyses have diverged since 2018. ERA5 masked to the HadISDH spatial coverage differs little from the complete ERA5 anomaly time series (dashed lines in Fig. 2.21), especially over the last 30 years. Global trends in the masked versus complete ERA5 for *q* are closer to, but still less than, those from HadISDH (Table 2.6), but practically identical for RH. Interestingly, masked and complete ERA5 RH_{land} and RH_{ocean} anomalies are persistently more saturated than HadISDH pre-1990. Simmons et al. (2021) note an increase in the number of temperature observations, particularly those sampling different hours of the day around between 1988 and 1990; however, it is not clear how this would lead to biases in RH.

2. TOTAL COLUMN WATER VAPOR—C. A. Mears, J. P. Nicolas, O. Bock, S. P. Ho, and X. Zhou

In 2021, global land and ocean averages of total column water vapor (TCWV) were above the 1991–2020 climatological averages, but were generally lower than the 2015–20 period which showed high vapor values. This is not surprising because La Niña conditions, which were present for most of the year, have a cooling effect on global surface and tropospheric temperatures, thus lowering the water-holding capacity of the global atmosphere. In reanalysis output, where time series are available for the entire 1979–2021 period, 2021 was the fourth (MERRA-2, anomaly = 0.477 kg m^{-2}), seventh (ERA5, anomaly = 0.264 kg m^{-2}), and eighth (JRA55, anomaly = 0.383 kg m^{-2}) highest vapor year since 1979. Time series of global averages agree well in all datasets (Fig. 2.22). Part of the discrepancy between the Global Navigation Satellite System (GNSS) time series and reanalysis over land is due to the limited spatial sampling afforded by the GNSS network. While TCWV decreased sharply from 2020 to 2021 globally and over ocean in all the datasets used in this assessment, there is substantial spread in the amount of this decrease over land.

The global map of TCWV anomalies from MERRA-2 (presented as percent of annual mean values to show extratropical changes more clearly) for 2021 (Plate 2.1i) reveals large low vapor anomalies in the eastern South Pacific, with low vapor anomalies close to the equator along a northwest–southeast oriented band and high vapor anomalies farther south. This pattern denotes the southwest displacement of the South Pacific Convergence Zone (SPCZ) that is typically associated with La Niña conditions (Brown et al. 2020). Prominent low vapor anomalies also occurred over West Antarctica and the adjacent sector of the Southern Ocean. Much of the rest of the globe showed wet anomalies, with the largest relative values observed over the Maritime Continent, South and East Asia, the northern Pacific, the southwest Atlantic, and eastern Canada, which correspond to regions with positive anomalies in surface temperature and lower tropospheric temperature (Plates 2.1.a,f). While the 2020/21 and 2021/22 boreal winters were both marked by La Niña conditions, the pattern of low vapor in the tropical Pacific along the SPCZ region was significantly more pronounced than what has been typically observed during La Niña events since 1980, and during the previous La Niña winter in 2017/18 (Fig. 2.23).

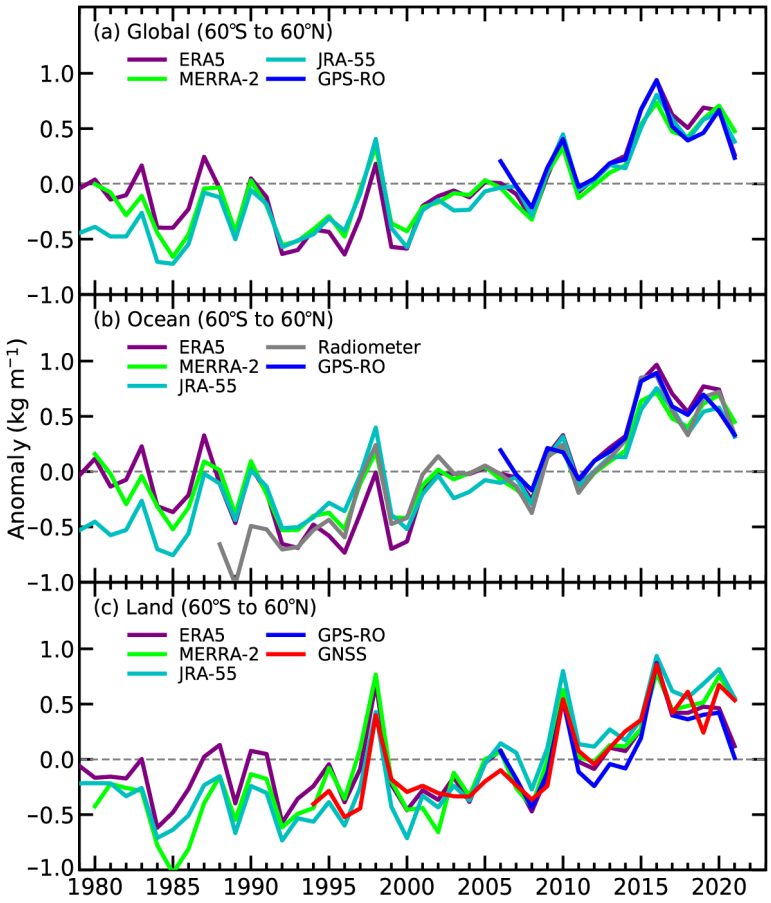

Fig. 2.22. Time series of yearly-mean TCWV anomalies (kg m^{-1}) from reanalysis, GPS-RO, GNSS, and satellite radiometers. All averages are over latitudes from 60°S to 60°N.

This assessment of global TCWV is based on data from three global reanalysis products: ERA5 (Hersbach et al. 2020), MERRA-2 (Gelaro et al. 2017), and JRA-55 (Kobayashi et al. 2015), as well as measurements made by satellite-borne microwave radiometers over the ocean (RSS Satellite; Mears et al. 2018), Global Positioning System–Radio Occultation (GPS-RO) observations from the COSMIC, Metop-A, -B, and -C and COSMIC2 satellite missions (satellite RO; Ho et al. 2020a,b, 2010a,b; Teng et al. 2013; Huang et al. 2013), and from ground-based GNSS stations (Bock 2020). The RSS satellite measurements are only available over the ocean, while GNSS stations are generally located on land. GPS-RO is available for both land and ocean. All three reanalyses assimilate satellite microwave radiometer and GPS-RO data and are therefore not fully independent from these two datasets. Ground-based GNSS measurements are not assimilated and are thus independent.

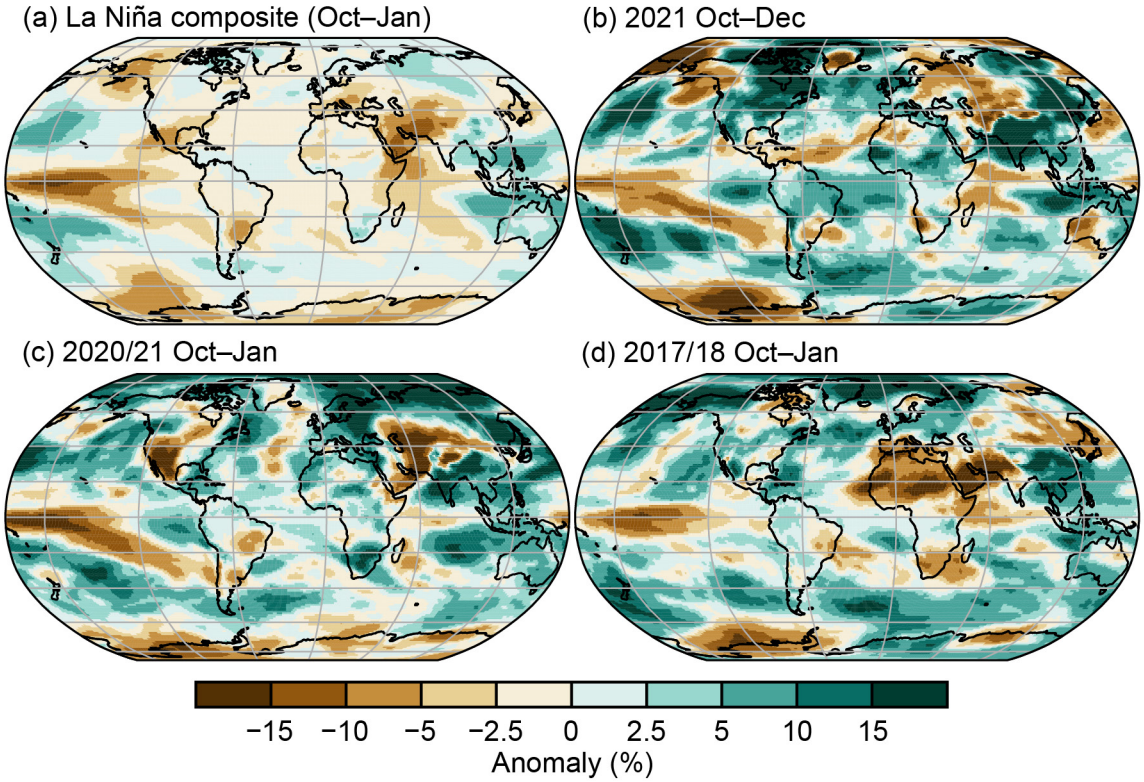

Fig. 2.23. Maps of TCWV anomalies (%) during La Niña events from the MERRA2 reanalysis. (a) Mean anomaly for the previous 12 La Niña seasons (Oct–Jan for 1983, 1984, 1988, 1995, 1998, 1999, 2005, 2007, 2010, 2011, 2017, and 2020). (b) Oct–Dec 2021 and (c) Oct–Jan 2020/21 anomalies. The La Niña periods highlighted in (b) and (c) show substantial drying south of the equator in the tropical Pacific, a feature less prominent in (d) Oct–Jan 2017/18 and in the composite in (a).

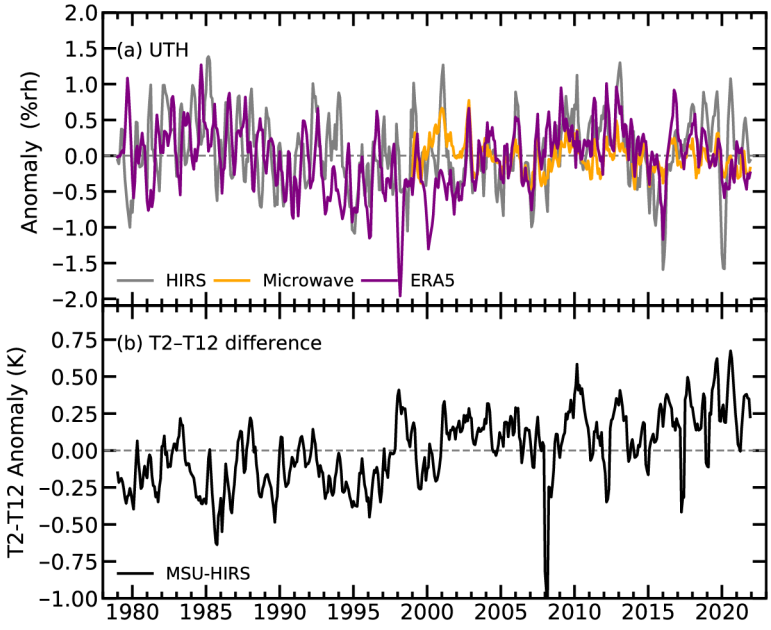

Fig. 2.24. (a) Time series of upper tropospheric humidity anomalies (%rh) from three datasets (see text for details). The anomalies are computed for area averaged data using the base period 1991–2020. (b) Difference (K) between the temperature and water vapor brightness temperature measurements in the upper troposphere.

3. UPPER TROPOSPHERIC HUMIDITY—V. O. John, L. Shi, E.-S. Chung, R. P. Allan, S. A. Buehler, and B. J. Soden

Upper tropospheric humidity (UTH) was slightly below the 1991–2020 average in 2021. Figures 2.24a,b show the monthly time series of the humidity datasets and a difference time series between the temperature and water vapor brightness temperature measurements in the UT, respectively. The large-scale relative humidity in the upper troposphere remains roughly constant, as expected from theoretical considerations (Ingram 2010); however, moistening in terms of the water vapor content of the UT is clearly evident from the lower panel. Here, there is a positive trend in the difference between T2 (brightness temperature of MSU Channel 2/AMSU-A Channel 5, which is sensitive to the UT temperature) and T12 (brightness temperature of HIRS Channel 12, which is sensitive to the UT water vapor). The trend in T2 and T12 indicates that the

emission level of the HIRS water vapor channel is shifting higher due to an increase in water vapor over time, while the emission level of the temperature sounding channel located in the 60-GHz oxygen absorption band remains unchanged, because the oxygen concentration does not change over time (Chung et al. 2016).

Water vapor is the strongest greenhouse gas in the atmosphere. Therefore, monitoring of water vapor in the upper troposphere (UT), owing to the cold temperature there, is crucial to determine one of the strongest positive feedback factors to the anthropogenic warming of the climate system (Coleman and Soden 2021). Three of the four datasets used in this work to monitor changes of water vapor in the UT are satellite based: 1) infrared based upper tropospheric humidity (UTH) derived from HIRS measurements starting in the late 1970s (Shi and Bates 2011), 2) microwave-based UTH derived from AMSU-B and MHS measurements starting in the late 1990s (Chung et al. 2013), and 3) mid-to-upper tropospheric temperature derived from MSU/AMSU-A measurements starting in the late 1970s (Zou and Wang 2011). The fourth dataset is relative humidity in the UT from the ERA5 reanalysis (Hersbach et al. 2020).

The agreement among the three UTH datasets is fairly good; the correlations of the HIRS and ERA5 data with the microwave data during their common period (1999–2021), are 0.6 and 0.5, respectively, despite their differences. For example, satellite data represent a layer average UTH with one satellite sampling the same location over Earth only two times a day while ERA5 data represent the 400-hPa level RH with hourly sampling. The microwave data have almost all-sky sampling while the HIRS data sample have only clear-sky conditions; this sampling difference is one reason for the higher interannual variability in the HIRS data as illustrated in John et al. (2011). In recent years, the HIRS data behave differently from the other two datasets: the mean value of UTH anomaly during 2021 for the HIRS data is 0.08 %rh, while for the microwave and the ERA5 data it is −0.15 and −0.18 %rh, respectively. This difference is due to the degradation in the quality of recent HIRS instruments (e.g., on board NOAA-19). The HIRS instrument era is slowly coming to an end and these instruments will soon be replaced by hyperspectral instruments, such as Infrared Atmospheric Sounding Interferometer (IASI). For the last three years (2019–21), simulated HIRS data from IASI spectra have been used in the creation of HIRS UTH data.

Plate 2.1j shows the 2021 anomaly map for the microwave UTH data. The patterns of the anomalies relate to large-scale weather conditions, with positive (negative) UTH anomalies associated with wetter (drier) conditions at the surface. This is due to the fact that one of the main drivers of UTH is convection; therefore, UTH is useful for monitoring changes in large-scale dynamics in the atmosphere. Clear La Niña patterns are visible, with positive anomalies over the Maritime Continent, India, and parts of Brazil and a strong dry signal in the western equatorial Pacific (centered near the data line). Prevailing drought conditions over the western United States are also reflected in the anomaly patterns. The patterns also reveal flooding conditions in northern Brazil and continued drought conditions over much of southern Brazil, Paraguay, Uruguay, and northern Argentina. Drought patterns in parts of the Horn of Africa, including Somalia, and in southern Madagascar are also clearly depicted.

4. PRECIPITATION—R. S. Vose, R. Adler, U. Schneider, and X. Yin

Precipitation over global land areas in 2021, as estimated from two different monitoring products, was slightly below the 1991–2020 long-term average (Fig. 2.25a). In particular, the global precipitation total anomaly according to the gauge-based product from the Global Precipitation Climatology Centre (GPCC; Becker et al. 2013) was −7.55 mm for 2021, and the blended gauge-satellite product from the Global Precipitation Climatology Project (GPCP; Adler et al. 2018) was −5.87 mm. The good agreement between the two products is in contrast to 2020, when GPCC depicted less precipitation than average whereas GPCP depicted slightly more than average. Given the modest discrepancy in 2020, it is not clear whether the global land surface was wetter in 2021 compared to 2020.

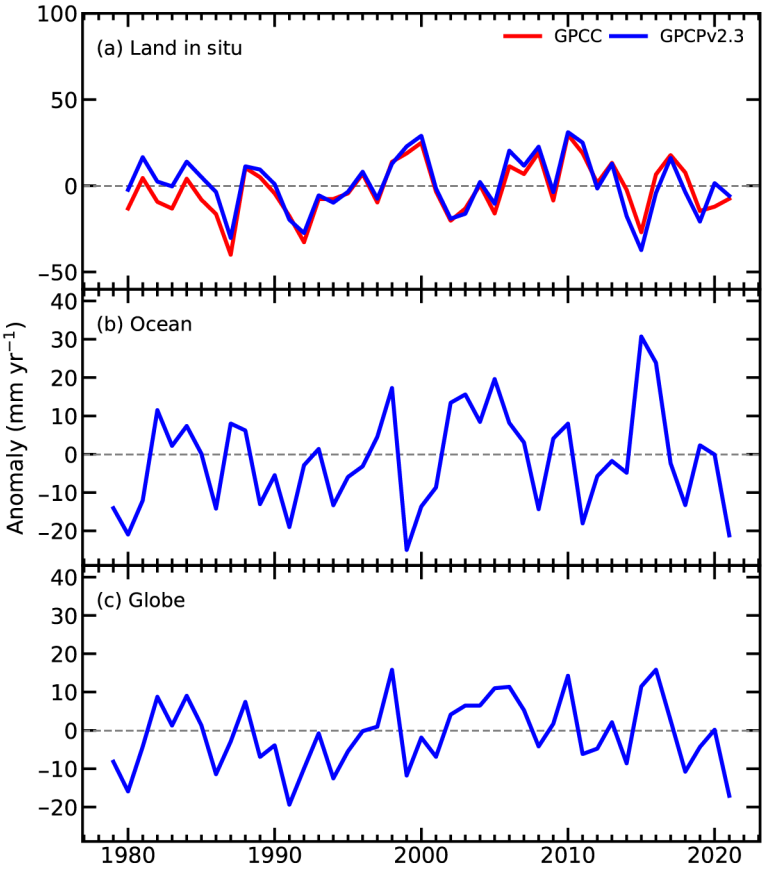

Fig. 2.25. Globally averaged precipitation anomalies (mm yr^{-1}) relative to the 1991–2020 base period over (a) land areas, (b) ocean areas, and (c) the globe. Land and ocean time series were created using a proportional land/sea mask at the 1° × 1° resolution scale.

Over the global oceans (Fig. 2.25b), the precipitation anomaly was –21.17 mm, and the global anomaly (Fig. 2.25c) was –17.07 mm, according to the GPCP product, both of which were substantial decreases from the previous year. Overall, the GPCP product ranks 2021 as the third-lowest year for precipitation in both the global and ocean records, which begin in 1979, after 1991 and 1999, respectively.

In many parts of the world, precipitation anomaly patterns in 2021 were consistent with the 'typical' La Niña pattern. For example, La Niña is often associated with more precipitation than average falling across southern Asia southeastward across the Maritime Continent and into the South Pacific Ocean. Northern South America and the equatorial Atlantic Ocean also tend to have above-average precipitation during La Niña. In contrast, much of the central Pacific Ocean near and south of the equator tends to receive much less precipitation than average, as do the eastern North Pacific and North Atlantic Oceans. However, in 2021 some areas exhibited patterns that ran counter to a 'canonical' La Niña event; for instance, La Niña usually means additional rainfall to Australia, but the anomaly map for 2021 shows a mixed pattern with expected abundant rainfall in the southeast and along the northern coast, but general dry conditions in the outback. In fact, the global land precipitation being below average is somewhat unusual compared to recent La Niña years when it was above average.

Over global land areas, the largest high precipitation anomalies in 2021 were across northern South America and eastern China, and the largest low precipitation anomalies were over central America, southeastern South America, the Middle East, southeastern Africa, and northern Australia (Plate 2.1k). Over the global oceans, a broad swath of large high precipitation anomalies extended from the eastern Indian Ocean to the Maritime Continent and then southeastward across the tropical western Pacific Ocean. The equatorial Atlantic Ocean and parts of the equatorial Pacific Ocean also received much more precipitation than average, as did part of the Southern Ocean near South America. In contrast, large low precipitation anomalies were apparent over much of the central Pacific Ocean south of the equator as well as over the western Indian Ocean, and to a somewhat lesser extent, over parts of the North Pacific and North Atlantic Oceans. Rainfall excesses helped to fuel frequent flood conditions, such as in Indonesia, Malaysia, and surrounding countries, as well as in northern South America and eastern Brazil. The dry anomalies were associated with continuing drought conditions over much of the southern half of South America and eastern Africa. See also section 2d5 and Chapter 7 for detailed information on region-specific extreme precipitation events.

5. LAND-BASED PRECIPITATION EXTREMES—S. Blenkinsop, M. R. Tye, M. G. Bosilovich, M. G. Donat, I. Durre, D. Lavers, A. J. Simmons, and M. Ziese

Overall, 2021 saw above-average frequencies of heavy and very heavy 24-hour precipitation (Figs. 2.26c,d) across several large regions but below-average intensities for the most extreme events in most areas (Plate 2.1l). Long-term changes in global precipitation extremes are difficult to quantify due to the local nature of events and sparse observations. These difficulties, such as different observing and reference periods and assessing means vs. totals, explain some of the discrepancies between extreme precipitation indices and below-average mean precipitation in 2021 (section 2d4). Using a combination of observational and reanalysis products, we summarize national-scale temporal variability of extreme precipitation indices (Table 2.7; NOAA 2022a).

Across the contiguous United States, the area experiencing a high proportion of precipitation from the highest 10th percentile 1-day events (NOAA Climate Extremes Index component 4; NOAA 2022b) was substantially above average, at 18.5%, the sixth largest area in the 112-year record

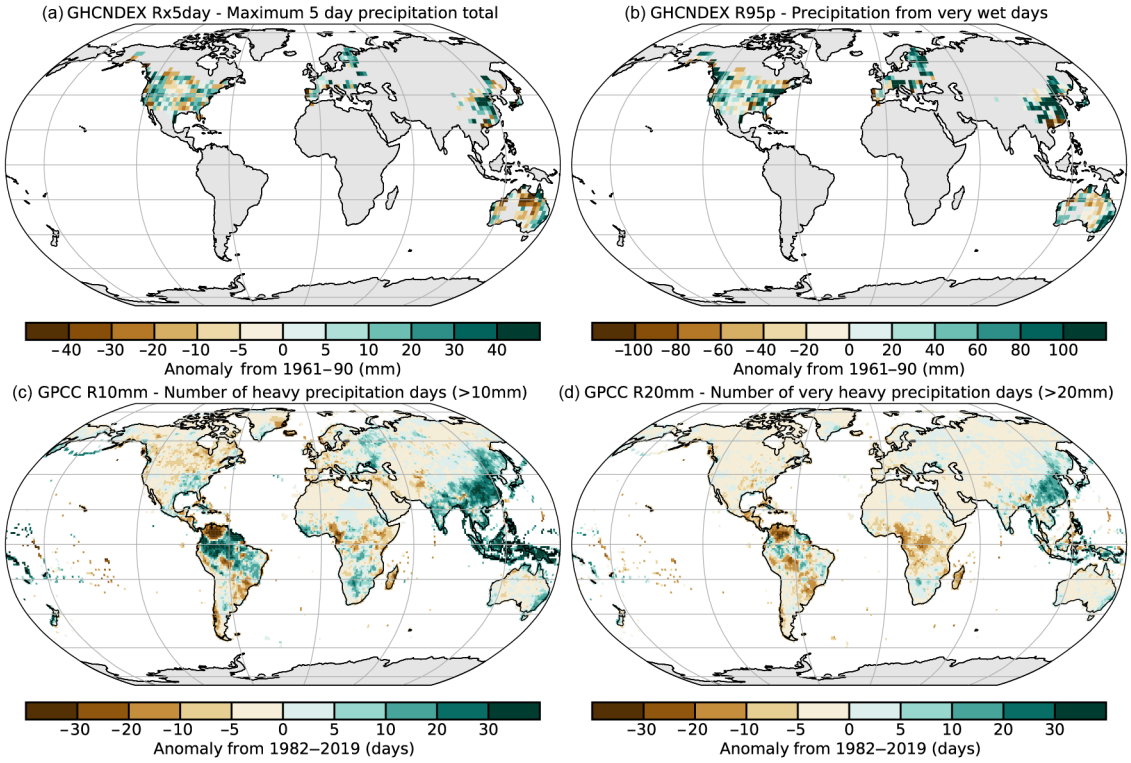

Fig. 2.26. Anomalies of 2021 indices: (a) Rx5day and (b) R95p (mm) derived from the in situ-based GHCNDEX relative to a 1961–90 baseline (Donat et al. 2013) and (c) R10mm and (d) R20mm (GPCC) relative to a 1982–2019 baseline.

Table 2.7. Indices used in this section and their definitions. Indices are expressed as anomalies relative to a baseline climatology which varies between data products.

Index	Name	Definition
Rx1day	Maximum 1-day precipitation	Annual maximum 1-day precipitation amount (mm)
Rx5day	Maximum 5-day precipitation	Annual maximum consecutive 5-day precipitation amount (mm)
R10mm	Heavy precipitation days	Count of days where daily precipitation total > 10mm (days)
R20mm	Very heavy precipitation days	Count of days where daily precipitation total > 20mm (days)
R95p	Total precipitation from very wet days	Total precipitation from days where the daily precipitation total exceeds the climatological baseline wet day 95th percentile
10th Percentile 1-day	NOAA Climate Extremes Index Component 4 (NOAA 2022a)	The percentage area of the United States experiencing extreme precipitation on days where the total daily precipitation exceeds the historical record (1910–present) baseline wet day 90th percentile, per year, winter (DJF), spring (MAM), summer (JJA), or autumn (SON) season

(Fig. 2.27a), while the same index for the autumn season indicated the largest area on record (17.4%). GHCNDEX (Donat et al. 2013; section 2b4) highlights several clusters of positive Rx1day and Rx5day (Fig. 2.26a; Table 2.7) anomalies in North America. Several storms occurred in California (Appendix Table A2.2), partly related to the clustering of strong Pacific storms in October, including a "bomb cyclone" and an exceptional atmospheric river that affected California and Oregon coasts (NOAA 2021a). Parts of Washington State experienced another atmospheric river event in mid-November, which caused record rainfall in around 20 locations in British Columbia (Canada), resulting in flooding and landslides (see section 7b1, Sidebar 7.1). In August, Hurricane Ida (Category 4) was the most significant storm to affect the eastern United States during the North Atlantic season, moving northeast after landfall in Louisiana, breaking the hourly observed rainfall record in New York City (WMO 2021b; NOAA 2021b).

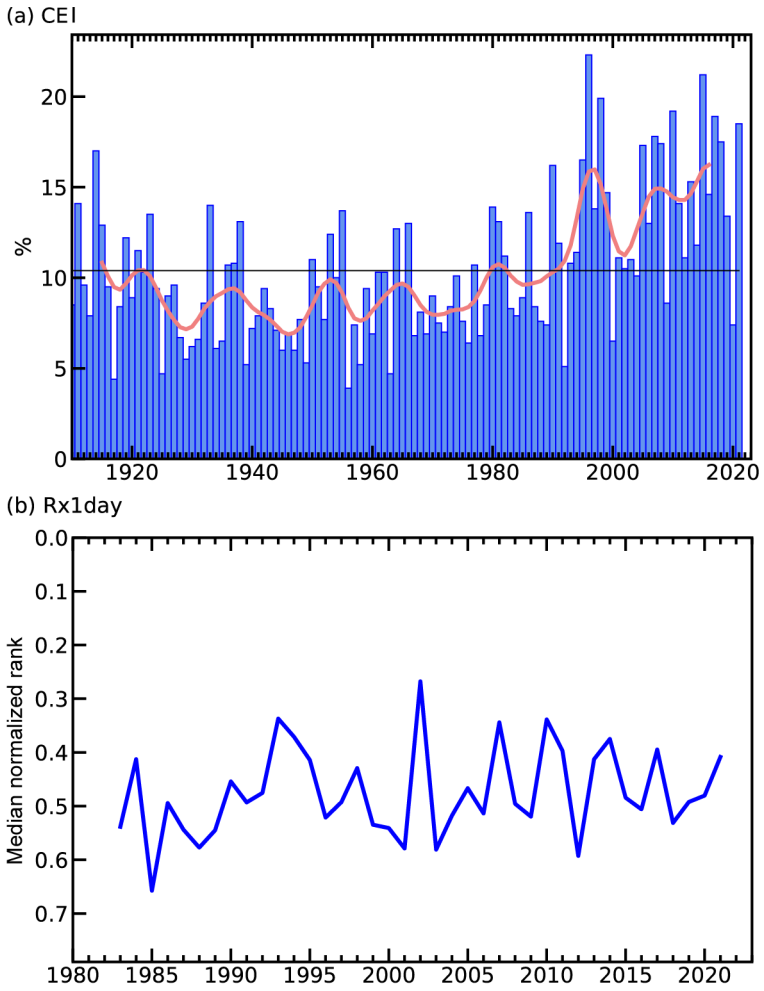

Fig. 2.27. (a) Annual percentage (%) of the contiguous United States with a much-greater-than-normal proportion of precipitation derived from extreme (highest 10th percentile) 1-day precipitation events for the period 1910–2021 (NOAA 2022a). The solid red line denotes a smoothed Gaussian filter, and the horizontal black line denotes the series mean. Note that methodological changes introduced after 2005 means that this series may produce higher values after this date. (b) Median normalized rank of annual Rx1day values for Europe. The annual rank of the Rx1day value at each gauge relative to its own record is derived from the European Climate and Assessment Dataset (Klein Tank et al. 2002) and is normalized by gauge length. The median of all the gauge normalized ranks is then calculated for each year, with low values denoting a higher median rank. Only gauges with at least 50 years of data were used to calculate the annual ranking statistics, and only years for which at least 5000 gauges returned an index value are shown.

Rain gauges from the European Climate and Assessment Dataset (Klein Tank et al. 2002) indicate 2021 was an average year for R10mm, R20mm, and Rx5day for Europe, but above average for Rx1day (Fig. 2.27b) and R95p, the latter ranking 9th and 11th, respectively, in the 39-year record. A cutoff low-pressure system contributed to severe flooding in western Germany and neighboring countries in mid-July (section 7f3; ECMWF 2021), with 18 (12) new Rx1day (Rx5day) records set in GHCNDEX. The 24-hour and 48-hour accumulations over western Germany were the highest in the 140-year record (Junghänel et al. 2021) and caused severe flooding. A rapid attribution study calculated an increased likelihood of such 1-day accumulations (factor of 1.2–9) in the region today compared to a 1.2°C cooler climate (Else 2021). Positive Rx1day anomalies (GPCC, Plate 2.1l) over Sweden and adjacent areas also saw six gauges in GHCNDEX with new records, including the city of Gävle (SMHI 2021).

The GPCC (Schamm et al. 2013) and GHCNDEX data show positive anomalies corresponding to a prolonged period of heavy rain in eastern parts of New South Wales, Australia, in late March, with some areas recording more than 500 mm of rain in 48 hours (Floodlist 2021b) and more than 50 new daily records for March (Bureau of Meteorology 2021a). More than 60 daily records were broken for November across New South Wales and Queensland, with widespread flooding

(Bureau of Meteorology 2021b,c). Combined, these contributed to considerable positive anomalies of R10mm and R20mm (Figs. 2.26c,d).

The datasets examined here are broadly consistent over southeast Asia in showing above-average frequencies of rainfall extremes, although the GPCC data show below-average intensities in Rx1day (Plate 2.1l). Cyclone Seroja produced 15 new monthly records for April over Western Australia (Bureau of Meteorology 2021d), after generating significant accumulations over Timor, Indonesia, and Singapore (WMO 2021b; Floodlist 2021c). Farther north, Cyclone Surigae brought record rainfall to the Philippines (NOAA 2021c) and parts of Cambodia and Vietnam (Floodlist 2021d,e) in April. An area of positive anomalies over northern and eastern China appears consistent across indices and datasets (Plate 2.1l, Figs. 2.26a–d), reflecting a series of extreme rainfall events; Typhoon In-fa generated several days of heavy rain in Henan Province in mid-July. Nearby Shanxi and Shaanxi Provinces also saw over 60 gauges reporting record accumulations in October (Floodlist 2021f) as moisture was transported from the South China Sea and Bay of Bengal.

Many areas with significant events in 2021 also have positive anomalies in GHCNDEX R95p (Fig. 2.26b), showing the important contribution of extremes to total precipitation. In GPCC, R95p also shows a strong contribution from extreme events over parts of Brazil and southern Africa. The R10mm and R20mm indices for GPCC (Figs. 2.26c,d) and ERA5 (Hersbach et al. 2020) show positive anomalies over northern Brazil and neighboring nations, associated with prolonged rainfall during May and June and again at the end of the year. Above-average Rx1day is also apparent over southeastern Brazil, which experienced widespread flooding early in the year (Plate 2.1l). Above-average R10mm and R20mm frequencies are also evident over several southern African nations (Figs. 2.26c,d). Tropical Cyclone Eloise was followed by several weeks of heavy rainfall at the start of 2021, with Beira, Mozambique, receiving close to its average total January precipitation in 24 hours (NOAA 2022c). Prolonged heavy rain in the summer also resulted in above-average values over southern Sudan and northern Uganda, contrasting with much of central Africa (Plate 2.1l).

Please refer to Chapter 7 (Regional Climates) for more details about precipitation events around the world.

6. CLOUDINESS—C. Phillips and M. J. Foster

The average global cloud fraction, as measured by MODIS *Aqua* C6.1 (Platnick et al. 2015), was 67.67% in 2021. This makes 2021 the third-cloudiest year in the 19-year *Aqua* satellite record, after 2010 and 2020. La Niña occurred over most of the past three years, though not all years with similar Niño-3.4 index values were associated with such positive cloud anomalies. Being a single satellite in a sun-synchronous orbit, MODIS *Aqua* data is limited to two global observations per day. *Terra* MODIS might have been included to add better representation, but electronics issues beginning in October 2020 forced degradation of the cloud products, so it must be omitted (Platnick 2022). Prior to those issues, the *Terra* global cloud anomaly had excellent correlation with *Aqua*, so single day and night observations seem to be sufficient. The annual anomalies for CERES-*Aqua*-MODIS (Trepte et al. 2010; Minnis et al. 2008), PATMOS-x v6.0 (Heidinger et al. 2013), MISR (Di Girolamo et al. 2010), CLARA-A2.1 (Karlsson et al. 2017, 2020, 2021), and PATMOD (MODIS *Aqua* processed with PATMOS-x cloud algorithms, unpublished) have been included for comparison; however, they have differed from MODIS *Aqua* C6.1 significantly in recent years (Fig. 2.28). For the sake of simplicity, the following analysis will focus on MODIS *Aqua* C6.1.

This MODIS record exhibits a small increasing trend in global cloudiness since the record began in 2003. The main positive contributing regions are the poles and the tropics, which are partially offset by negative trends in the subtropics and midlatitudes (Fig. 2.29). This trend makes especially cloudy years like 2021 more likely, though the rank for 2021 is unchanged in the detrended data.

Plate 2.1m shows a map of the average cloudiness anomaly in 2021. Naturally, regional anomalies are much larger than global anomalies, frequently on the order of 5%. The pattern of increased cloudiness in the western Pacific and reduced cloudiness in the central Pacific is common during

La Niña conditions, resulting from the invigoration of convection over high sea surface temperatures (SST) and suppression of convection over cool SSTs. Conversely, other cloud regimes like the marine stratocumulus of the eastern Pacific can exhibit an inverse relationship, with lower SSTs correlated with more cloudiness (Loeb et al. 2018b). Note the opposite signs of cloud and SST anomalies in the eastern Pacific contrasted with aligned signs in the western Pacific (Plate 2.1a).

In addition to the typical La Niña pattern in the Pacific in 2021, several regions experienced their highest percentage of cloudiness in the record, notably the Indian subcontinent, the Canadian Arctic, and part of East Antarctica. All of these locations were also anomalously cloudy in 2020. On the other hand, the southeast Atlantic near the coast of Africa has had a negative anomaly since 2018 and had a record minimum in 2021. While these regional anomalies are not the largest values seen in Plate 2.1m, they are highlighted here after inspecting their time series and considering their z-score (standard deviations from the mean) to ensure that they were truly cloud fraction outliers in 2021.

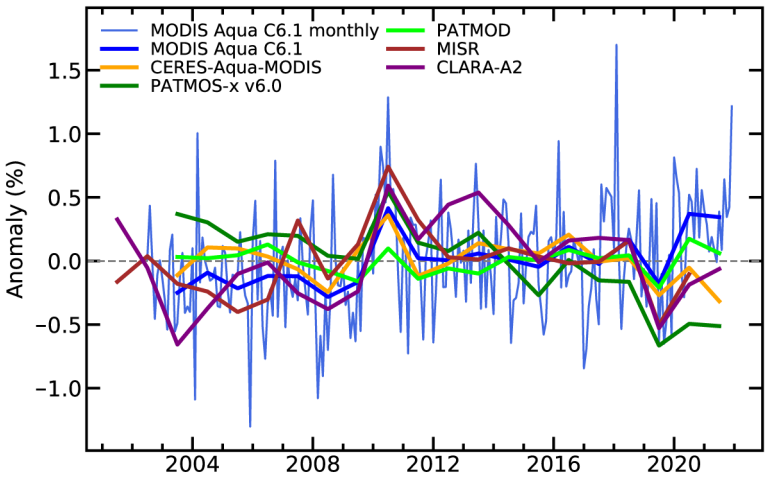

Fig. 2.28. Global average cloud fraction anomaly (%) relative to the 2003–21 reference period. PATMOS-x v6.0 anomalies were computed by backfitting a grid of joint seasonal-diurnal cloudiness models for all satellites simultaneously and taking the smoothed residual.

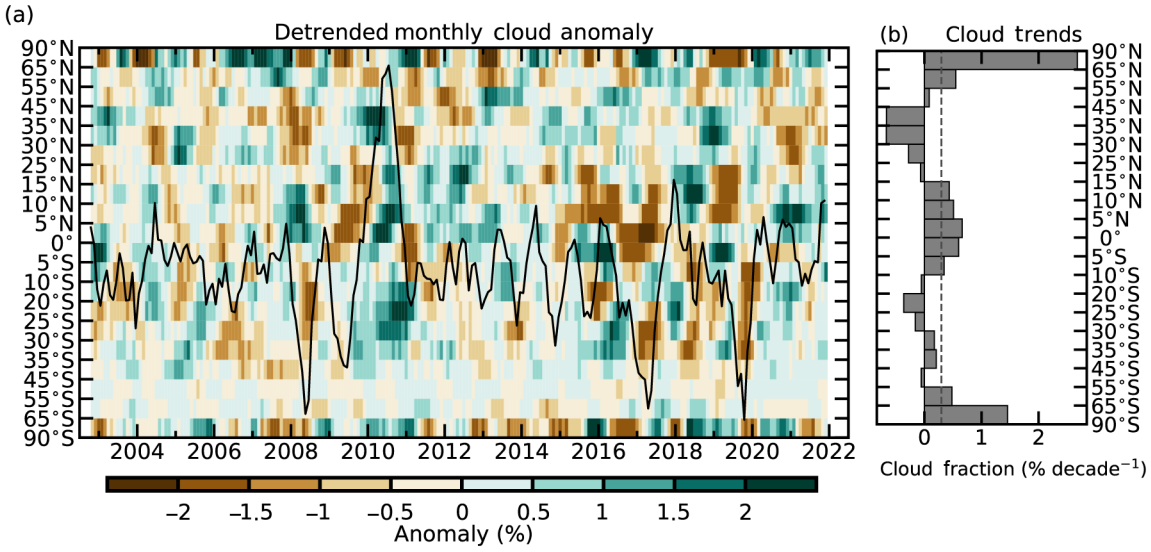

Fig. 2.29. (a) Zonal mean cloud fraction anomaly (%) from MODIS *Aqua* C6.1 with 20 latitude bands partitioned to have approximately equal area. Monthly anomalies are relative to the mean of all identical months between 1 Jul 2002 and 31 Jan 2022. Individual bands were detrended with trends computed using the complete years from 2003 through 2021. The detrended anomaly was then smoothed by a 6-month centered rolling mean filter. The smoothed detrended global anomaly is superimposed for reference as a black line, detached from any y-axis. (b) The extracted trends in cloud fraction (% decade^{-1}, aligned gray bars) for the period 2003–21 and the global mean trend (vertical dotted black line).

Clouds reduce both net infrared (IR) emission and solar absorption, and many factors influence the relative balance that determines the sign of the overall cloud radiative effect (section 2f1). The presented regional anomaly in total cloud fraction best describes the solar absorption component, e.g., positive cloud fraction anomalies suggest negative solar absorption anomalies. Calculating the change in full radiative balance would require information, such as independently estimating the changes in height-partitioned cloud fraction, which is difficult with passive satellite observations, due to obscuration from higher clouds. Direct observations of the radiation budget at the top-of-atmosphere are examined in section 2f1.

7. RIVER DISCHARGE AND RUNOFF—H. Kim and D. Tokuda

For five years consecutive years (since 2017), global average runoff has been greater than the 1981–2010 average. Runoff in 2021 was the 11th greatest (~84th percentile) in the 64-year record dating to 1958. It was slightly less than the 2020 average, which had the third greatest runoff (~97th percentile; Fig. 2.30); however, there were significant differences in global distributions of runoff (Plate 2.1n) and discharge (Plate 2.1o) anomalies compared to those of 2020.

Rivers in northern South America, such as the Amazon and Orinoco, experienced a strong wet phase of above-average discharge, after a relatively dry phase (below-average discharge) the previous year. In the Amazon, such a shift was particularly notable in the Rio Negro and Rio Solimoes, while Rio Madeira and Rio Tapajos have stayed drier than the 1981–2010 reference period. In Africa, the Nile has shifted into a dry phase, while the Congo, Niger, and Zambezi have stayed in the same phase as 2020. Northern North America had less water than in 2020, and the midwest and northeastern United States became drier than average, leading to less discharge. Northern Europe and western Siberian regions were drier than in 2020. Discharge in many European rivers, including the Dnieper, Don, Loire, Northern Dvina, Rhone, Rhine, Seine, and Volga, was below average. However, it is worth nothing that, in spite of the below-normal annual discharge, there was a devastating flood disaster in Europe, including the Ahr Valley, a tributary of Rhine River, in July 2021. The Danube discharged more freshwater into the Black Sea than usual. Compared to the prior year, most regions in Asia did not show noticeable changes except for southern China (e.g., the vicinity of the Pearl River), Indochina (e.g., the Mekong and Chao Phraya) and the Indus River region, where those regions experienced severe drought and thus had less discharge.

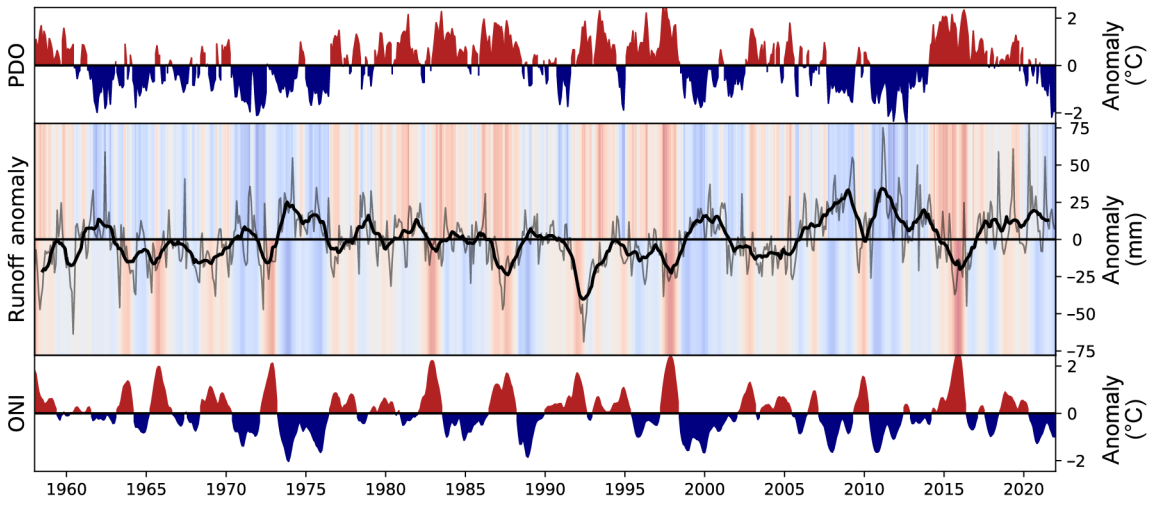

Fig. 2.30. Interannual variability of the Oceanic Niño Index (ONI; lower, °C), the Pacific Decadal Oscillation (PDO; upper, °C), and global runoff (middle; mm; thick line is 12-month moving average). The ONI and PDO are shaded red (positive phase) or blue (negative phase). Shading above and below the zero-line of global runoff is proportional to the PDO and ONI, respectively.

Runoff is a local residue of the water budget to be integrated along pathways turning into discharge, which is the most important freshwater resource to humanity. The El-Niño Southern Oscillation (ENSO) and Pacific Decadal Oscillation (PDO; Zhang et al. 1997) are well-known factors that influence global freshwater discharge (e.g., Kim and Tokuda 2020, 2021). Figure 2.30 depicts the long-term fluctuation of the total runoff and those climate modes. Positive and negative phases of ENSO and PDO correspond to drier and wetter conditions of global freshwater discharge, with ENSO and PDO accounting for around 47% of the total variance. The interannual variability and climatology of freshwater discharge into the major oceans are shown in Fig. 2.31 for the Pacific, Atlantic, Arctic, and Indian basins, where they receive 85% of global freshwater discharge, of which the drainage area reaches 75% of the total land surface area. The Pacific Ocean has received an increasing amount of freshwater discharge during the last two decades, reaching a record maximum in 2021, with above-average discharge throughout the entire year. Freshwater discharge into the Atlantic Ocean remained in a positive phase due to an anomalously large discharge during boreal summer (June–September). The Arctic Ocean received less discharge in 2021, and its month-to-month variability was near-average; however, there is an increasing trend present over the entire analysis period beginning in 1958. An increasing trend is also found in the

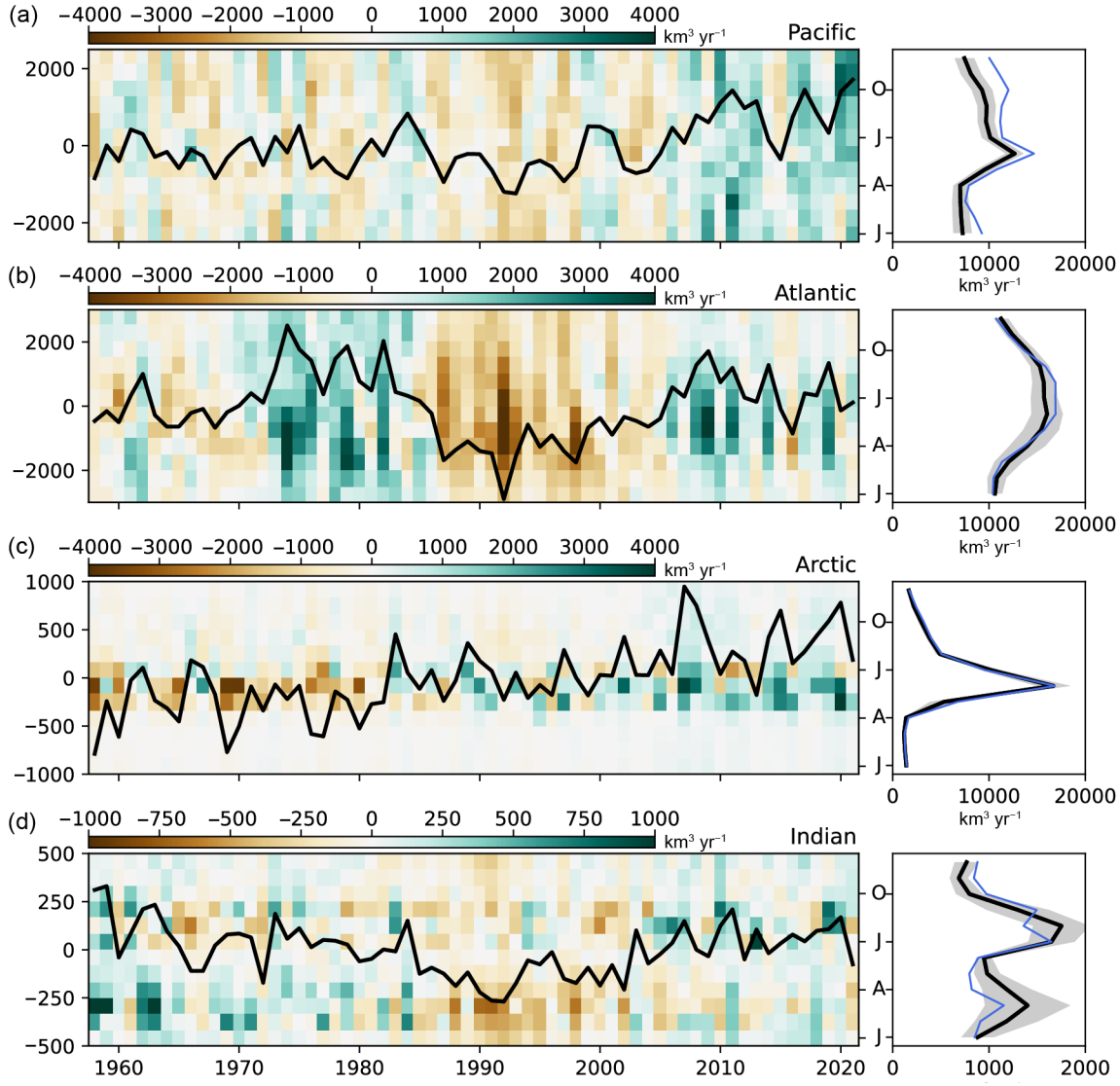

Fig. 2.31. (a–d, left panels) Interannual variability of freshwater discharge (km³ yr⁻¹) to global ocean basins. The black line and vertical shaded boxes indicate the annual mean and monthly anomaly, respectively. (a–d, right panels) Seasonality of freshwater discharge (km³ yr⁻¹) to global ocean basins. The thick black line, thin blue line, and gray shade indicate long-term climatology, seasonal variation during 2021, and 1 std. dev. of long-term variability, respectively.

Indian Ocean, but it is weaker and shorter, beginning around 1990. The Indian Ocean received slightly less discharge on average in 2021, with a less-than-normal amount occurring during the first wet season of the year.

The time series of natural variability-only estimates of global runoff and discharge were generated using global off-line hydrologic simulations by the Ensemble Land State Estimator (ELSE; Kim et al. 2009) on a 1° grid and a large-scale river routing and flood inundation model Catchment-based Macro-scale Floodplain (CaMa-Flood; Yamazaki et al. 2011) on a 30-minute drainage direction map (DDM30; Döll and Lehner 2002). The World Ocean Atlas 2018 (Garcia et al. 2019) was used to separate the freshwater discharge into each oceanic basin. The atmospheric boundary conditions were created based on the Japanese global atmospheric reanalysis (JRA-55; Kobayashi et al. 2015), and the Global Precipitation Climatology Centre (GPCC) Monitoring Product version 2020 (Schneider et al. 2020) was used to adjust bias in the reanalysis precipitation field.

8. GROUNDWATER AND TERRESTRIAL WATER STORAGE—M. Rodell and D. Wiese

Changes in terrestrial water storage (TWS), which is the sum of groundwater, soil moisture, surface water, snow, and ice, have been measured on regional to global scales by the Gravity Recovery and Climate Experiment (GRACE) and GRACE Follow On (GRACE-FO) satellite missions on a monthly basis since 2002 (Tapley et al. 2004; Landerer et al. 2020). Interannual changes tend to be dominated by snow and ice at high latitudes and in alpine regions, by surface water in the wet tropics, and by groundwater elsewhere (Getirana et al. 2017).

Plate 2.1p displays observed changes in mean annual TWS between 2021 and 2020 as equivalent heights of water in cm. Changes in TWS were mixed across Eurasia. Most of western Europe continued to recover from the 2019 drought, while Scandinavia in the north dried (lost TWS) after a wet 2020. Copious rain increased TWS in southern India, where it was already elevated at the start of the year. To the east, the Indochina peninsula recovered from drought, receiving abundant rainfall from Typhoon Surigae (see section 4g5). Northeastern China also gained water, while drought afflicted areas south and west of the Caspian Sea. In Australia, TWS increased along the northern and southeastern coasts. Droughts in Africa caused TWS decreases in Angola and Madagascar, while TWS increased rapidly in Zimbabwe and adjacent areas at the start of 2021, including a 2-m increase in the level of Lake Kariba. In North America, TWS declines extended from southern California into southern Canada, regions where drought conditions prevailed, and across to the Great Lakes region, where declines exceeded 12 cm equivalent height of water in some parts. However, TWS in the center of the continent (including the Great Lakes region) had been elevated since 2019, when record flooding occurred, and the decrease in 2021 was largely a return to more typical conditions. Northern South America gained a massive amount of water, with increases exceeding 12 cm over a large area, but TWS declined in southern Brazil. Time series of zonal mean and global mean monthly TWS anomalies, after removing the seasonal cycle, are plotted in Figs. 2.32 and 2.33, respectively. TWS declines

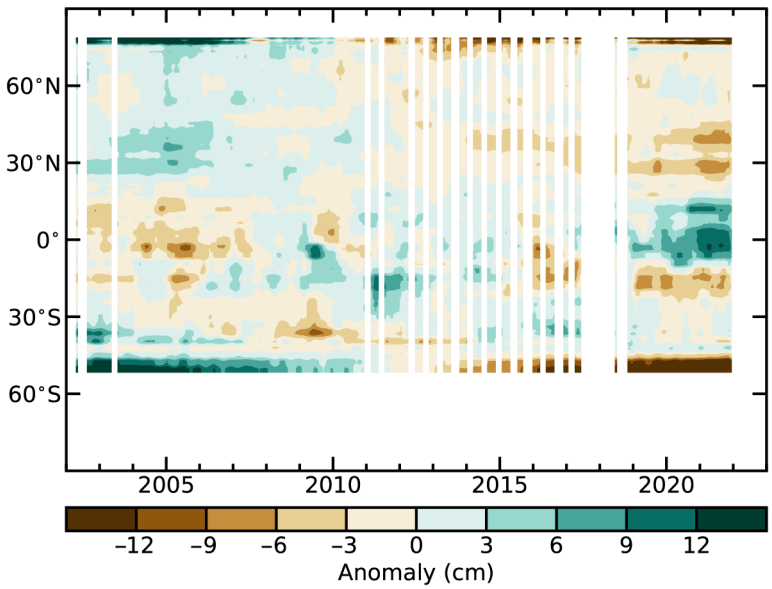

Fig. 2.32. Zonal means of terrestrial water storage anomalies, excluding those in Antarctica, Greenland, the gulf coast of Alaska, and polar islands, in cm equivalent height of water, based on gravity observations from GRACE and GRACE-FO. The anomalies are relative to a 2003–20 base period.

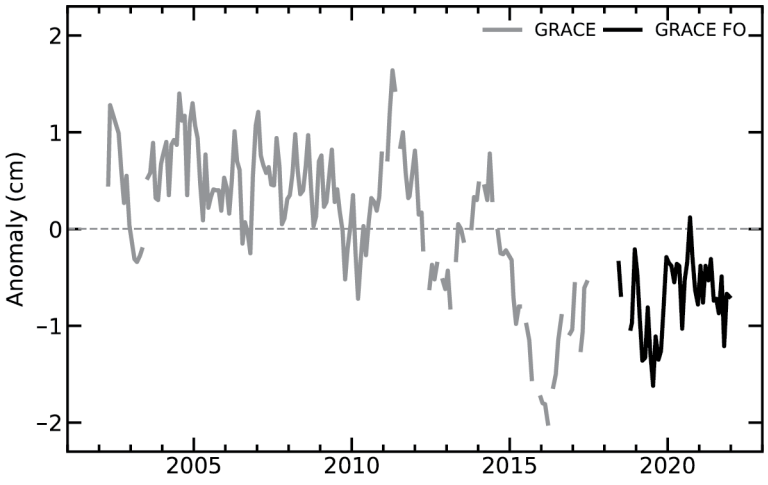

Fig. 2.33. Global average terrestrial water storage anomalies from GRACE (gray) and GRACE-FO (black), in cm equivalent height of water, relative to a 2003–20 base period.

in Antarctica, Greenland, the Gulf Coast of Alaska, and polar islands are attributed to ice sheet and glacier ablation as opposed to meteorological variations, so those regions were excluded from the calculations for Figs. 2.32 and 2.33. However, the effects of additional high latitude ice mass losses remain. The large TWS increase, seen straddling the equator in Fig. 2.32, corresponds to the massive wet anomaly in northern South America. The TWS decline just south of 30°N is due almost entirely to long-term groundwater depletion in northern India (Rodell et al. 2018), exacerbated by a drought just east of that area in 2021 (section 2d10). The TWS decline near 40°N mainly reflects drought across the western and central United States, drought stretching from Turkey to the Caspian Sea (including water level declines in that sea), and long-term groundwater depletion associated with agricultural irrigation in the North China Plain (Rodell et al. 2018). Droughts in southern Brazil and Angola caused the TWS decline near 15°S. Overall, global-scale TWS variability in 2021 was muted compared with past years (Plate 2.1p). Owing to the scarcity of in situ TWS measurement records, we relied on TWS data derived from GRACE and GRACE-FO satellite observations of Earth's time-varying gravity field. Uncertainty in the derived TWS anomalies is heterogeneous, but as a point of reference, uncertainty in monthly TWS anomalies is typically around 1–2 cm equivalent height of water at 500,000 km^2 and larger scales (Wiese et al. 2016).

9. SOIL MOISTURE—R. van der Schalie, W. Preimesberger, P. Stradiotti, M. van der Vliet, L. Mösinger, N. J. Rodríguez-Fernández, R. Madelon, S. Hahn, M. Hirschi, R. Kidd, R. A. M. de Jeu, and W. A. Dorigo

Soil moisture plays a key role in land–atmosphere interaction due to its defining effect on boundary conditions for energy and water fluxes (Seneviratne et al. 2010). In 2021, global satellite-observed soil moisture recorded wetter-than-usual conditions (Fig. 2.34). Note that wetter/drier within this section refers to higher/lower soil moisture volumes in the first centimeters of the soil as compared to the 1991–2020 reference period. The discrepancy between NH and SH, as recorded in 2020 (van der Schalie et al. 2021), was strongly reduced, with NH continuing to be wetter-than-usual and SH observing near-neutral conditions. Given that North America and central Asia experienced dry conditions, the wet conditions in Europe, eastern Asia, and the Indian subcontinent more than compensated for that in the NH average. For the SH, widespread dry

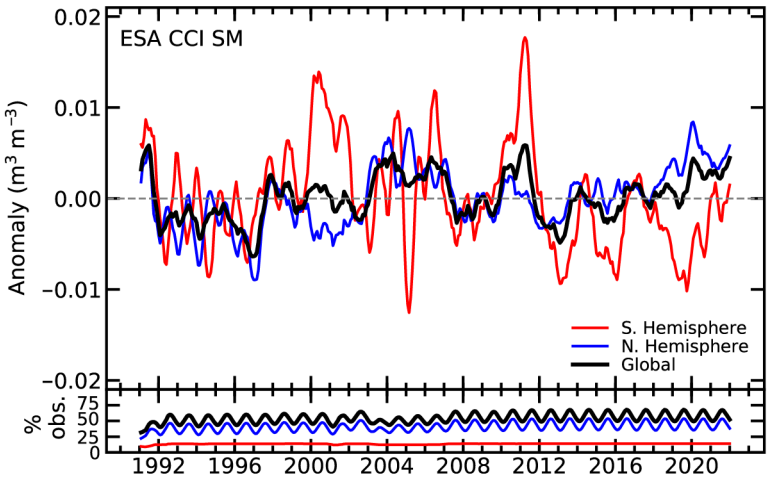

Fig. 2.34. Time series of global (black), NH (blue), and SH (red) monthly surface soil moisture anomalies for the period 1991–2021 (upper, m^3 m^{-3}; 1991–2020 base period) and the valid retrievals as a percentage of total global land surface (lower, %). Data are masked where no retrieval is possible or where the quality is not assured and flagged due to dense vegetation, frozen soil, radio frequency interference, and so forth. (Source: ESA CCI Soil Moisture.)

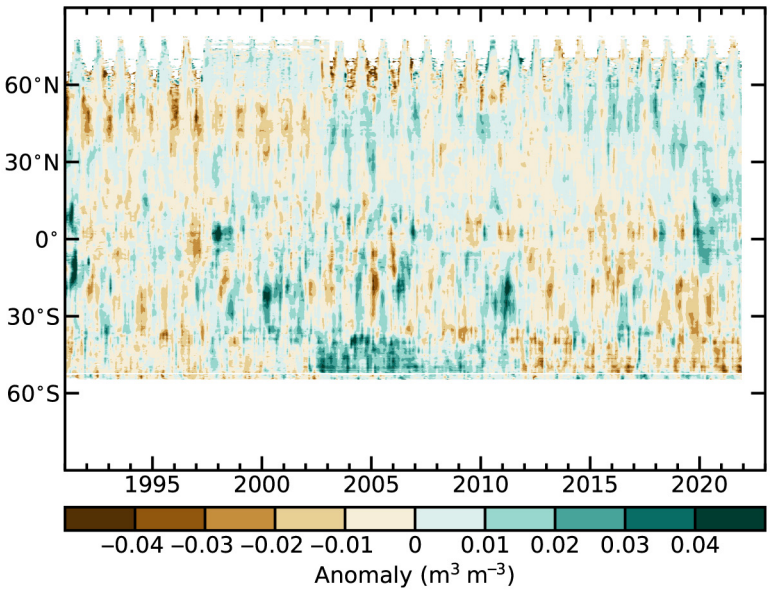

Fig. 2.35. Time–latitude diagram of monthly surface soil moisture anomalies ($m^3 m^{-3}$; 1991–2020 base period). Data are masked where no retrieval is possible or where the quality is not assured and flagged due to dense vegetation, frozen soil, radio frequency interference, and so forth. (Source: ESA CCI Soil Moisture.)

conditions in central to southern South America are balanced out by wet anomalies seen in other regions.

These findings are clearly shown in Fig. 2.35, where NH and equatorial latitudes show positive anomalies since early 2020. South of 15°S in the SH, consistent negative anomalies have been present since at least 2018, moving closer to neutral conditions in 2021. More detailed maps of the spatial distribution are shown in Plate 2.1o (average for 2021) and Appendix Fig. A2.12 (monthly).

Linked to the La Niña conditions in winter, part of North America (Mexico) started the year with mostly negative anomalies (Appendix Fig. A2.12). These negative anomalies expanded northward to the western and central United States and Canada during the first four months of the year. The dry conditions in the Canadian Prairies and Montana intensified during an extreme heatwave that occurred in June and July (Philip et al. 2021; section 2b4). The wetter-than-normal autumn that followed eased the anomalies, resulting in close-to-normal conditions at the end of the year. The southeastern United States recorded a widespread positive anomaly over 2021, caused by above-normal precipitation (NOAA 2022e; section 2d4).

In 2021, the southern half of South America mostly saw a continuation (van der Schalie et al. 2021) of drier-than-normal soil moisture conditions. These conditions were linked to the drought in the La Plata basin covering Uruguay, Bolivia, Paraguay, northeastern Argentina, and southern Brazil (Naumann et al. 2021). Southern regions in Argentina, e.g., Patagonia and surrounding areas, also experienced drier-than-normal soil moisture conditions. In northern South America, Venezuela, and Colombia experienced wetter-than-normal conditions throughout 2021, while in northeastern Brazil and northern Chile the positive anomalies were linked to heavy rain in the last three months of the year (sections 2d4, 7d).

Overall, Europe had wet soil moisture conditions, which were most intense in the western coastal and central-north areas and around the Black Sea region (contrasting with negative anomalies along the southern coast of the Black Sea and in the Middle East in April/May). The positive anomalies align with heavy rainfall and flooding throughout Europe during the summer (sections 2d5, 7f). Scandinavia and southern Spain were the only regions that recorded an overall drier-than-normal status for 2021.

The drought in the northern coastal regions of Africa, e.g., Morocco and Tunisia, were reflected in the widespread drier-than-normal soil moisture conditions. Western Africa and the Sahel started 2021 with above-average conditions, which later became drier-than-normal due to drought. Southern Chad and Sudan experienced wet conditions, caused by heavy rains during the summer. Eastern Africa had both positive anomalies (linked to widespread flooding in inland regions like South Sudan) and negative anomalies (regions experiencing droughts like Somalia and Kenya). Southern Africa had a clear split between below-average soil moisture conditions in Angola, Namibia, south Madagascar and southwest South Africa and above-average conditions in Botswana and northeast South Africa. This seems to align better with the precipitation extremes (section 2d5) and terrestrial water storage (section 2d8) than general precipitation anomalies

(section 2d4). In late 2021, drier-than-usual conditions were present in Madagascar and Tanzania, following wetter-than-usual conditions at the beginning of the year.

In Russia, Siberia and surrounding regions experienced low rainfall and high temperatures that continued below-average soil moisture conditions overall. These negative anomalies were widespread throughout much of central Asia, with countries like Kazakhstan, Kyrgyzstan, Turkmenistan, and Uzbekistan experiencing drought events. For Siberia, this was a continuation of 2020 conditions. India, Thailand, Mongolia, and large parts of China observed positive anomalies, caused by above-average precipitation (section 2d4). Northeastern China and southern India are particularly noteworthy, as they recorded the highest wet anomalies globally of 2021, linked to the second highest rainfall totals since 1961 in parts of China (Li et al. 2022) and highest recorded November rainfall since 1901 in southern India (IMD 2022).

The wetting trend in Australia continued in 2021, partly related to La Niña, with most regions recording average or above-average soil moisture levels. The most intense positive anomaly was detected over New South Wales, which coincides with the above-average rainfall in that region (section 2d4). New Zealand generally saw average soil moisture conditions.

The soil moisture anomalies (representing the top ~5 cm of the soil) used in this analysis were derived from the COMBINED product of ESA's Climate Change Initiative for Soil Moisture v06.2 (https://climate.esa.int/en/projects/soil-moisture/; Dorigo et al. 2017), a merged product based on multiple active (Wagner et al. 2013) and passive microwave (van der Schalie et al. 2017) sensors. Merging is done based on both the quality and the temporal and spatial availability of observations (Gruber et al. 2017, 2019).

10. MONITORING GLOBAL DROUGHT USING THE SELF-CALIBRATING PALMER DROUGHT SEVERITY INDEX—J. Barichivich, T. J. Osborn, I. Harris, G. van der Schrier, and P. D. Jones

The ongoing increase in global drought area, based on different severities of the self-calibrating Palmer Drought Severity Index (scPDSI), that began in mid-2019 (Barichivich et al. 2020) reached a new historical peak around August 2021 (Fig. 2.36), surpassing the previous high peak in October 2020 (Barichivich et al. 2021). Around 5.9% of the global land area experienced extreme drought conditions in September 2021, matching the earlier historical peak in October 1984. The extent of severe plus extreme drought conditions in 2021 peaked at 17% of the global land area in July and August, surpassing the earlier historical peak of this drought severity in December 2002 (16.6%). Similarly, moderate or worse drought conditions peaked in August at 32% of the global land area, surpassing the earlier historical peak in November 2002 (31.6%).

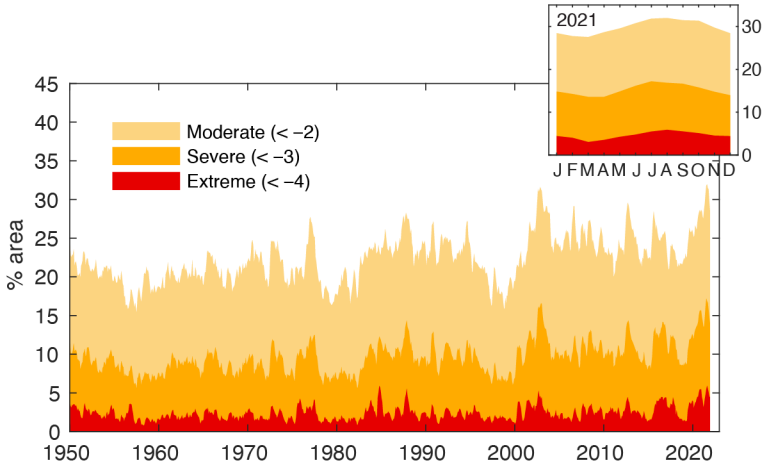

Fig. 2.36. Percentage of global land area (excluding ice sheets and deserts) with scPDSI levels of less than –2, –3, and –4, indicating moderate, severe, and extreme drought, respectively, for each month of 1950–2021.

The most extensive severe-to-extreme drought conditions in 2021 occurred across most of South America and western North America (Plate 2.1r), whereas the most extensive severe-to-extreme drought conditions in 2020 had been in Europe (Barichivich et al. 2021). Widespread drought in South America was mostly due to an intensification of previous drought (Fig. 2.37), leading to the expansion and intensification of earlier drought hotspots in central Chile and the Chaco region in northern Argentina (Barichivich et al. 2021). The ongoing protracted drought in central Chile reached its 12th consecutive year in 2021, becoming the longest drought in the historical record in the region. In

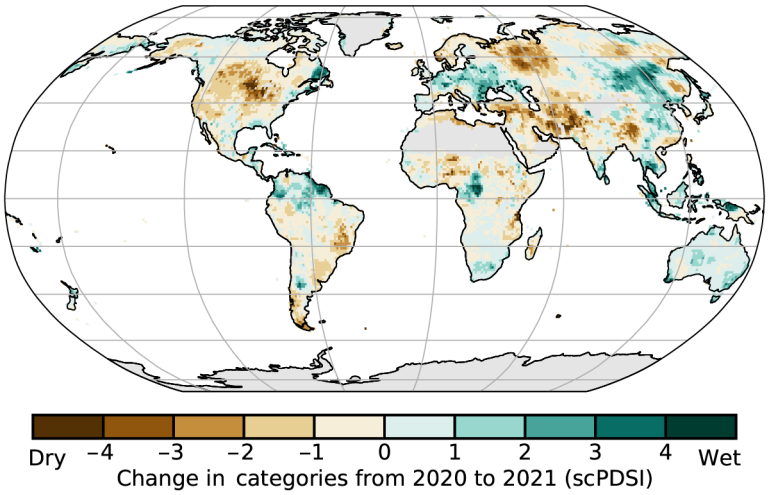

Fig. 2.37. Change in drought categories from 2020 to 2021 (mean scPDSI for 2021 minus mean scPDSI for 2020). Increases in drought severity are indicated by negative values (brown), decreases by positive values (blue). No calculation is made where a drought index is meaningless (gray areas: ice sheets or deserts with approximately zero mean precipitation).

North America, the intensification and expansion of drought through most of the western and formerly wetter central United States in 2021 (Fig. 2.37) weakened the east–west moisture contrast observed across the country since 2017 (Plate 2.1r). Under these persistent drought conditions, California saw another extreme season of wildfires (section 2h3), which was intensified by La Niña conditions.

Previous extensive severe-to-extreme drought across central Europe eased to moderate drought in 2021 (Fig. 2.37). Wet conditions in northern Europe from the British Isles to Scandinavia and western Russia continued through 2021 (Plate 2.1r). In northern Africa, previous drought conditions intensified along the Mediterranean coast. Most of tropical Africa saw a continuation of wet conditions from 2019 (Plate 2.1r), though changes in moisture anomalies in this region are uncertain due to the sparse coverage of meteorological station data. Persistent severe-to-extreme drought conditions in southern Africa since 2018 continued through 2021 but eased slightly compared to 2020 (Fig. 2.37).

In Australia, previous drought eased, but most of the country continued under drought conditions during 2021 (Plate 2.1r). In contrast, the Maritime Continent (Southeast Asia) experienced wet conditions, and previous drought in region eased, particularly across Vietnam. A large stretch along northeastern Siberia and the Far East region of Russia saw an intensification and expansion of severe drought along with extreme heat (Plate 2.1r), which led to unprecedented wildfires. Most of the Middle East from Turkey to Pakistan saw an intensification of drought to moderate-to-severe conditions.

Hydrological drought results from a period of abnormally low precipitation, sometimes exacerbated by a concurrent increase in evapotranspiration (ET). Its occurrence can be apparent in reduced river discharge, soil moisture, and/or groundwater storage, depending on season and duration of the event. Here, a simple estimate of drought called the self-calibrating Palmer Drought Severity Index (Wells et al. 2004; van der Schrier et al. 2013) is presented, using global precipitation and Penman-Monteith Potential ET from an early update of the CRU TS 4.06 dataset (Harris et al. 2020). Moisture categories are calibrated over the complete 1901–2021 period to ensure that "extreme" drought and pluvial (wet periods) relate to events that do not occur more frequently than in approximately 2% of the months. This calibration affects direct comparison with other hydrological cycle variables in Plate 2.1r that use a different baseline period.

This year's update is based on an extensively revised dataset that incorporates new estimates of some variables in CRU TS4.06 compared with CRU TS4.05 used in the report on 2020 (Barichivich et al. 2021). The revisions affect both precipitation (via an improved baseline climatology) and potential ET (all input variables are affected by the improved baseline climatology, and cloud cover is further modified by a new method for estimating it from diurnal temperature range). These revisions modify the scPDSI drought index values throughout, including during the mid-1980s period of extensive drought, which has a reduction in the extent of drought compared to that previously estimated.

11. LAND EVAPORATION—D. G. Miralles, A. Koppa, Q. Gou, D. Rains, P. Hulsman, H. E. Beck, and M. F. McCabe

In 2021, most regions experienced positive anomalies (more evaporation than normal), relative to the 30-year reference period (1991–2020), as illustrated in Plate 2.1s. Unusually high values were experienced in southeast Asia and India, eastern Australia, Amazonia, and the Congo rainforest. Some of these anomalies related to higher-than-normal radiation and temperatures (section 2b1). In Amazonia, the high evaporation also reflects above-average rainfall in 2021 (Espinoza et al. 2022; section 2d4); precipitation in rainforests can enhance evaporation via interception loss, i.e., the intense vaporization of water from wet vegetation canopies (van Dijk et al. 2015). In eastern Australia, positive evaporation anomalies mostly were in response to the exceptionally wet autumn in 2021, which caused floods during the month of March (Reid et al. 2021; section 2d4). On the other side of the spectrum, anomalously low evaporation was recorded in Angola and across the Horn of Africa, in the Mato Grosso and Caatinga regions in Brazil, in western North America, and in the Middle East. These negative anomalies in water-limited regions are mostly related to below-normal rainfall (Orimoloye et al. 2022; section 2d4). In the Horn of Africa, the negative evaporation anomalies relate to a multi-year drought (sections 2d10, 7e4).

The globally averaged land evaporation in 2021 was above the 1991–2020 mean, but slightly below the positive 1980–2021 trend (Fig. 2.38). This long-term trend of +0.76 mm yr^{-1} falls within the high-end of the values previously published in the literature (Y.-Q. Zhang et al. 2016; Brutsaert et al. 2017; Anabalón and Sharma 2017), although this value is still substantially lower than the latest estimates of +2.30 mm yr^{-1} based on gravimetric remote sensing for the period 2003–19 (Pascolini-Campbell et al. 2021). The overall positive global evaporation anomaly in 2021 resulted from mean positive anomalies in both hemispheres (Fig. 2.38), which persisted at most latitudes throughout the entire year (Fig. 2.39). The positive anomalies in Southern Hemisphere mean evaporation—that were also reflected in the global means—are a characteristic signature of La Niña conditions (Miralles et al. 2014; Martens et al. 2018), such as those that prevailed during 2020 and 2021 (see SOI in Fig. 2.38). This ENSO-induced variability in evaporation is superimposed upon the long-term trend, which is attributed to increasing global temperatures (Miralles et al. 2014) and terrestrial greening (Cheng et al. 2017).

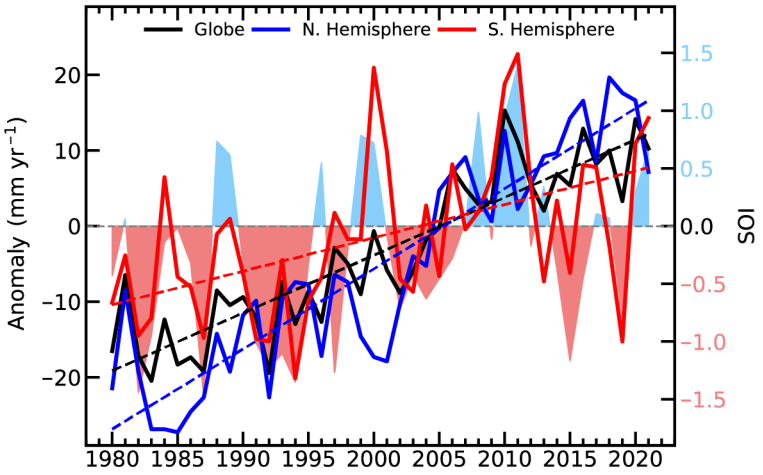

Fig. 2.38. Land evaporation anomaly (mm yr^{-1}; 1991–2020 base period) for the NH, SH, and the entire globe (blue, red, and black solid lines, respectively). Linear trends in evaporation (dashed lines) and the Southern Oscillation Index (SOI) from CRU (right axis, shaded area) are also shown. (Source: GLEAM.)

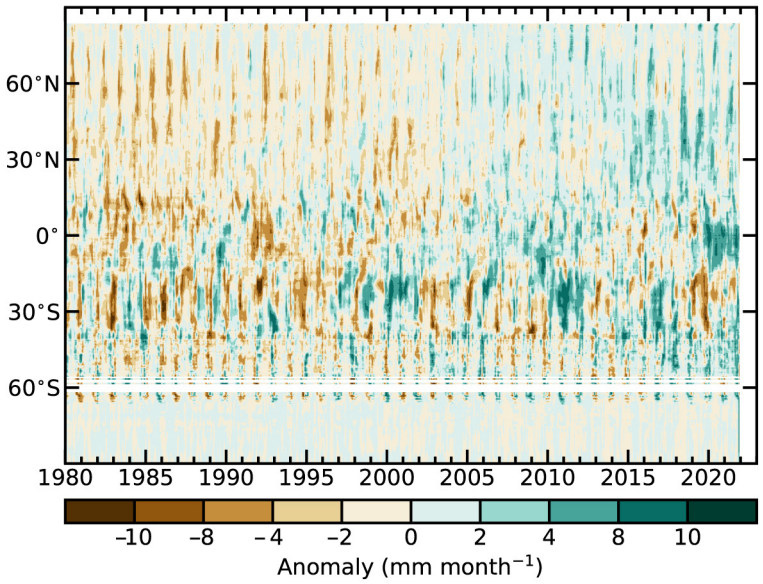

Fig. 2.39. Zonal mean terrestrial evaporation anomalies (mm $month^{-1}$; relative to 1991–2020 base period). (Source: GLEAM.)

The evaporation data that serve as the basis for these results come from version 3.6 of the Global Land Evaporation Amsterdam Model (GLEAM; Miralles et al. 2011). GLEAM v3.6 is based on microwave observations (of surface soil moisture, vegetation optical depth, and snow water equivalent), a precipitation dataset produced by blending gauge, satellite, and reanalysis sources (Beck et al. 2019), and a new bias-corrected, reanalysis-based product as atmospheric forcing (Beck et al. 2022). The accuracy of GLEAM v3 has been reported to be in the order of 0.7 mm day^{-1} (unbiased root mean square error), and its correlation against in situ eddy-covariance measurements is around 0.8 on average (Martens et al. 2017). While the ability to routinely monitor evaporation dynamics is critical for agriculture and water management, as well as to diagnose climate changes, global evaporation datasets (such as GLEAM v3.6) are still subject to model assumptions and uncertainties derived from parameterizations. In particular, the accuracy of the reported long-term trends is affected by the indirect representation of the influence of CO_2 and atmospheric aridity on stomatal conductance (Martens et al. 2017).

e. Atmospheric circulation

1. MEAN SEA LEVEL PRESSURE AND RELATED MODES OF VARIABILITY—B. Noll, D. Fereday, and N. Fedaeff

Global climate variability is influenced by the El Niño-Southern Oscillation (ENSO; indicated in the atmosphere by the Southern Oscillation Index [SOI]), as well as hemispheric-specific modes such as the Arctic Oscillation (AO), the North Atlantic Oscillation (NAO) and the Pacific/North America (PNA) pattern in the Northern Hemisphere (NH), and the Southern Annular Mode (SAM), also known as the Antarctic Oscillation (AAO), in the Southern Hemisphere (SH; see Kaplan 2011 for more details).

In 2021, La Niña conditions were present from January to May and then again from August through the end of the year, according to monthly Niño-3.4 SST anomalies (see also section 4b). The atmospheric response to La Niña was characterized by SOI values that were predominantly positive through the year. During July, a negative Indian Ocean dipole (IOD) event became established, in association with above-normal ocean temperatures in the tropical eastern Indian Ocean and cooler conditions relative to normal in the west (see section 4f). The development of an IOD event is correlated with ENSO by way of variations in the Walker Circulation (Behera et al. 2006). The overlying atmospheric pattern was dominated by the sinking branch of the Walker Circulation over the central and eastern Pacific and stronger-than-normal rising branch over Australia, the Maritime Continent, and the eastern Indian Ocean. These large-scale patterns influenced global atmospheric circulation patterns during the year.

In the NH, the PNA was on average negative in 2021, consistent with La Niña conditions (Yeh et al. 2018; Plate 2.1r). The principal large-scale circulation features occurred in the 2020/21 and 2021/22 winters. January and February 2021 saw a negative NAO, following a January sudden stratospheric warming (SSW; Figs. 2.40a,c). In SSW events, which occur in around 60% of boreal winters (Rao et al. 2019), the stratospheric polar vortex is disrupted by planetary-scale tropospheric waves. These waves may have been amplified in winter 2020/21 by reduced Arctic sea ice and a deepened Aleutian Low (Lu et al. 2021). In the weeks following SSW, the signal descends, often leading to the negative AO/NAO phase (Baldwin and Dunkerton 2001). The 2021 SSW followed this pattern (Figs. 2.40a,c), with the negative NAO in February possibly driven by the Madden-Julian Oscillation (MJO; Cassou 2008; Lockwood et al. 2022). Cold February conditions in northern Eurasia and eastern North America were a typical response to the negative AO/NAO.

By contrast, the winter 2021/22 stratospheric polar vortex was stronger than average (Fig. 2.40b). A strong vortex favors a positive NAO (Baldwin and Dunkerton 2001); although the December NAO was overall negative (Fig. 2.40d), the late-winter NAO was positive, consistent with the strong vortex. These contrasting winters (Figs. 2.40e,f) highlight some of the NAO drivers that vary interannually, reinforcing or counteracting each other (Scaife et al. 2014).

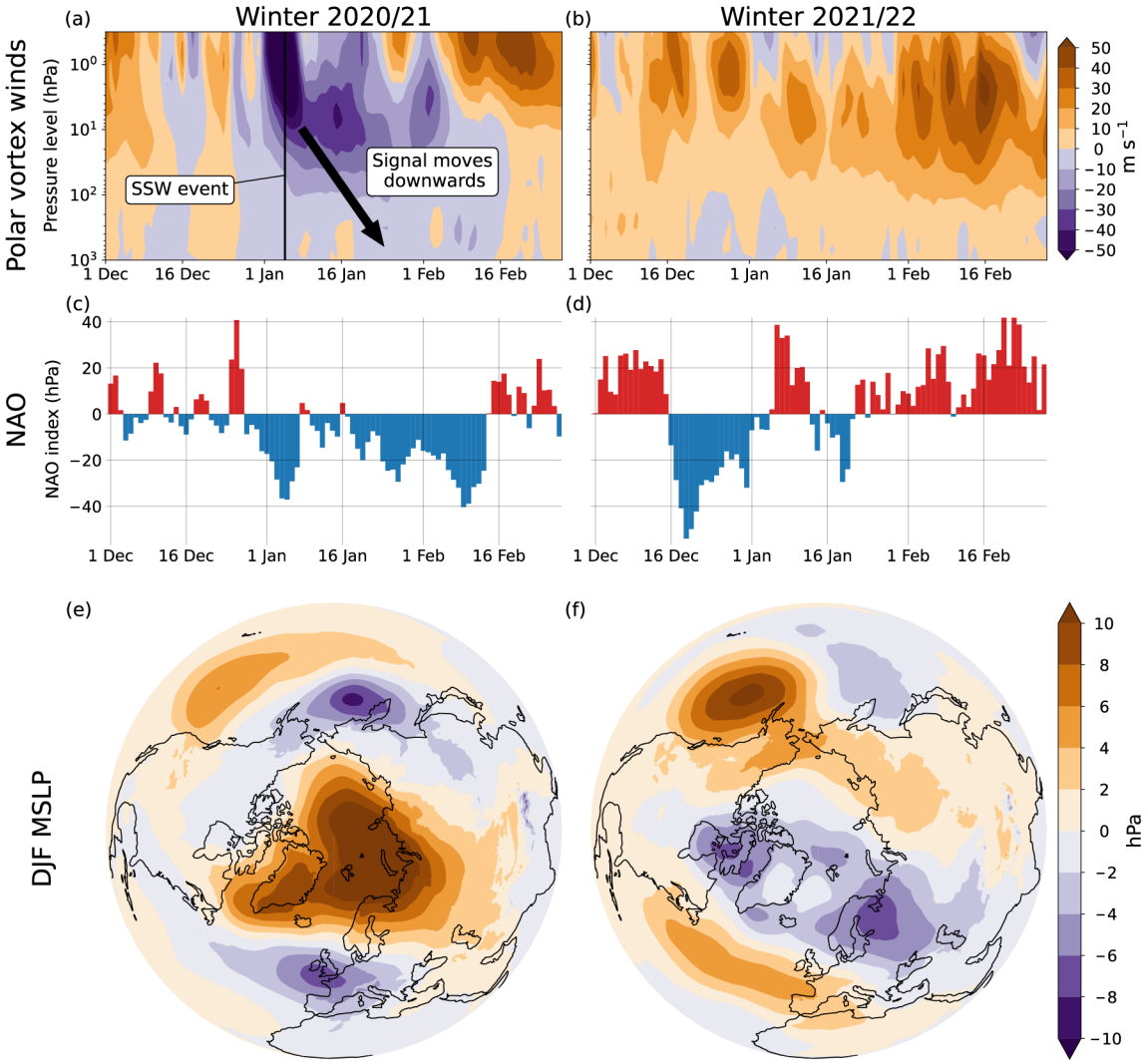

Fig. 2.40. Circulation differences between 2020/21 and 2021/22 boreal winters. (a),(b) Time–height cross section of zonal mean zonal wind anomalies (m s^{-1}) at 60°N (Met Office analysis). (c),(d) Daily North Atlantic Oscillation (NAO) index (Azores minus Iceland MSLP, hPa) anomaly, 1981–2010 base period (NCEP reanalysis). (e),(f) DJF mean MSLP anomaly (hPa), 1981–2010 base period (ERA5 reanalysis).

The SH featured a positive SAM during 73% of the year in 2021 (Fig. 2.41e). This was the fourth-highest percentage (and highest SAM index, section 2e3) since 1979. Accordingly, a broad area of higher-than-normal air pressure extended from east of New Zealand, across the South Pacific, and into southern Chile and Argentina (Figs. 2.41a–d). This was associated with New Zealand's warmest year on record, during which northerly quarter winds (315°W to 45°E) frequently affected the country, drawing down warmth from the tropics and contributing to a marine heatwave event in its coastal waters (NIWA 2021). Conversely, and as is consistent with the positive phase of the SAM, air pressure was lower than normal around much of Antarctica and the Southern Ocean (Figs. 2.41a–d). This was also linked to a stronger-than-normal stratospheric polar vortex above the South Pole, which contributed to very cold temperatures and the fifth-largest Antarctic sea ice extent for the month of August on record (NOAA 2021; see section 6e). Pressures were slightly lower than normal over Australia, as influenced by the combined effect of the IOD and La Niña teleconnection (Figs. 2.41a–d). 2021 was Australia's coolest year since 2012 and wettest since 2016, which resulted in a recharge of water storage following drought events from 2017 to 2019 (Bureau of Meteorology 2022; see also section 7h4).

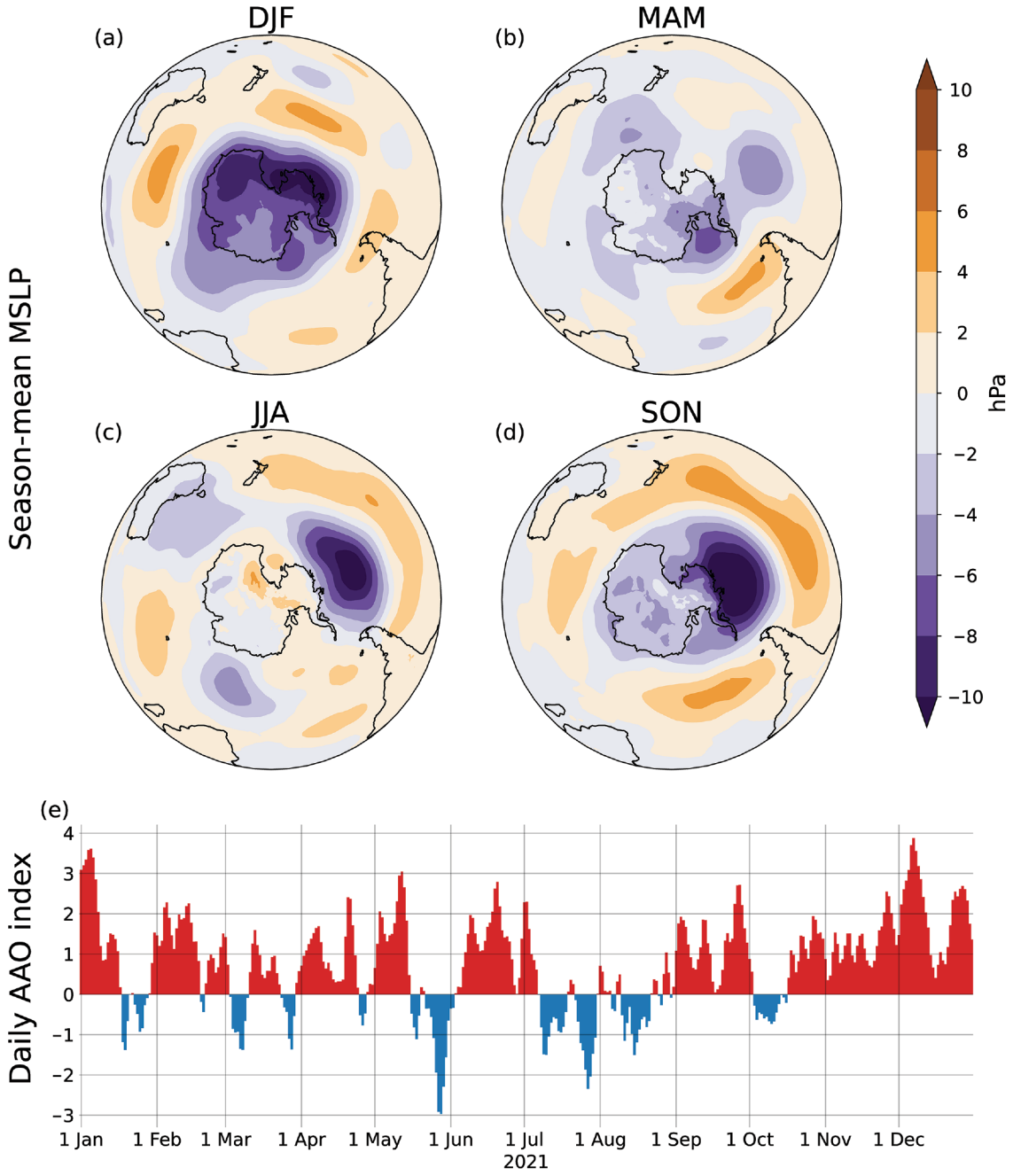

Fig. 2.41. Southern Hemisphere circulation in 2021. Seasonal mean MSLP anomalies (hPa) for (a) DJF 2020/21, (b) MAM 2021, (c) JJA 2021, and (d) SON 2021, 1981–2010 base period (ERA5 reanalysis). (e) Daily AAO index time series (NOAA CPC).

2. LAND AND OCEAN SURFACE WINDS—C. Azorin-Molina, R. J. H. Dunn, L. Ricciardulli, C. A. Mears, J. P. Nicolas, and T. R. McVicar

After about eight years of weak positive (near zero) anomalies in observed land surface winds (i.e., ~10 m above the ground), negative anomalies (with respect to the 1991–2020 climatology; Table 2.8) were recorded in the Northern Hemisphere (–0.028 m s^{-1}) in 2021, primarily in eastern North America (–0.063 m s^{-1}) and western Europe (–0.095 m s^{-1}). These exceptionally low winds, for example, in areas of the United Kingdom (Plate 2.1u), have not occurred in East Asia (+0.045 m s^{-1}), central Asia (+0.080 m s^{-1}), or South America (+0.080 m s^{-1}). Overall, the stilling (Roderick et al. 2007) observed before the 2010s (McVicar et al. 2012) ceased in the last decade, with a weak reversal or stabilization of surface winds globally (Zeng et al. 2019) and regionally (Minola et al. 2022; Fig. 2.42a). Two thresholds of wind intensities (i.e., > 3 m s^{-1} and > 10 m s^{-1}) show an opposite trend behavior with no trends (or even positive ones) for moderate winds (> 3 m s^{-1}; Fig. 2.42c) and moderate slowdowns for strong winds speeds (> 10 m s^{-1}; Fig. 2.42d), e.g., in South

Table 2.8. Northern Hemisphere (20°–70°N) and regional statistics for land surface wind speed (m s^{-1}) using the observational HadISD3 dataset for the period 1979–2021.

Region	Mean 1991–2020 (m s^{-1})	Anomaly 2021 (m s^{-1})	Trend 1979–2021 (m s^{-1} $decade^{-1}$) and 5th–95th percentile confidence range	Number of stations
Northern Hemisphere	3.309	−0.028	−0.059 (−0.073 to 0.044)	2886
North America	3.639	−0.063	−0.073 (−0.089 to 0.055)	853
Europe	3.652	−0.095	−0.052 (−0.073 to 0.034)	933
Central Asia	2.737	+0.080	−0.077 (−0.123 to 0.048)	304
East Asia	2.717	+0.045	−0.031 (−0.046 to 0.017)	534
South America	3.451	+0.080	+0.051 (−0.032 to 0.069)	101

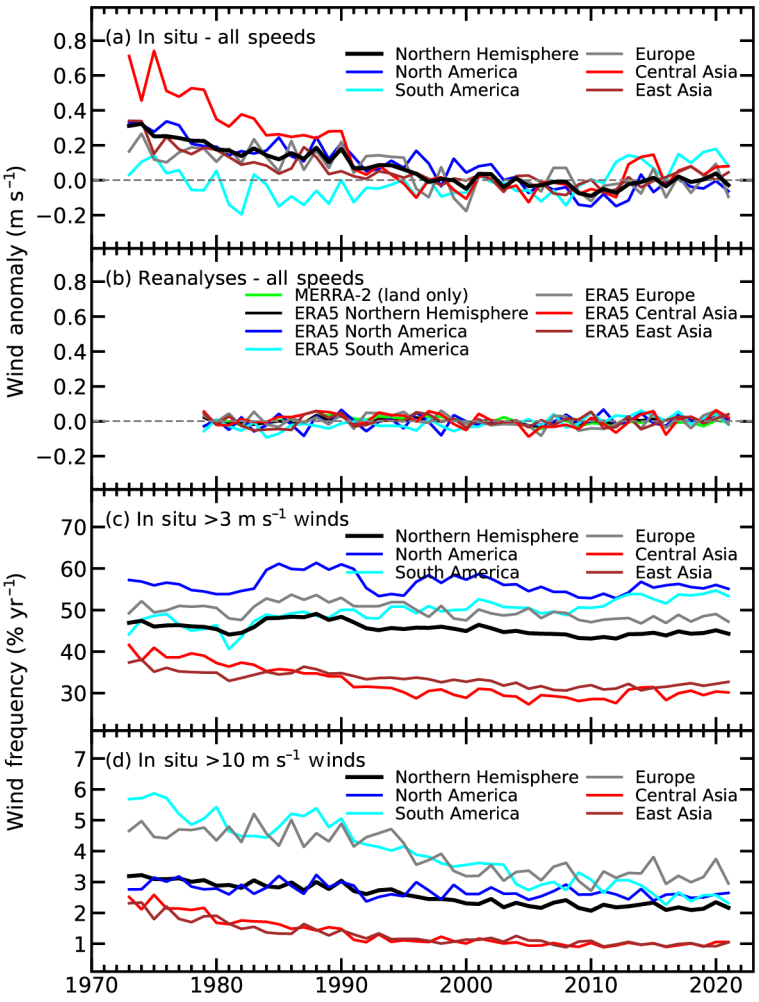

Fig. 2.42. Northern Hemisphere (20°–70°N) and regional annual time series of land surface wind speed anomaly (m s^{-1}; 1991–2020 base period) using (a) HadISD3 (1973–2021) observational dataset and (b) ERA5 (1979–2021) and MERRA-2 (1980–2021) reanalyses. HadISD3 occurrence frequencies (% yr^{-1}) for wind speeds (c) > 3 m s^{-1} and (d) > 10 m s^{-1}.

America (Azorin-Molina et al. 2021; Zhang et al. 2021).

This annual land surface wind report for 1979–2021 is based on 1) global in situ anemometer observations from the HadISD3 dataset (1973–2021; Dunn et al. 2012, 2016, 2019) and 2) two gridded reanalysis products: ERA5 (1979–2021; Hersbach et al. 2020) and MERRA-2 (1980–2021; Gelaro et al. 2017). Compared to in situ observations, the magnitudes of the anomalies from the reanalyses are smaller and do not reproduce their multidecadal variability (Fig. 2.42b; Torralba et al. 2017; Ramon et al. 2019; Wohland et al. 2019); observations are the basis for quantifying wind changes.

Over most land regions, the last 43 years (1979–2021) have seen a declining long-term trend (Northern Hemisphere: −0.059 m s^{-1} $decade^{-1}$; Table 2.8). This stilling has ceased or even reversed since the ~2010s, but winds are not yet back up to 1979 levels, so on average a long-term decline in global land wind speeds is still observed. South America, however, has experienced a positive trend (though with many fewer stations). Despite the lack of land-based observations in the Southern Hemisphere, both in situ and ERA5 data in Fig. 2.43 support this interhemispheric asymmetry of wind speed changes, also projected for the twenty-first century (Deng et al. 2022; Yu et al. 2022), such as a dominance of decreases across midlatitude regions of the Northern Hemisphere and weak increases in the Southern Hemisphere (e.g., parts of Antarctica and the Southern Ocean).

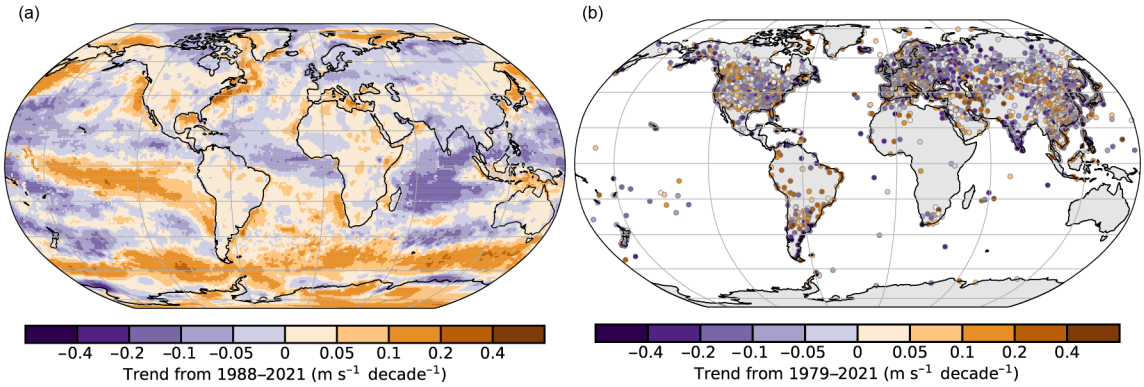

Fig. 2.43. Wind speed trends (m s^{-1} $decade^{-1}$) from (a) ERA5 reanalysis output over land/ice and Remote Sensing Systems (RSS) satellite radiometers (SSM/I, SSMIS, TMI, GMI, AMSR2, ASMR-E, and WindSat) over ocean (shaded areas) for the period 1988–2021 and (b) the observational HadISD3 dataset over land (circles) for the period 1979–2021.

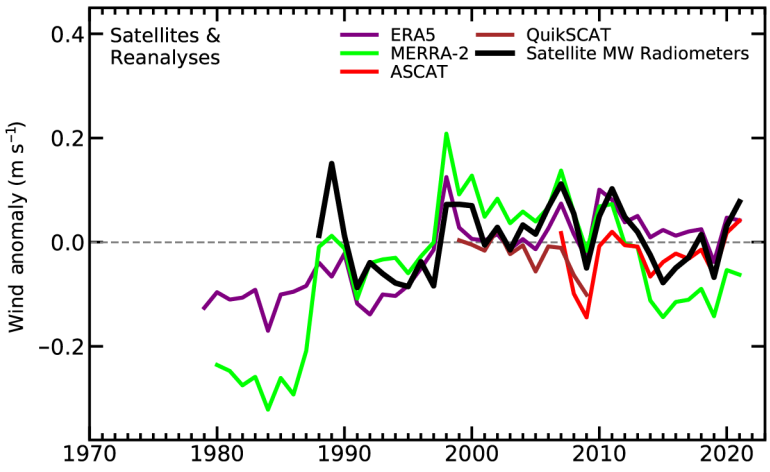

Fig. 2.44. Annual anomalies of global mean wind speed (m s^{-1}; 1991–2020 base period) over the ocean from satellite radiometers and scatterometers, MERRA-2, and ERA5.

The assessment of ocean surface winds for 1988–2021 was conducted using ERA5 reanalysis and satellite-based products including the Special Sensor Microwave/Imager (SSM/I), the Special Sensor Microwave Imager/Sounder (SSMIS), the Advanced Microwave Scanning Radiometer (AMSRE and AMSR2), TMI, GMI, WindSat, QuikSCAT, and ASCAT (Wentz 1997; Wentz et al. 2007, 2015; Ricciardulli and Wentz 2015; Ricciardulli and Manaster 2021). In 2021, positive anomalies were recorded by satellite radiometers (RSS: +0.078 m s^{-1}), slightly larger than satellite scatterometers (ASCAT: +0.041 m s^{-1}) and reanalysis (ERA5: +0.030 m s^{-1}) (Fig. 2.44). The most prominent positive anomalies were recorded over the Southern Ocean, specifically in the South Pacific (> +1.2 m s^{-1}) associated with a positive SAM phase, along with the equatorial Pacific Ocean, Gulf of Alaska, and Bering Sea (Plate 2.1u). This agrees with previous studies (e.g., Deng et al. 2022), which report a strengthening and shifting poleward of Southern Hemisphere westerlies. In contrast, large negative anomalies occurred in the North Atlantic, equatorial Atlantic, and Indian Oceans. Changes in ocean surface winds show a dominance of negative trends for 1988–2021, especially in the Indian and West Pacific Oceans (Fig. 2.43). Positive trends prevail in the Southern Ocean, the Pacific trade winds, the Bering Sea, and near the coastlines (e.g., North America; Young and Ribal 2019).

Studies investigating the trends and variability of surface winds demonstrated that the primary driver is exerted by internal decadal ocean–atmosphere oscillations (Zeng et al. 2019; Zhou et al. 2021), as modulated by changes in the temperature gradient (Zhang et al. 2021) induced by anthropogenic greenhouse gas forcings (Deng et al. 2021, 2022). Regionally and locally, land-use changes (Minola et al. 2022) and/or instrumentation issues (Azorin-Molina et al. 2018; Safaei Pirooz et al. 2020) have an impact on wind changes. Recent studies predict an interhemispheric asymmetry of future wind speed changes due to the reduction in Hadley, Ferrel, and Polar cells over the Northern Hemisphere and the strengthening of the Hadley cell over the Southern Hemisphere (Zha et al. 2021).

3. UPPER AIR WINDS—L. Haimberger, M. Mayer, and V. Schenzinger

The 2021 global mean wind speed anomaly at 850 hPa was about 0.1 m s^{-1} above the 1991–2020 climatology (Fig. 2.45a). The neutral or positive long-term wind trends at 850 hPa in the NH (40°–60°N) extratropics and in the global mean are now more consistent with surface winds (section 2e2), where the wind stilling reported in past annual reports has ceased or even reversed (section 2e2). As 2021 was the year with the highest Southern Annular Mode (SAM) index (average 0.8, estimated from NOAA monthly data) since 1979, we show the 70°–50°S average zonal wind time series in (Fig. 2.45b). The correlation coefficient between the AAO index and the 70°–50°S zonal mean 850-hPa wind speed on monthly timescales, calculated for 1979–2021, is 0.9. Thus, it is not surprising that the annual mean wind speed anomaly in this latitude belt was clearly positive in 2021, with maxima in autumn (not shown). Consistent with climate model predictions (Lee et al. 2019) there has been a notable increase in wind speed in this latitude belt, with highly significant trends 1991–2021 between 0.16 and 0.22 m s^{-1} $decade^{-1}$. Large positive zonal wind speed anomalies occur at 850 hPa over nearly all longitudes of the Southern Ocean (Plate 2.1v).

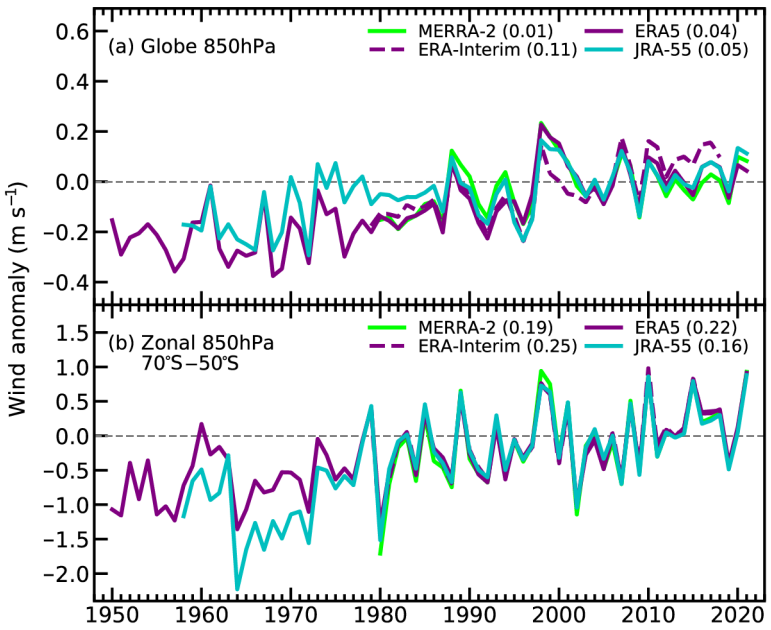

Fig. 2.45. Annual anomalies of (a) global mean, (b) 50°–70°S belt zonal mean wind speed (m s^{-1}; 1991–2020 base period) at 850 hPa from four reanalyses (ERA5 [Hersbach et al. 2020], ERA-Interim [Dee et al. 2011], MERRA-2 [Gelaro et al. 2017], and JRA-55 [Kobayashi et al. 2015]). The numbers in parentheses are linear trends in m s^{-1} $decade^{-1}$ for the period 1991–2020. ERA-Interim time series ends in 2019.

As in previous years, we consider large-scale anomalies in upper air winds through the velocity potential (χ) and divergent winds at 200 hPa. This diagnostic is particularly sensitive to changes in tropical convective activity and associated changes to the Walker Circulation. The most prominent seasonal anomalies of the velocity potential in 2021 were present during boreal autumn (SON), with negative χ anomalies centered over the Indo-Pacific Warm Pool and positive χ anomalies extending from the central tropical Pacific into the northern subtropical Atlantic. The negative anomaly is consistent with strengthened convective activity arising from increased SSTs in the eastern Indian Ocean (associated with weakly negative Indian Ocean dipole conditions during August–November; see section 4f) and in the western tropical Pacific (associated with moderate La Niña conditions; see sections 2e1, 4b). Moreover, a few weak Madden-Julian Oscillation (Madden and Julian 1971) events were observed over the Maritime Continent during SON 2021 (see section 4c), which contributed additionally to convective activity in that region. The positive χ anomalies over the eastern tropical Pacific as well as westerly anomalies of 200-hPa divergent wind in the western equatorial Pacific are consistent with below-average SSTs in this region (La Niña). Interestingly, the center of the positive χ anomaly, as well as the convergence of 200-hPa winds, extended well into the western subtropical Atlantic. Anomalies in the χ field have been used to link tropical cyclone activity with large-scale tropical climate anomalies (e.g., Wood et al. 2020; Bell and Chelliah 2006). However, despite the strong χ anomaly pattern, tropical cyclone activity during the 2021 season was close to climatology in all Northern Hemisphere basins in terms of accumulated cyclone energy (ACE; see section 4g); only named storms in the Atlantic basin were 50% above average.

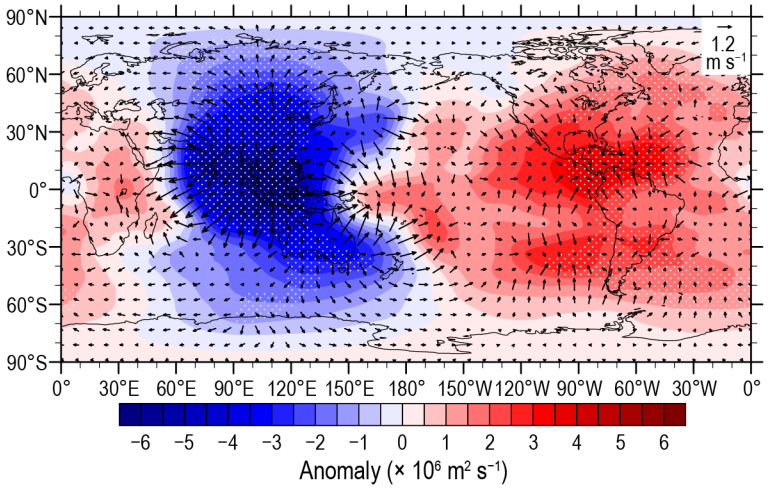

Fig. 2.46. Anomalous velocity potential (× 10^6 m^2 s^{-1}) and divergence winds (arrows, m s^{-1}) in SON 2021 from ERA5 (1991–2020 climatology) at 200 hPa. Stippling denotes anomalies exceeding 1.65σ of the temporal standard deviation of seasonally averaged velocity potential anomalies.

The availability of wind observations from the Aeolus instrument has been shown to constrain the uncertainties of notoriously difficult upper level divergence patterns and tropical weather forecast errors on short timescales (Rennie et al. 2021; Martin et al. 2021). Since those data will be used in future reanalyses (ERA5 does not yet assimilate Aeolus data), we looked at systematic impacts on seasonal means of winds and divergence to assess the potential for temporal discontinuities in these datasets. The root-mean square (rms) difference between velocity potentials from ECMWF assimilation experiments with/without Aeolus reaches only 2% of the rms value of the anomaly diagnostic in Fig. 2.46. Similar analysis of upper tropospheric zonal mean cross-equatorial velocity and divergence showed only negligible systematic differences, although on shorter time scales (sub-monthly) differences can become considerable. Overall these results suggest that Aeolus data are not expected to introduce major spurious shifts at their advent on seasonal and longer time scales, at least not in the quantities considered here.

After its latest disruption in 2020, the behavior of the quasi-biennial oscillation (QBO) in 2021 can be characterized as typical, comparable, for example, with 1958, 1981, 2009, and 2014. The westerly phase was at its strongest at 50 hPa in April, with a speed of 12.8 m s^{-1}. The following easterly phase, that has persisted above 15 hPa since April 2019, reached −36.8 m s^{-1} in October at the 20 hPa level, which is stronger than average, but not exceptional. This phase descended at a rate of about 0.61 km $month^{-1}$, which is close to the long term (60-year) average (−0.66 ± 0.75 km $month^{-1}$).

f. Earth radiation budget

1. EARTH RADIATION BUDGET AT TOP-OF-ATMOSPHERE—T. Wong, P. W. Stackhouse Jr., P. Sawaengphokhai, J. Garg, and N. G. Loeb

The top-of-atmosphere (TOA) Earth radiation budget (ERB) is defined as the difference between incoming total solar irradiance (TSI) and outgoing radiation from Earth, given by the sum of reflected shortwave (RSW) and outgoing longwave radiation (OLR). Regional imbalances in TOA ERB drive atmospheric and oceanic circulations.

An analysis of CERES TOA ERB measurements (Table 2.9) shows that the global annual mean OLR and RSW decreased by 0.65 W m^{-2} and 0.10 W m^{-2} in 2021, relative to 2020 (rounded to nearest 0.05 W m^{-2}). In contrast, the global annual mean TSI and net radiation increased by 0.05 W m^{-2} and 0.80 W m^{-2}, over the same period. Figure 2.47 shows regional annual mean maps of the difference between 2021 and 2020 in TOA OLR and TOA RSW. The largest reductions in OLR and increases in RSW are seen over the tropical western Pacific Ocean, Philippines, Indonesia, and New Guinea. Negative OLR and positive RSW differences also occur over the eastern Pacific Ocean, off the coast of Peru. The largest increases in OLR and decreases in RSW are observed in the tropical western Indian Ocean. These regional changes are associated with ENSO oscillation in the tropics as La Niña conditions persisted throughout much of 2021. Relative to the multiyear average from 2001 to 2020, the 2021 global annual mean TOA flux anomalies are +0.05, 0.0, −0.75, and +0.70 W m^{-2} for OLR, TSI, RSW, and total net flux (Table 2.9). These anomalies are within their respective 2-sigma interannual variability (Table 2.9) for this period.

Table 2.9. Global annual mean TOA radiative flux changes between 2020 and 2021, the 2021 global annual mean radiative flux anomalies relative to their corresponding 2001–20 mean climatological values, and the 2-sigma interannual variabilities of the 2001–20 global annual mean fluxes (all units in W m^{-2}) for the outgoing longwave radiation (OLR), total solar irradiance (TSI), reflected shortwave (RSW), absorbed solar radiation (ASR, determined from TSI-RSW) and total net fluxes. All flux values have been rounded to the nearest 0.05 W m^{-2} and only balance to that level of significance.

	One-Year Change (2021 minus 2020) (W m^{-2})	2021 Anomaly (Relative to Climatology) (W m^{-2})	Climatological Mean (2001–20) (W m^{-2})	Interannual Variability (2001–20) (W m^{-2})
OLR	−0.65	+0.05	240.25	±0.65
TSI	+0.05	0.00	340.00	±0.15
RSW	−0.10	−0.75	99.00	±0.95
ASR	+0.15	+0.75	241.00	±0.90
Net	**+0.80**	**+0.70**	**0.80**	**±0.80**

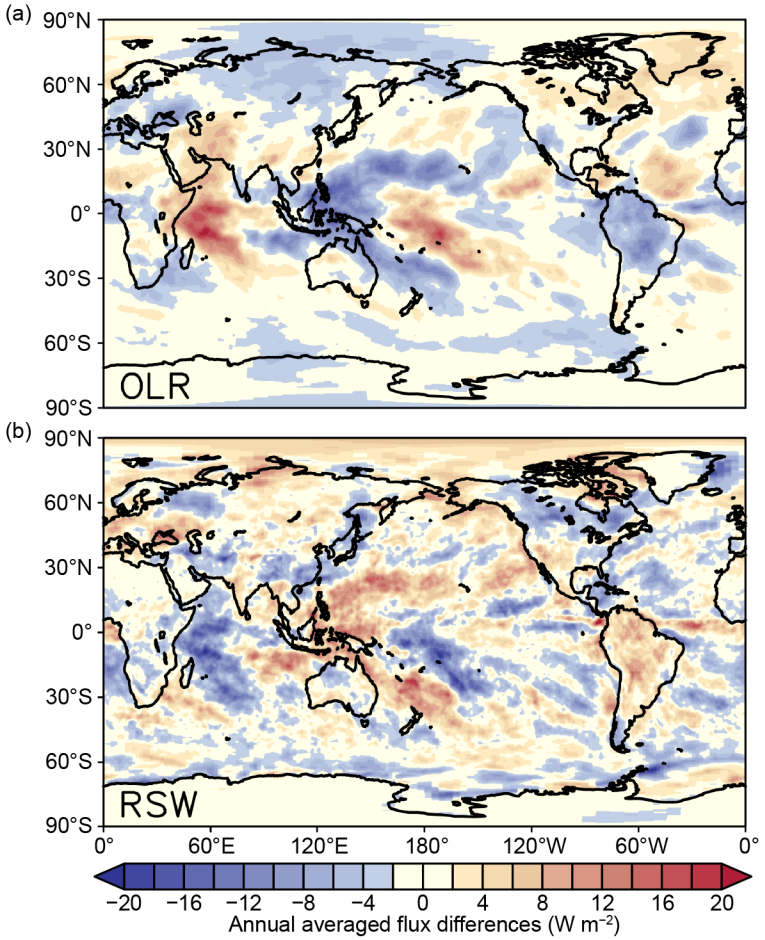

Fig. 2.47. Annual average TOA flux differences between 2021 and 2020 for (a) outgoing longwave radiation (OLR) and (b) reflected shortwave (RSW) radiation (W m^{-2}). The annual mean maps for 2021 were derived after adjusting Dec 2021 FLASHFlux v4A using the difference between EBAF and FF v4A in 2020.

Throughout 2021, the global monthly mean TOA OLR anomaly varied between positive and negative values (Fig. 2.48). OLR anomalies peaked at +0.7 W m^{-2} in February, but otherwise fluctuated between ±0.5 W m^{-2} the rest of the year. These results are consistent with NOAA HIRS (Lee and NOAA CDR Program 2011) and NASA AIRS (Susskind et al. 2012) OLR datasets (not shown). For the year as a whole, the 2021 global annual mean TOA OLR anomaly was +0.05 W m^{-2}. The global monthly mean TOA absorbed solar radiation (ASR, determined from TSI minus RSW) anomaly remained positive throughout 2021, peaking at +1.4 W m^{-2} in June. For the year as a whole, the 2021 global annual mean TOA ASR anomaly was +0.75 W m^{-2}. The global monthly mean TOA total net anomaly, which is calculated from ASR anomaly minus OLR anomaly, also stayed positive throughout 2021, topping out at +1.8 W m^{-2} in June. For the year as a whole, the 2021 global annual mean TOA total net anomaly was +0.70 W m^{-2}. The Earth energy imbalance (EEI) that had been observed prior to 2020 grew even larger during 2021, so that the doubling in observed EEI between 2005 and 2019 from both CERES and in situ observations (Loeb et al. 2021) continued to substantially increase, primarily because of an increase in ASR radiation. It should be noted that a 21-year trend is not necessarily indicative of a longer-term trend. At this timescale, internal variability in the climate system can offset or augment any forced, longer-term trend in net radiation.

The TSI data were obtained from the Total Irradiance Monitor aboard the Solar Radiation and Climate Experiment (SORCE) mission (Kopp and Lean 2011), the Royal Meteorological Institute

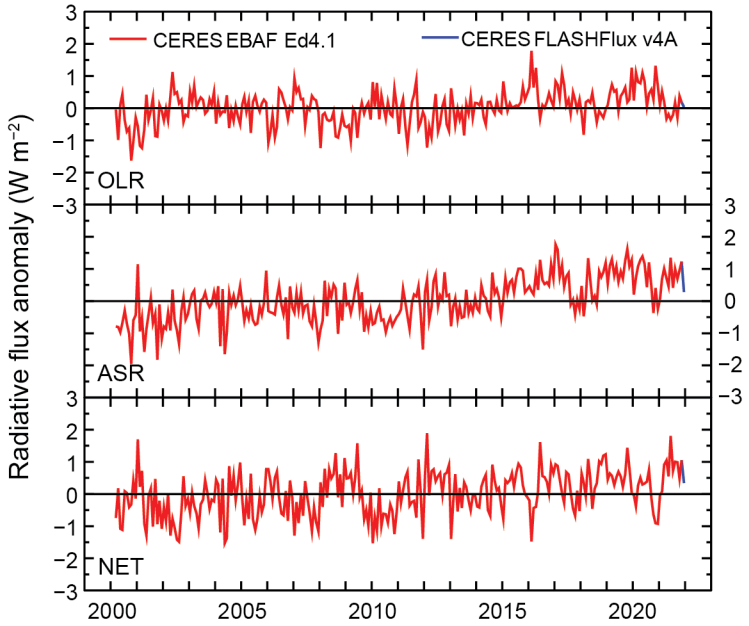

Fig. 2.48. Time series of global monthly mean deseasonalized anomalies (W m^{-2}) of TOA Earth radiation budget for outgoing longwave radiation (OLR; upper), absorbed solar radiation (ASR, determined from TSI-RSW; middle), and total net (TSI-RSW-OLR; lower) from Mar 2000 to Dec 2021. Anomalies are relative to their calendar month climatology (2001–20). Time series shows the CERES EBAF Ed4.1 1° data (Mar 2000–Nov 2021) in red and the CERES FLASHFlux version 4A data (Dec 2021) in blue; see text for merging procedure (Sources: https://ceres-tool.larc.nasa.gov/ord-tool/jsp/EBAF41Selection.jsp and https://ceres-tool.larc.nasa.gov/ord-tool/jsp/FLASH_TISASelection.jsp.)

of Belgium composite dataset (Dewitte et al. 2004), and the Total Solar and Spectral Irradiance Sensor-1 (TSIS-1, Coddington, 2017) mission, all renormalized to the SORCE Version 15. The TOA RSW and TOA OLR data, which are constructed with measurements from the CERES instruments (Wielicki et al. 1996, 1998) aboard *Terra* and *Aqua* spacecraft, are based on the CERES EBAF (Energy Balanced and Filled) Ed4.1 product (Loeb et al. 2009, 2012, 2018a) for March 2000–November 2021 and the CERES Fast Longwave and Shortwave Radiative Fluxes (FLASHFlux) version 4A product (Kratz et al. 2014) for December 2021. The FLASHFlux to EBAF data normalization procedure (Stackhouse et al. 2016) results in 2-sigma monthly uncertainties of ±0.30, ±0.04, ±0.18, and ±0.48 W m^{-2} for the OLR, TSI, RSW, and total net radiation, respectively.

2. MAUNA LOA APPARENT TRANSMISSION—J. A. Augustine, K. O. Lantz, H. Telg, J.-P. Vernier, and M. Todt

One of the longest records in the atmospheric sciences is the apparent atmospheric transmission at the Mauna Loa Observatory on Hawaii, which dates to 1958. Atmospheric transmission describes the fraction of solar radiation impinging at the top-of-atmosphere that is transmitted vertically to the surface. Because of its high altitude (3397 m a.s.l.), transmission at Mauna Loa is primarily affected by stratospheric aerosols, although tropospheric effects occur when dust from springtime storms in Asia pass over the island (Bodhaine et al. 1981). Since Mauna Loa is located near 20°N latitude, its transmission primarily reflects events in the Northern Hemisphere and is relatively uninfluenced by those in the Southern Hemisphere.

The updated time series of apparent transmission at Mauna Loa through 2021 is presented in Fig. 2.49. Recent trends show a gradual reduction in late 2017 and early 2018, caused by pyrocumulonimbus in Canada, and the June 2019 eruption of Raikoke in the Kuril Islands, ~800 km northeast of Japan. In 2020, transmission stabilized at a low level that was maintained by the eruption of Taal in the Philippines in January, remnants of Raikoke, and California wildfires (Augustine et al. 2020, 2021).

The inset of Fig. 2.49 shows the new data for 2021. The annual average of 0.925 is 0.009 lower than the background. The transmission held steady in early 2021 from the relatively low levels of

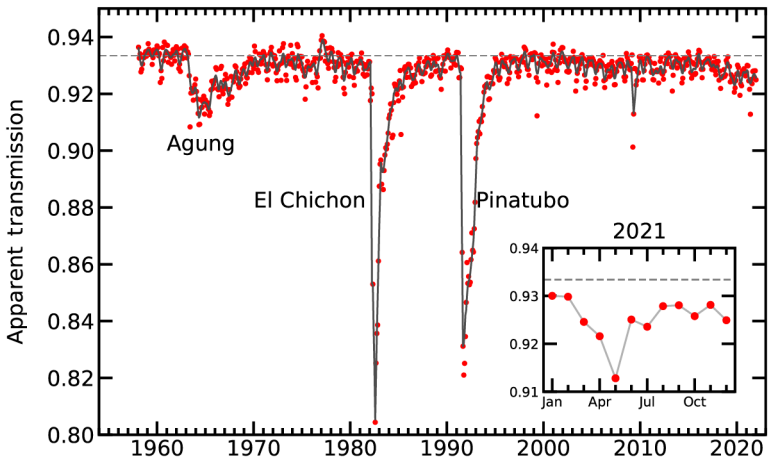

Fig. 2.49. Apparent transmission at Mauna Loa, Hawaii, from 1958 through 2021. Red dots are monthly averages of morning apparent transmission, the gray curve in the full time series plot is a LOWESS fit with a six-month smoother applied, and the horizontal dashed gray line is the average transmission for the clean period before the volcanic eruption of Mount Agung. Insert is an enlargement of the newest data for 2021.

the previous year. Significant aerosol activity began on 15 March with the largest sandstorm in the Gobi Desert since 2010, lofting dust up to 8 km (Gui et al. 2021). HYSPLIT trajectory analysis shows that dust plumes reached Mauna Loa in seven days. Volcanoes La Soufriere (Caribbean Island of St. Vincent) and Fukutoku-Okanoba (25 m below sea level, ~60 km south of Iwo Jima) erupted explosively during 9–12 April and 13 August, respectively. Fukutoku-Okanoba's plume extended only to the lower boundary of the stratosphere, and trajectory analysis revealed its plume never reached Mauna Loa.

La Soufriere erupted at least 20 times on four consecutive days. Its plume was observed as high as 20 km by MISR, well into the lower stratosphere (LS), and HYSPLIT trajectory analysis showed that it reached Mauna Loa one month later. CALIPSO detected a strong signal between 21 and 23 km in mid-August between the equator and 35°N. Lidar observations on Mauna Loa detected a large signal just above 21 km on 20 August, and SAGE tracked that same signal in the stratosphere through October. Balloon-borne aerosol concentration measurements in Kansas (United States) in August and later in France detected high aerosol concentrations at 20–21 km. Similar observations in Boulder, Colorado, show near-normal concentrations in the LS through mid-April, followed by elevated values between 15 and 19 km through the end of the year, albeit decreasing a bit in December. It also shows a small peak near 21 km in early October. Together, these observations strongly suggest that La Soufriere's plume circled the globe in the LS for the remainder of 2021.

Extensive pyro cumulonimbus activity occurred in the western United States and Canada in July and August. These events were associated with the drought and heat wave over the affected regions at that time (sections 2b4, Sidebar 7.1); however, CALIPSO and HYSPLIT analyses show the smoke plumes initially traveled northward and remained north of 30°N, well displaced from Mauna Loa.

Apparent transmission is calculated from the ratio of direct-normal pyrheliometer measurements at two solar elevations, following Ellis and Pueschel (1971). An average of three successive ratios, from morning pyrheliometer measurements made at 2, 3, 4, and 5 atmospheric pathlengths, is considered representative for the day. While any of these ratios are mathematically equivalent to a vertical transmission, variability at the longer pathlengths render the calculation an "apparent" transmission. Only morning data are used because upslope afternoon winds often carry sea level aerosols to the summit.

Sidebar 2.1: **Lightning**—M. FÜLLEKRUG, E. WILLIAMS, C. PRICE, S. GOODMAN, R. HOLZWORTH, K. VIRTS, AND D. BUECHLER

The World Meteorological Organization (WMO) recently declared lightning flashes to be an essential climate variable (ECV), based on a recommendation by the Task Team on Lightning Observation for Climate Applications (TT-LOCA) as part of the Atmospheric Observation Panel for Climate (AOPC) of the WMO and the Global Climate Observing System (GCOS; Aich et al. 2018; WMO 2019a). This endorsement reinforces the WMO Integrated Global Observing System (WIGOS) Vision 2040 (WMO 2019b) toward the operational observation of lightning by space agencies during the coming decades.

Lightning flashes are generated by thunderstorms, which develop when hot and humid air destabilizes the atmosphere and enables deep convection. As a result, the lightning ECV is grouped with other ECVs describing the atmosphere (Bojinski et al. 2014) which are closely related to thunderstorm development, such as the Earth radiation budget, upper-air temperature, water vapor, wind speed, and cloud properties (see sections 2f1, 2b1, 2b5, 2d2, 2e2, and 2d6). The lightning ECV is also related to ECVs that impact atmospheric composition, such as lightning NOx and cloud condensation nuclei (see sections 2g3 and 2g6).

Lightning is a natural hazard associated with the severe weather impacts of thunderstorms including high wind speeds with falling trees and branches, intense precipitation causing flooding, large hail affecting transport vehicles and crops, and cloud-to-ground lightning which can lead to casualties, ignite wildland fires, and cause significant damage to infrastructure, such as power lines (Cooper and Holle 2019; Holle 2016). Lightning has significant societal implications for public safety (Holle et al. 1999), power distribution (Piantini 2020), aviation (Ryley et al. 2020), and wildfires (Holzworth et al. 2021). Wildfires can increase convective instability for pyrocumulus to develop (Rudlosky et al. 2020; Liu et al. 2021; Augustine et al. 2021). Lightning is

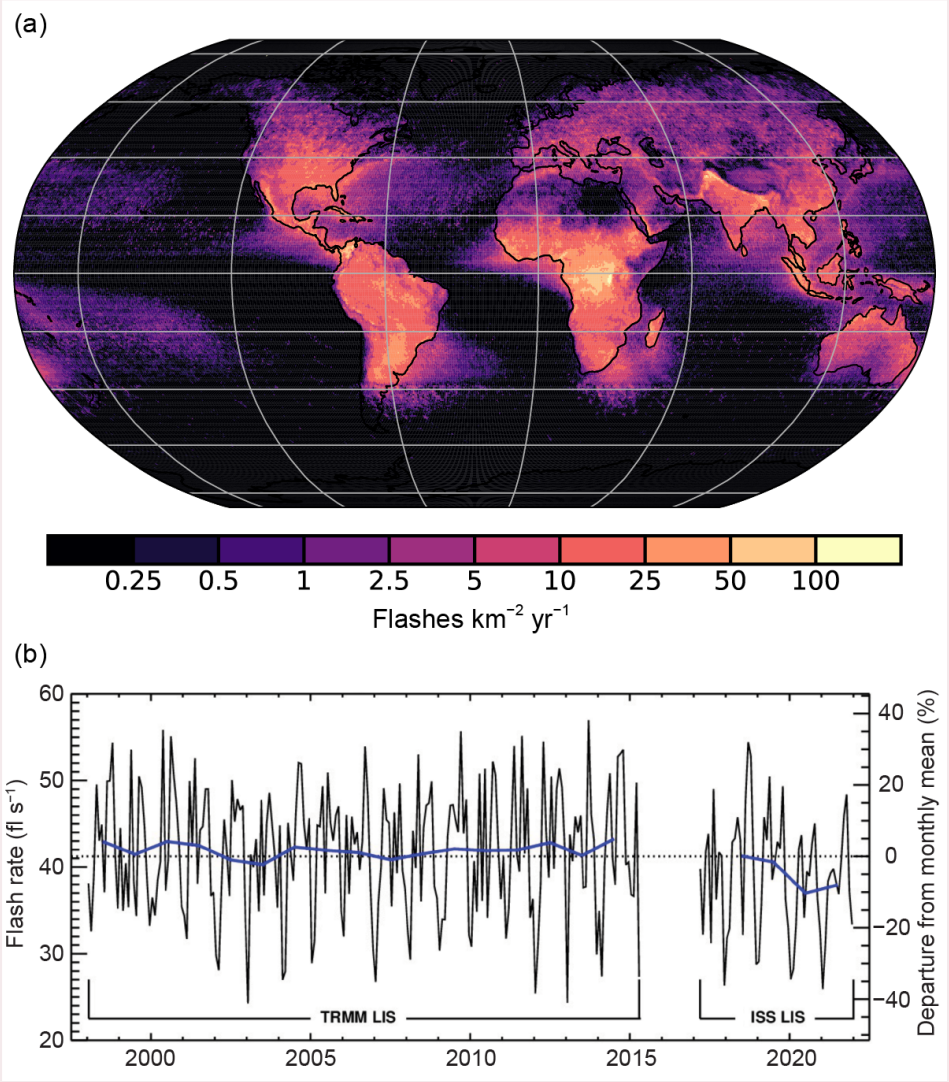

Fig. SB2.1. Lightning observations from space. (a) Global distribution of lightning flash rate density (fl km^{-2} yr^{-1}) for the period of record 1995–2021 from NASA's low earth orbit lightning imagers OTD (Optical Transient Detector, May 1995–Apr 2000), TRMM LIS (Lightning Imaging Sensor, Jan 1998–Dec 2014) and ISS LIS (Feb 2017–Dec 2021). Global lightning is dominant over the continental tropical belt. (b) Monthly (solid black) and annual (blue) mean lightning flash rates (fl s^{-1}) observed by the TRMM and ISS LIS instruments within the ±38° latitudinal coverage of the TRMM orbit. The black dotted line is the combined mean monthly global flash rate (41.2 fl s^{-1}). The mean monthly flash rate varies from ~24 to 57 fl s^{-1}. The seasonal variations are due to the annual cycle of lightning activity linked to the larger land area of the Northern Hemisphere. (Source: Courtesy of the NASA Lightning Imaging Sensor Science Team.)

closely linked to precipitation formation (Piepgrass et al. 1982; Petersen and Rutledge 1998), upper tropospheric water vapor concentrations (Price and Asfur 2006), and the ice providing for cirrus formation (Kent et al. 1995), allowing lightning to act as a proxy measure for some of these difficult-to-quantify meteorological parameters.

Lightning is currently monitored with lightning imagers on satellites (Christian et al. 2003; Blakeslee et al. 2020) and by commercial ground-based lightning detection networks based on radio wave detection (e.g., DiGangi et al. 2021; Said et al. 2010; Virts et al. 2013). The global climatology of lightning, based on satellite optical observations, is shown in Fig. SB2.1a (Christian et al. 2003; Goodman and Christian 1993; Blakeslee et al. 2020; Rudlosky and Virts 2020). The global lightning climatology follows solar insolation with a longitudinal migration that corresponds to a diurnal temperature variation (Price 1993) and a latitudinal migration that corresponds to an annual temperature variation (Christian et al. 2003; Williams 2020). The strong continental dominance of lightning has origins in both thermodynamics (Williams and Stanfield 2002a) and in aerosol-modulated cloud physics (Rosenfeld et al. 2008; Stolz et al. 2015). Their relative contributions are currently in debate, where the strong continental dominance of cloud condensation nuclei (CCN) is recognized (Williams et al. 2002b).

Satellite measurements and global lightning detection networks have not been operational long enough to detect substantial long-term changes in lightning activity (Fig. SB2.1b; Williams et al. 2019). Therefore, scientific studies use alternative methods over longer time scales to address climate questions. The thunder day is a WMO observation that has been carried out for more than a century in many countries (Brooks 1925) and represents a 24-hour day, for which thunder was heard at official national meteorological stations. Evidence has accrued that thunder days have been increasing over the last century, specifically at high latitudes (Kitagawa et al. 1989; Williams 2009; Pinto et al. 2013; Lavigne et al. 2019). Significant increases in thunderstorm activity over Africa since the 1990s have been detected using climate proxy data from reanalysis (Harel and Price 2020).

The declaration of the WMO elevates lightning flashes to a climate quantity due to its importance in climate change. It is generally agreed that lightning activity increases as the climate warms (Williams 1992, 1994; Price and Rind 1994; Romps et al. 2014), based on both considerations of the Clausius-Clapeyron relation and on the empirical evidence that CAPE increases with temperature in global climate models (Del Genio et al. 2007). The evidence for lightning increases in the Arctic (Holzworth et al. 2021), where the annually averaged Arctic near-surface air temperature increased by 3.1°C from 1971 to 2019, i.e., three times faster than the global average (AMAP 2021), which is consistent with a thermodynamic influence on lightning Fig. SB2.2. Global aerosols may decline as alternative energy sources and the reliance on fossil fuels are considered, as exemplified during the COVID-19 lockdown, such that the reduction of aerosols may diminish lightning via cloud microphysics (Stolz et al. 2015; Williams et al. 2002b). Lightning flashes also serve as a diagnostic for key manifestations of climate variability associated with deep convection. Examples include climate induced severe local convective storms accompanied by extraordinary lightning (Zipser et al. 2006; Holzworth et al. 2019; Virts and Goodman 2020; Peterson et al. 2022), the El Niño-Southern Oscillation (Goodman et al. 2000; Chronis et al. 2008; Satori et al. 2009; Williams et al. 2021), the Madden Julian Oscillation (Anyamba et al. 2000), planetary waves (Grandt 1992; Satori et al. 2009), and warming in the Arctic (Bieniek et al. 2020; Holzworth et al. 2021; Chen et al. 2021; Finney 2021).

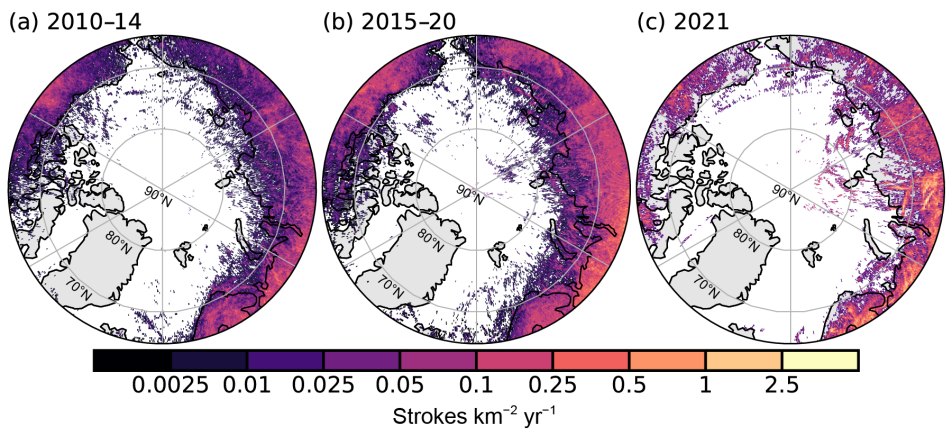

Fig. SB2.2. Arctic lightning densities (strokes km^{-2} yr^{-1}) recorded by the World Wide Lightning Location Network (WWLLN) and averaged over Jun–Aug during the years 2010–14, 2015–20, and 2021. The lightning flash densities increased during 2015–20 compared to 2010–14. In 2021, northern Europe and much of northern Russia continued to experience higher overall lightning densities. Eastern Russia and northern North America generally experienced less lightning than the 2015–20 period.

Lightning is a major source of NOx in the atmosphere (Gordillo-Vázquez et al. 2019; Schumann and Huntrieser 2007; Price et al. 1997), which contributes to climate change in a feedback loop (IPCC 2021). In particular, lightning NOx is a precursor to tropospheric ozone formation which is a greenhouse gas and also a designated ECV. The climate assessment of lightning needs to differentiate lightning occurrence frequencies against the effects of natural and man-made aerosol (Thornton et al. 2017; Wang et al. 2018; Williams 2020), which is also an ECV.

Lightning is becoming more important as a natural hazard, due to increasing vulnerability of critical infrastructures, such as electrical power grid and communications, and the growth in global population and associated lightning casualties, primarily in developing countries. Even if lightning activity remained constant in the future, its societal impact will increase dramatically. If lightning also increases with climate change, this impact may worsen.

g. Atmospheric composition

1. LONG-LIVED GREENHOUSE GASES—X. Lan, B. D. Hall, G. Dutton, J. Mühle, J. W. Elkins, and I. J. Vimont

Atmospheric burdens of many greenhouse gases, especially the long-lived greenhouse gases (LLGHGs) carbon dioxide (CO_2), methane (CH_4), and nitrous oxide (N_2O), have been increasing significantly since the industrial revolution, mainly as a result of human activity. The 2021 growth of atmospheric CH_4 reached another record high since systematic measurement started in 1983, while annual growth of CO_2 was the fifth highest since 1958 and N_2O was the third highest since 2001.

Carbon dioxide is the most important and prevalent anthropogenic GHG. In 2021, the annually averaged atmospheric CO_2 abundance at Mauna Loa Observatory (MLO) reached 416.5 ± 0.1 ppm (parts per million by moles in dry air; 1-σ uncertainties). Globally averaged CO_2, derived from remote marine boundary layer measurements, was 414.7 ± 0.1 ppm in 2021 (Fig. 2.50a; www.gml.noaa.gov/ccgg/trends). This is 49% above the atmospheric pre-industrial abundance of CO_2 of ~278 ppm, based on air extracted from ice in Greenland and Antarctica (Etheridge et al. 1996). Annual growth in global mean CO_2 has risen steadily from 0.6 ± 0.1 ppm yr^{-1} in the early 1960s to an average of 2.4 ppm yr^{-1} during the last decade, 2011–20 (Fig. 2.50a). The annual increase in global mean CO_2 in 2021 was 2.6 ± 0.1 ppm (Table 2.10), the fifth highest since the accurate measurements started in 1958.

The main driver of increasing atmospheric CO_2 is fossil fuel (FF) burning,

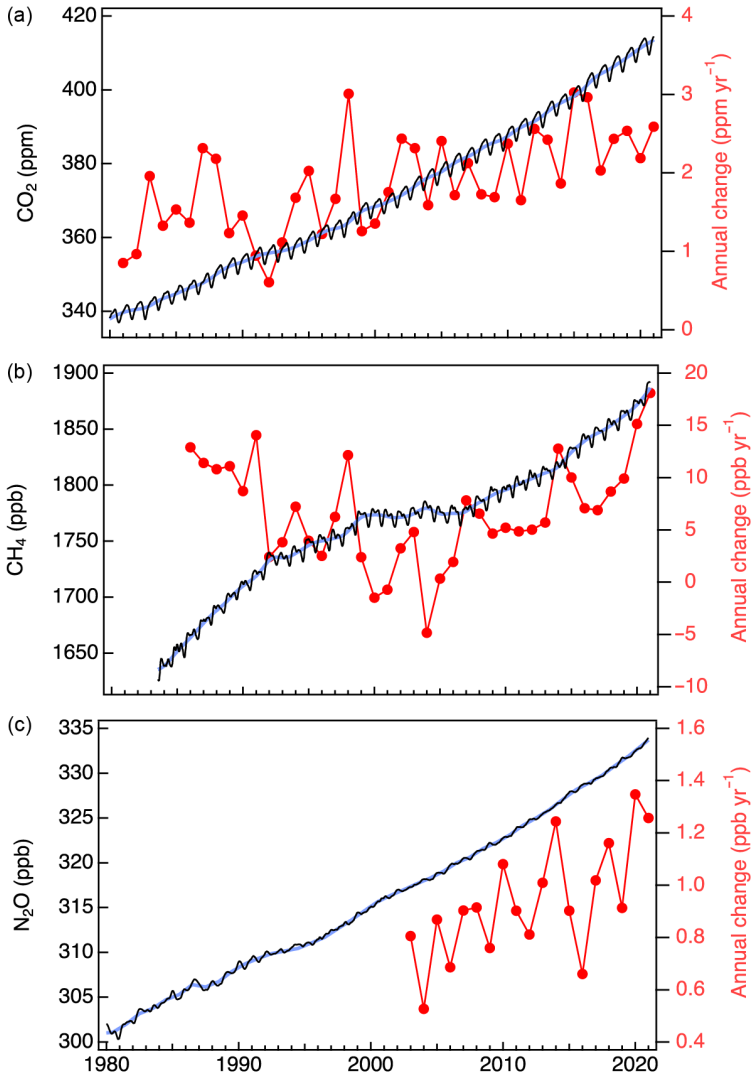

Fig. 2.50. Global mean dry-air surface mole fractions (approximately weekly data in black, left axis) and annual change (red, right axis) of (a) CO_2 (ppm), (b) CH_4 (ppb), and (c) N_2O (ppb) derived from the NOAA Global Greenhouse Gases Reference Network. Deseasonalized trend curves (see Dlugokencky et al. 1994b for methods) are shown in blue. N_2O data prior to 2001 are too sparse to allow robust estimates of annual growth rates.

Table 2.10. Summary table of long-lived greenhouse gases for 2021 (CO_2 mole fractions are in ppm, N_2O and CH_4 in ppb, and all others in ppt).

Industrial Designation or Common Name	Chemical Formula	AGGI	Radiative Efficiency (W m^{-2} ppb^{-1})[a]	Radiative Forcing (W m^{-2})	Mean surface mole fraction, 2021 (change from 2020)[b]	Lifetime (years)
Carbon Dioxide	CO_2	Y	1.37×10^{-5}	2.08	414.7 (2.3)	—
Methane	CH_4	Y	3.63×10^{-4}	0.52	1895.8 (16.7)	9.1
Nitrous Oxide	N_2O	Y	3.00×10^{-3}	0.20	334.2 (1.2)[c]	123
Chlorofluorocarbons						
CFC-11	CCl_3F	Y	0.26	0.059	222.2 (–1.8)[c]	52
CFC-12	CCl_2F_2	Y	0.32	0.161	493.9 (–3.2)[c]	102
CFC-113	CCl_2FCClF_2	Y	0.30	0.021	68.5 (–0.5)[c]	93
Hydrochlorofluorocarbons						
HCFC-22	$CHClF_2$	Y	0.21	0.052	248.9 (1.1)	11.9
HCFC-141b	CH_3CCl_2F	Y	0.16	0.004	24.6 (0.01)	9.4
HCFC-142b	CH_3CClF_2	Y	0.19	0.004	21.5 (–0.2)	18
Hydrofluorocarbons						
HFC-134a	CH_2FCF_3	Y	0.16	0.017	118.9 (5.8)	14
HFC-152a	CH_3CHF_2	Y	0.10	< 0.001	7.2 (0.2)	1.6
HFC-143a	CH_3CF_3	Y	0.16	0.004	26.5 (1.6)	51
HFC-125	CHF_2CF_3	Y	0.23	0.007	34.7 (3.4)	30
HFC-32	CH_2F_2	N	0.11	0.002	23.6 (3.1)	5.4
HFC-23	CHF_3	Y	0.18	0.006	34.9 (0.2)	228
HFC-365mfc	$CH_3CF_2CH_2C$	N	0.22	< 0.001	1.05 (0.03)	8.9
HFC-227ea	CF_3CHFCF_3	N	0.26	< 0.001	1.87 (0.17)	36
Chlorocarbons						
Methyl Chloroform	CH_3CCl_3	Y	0.07	< 0.001	1.2 (–0.2)	5.0
Carbon Tetrachloride	CCl_4	Y	0.17	0.013	76.2 (–1.1)[c]	32
Methyl Chloride	CH_3Cl	N	0.01	< 0.001	547.2 (–1.7)	0.9
Bromocarbons						
Methyl Bromide	CH_3Br	N	0.004	<< 0.001	6.61 (–0.06)	0.8
Halon 1211	$CBrClF_2$	Y	0.29	0.001	3.03 (–0.09)	16
Halon 1301	$CBrF_3$	Y	0.30	0.001	3.31 (0.01)	72
Halon 2402	$CBrF_2CBrF_2$	Y	0.31	< 0.001	0.396 (–0.03)	28
Fully fluorinated species						
Sulfur Hexafluoride	SF_6	Y	0.57	0.006	10.63 (0.35)	> 600
PFC-14	CF_4	N	0.09	0.005	87.4 (0.2)	~ 50 000
PFC-116	C_2F_6	N	0.25	0.001	5.03 (0.02)	~ 10 000
PFC-218	C_3F_8	N	0.28	< 0.001	0.721 (0.003)	~ 2600
PFC-318	*c*-C_4F_8	N	0.32	< 0.001	1.90 (0.01)	~ 3200

[a] Radiative efficiencies and lifetimes were taken from Appendix A in WMO (2018), except for SF_6 lifetime from Ray et al. (2017), CH_4 lifetime from Prather et al. (2012). For CO_2, numerous removal processes complicate the derivation of a global lifetime. AGGI = Annual Greenhouse Gas Index. For radiative forcing, see https://www.esrl.noaa.gov/gmd/aggi/aggi.html

[b] Mole fractions are global, annual surface means determined from NOAA Global Greenhouse Gas Reference Network marine boundary layer sites, except for PFC-14, PFC-116, PFC-218, PFC-318, and HFC-23, which were measured by AGAGE (Mühle et al. 2010; Miller et al. 2010). Changes indicated in brackets are the differences between the 2021 and 2020 means. These values differ from the growth rates reported in the main text and figures, which represent the net addition of a LLGHG to the atmosphere over the course of a year, calculated by differencing (approximately) the 1 Jan atmospheric abundances in successive years. All values are preliminary and subject to minor updates.

[c] Global mean estimates derived from multiple NOAA measurement programs ("Combined Dataset").

with emissions (including ~5% from cement production) increasing from 3.0 ± 0.2 Pg C yr^{-1} in the 1960s to 9.5 ± 0.5 Pg C yr^{-1} in the past decade (2011–20; Friedlingstein et al. 2021). About half of the overall FF emitted CO_2 since 1958 has remained in the atmosphere, while the rest has been stored by the ocean and the terrestrial biosphere. While emissions of CO_2 from FF combustion drive are increasing atmospheric burden, the interannual variability in the CO_2 growth rate is mostly driven by terrestrial biosphere exchange of CO_2, which is confirmed by measurements of its ^{13}C:^{12}C ratio (e.g., Keeling et al. 1985; Alden et al. 2010). Terrestrial biosphere flux variability is influenced by both temperature and moisture anomalies (Cox et al. 2013; Hu et al. 2019; Humphrey et al. 2018) often associated with ENSO.

For 2020, FF CO_2 emissions declined by 5.4%, relative to 2019, due to the COVID-19 pandemic (Friedlingstein et al. 2021). However, this reduction is not obvious in observed global atmospheric CO_2 signals, because it is a relatively small signal compared with the natural variability from terrestrial biosphere exchange. The estimated 5.4% reduction in global CO_2 emissions of 10 Pg C yr^{-1} would result in a ~0.24 ppm decrease in global CO_2 (given a conversion factor of 2.12 Pg C ppm^{-1}; Ballantyne et al. 2012), which is within the 1 std. dev. interannual variability of 0.4 ± 0.1 ppm yr^{-1} of CO_2 annual growth in 2010–19. Yet at least one analysis has detected regional impacts of COVID-19 on total column-CO_2 (Weir et al. 2021). Preliminary data for 2021 suggest a rebound in FF CO_2 emissions relative to 2020 of +4.9 ± 0.8% globally (Friedlingstein et al. 2021).

While a pulse of CO_2 will last in the atmosphere for thousands of years (Archer and Brovkin 2008), atmospheric CH_4 has a lifetime of about nine years, meaning that its atmospheric abundance (and radiative forcing) can be reduced much more quickly (United Nations Global Methane Assessment 2021). Global mean tropospheric CH_4 abundance increased to 1895.7 ± 0.6 ppb (parts per billion by moles in dry air) in 2021, a 162% increase compared to its pre-industrial level of 722 ± 15 ppb. Since the beginning of NOAA's systematic CH_4 measurements in 1983, global CH_4 abundance rose and then flattened prior to 2006 (Fig. 2.50b), which is consistent with an approach to steady state if there was no trend in its lifetime driven by CH_4 sinks (Dlugokencky et al. 2003). Atmospheric CH_4 growth restarted in 2007 and has significantly accelerated since 2014 (Fig. 2.50b). Preliminary measurement results show continued large growth in 2021, about 18.1 ± 0.4 ppb, following a similarly large increase seen in 2020 (15.1 ± 0.4 ppb).

Given the complexity of the CH_4 budget, the scientific community has not reached consensus on reasons for the magnitudes and long-term trends of many CH_4 sources. Fossil fuel exploitation is estimated to account for ~19% of total global CH_4 emissions since 2000 based on top-down approaches that use atmospheric CH_4 measurements and inverse models (Saunois et al. 2020). However, studies including radioactive (^{14}C:C) or stable (^{13}C:^{12}C) carbon isotope ratios of CH_4 suggest a much larger fraction of fossil emissions (~30% in 1984–2016; Lassey et al. 2007; Schwietzke et al. 2016; Lan et al. 2021). Measurements of ^{13}C:^{12}C in CH_4 also suggest that increased emissions from biogenic sources (e.g., wetlands and ruminant animals) are the dominant drivers for the post-2006 growth (Lan et al. 2021; Chang et al. 2019; Nisbet et al. 2019; Schaefer et al. 2016; Schwietzke et al. 2016).

It is an ongoing investigation to decipher the post-2019 CH_4 surge. A reduction in the global abundance of the hydroxyl radical (OH, the main sink for CH_4) may have contributed to the growth in 2020 due to the COVID-19 pandemic reduction in major OH precursors, NO_x and CO (Laughner et al. 2021). However, reduced OH abundance due to COVID-related pollution reductions is unlikely to contribute significantly to the continued rapid increase in 2021.

Nitrous oxide (N_2O) is an ozone-depleting LLGHG mainly emitted from natural and agricultural soils, animal manure, and the oceans (Ravishankara et al. 2009; Davidson 2009). Its atmospheric lifetime is about 123 years (Ko et al. 2013). Atmospheric N_2O has been increasing steadily throughout the industrial era, except for a brief period in the 1940s (MacFarling Meure et al. 2006; Thompson et al. 2019). The mean global atmospheric N_2O abundance in 2021 was 334.3 ± 0.1 ppb, a 24% increase over its preindustrial level of 270 ppb. The annual increase of 1.3 ± 0.1 ppb in 2021

(Fig. 2.50c) was higher than the average annual increase over 2011–20 (1.0 ± 0.2 ppb) and was the third highest growth since 2001. It is an ongoing investigation to understand the drivers for the large N_2O growth in 2021 and the record growth in 2020 (1.4 ± 0.1 ppb).

The increased burdens of LLGHGs are largely responsible for increasing global temperature (IPCC 2013). The impacts of these LLGHGs on global climate are estimated based on their abilities to change the global radiative energy balance. Compared with preindustrial times (1750), increasing atmospheric CO_2 abundance has increased radiative forcing by > 2.1 W m^{-2}. The increase in CH_4 has contributed to a 0.53 W m^{-2} increase in direct radiative forcing while the CH_4-related production of tropospheric O_3 and stratospheric H_2O has also contributed to ~0.30 W m^{-2} indirect radiative forcing (Myhre et al. 2014). While the atmospheric burdens of some greenhouse gases, such as chlorofluorocarbons, have declined in recent decades, the combined radiative forcing of CO_2, CH_4, and N_2O, in addition to other LLGHGs (all of which are halogenated compounds), has increased each year (Fig. 2.51). In 2021, the combined radiative forcing from all LLGHGs (Table 2.10) was 3.2 W m^{-2}, which is 3.6 times greater than in 1950, at the start of the "Great Acceleration." NOAA's Annual Greenhouse Gas Index (AGGI; Fig. 2.51) summarizes trends in the combined direct radiative forcing by all LLGHGs (Hofmann et al. 2006). This index represents the annual cumulative radiative forcing of LLGHGs relative to the Kyoto Protocol baseline year of 1990. The AGGI value of 1.49 in 2021 indicates an increase of 49% in radiative forcing of LLGHGs compared to 1990.

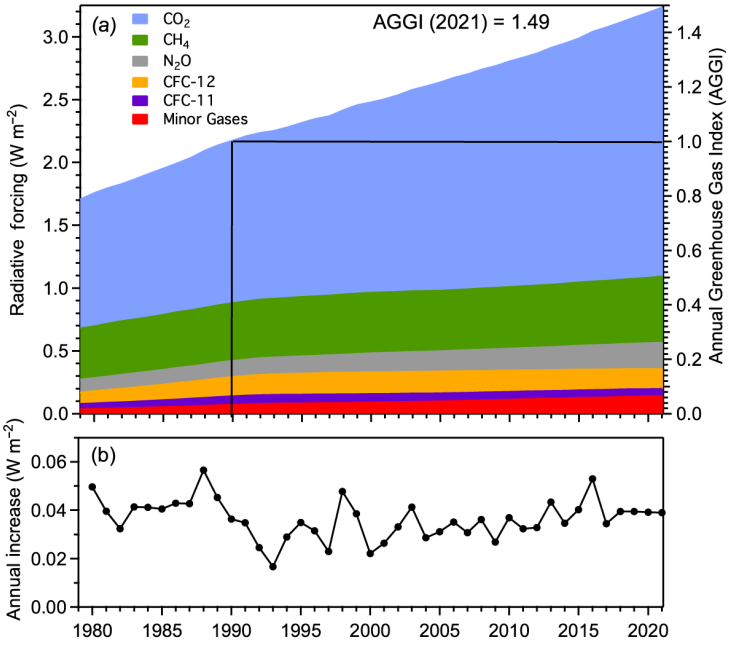

Fig. 2.51. (a) Direct radiative forcing (W m^{-2}) due to five major long-lived greenhouse gases (LLGHG) and 15 minor gases (left axis; see Table 2.10 for details of the 15 minor gases) and the associated values of the NOAA AGGI (right axis). The Annual Greenhouse Gas Index (AGGI) is defined to have a value of 1 in 1990. (b) Annual increase in direct radiative forcing (W m^{-2}).

2. OZONE-DEPLETING SUBSTANCES—I. J. Vimont, B. D. Hall, G. Dutton, S. A. Montzka, C. Siso, M. Crotwell, and M. Gentry

Halogenated trace gases affect the radiative energy balance of the atmosphere and climate through their direct absorption of infrared energy and through their ability to deplete stratospheric ozone (Karpechko and Maycock 2018). Halogenated compounds, such as chlorofluorocarbons (CFCs), hydrochlorofluorocarbons (HCFCs), hydrofluorocarbons (HFCs), chlorocarbons, and bromocarbons are controlled by the 1987 Montreal Protocol (https://www.unep.org/ozonaction/who-we-are/about-montreal-protocol) and its subsequent amendments.

The effect of these controls can be seen clearly in the overall decline in the atmospheric abundance of many of the controlled gases (Engel and Rigby 2018); however, even after production ceases, declines in atmospheric abundance vary by compound because these chemicals have different lifetimes, as well as different sizes of "banks" (i.e., reservoirs of produced, but not yet emitted chemicals). For example, by 2021, CFC-11 and CFC-12 had declined from their peak abundance by only around 17% and 9% despite a reported global phase-out by 2010, whereas methyl chloroform (phased out in 2015) had decreased by 99% (Fig. 2.52; Table 2.10). These differences are explained by 50-yr and 100-yr lifetimes for the CFCs versus 5 years for methyl chloroform, and the presence of substantial (and leaky) banks for the CFCs, but not for methyl chloroform.

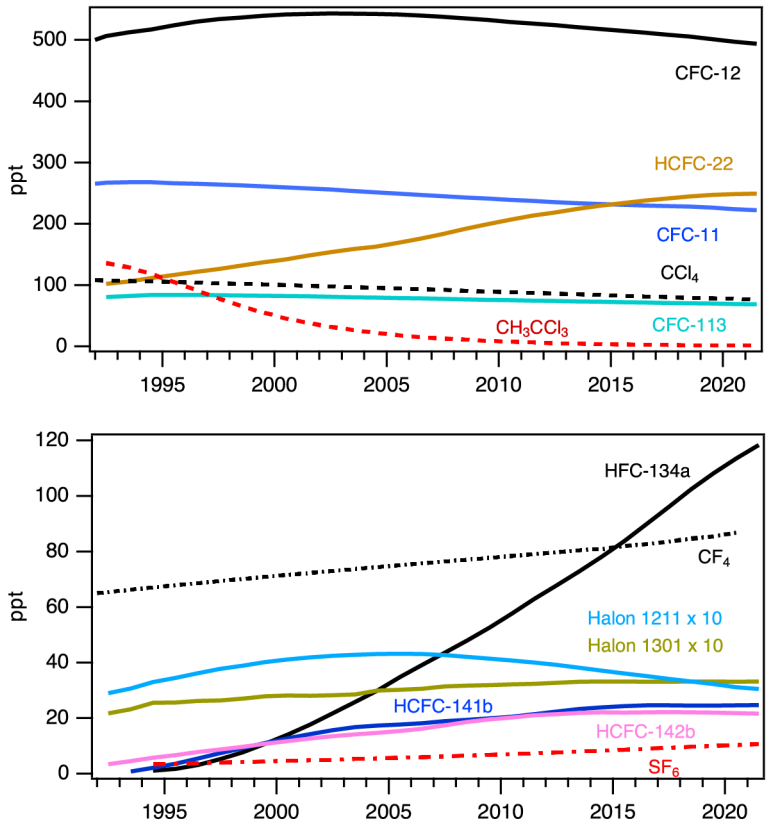

Fig. 2.52. Global mean abundances (mole fractions) at Earth's surface (parts per trillion = nmol mol^{-1} in dry air) for several halogenated gases, many of which also deplete stratospheric ozone. See Table 2.10 for the 2021 global mean mole fractions of these and other gases.

Long-term monitoring of the abundances of these species has proved to be important for ensuring the success of the Montreal Protocol. The decline of CFC-11 mole fractions in the atmosphere slowed down unexpectedly after 2012, which led to the discovery of renewed increases in global emissions through 2018 (Montzka et al. 2018; Rigby et al. 2019). Shortly after this discovery was announced in 2018, the mole fraction decline observed for CFC-11 accelerated to rates that were comparable to those measured before 2012. One possible, yet unverified, cause of the observed decline in CFC-11 global emissions is a decrease in unreported production of this chemical (Montzka et al. 2021).

HCFCs are another important set of ozone-depleting compounds controlled by the Montreal Protocol, and overall trends in recent years reflect reduced levels of production and consumption. A select number of HFCs, which are used as substitutes for ozone depleting substances (ODSs) in some applications, are scheduled for phase down by the Kigali Amendment to the Montreal Protocol, but these controls are only now coming into effect so have not substantially altered their mole fraction tendencies; some HFCs, such as HFC-134a, are steadily increasing in the atmosphere.

Equivalent effective stratospheric chlorine (EESC) is a measure of the reactive ozone-depleting halogen loading at a given time and place in the stratosphere, calculated from global mean surface mole fractions and consideration of mixing processes, time-dependent trace gas destruction in the stratosphere, and the relative ozone-destruction efficiency of bromine versus chlorine (Daniel et al. 1995; Montzka et al. 1996; Newman et al. 2007). Midlatitude EESC is calculated using a 3-year mean age-of-air, while Antarctic EESC is calculated with a 5.5-year mean age-of-air, as detailed in Newman et al. (2007). The abundance of reactive halogen in the midlatitude stratosphere is lower than in the Antarctic stratosphere, because air reaching the Antarctic has been in the stratosphere longer and has been transported to higher altitudes, which leads to more ODS destruction and release of reactive halogen (Montzka, Reimann et al. 2011). Most of the reactive

halogen in the atmosphere is due to CFCs, and they contribute strongly to EESC (Fig. 2.53) and still have high abundance in the atmosphere.

At the beginning of 2021, EESC in the midlatitudes was 1549 ppt, which represents a 20% decrease from its maximum value of 1936 ppt in 1997 (https://www.gml.noaa.gov/odgi; Fig. 2.53a). Antarctic EESC was 3659 ppt at the beginning of 2021, a 12% decrease from its maximum value of 4152 in 2001 and 2002 (https://www.gml.noaa.gov/odgi; Fig. 2.53b). To provide context for changes in the EESC, the Ozone Depleting Gas Index (ODGI) was developed. The ODGI is derived for both the midlatitude and Antarctic stratosphere by rescaling EESC values in these regions, where an ODGI of 100 represents the peak EESC value, and 0 represents the value of EESC at 1980 (Hoffmann and Montzka 2009; https://www.gml.noaa.gov/odgi). Ozone destruction had already begun by 1980, but a return of stratospheric halogen to levels last seen in 1980 would represent a major milestone for the Montreal Protocol. At the beginning of 2021, the Antarctic ODGI (ODGI-A) was 75.3 and midlatitude ODGI (ODGI-M) was 50.1. Reactive halogen abundance in the Antarctic stratosphere has declined 24.7% (100% minus 75.3%) of the way back to the 1980 benchmark value. In the midlatitudes, the decline is nearly half of that needed to reach the 1980 benchmark value. Currently, ODGI-A and ODGI-M are projected to reach 0 around 2076 and 2049, respectively (Carpenter et al. 2018; https://www.gml.noaa.gov/odgi).

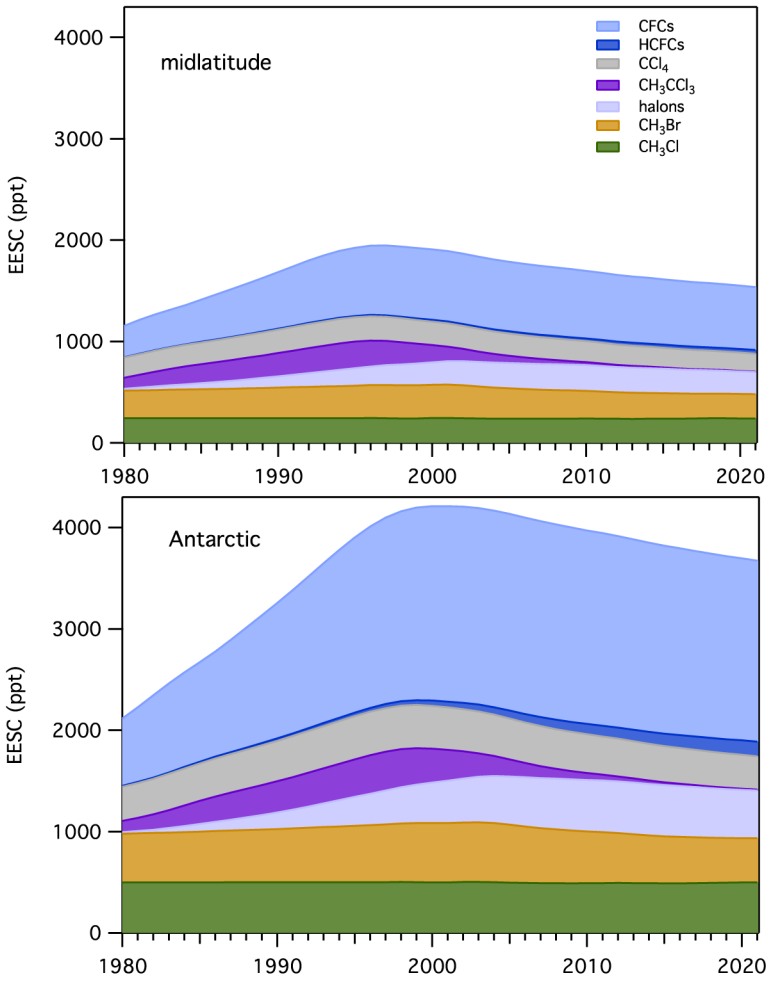

Fig. 2.53. Equivalent effective stratospheric chlorine (EESC, ppt) for the (a) midlatitude and (b) Antarctic stratosphere derived from surface measurements. The EESC values represent EESC on 1 Jan of each year.

3. AEROSOLS—S. Rémy, N. Bellouin, Z. Kipling, M. Ades, A. Benedetti, and O. Boucher

Aerosols represent a serious public health issue in many countries and hence are subject to monitoring and forecasting worldwide as part of air quality policies. Atmospheric aerosols also play an important role in the climate system, by scattering and absorbing radiation and by affecting the life cycle, optical properties and precipitation activity of clouds (IPCC 2021).

The Copernicus Atmosphere Monitoring Service (CAMS; http://atmosphere.copernicus.eu) runs a near-real time (NRT) global analysis of aerosols and trace gases. The CAMS project also produced a reanalysis of global aerosols and trace gases that covers the years 2003 to 2021: the CAMS reanalysis (Inness et al. 2019), by combining state of the art numerical modeling and aerosol remote sensing retrievals from MODIS (Levy et al. 2013) and the Advanced Along Track Scanning Radiometer (AATSR; Popp et al. 2016). Verification of aerosol optical depth (AOD) at 500 nm, against independent AERONET observations, shows that the CAMS reanalysis has a smaller bias and error than its predecessors: the CAMS interim reanalysis (Flemming et al. 2017) and the MACC reanalysis (Inness et al. 2013). This section uses data exclusively from the CAMS reanalysis.

AOD at 550 nm in 2021 (Fig. 2.54a) shows maxima over the polluted regions of India and China, as well as from dust over the Sahara and the Middle East. High values from seasonal or occasional extreme fires are seen over equatorial Africa and Siberia. The high values over Hawaii and close to Mexico City are a known artifact of the CAMS reanalysis related to volcanic outgassing. Figure 2.54b shows the time series of monthly and annual globally-averaged total AOD during 2003–21. Figure 2.54b shows strong seasonality, driven mainly by dust episodes between March and July in the Sahara, Middle East, and Taklimakan/Gobi deserts and seasonal biomass burning in Africa, South America, and Indonesia. Globally averaged AOD in 2021 was on average slightly higher than in 2020, by 0.6%, but with marked seasonal differences: the boreal summer months saw some of the highest values since 2003, but the winter months saw the lowest values since 2014/15. A series of exceptional fires in Siberia and North America contributed to the high values in July and August.

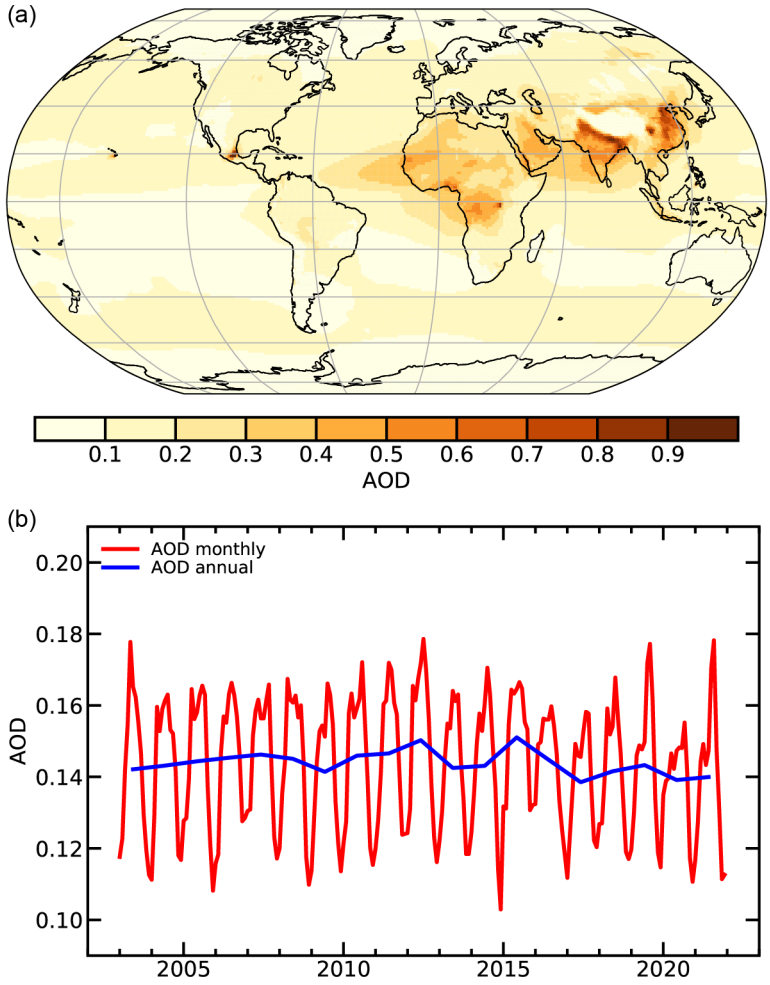

Fig. 2.54. (a) Global aerosol optical depth (AOD) at 550 nm in 2021. (b) Global average of total AOD at 550 nm averaged over monthly (red) and annual (blue) periods for 2003–21.

These exceptionally large biomass burning aerosol events caused the positive anomalies relative to the 2003–20 mean over Siberia and parts of North America in Plates 2.1u,v, while the positive anomalies over India and Iran were mostly caused by anthropogenic pollution events and are consistent with a positive AOD trend in these regions (see Figs. 2.55b,c). These fires also explain most of the extreme aerosol days shown in Plates 2.1u,v. Two large volcanic eruptions occurred in 2021. The Cumbre Vieja volcano (September) in the Canary Islands explains a positive anomaly there, while the Caribbean eruption of La Soufriere in Saint Vincent (April) injected a small amount of aerosols into the stratosphere. Dust storm activity was, in general, less than usual over most of the Sahara and Taklimakan, while the negative AOD anomalies over East Asia, Europe, and the Amazon basin can be explained by ongoing long-term decreasing trends of aerosol emissions and burden in these regions.

These trends are shown in Figs. 2.55b (2003–21) and 2.55c (2012–21). Between 2003 and 2021, there are significant negative AOD trends over most of the United States, Europe, East Asia, and the Amazon basin, the latter from reduced deforestation and associated burning activity. Positive trends are noted over Siberia, driven by biomass burning events, as well as over India and Iran, driven by an increase in anthropogenic emissions (Satheesh et al. 2017). Between 2012 and 2021, the picture is slightly different: there is no decreasing trend over the United States and the Amazon basin, indicating that most of the 2003–21 trend can be explained by changes between 2003 and 2012. Similarly, the 2012–21 negative trend over Europe is smaller than the 2003–21 trend, while it is the opposite over East Asia, which is consistent with the observed decrease of most anthropogenic emissions there since around 2012 (Li et al. 2017). A stronger positive trend between 2012 and 2021 is noted over most of Iran, while over the same period the positive trend over India is smaller than the 2003–21 trend.

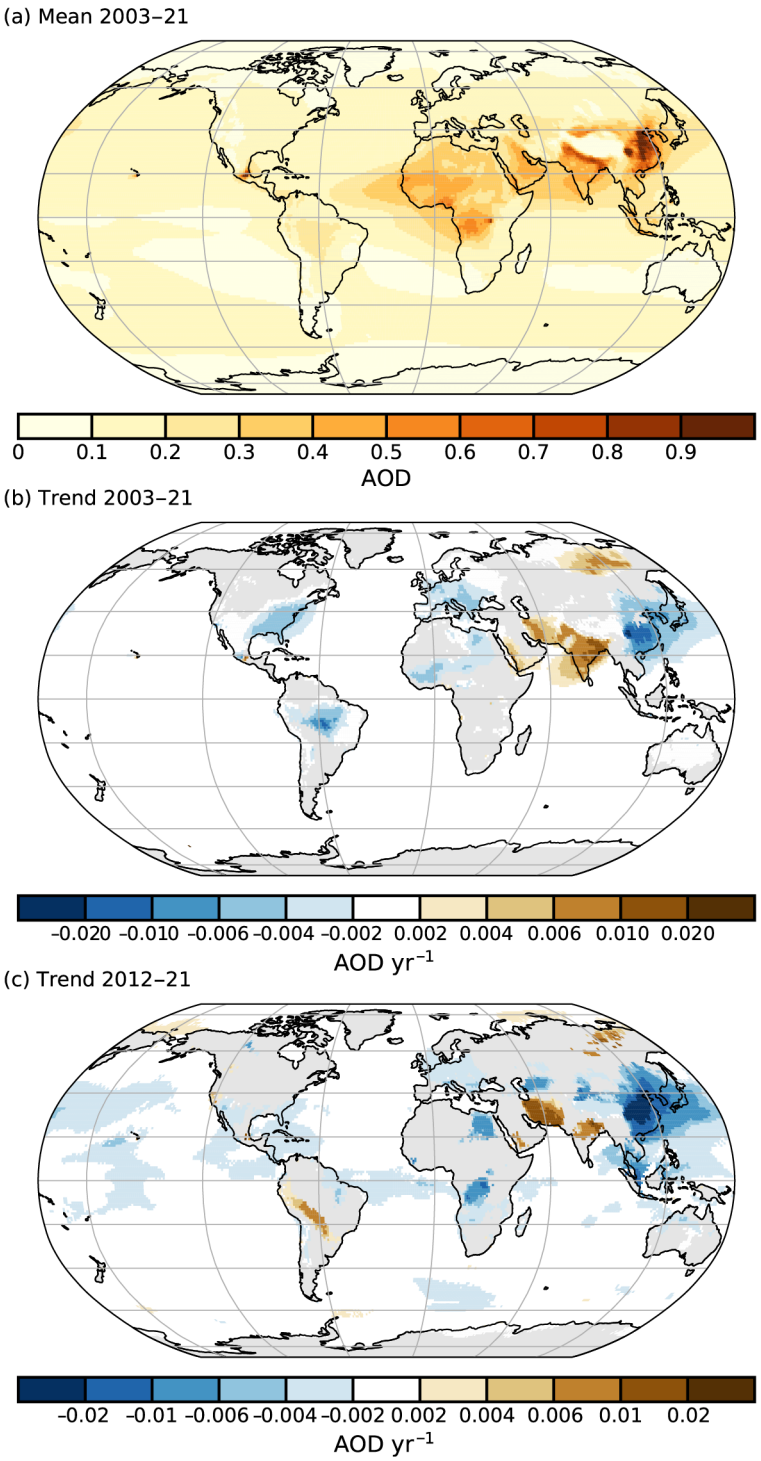

Fig. 2.55. (a) Total AOD at 550 nm averaged over the period 2003–21. Note the regional differences, with much greater total AOD values over parts of northern Africa, the Arabian Peninsula, southern Asia, and eastern China. Linear trends of total AOD (AOD unit yr^{-1}) for (b) 2003–21 and (c) 2012–21. Only trends that are statistically significant (95% confidence level) are shown. Regions with decreasing trends include the eastern United States, most of Europe, parts of Brazil and China, as well as the Korean Peninsula and Japan.

The AOD climatology between 2003 and 2021 (Fig. 2.55a) is close to the 2021 mean; it shows maxima over the highly populated regions of India and China, mainly caused by anthropogenic emissions, as well as over the Sahara, Middle East, and Taklimakan/Gobi from desert dust, and over central Africa, Indonesia, and the Amazon basin from fire emissions. The high values over Hawaii and close to Mexico City are a known artifact of the CAMS reanalysis related to volcanic outgassing.

Anthropogenic AOD and radiative forcing resulting from aerosol–radiation (RFari) and aerosol–cloud interactions (RFaci) are shown in Fig. 2.56 for 2021 and the period 2003–21. They are estimated using the methods described in Bellouin et al. (2020). The year 2021 was characterized by lower anthropogenic AOD and weak RFari and RFaci relative to the past 19 years. This decreasing trend is not yet statistically significant but is consistent with the decreasing trends in industrial and smoke aerosols seen in many regions, as mentioned above. The AOD anomalies for 2021 shown in Plate 2.1u exert a relatively weak top-of-atmosphere radiative forcing in part because they are mostly caused by aerosols that are fairly absorbing, which decreases their ability to scatter radiation back to space. These aerosols, however, still exert a sizeable radiative forcing at the surface.

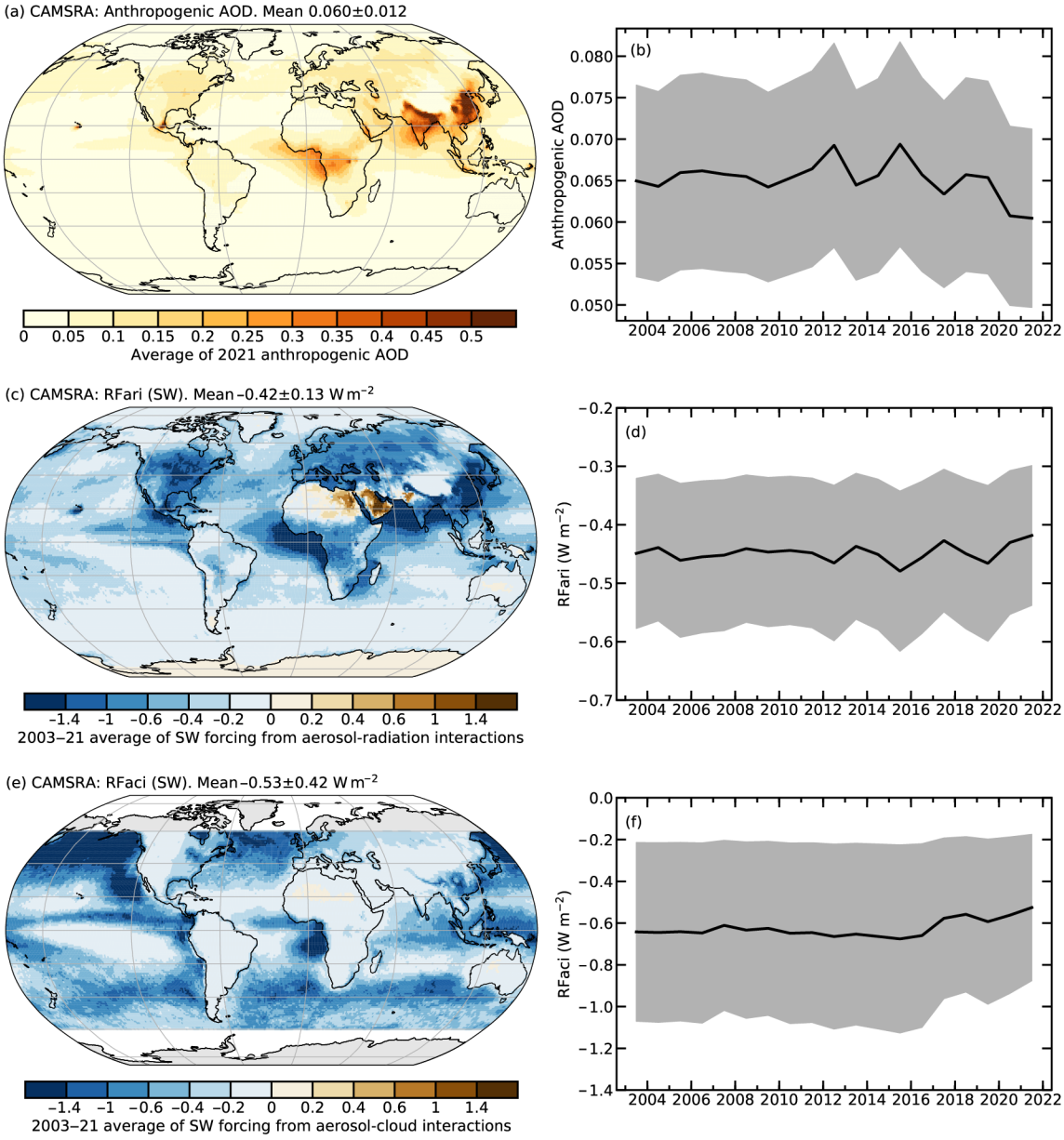

Fig. 2.56. CAMSRA (a) 2021 average of anthropogenic aerosol optical depth (AOD); (b) global annual average of anthropogenic AOD from 2003 to 2021. Radiative forcing (W m^{-2}) in the shortwave (SW) spectrum due to (c),(d) aerosol–radiation (RFari) and (e),(f) aerosol–cloud interactions (RFaci). The left column shows the average distribution for the period 2003–21. The right column shows a time series of global averages for the same period, with the 1-σ uncertainties of these estimates shown in gray.

4. STRATOSPHERIC OZONE—M. Weber, W. Steinbrecht, C. Arosio, R. van der A, S. M. Frith, J. Anderson, L. M. Ciasto, M. Coldewey-Egbers, S. Davis, D. Degenstein, V. E. Fioletov, L. Froidevaux, D. Hubert, D. Loyola, C. Roth, A. Rozanov, V. Sofieva, K. Tourpali, R. Wang, and J. D. Wild

Ninety percent of atmospheric ozone resides in the stratosphere with a maximum in the lower stratosphere. Stratospheric ozone protects Earth's biosphere from harmful ultraviolet (UV) radiation. Increases in anthropogenic ozone-depleting substances (ODS) thinned stratospheric ozone until the mid-1990s. The phase-out of ODS, mandated by the Montreal Protocol in the late 1980s (section 2g2), slowed stratospheric ozone loss, with some regions now showing a slow recovery. In addition, the rate and even the sign of long-term ozone changes depend on changes in chemical composition and stratospheric circulation caused by increasing concentrations of long-lived greenhouse gases (LLGHG) and varies by region and altitude. The clearest signs of ozone recovery related to ODS changes are evident in the upper stratosphere (WMO 2018).

The annual mean total ozone distribution in 2021 (Plate 2.1x) shows generally negative ozone global anomalies, except for two bands centered near 20° latitude on both sides of the equator, where ozone is higher by about 5 DU than the decadal mean (1998–2008). This pattern (low ozone in the inner tropics and high ozone in the outer tropics) is typical during the easterly wind shear phase of the quasi-biennial oscillation (QBO-east). During QBO-east, the meridional stratospheric circulation is generally stronger, resulting in enhanced ozone transport into the subtropical latitudes (Baldwin et al. 2001; Weber et al. 2011; Lawrence et al. 2020; Plate 2.1x). Negative total ozone anomalies in the Southern Hemisphere extratropics are possibly related to the combination of the unusually long-lasting Antarctic ozone hole of 2020, extending into 2021, and the large ozone hole in the second half of 2021. The westerly phase of the QBO in late autumn of 2020 likely resulted in weaker ozone transport and higher polar ozone deficits in the Northern Hemispheric winter of 2021.

Figure 2.57 shows the long-term evolution of annual total column ozone for different zonal bands (near-global, NH, tropics, and SH), and for polar caps in March (for the NH cap) and October (for the SH cap). These are the months when polar ozone losses are usually at their maximum after a cold stratospheric winter in the respective hemispheres, which occurs every year in the SH ("ozone hole") but is more sporadic in the NH (see sections 6h and 5j, respectively). Total ozone shows above-average total ozone levels in 2021 in the outer tropical/subtropical region (Plate 2.1x). At middle latitudes, total ozone is at the lower range of the values from the last two decades (Figs. 2.57b,e; Plate 2.1x). Total ozone was near the minimum annual mean values observed during the entire 43-year satellite observation period in the SH extratropics and above Antarctica in October (Figs. 2.57d,e; see section 6h).

ODS-related total ozone changes since 1996 are on the order of +0.5% decade^{-1} in the extratropics of both hemispheres, but opposing long-term changes in atmospheric dynamics contributed to near-zero overall trends in the NH extratropics from 2000 to present (Coldewey-Egbers et al. 2022; Weber et al. 2022). Mean total ozone levels during the period 2017–20 are still 4% and 5% below the 1964–1980 mean in the extratropics of the NH and SH extratropics, respectively (Figs. 2.57b,d; Weber et al. 2022).

Figure 2.58 shows ozone time series at two altitudes in the lower (50 hPa/22 km altitude) and upper stratosphere (2 hPa/42 km altitude). The ozone evolution at both levels is broadly consistent with the projected range from various models of the Phase 1 Chemistry Climate Model Initiative (CCMI) using current scenarios of ODS and GHG changes (thick gray line in Fig. 2.57a and shaded area in Fig. 2.58; SPARC/IO3C/GAW 2019).

In 2021 SH extratropical lower stratospheric ozone was close to the lowest values seen in the last decade but higher than in 2020. The lower values are related to the above-average sizes of the Antarctic ozone holes in 2020 and 2021 (see section 6h).

The earliest and clearest sign of ODS-related ozone recovery was detected in the upper stratosphere, where dynamic variability plays a lesser role (e.g., Newchurch et al. 2003; Godin-Beekmann

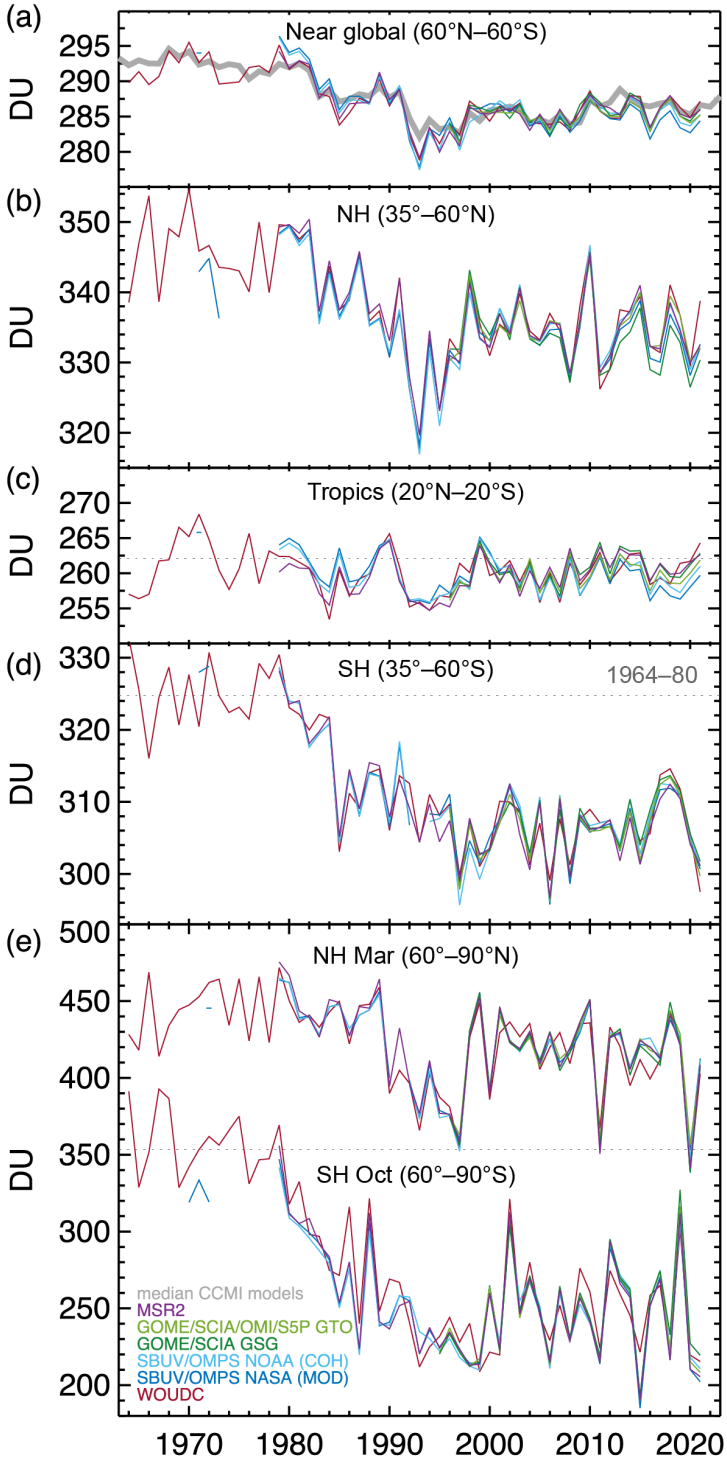

Fig. 2.57. Time series of annual mean total column ozone (DU) for (a) global (60°S–60°N), (b) NH (35°–60°N), (c) tropics (20°S–20°N), and (d) SH (35°–60°S); and (e) polar (60°–90°) total column ozone in Mar (NH) and Oct (SH), the months when polar ozone losses usually are largest. Data are from WOUDC (World Ozone and Ultraviolet Radiation Data Centre) ground-based measurements combining Brewer, Dobson, SAOZ (Système D'Analyse par Observations Zénithales), and filter spectrometer data (red: Fioletov et al. 2002, 2008); the BUV/SBUV/SBUV2/OMPS merged products from NASA (V8.7. dark blue, Frith et al. 2014, 2017), and NOAA (V8.8, light blue: J. D. Wild and L. M. Ciasto, person. comm. 2019); the GOME/SCIAMACHY/GOME-2 products GSG from University of Bremen (dark green, Weber et al. 2022), and GTO from ESA/DLR (light green, Coldewey-Egbers et al. 2015; Garane et al. 2018). MSR-2 (purple) assimilates nearly all ozone datasets after corrections based on the ground-based data (van der A et al. 2015). All datasets have been bias-corrected by subtracting averages for the reference period 1998–2008 and adding back the mean of these averages. The dotted gray lines in each panel show the average ozone level for 1964–80 calculated from the WOUDC data. The thick gray line (panel a) shows the median from chemistry-climate (CCMI)-1 ref C2 model runs (SPARC/IO3C/GAW 2019). Most of the observational data for 2021 are preliminary.

et al. 2022). Upper stratospheric ozone has shown an increase of about +2% decade^{-1} since the late 1990s (e.g., Steinbrecht et al. 2017; Arosio et al. 2019; Szelag et al. 2020; Sofieva et al. 2021; Godin-Beekmann et al. 2022). In general, ozone observations in the lower stratosphere suggest little change or even a continuing decline over the last two decades (Fig. 2.58; Ball et al. 2018, 2020; Chipperfield et al. 2018; Wargan et al. 2018; Godin-Beekmann et al. 2022).

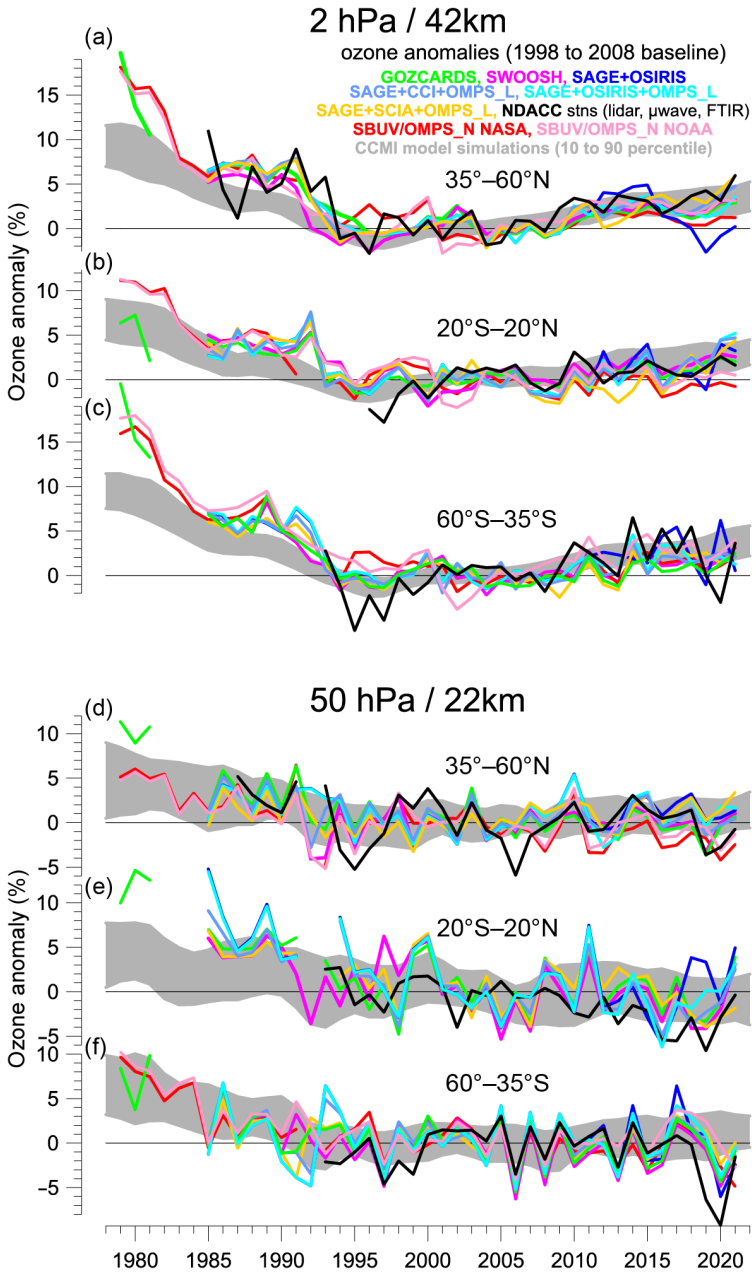

Fig. 2.58. Annual mean anomalies of ozone (%) in (a–c) the upper stratosphere near 42-km altitude or 2-hPa pressure and (d–f) in the lower stratosphere, near 22 km or 50 hPa for the NH (35°–60°N; a,d), tropics (20°S–20°N; b,e), and SH (35°–60°S; c,f), respectively. Anomalies are GOZCARDS referenced to the 1998–2008 baseline. Colored lines are long-term records obtained by merging different limb (SWOOSH, SAGE+OSIRIS, SAGE+CCI+OMPS-L, SAGE+SCIAMACHY+OMPS-L) or nadir-viewing (SBUV, OMPS-N) satellite instruments. The nadir-viewing instruments have much coarser altitude resolution than the limb-viewing instruments. This can cause differences in some years, especially at 50 hPa. The black line is from merging ground-based ozone records at seven NDACC stations employing differential absorption lidars and microwave radiometers. See Steinbrecht et al. (2017), WMO (2018), and Arosio et al. (2018) for details on the various datasets. Gray shaded area shows the range of chemistry–climate model simulations from CCMI-1 refC2 (SPARC/IO3C/GAW, 2019). Ozone data for 2021 are not yet complete for all instruments and are still preliminary.

5. STRATOSPHERIC WATER VAPOR—S. M. Davis, K. H. Rosenlof, D. F. Hurst, H. Vömel, and R. Stauffer

The amount of water vapor (WV) entering the stratosphere is controlled to a large degree by temperature variability in the tropical tropopause layer (TTL; ~14–19 km) and particularly at the cold-point tropopause (CPT), with more WV entering the stratosphere when CPT temperatures are higher. Variations in this so-called entry value of water vapor exerts a strong influence on overall stratospheric WV concentrations, as methane oxidation in the upper stratosphere and mesosphere represents the only other consistent source for WV in the stratosphere. Thus, processes that lead to variations in TTL and CPT temperatures on various timescales can affect stratospheric WV on a global scale.

For quantifying interannual changes in stratospheric WV, the *Aura* satellite's Microwave Limb Sounder (MLS) instrument provides a nearly continuous global (82°S–82°N) record of measurements dating back to August 2004. In 2021, de-seasonalized tropical (15°S–15°N) WV anomalies from *Aura* MLS were positive (wet) for all but one month of the year in the lowermost stratosphere at 82 hPa (~17 km; Fig. 2.59b). These WV anomalies ranged from −0.02 ppm (parts per million, i.e., μmol mol^{-1}) in June to +0.6 ppm in November, corresponding to deviations from the climatological monthly mean of −1% and +16%, respectively.

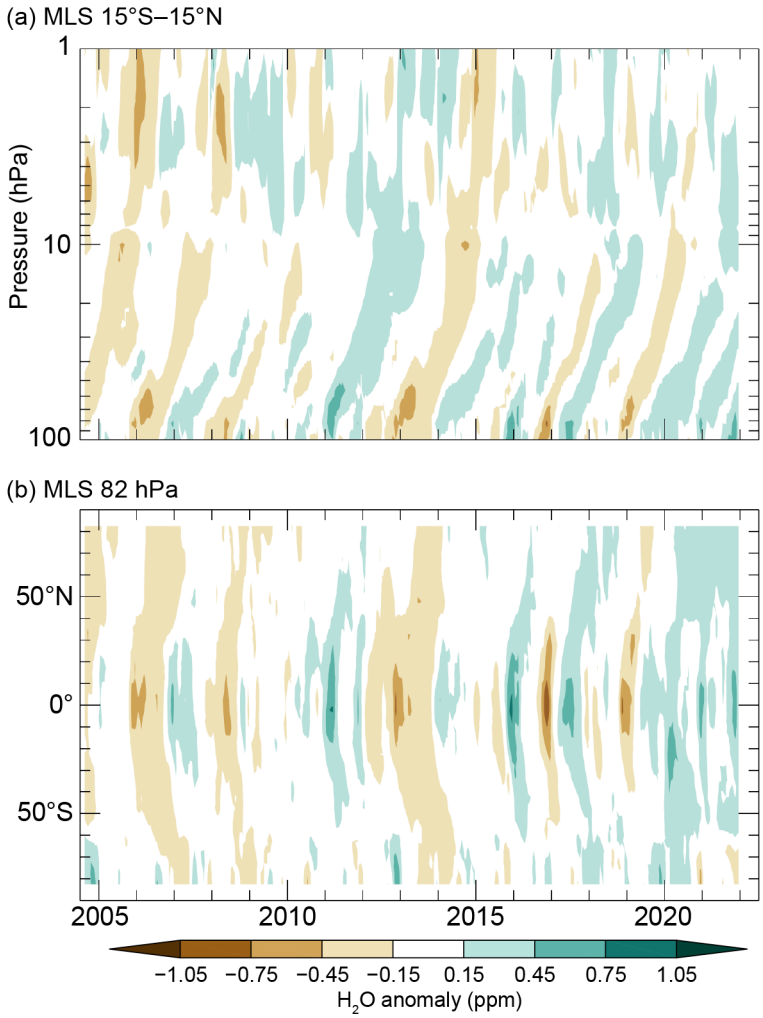

Fig. 2.59. (a) Time series of vertical profiles of tropical (15°S–15°N) lower stratospheric water vapor (WV) anomalies and (b) latitudinal distributions of WV anomalies (ppm) at 82 hPa. Both are based on version 5.0 *Aura* MLS data. Anomalies are differences from the mean 2004–20 WV mixing ratios for each month. (b) Propagation of tropical lower stratospheric WV anomalies (ppm) to higher latitudes in both hemispheres as well as the influences of dehydrated air masses from the Antarctic polar vortex as they are transported toward the SH midlatitudes at the end of each year. Tick marks denote the beginning of each year.

The tropical WV anomalies ascend in the so-called "tropical tape recorder" (i.e., the height–time plot of tropical-average WV showing the imprint of TTL temperatures on WV entering the stratosphere [Mote et al. 1996]) as illustrated in Fig. 2.59a, which shows a wet anomaly beginning around the middle of 2021 at 100 hPa and ascending for the duration of the year. At 100 hPa, the de-seasonalized tropical WV anomalies for August 2021 (+0.4 ppm, 8% above average) and September 2021 (+0.5 ppm, +11%) were the wettest over the MLS record for their respective months. In the following months, the strong positive anomalies were observed at the next highest MLS levels (82 hPa and 68 hPa) as the air ascended into the stratosphere as part of the mean meridional overturning circulation. The 82-hPa level had its wettest October on record (+0.4 ppm, +10%) in 2021, as did November (+0.4 ppm, +9%) and December (+0.4 ppm, +10%) at the 68 hPa level. The progression of these strong wet anomalies is illustrated further in Fig. 2.60, which shows maps of the anomalies as they propagate upward. In addition to propagating upwards, the 2021 tropical

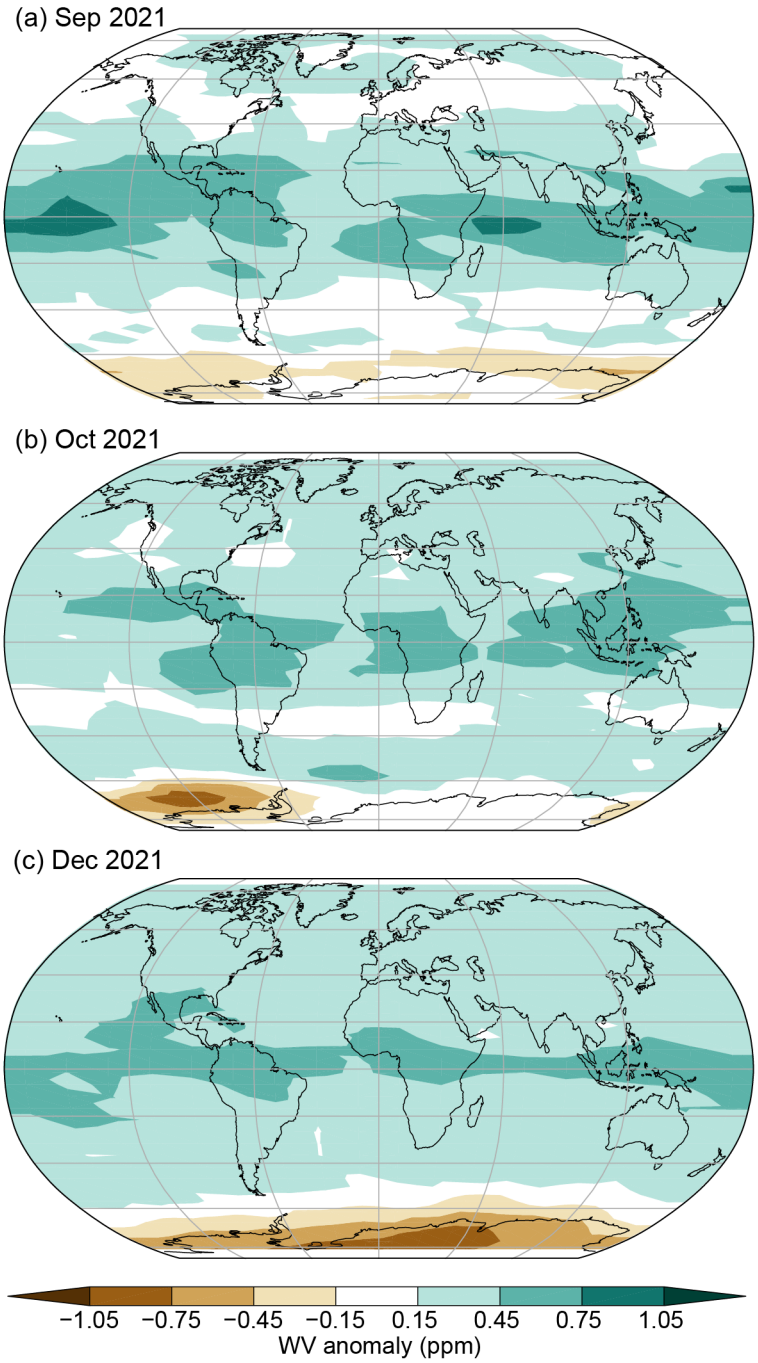

Fig. 2.60. Deseasonalized monthly lower stratospheric *Aura* Microwave Limb Sounder (MLS) version 5.0 anomalies (ppm; 2004–20 base period) at (a) 100 hPa in Sep 2021, (b) 82 hPa in Oct 2021, and (c) 68 hPa in Dec 2021.

WV anomaly exhibits a typical "U-shaped" behavior with time in the latitude–time plane at 82 hPa, as the anomalies propagate poleward in each hemisphere (Fig. 2.59b).

The behavior of lowermost stratospheric WV, observed by *Aura* MLS, is broadly consistent with balloon-borne frost point hygrometer soundings at five locations, as shown in Fig. 2.61. The newest version 5.0 of the MLS data, as well as the previous 4.2 version, are included in this figure to illustrate the reduction in drift relative to the frost point (FP) data in the newest version 5.0 data. Although the drift is not completely removed, the 2021 WV anomalies in v5.0 data are ~0.1 ppm less than in v4.2 for most sites. At the tropical stations, the WV anomalies are highly correlated with the tropical CPT temperature anomalies, as expected.

In 2021, the tropical CPT temperatures were anomalously high throughout the entire year, with an annual mean anomaly of +0.77K. It is well established that interannual variations in CPTs are correlated with interannual variability in climate phenomena such as the El Niño-Southern Oscillation (ENSO) and the quasi-biennial oscillation (QBO) in equatorial stratospheric winds (Dessler et al. 2014).

La Niña conditions were present for all months of 2021, except June and July (see section 4b). In boreal winter, La Niña is known to result in weaker tropical lower stratospheric upwelling, anomalously higher CPTs, and enhanced water vapor in the tropical lower stratosphere (e.g., Garfinkel

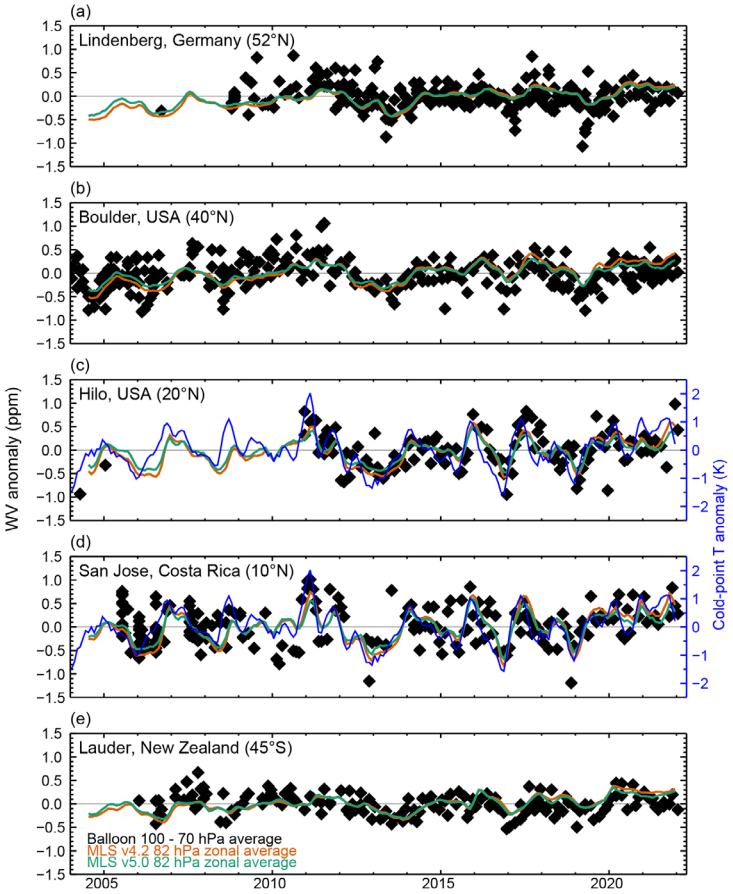

Fig. 2.61. Lower stratospheric water vapor (WV) anomalies (ppm) over five balloon-borne frost point (FP) hygrometer stations. (a–e) each shows the lower stratospheric anomalies of individual FP soundings (black) and of monthly zonal averages for versions 4.2 (orange) and 5.0 (green) of Microwave Limb Sounder (MLS) data at 82 hPa in the 5° latitude band containing the FP station (orange). The new MLS v5.0 data includes a correction for a drift contained in the earlier version 4.2 data (Hurst et al. 2016; Livesey et al. 2021), which were used in previous *State of the Climate* reports (e.g., Davis et al. 2021). High-resolution FP vertical profile data were averaged between 70 hPa and 100 hPa to emulate the MLS averaging kernel for 82 hPa. Each MLS monthly zonal mean was determined from 2000–3000 profiles. Anomalies for MLS and FP data are calculated relative to the 2004–20 period for sites except for Lindenberg (2009–21) and Hilo (2011–21). Tropical CPT anomalies based on the MERRA-2 reanalysis (d, blue curve), which are generally well correlated with the tropical lower stratospheric WV anomalies, are the driving force behind the variations in tropical WV during 2021.

et al. 2021). The positive anomalies in tropical lower stratospheric WV at the beginning of 2021 and again at the end of the year are consistent with the known behavior associated with La Niña.

Equatorial winds from the Singapore radiosonde wind data, which are a commonly used proxy for the QBO phase, were westerly at 50 hPa throughout 2021, until shifting to easterly in December. The QBO westerly phase is associated with anomalously weak tropical upwelling and anomalously high temperatures. Thus, although no formal attribution is attempted here, the combination of a La Niña phase and QBO westerlies likely contributed to the anomalously high CPTs and enhanced tropical lowermost stratospheric WV in 2021.

6. TROPOSPHERIC OZONE—O. R. Cooper, J. R. Ziemke, and K.-L. Chang,

Tropospheric ozone is a short-lived climate forcer that either originates naturally in the stratosphere or is produced in situ by photochemical reactions involving sunlight and precursor gases, such as nitrogen oxides (NO_x), non-methane volatile organic compounds, methane, and carbon monoxide (Archibald et al. 2020). Tropospheric ozone has a strong seasonal cycle that peaks in either spring or summer in response to the regional availability of sunlight, ozone precursors, and long-range transport (Cooper et al. 2014). Ozone precursors can originate naturally from wildfires, biogenic hydrocarbon emissions, lightning NO_x, and biogenic NO_x emissions from soils, and also from anthropogenic sources such as fossil fuel and biofuel combustion or crop burning. Tropospheric ozone also acts as a pollutant near the surface, impacting human health and vegetation (Fleming et al. 2018; Mills et al. 2018).

Long-term trends of tropospheric ozone were recently assessed by the IPCC (Gulev et al. 2021; Naik et al. 2021). An ensemble of chemistry-climate models indicates that the tropospheric ozone burden (TOB) has increased by 45% since 1850. The model-estimated present-day TOB of 347 ± 28 Tg agrees well with the observed value of 338 ± 6 Tg determined from satellite products and ozonesondes. An observation-based quantification of TOB is not possible prior to 1998 due to insufficient global coverage by satellites and ozonesondes (Gaudel et al. 2018). However, model estimates of a constant global increase of tropospheric ozone since the 1950s are consistent with the observed increase since the mid-1990s (Tarasick et al. 2019).

Combined *Aura* Ozone Monitoring Instrument (OMI) and Microwave Limb Sounder (MLS) satellite ozone measurements (OMI/MLS) indicate increasing TOB since the record began in 2004 (Ziemke et al. 2019). In 2021, broad regions of positive tropospheric column ozone (TCO) anomalies were found in the NH midlatitudes (~1.2 DU; 4%), with smaller anomalies of ~1 DU or less elsewhere (Plate 2.1y). Hemispheric and global TOB and their 95% confidence levels for 2021 were 159 ± 6 Tg (0°–60°N), 148 ± 8 Tg (0°–60°S), and 307 ± 10 Tg (60°S–60°N). Globally (60°S–60°N), the 2004–21 TOB increase was 1.48 ± 0.40 Tg yr^{-1}, or ~9% (Fig. 2.62). Spatially, the trends are overwhelmingly positive,

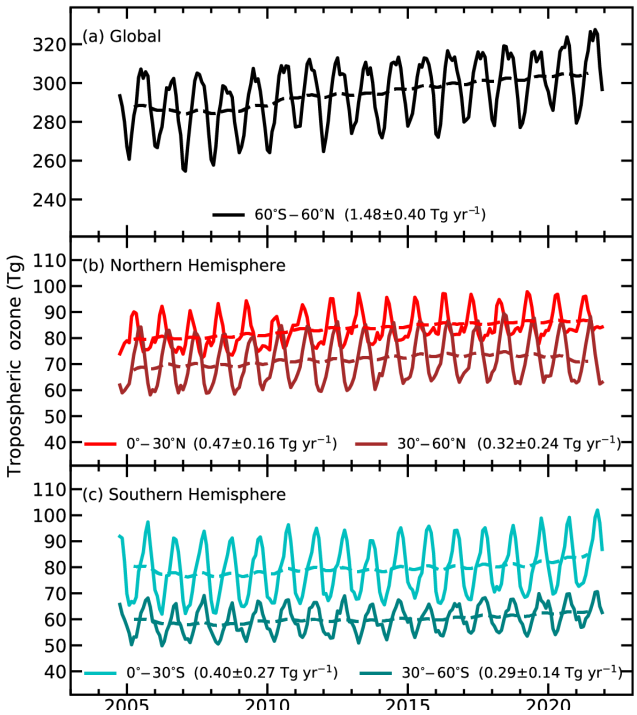

Fig. 2.62. Monthly averages (solid lines) and 12-month running means (dashed lines) of OMI/MLS tropospheric ozone burdens (Tg) from Oct 2004 through Dec 2021. (a) 60°S–60°N monthly averages with 12-month running mean, (b) monthly averages and running means for the NH tropics and midlatitudes, and (c) monthly averages and running means for the SH tropics and midlatitudes. Slopes of linear fits to the data are presented with their 95% confidence-level uncertainties. Vertical resolution of OMI/MLS monthly TCO is ~3 km about the tropopause with ~2 DU (7%) precision regionally; trend uncertainties are about 0.5 DU decade^{-1} (1.5% decade^{-1}).

reaching ~+3.2 DU decade^{-1} (~+1% yr^{-1}) east of China and Southeast Asia (Fig. 2.63), consistent with model simulations of increasing fossil fuel emissions from Southeast, East, and South Asia (Y. Zhang et al. 2016; Ziemke et al. 2019) and also consistent with ozone trends since the mid-1990s based on in situ observations in the boundary layer and free troposphere (Gaudel et al. 2020; Chang et al. 2022). Models indicate that ozone produced in these areas is transported northward and eastward in the free troposphere over the North Pacific Ocean (Zhang et al. 2020) as supported by the trend patterns in Fig. 2.63. Positive trends in the SH extra-tropics have been linked to a broadening of the Hadley circulation (Lu et al. 2018).

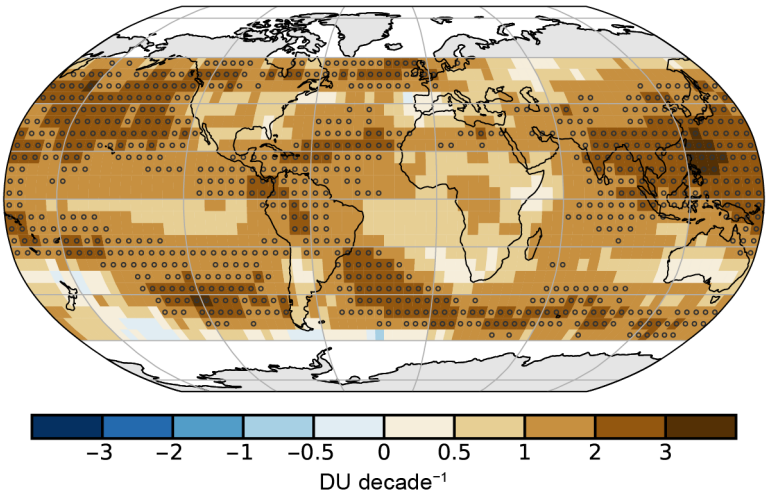

Fig. 2.63. Linear trends in OMI/MLS tropospheric column ozone (DU decade^{-1}) on a 5° × 5° grid from Oct 2004 through Dec 2021. Circles denote trends with *p*-values < 0.05. Trends were calculated using a multivariate linear regression model (e.g., Randel and Cobb 1994 and references therein) that included a seasonal cycle fit and the Niño 3.4 index as an ENSO proxy; trend uncertainties included autoregressive adjustment via Weatherhead et al. (1998).

At the surface, six baseline sites are available for quantifying multi-decadal ozone trends through the end of 2021 (Fig. 2.64; Table 2.11). At northern high latitudes, ozone increased at a rate of 0.57 ± 0.33 ppbv decade^{-1} since 1973 at Barrow Observatory, but decreased by 2.43 ± 0.97 ppbv decade^{-1} since 2000 at Summit, Greenland. At northern midlatitudes, ozone decreased by 0.96 ± 1.22 ppbv decade^{-1} since 1988 at Tudor Hill, Bermuda, but with large fluctuations. Mauna Loa Observatory, Hawaii, is located at the interface of the tropics and northern midlatitudes, allowing the ozone record to be split into mutually exclusive times series representing moist air (primarily a tropical origin) and dry air (primarily a midlatitude origin). Ozone in the MLO dry air (midlatitude) increased by 2.04 ± 0.41 ppbv decade^{-1} since 1974, while ozone in the MLO moist air (tropical) increased by 1.00 ± 0.38 ppbv decade^{-1}. In the southern high latitudes ozone at Arrival Heights, Antarctica has changed little since 1996. The trend at the South Pole, the most remote location on Earth, is +0.36 ± 0.37 ppbv decade^{-1} since 1975. While these data provide a range of trends at remote locations, they are too sparse to provide a global mean surface trend, and surface trends do not necessarily reflect trends in the free troposphere (Cooper et al. 2020).

Recent ozonesonde, lidar, and FTIR observations show a small ozone decrease in the NH mid- and lower troposphere (1–8 km) in 2020 in response to ozone precursor emissions reductions associated with the COVID-19 pandemic (Steinbrecht et al. 2021; Miyazaki et al. 2021). The decrease was strongest in the northern midlatitudes, with reductions of 5–6% above Europe and western North America (Chang et al. 2022). Future assessments will determine if this decrease was a temporary fluctuation or if it will have a long-term impact on the TOB trend.

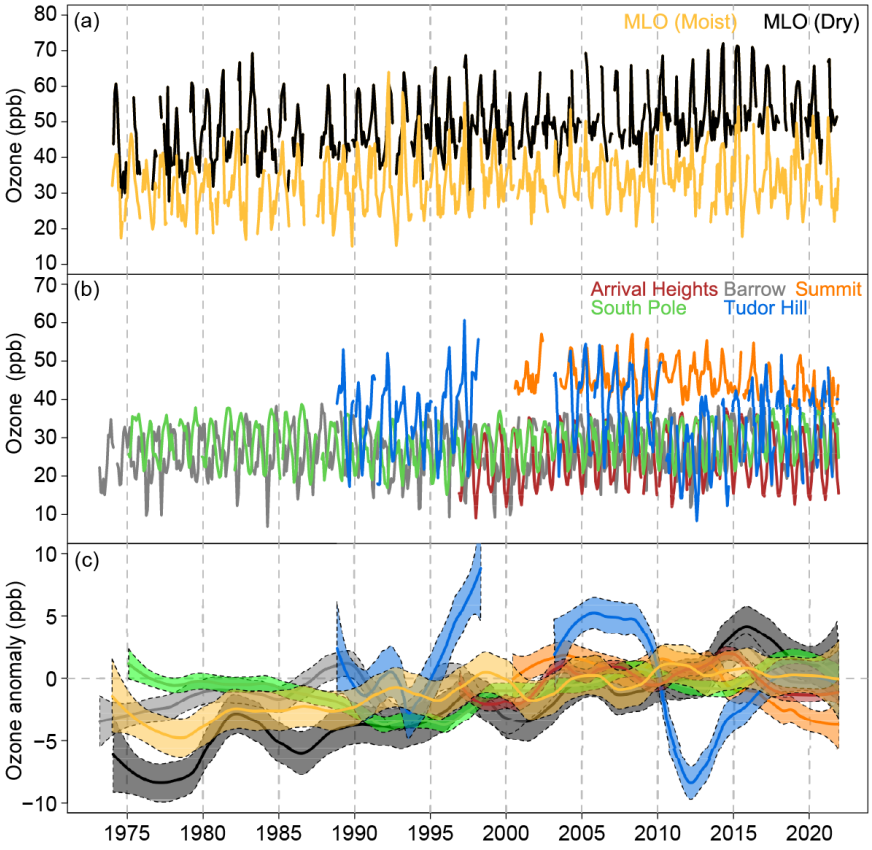

Fig. 2.64. (a) Nighttime monthly mean ozone values (ppb) at Mauna Loa (MLO), split into mutually exclusive times series, representing moist air (yellow, primarily a tropical origin) and dry air (black, primarily a midlatitude origin) based on observed relative humidity values (Gaudel et al. 2018). (b) Monthly mean surface ozone (ppb) at Barrow Observatory, Alaska (gray), Summit, Greenland (orange), Tudor Hill, Bermuda (blue), Arrival Heights, Antarctica (red), and South Pole (green). Monthly means are produced for months with at least 50% data availability, using observations from all 24 hours of the day. The locations of each site are listed in Table 2.11. (c) The same time series after conversion to monthly anomalies referenced to the monthly climatological values over 2000–20 and smoothed variability based on the LOWESS (locally weighted scatterplot smoothing) regression.

Table 2.11. Ozone trends at the six baseline monitoring sites shown in Fig. 2.64. Trends are estimated by the generalized least squares method, based on monthly anomalies referenced to the monthly climatological values over the period 2000–20 (Chang et al. 2021) and reported with 95% confidence intervals and *p*-values.

Site name Latitude, longitude, elevation (m)	Years with data	trend, ppbv decade^{-1}	*p*-value
Summit, Greenland 72.6°N, 38.5°W, 3238 m	2000–present	–2.43 ± 0.97	$p<0.01$
Barrow, Alaska 71.3°N, 156.6°W, 11 m	1973–present	0.57 ± 0.33	$p=0.00$
Tudor Hill, Bermuda 32.3°N, 64.9°W, 30 m	1988–98, 2003–present	–0.96 ± 1.22	$p=0.12$
Mauna Loa Observatory (MLO), Hawaii 19.5°N, 155.6°W, 3397 m	1973–present	2.04 ± 0.41 (dry air) 1.00 ± 0.38 (moist air)	$p<0.01$ $p<0.01$
Arrival Heights, Antarctica 77.8°S, 166.8°W, 50 m	1996–present	0.34 ± 0.59	$p=0.25$
South Pole, Antarctica 90.0°S, 59.0°E, 2840 m	1975–present	0.36 ± 0.37	$p=0.05$

7. CARBON MONOXIDE—J. Flemming and A. Inness

Carbon monoxide (CO) is emitted into the atmosphere by incomplete combustion from anthropogenic sources and from wildfires. The chemical production of CO in the atmosphere from formaldehyde as part of the oxidation chains of methane (CH_4), isoprene, and other volatile organic trace gases (Stein et al. 2014) is larger than these admissions. Oxidation of CO with the hydroxyl radical (OH) is the main loss process for CO. The greater abundance of OH in summer is a main driver for the typical CO seasonal cycle that peaks in boreal and austral winter. Carbon monoxide is an indirect short-lived climate forcer because it is an important precursor for tropospheric ozone (Szopa et al. 2021; section 2g6) and because it impacts OH, which controls the lifetime of CH_4.

Carbon monoxide concentrations doubled between the 1850s and the 2000s based on model studies (Griffiths et al. 2020). Based on a limited number of ice core samples, Northern Hemisphere (NH) CO levels were the highest (around 160 ppb) in the 1970s (Petrenko et al. 2013) but later declined by 30 ppb to 130 ppb by 2008. Surface CO concentrations have been measured as part of the global atmospheric watch (GAW) network using in situ sensors and flask observations in a routine way by NOAA's Global Monitoring Laboratory and other agencies since the 1990s (WMO 2021a). Tropospheric CO is observed, in situ, by the In-service Aircraft for a Global Observing System (IAGOS) aircraft observation program (Nédélec et al. 2015) and the Network for the Detection of Atmospheric Composition Change (NDACC; De Mazière et al. 2018) of ground-based remote sensing Fourier Transform Infrared Spectroscopy (FTIR) instruments, which provides atmospheric CO profiles. The advent of CO satellite sensors measuring CO in the early 2000s allowed more detailed monitoring of the global CO burden (Worden at al. 2013; Yin et al. 2015; Bucholz et al. 2021) in particular by assimilating these observations in atmospheric composition reanalyses (Flemming et al. 2017; Gaubert et al. 2017; Inness et al. 2019). The trend of the CO burdens and CO surface concentrations since the early 2000s varies spatially, but there is qualitative agreement between satellite-derived trends in CO burden and surface trends obtained from background in situ observations: the NH shows a decline of CO varying between 0.3% and 1.3% yr^{-1}, while SH values did not change significantly (Szopa et al. 2021).

Figure 2.65a shows a time series of the monthly global burden of CO from CAMS reanalysis for the period 2003–21. The total CO burden has reduced by 1.4 Tg yr^{-1} (based on a linear trend), and piecewise trends for the periods 2003–07, 2008–09, and 2009–21 are –3.1, –14.3, and 0.0 Tg yr^{-1} (Flemming and Inness 2018).

The spatial distribution of the annual CO anomalies, with respect to the period 2003–21, is shown in Plate 2.1z. Stronger-than-usual wildfire activity in northeastern Russia, starting in summer 2021 led to a widespread positive CO anomaly in mid- and higher latitudes of the NH, which was further increased by active wildfires in Canada and the western United States in August. This led to the highest monthly mean CO burdens in the Arctic region (60°–90°N) for the period covered by the CAMS reanalysis (Fig. 2.65b). Positive anomalies also occurred over India, caused by intensive agricultural waste burning in January and February. La Niña conditions in the tropical Pacific resulted in a pronounced negative CO anomaly over maritime Southeast Asia in the autumn period due to lower-than-normal biomass burning (Inness et al. 2015).

CAMS produced a retrospective analysis of CO, aerosols, and ozone for the period 2003–21 by assimilating satellite retrievals of atmospheric composition with the ECMWF model (Inness et al. 2019). The CAMS reanalysis-assimilated thermal infrared (TIR) total column CO retrievals (V6 from 2003 to 2016, near-real-time (NRT) V7 from January 2017 to June 2019, NRT V8 from July 2019 onward) from the MOPITT instrument (Deeter et al. 2014, 2017, 2019) globally, only excluding observations poleward of 65°N/S, using the ECWMF 4D-VAR data assimilation system. Anthropogenic emissions were taken from the MACCity inventory (Granier et al. 2011) that accounts for projected emission trends according to the IPCC Representative Concentration Pathway 8.5 scenario, but COVID-19 related emissions modifications were not applied. Biomass burning emissions (section 2h3) were taken from the Global Fire Assimilation System (v1.2; Kaiser et al. 2012) that is based on

MODIS fire radiative power retrievals (Giglio et al. 2016). A monthly mean climatology of biogenic emissions was taken from the MEGAN2.1 model following Sindelarova et al. (2014).

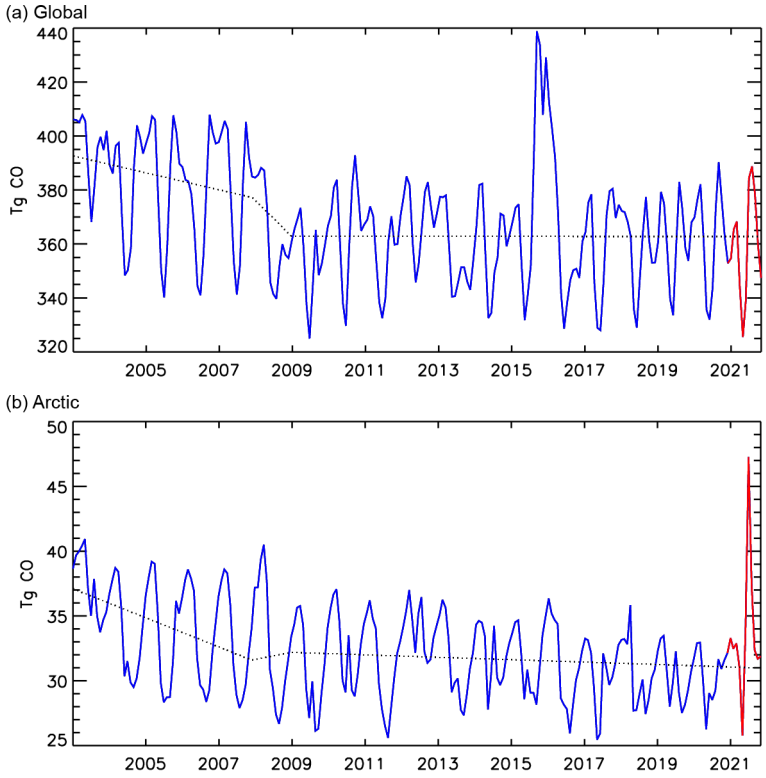

Fig. 2.65. Time series of the mean burden of CO for the (a) globe and (b) Arctic from the CAMS reanalysis and a piecewise linear trend for the periods 2003–07, 2008, and 2009–20.

h. Land surface properties

1. LAND SURFACE ALBEDO DYNAMICS—G. Duveiller and N. Gobron

The land surface was predominantly darker than normal during 2021 compared to the 2003–20 baseline in terms of visible broadband white-sky albedo and normal for near-infrared albedo (see Plates 2.1ac and 2.1ad, respectively). The patterns of surface albedo largely follow the dynamics of snow cover and vegetation dynamics, and 2021 was no exception. Several regions across the world had brighter surfaces due to above-average snow cover in either the beginning of the year (south/central United States, Spain, large parts of northern Europe), the end of the year (northwestern America and easternmost Russia, parts of the Tibetan plateau), or both (northeastern China). Lack of snow darkened the overall surface albedo in central North America and Quebec, Canada, in southeastern Europe, and in various parts of Russia (section 2c5). Where vegetation is greener (positive FAPAR anomalies; section 2h2), its contributions darken the surface overall by reducing the visible albedo, while near-infrared albedo rises slightly as denser vegetation scatters more light in this part of the spectrum. However, an exception to this case appeared in southern Africa where a decrease in near-infrared albedo occurred despite the increase in vegetation, possibly due to anomalously wet conditions. In contrast, the strong soil moisture deficit associated with the drought in the La Plata basin (section 2d10) resulted in an increase in visible albedo due to the drier conditions.

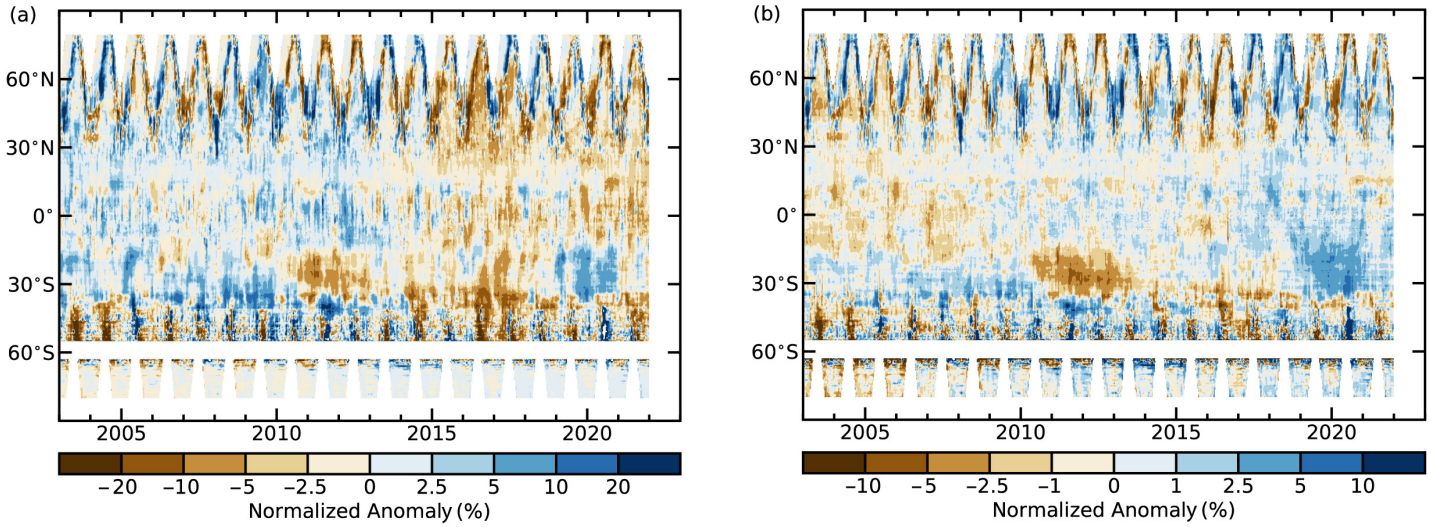

Fig. 2.66. Zonally averaged (a) white sky visible and (b) near-infrared albedo anomalies (%) for the period 2003–21 using a 2003–20 base period.

Surface albedo also largely follows the trends of decreasing snow cover observed in the past years (Figs. 2.66, 2.67). Also, as higher temperatures and CO_2 fertilization increase vegetation cover, the surface darkens considerably in terms of visible albedo and brightens slightly in terms of near-infrared albedo. The year 2021 seems to confirm that this general trend is also applicable to visible albedo anomalies in the Southern Hemisphere, when a return to negative values was observed after two years of positive values.

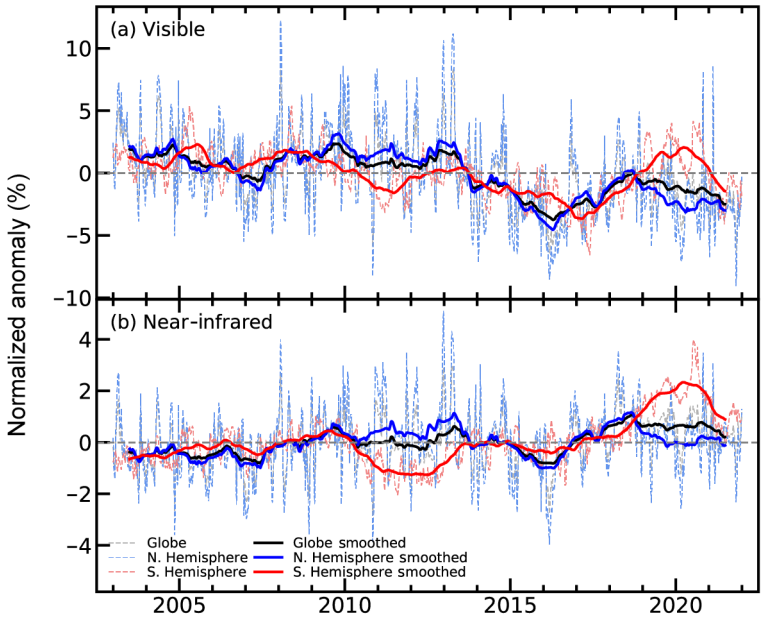

Fig. 2.67. Global (black lines), NH (blue), and SH (red) land surface (a) visible and (b) near-infrared albedo anomalies (%) for the period 2003–21 using a 2003–20 base period. Dotted lines denote each monthly period; solid lines indicate the 6-month running averaged mean.

This analysis is based on satellite records of visible and near-infrared white-sky albedo estimated from the Moderate Resolution Imaging Spectroradiometer (MODIS) instrument onboard the *Aqua* and *Terra* satellite platforms (Schaaf et al. 2002). White-sky albedo, also known as bihemispherical reflectance, is defined as the fraction of radiation that is reflected in the absence of a direct radiation component and when the diffuse radiation component is isotropic. Various studies have shown that these products well-represent ground properties, whether it is ice sheets (Stroeve et al. 2013) or vegetation (Cescatti et al. 2012). The baseline reference period is 2003–20, covering the extent of the MODIS record where data from both satellite platforms (*Terra* and *Aqua*) are available.

2. TERRESTRIAL VEGETATION DYNAMICS—N. Gobron

The fraction of absorbed photosynthetically active radiation (FAPAR) is used to track the overall land productivity associated with atmospheric CO_2 fixation. FAPAR anomalies in 2021 relative to the 1998–2020 mean show large surface variations, in terms of values and coverage, of vegetation productivity worldwide (Plate 2.1ae).

The greatest negative anomalies occurred over Central Asia, which had a record heatwave (see section 7g). The African continent also had strong negative anomalies in the east, over Somalia and Kenya, which were present during the entire year but strongest at the end of the year. To a lesser extent, the western coast from the Tropic of Capricorn to Nigeria also experienced numerous extreme events, with both droughts and floods that resulted in lower-than-average FAPAR. Negative anomalies were also present over far southern Africa and the southern half of Madagascar due to persistent drought inducing crop losses and other vegetation cover. The North American continent showed several negative hot-spots, including Montana, North Dakota, and Saskatchewan and along the Pacific coast, from California to Oregon, due to a series of wildfires that resulted from an exceptional heatwave and drought. Northeastern South America had low FAPAR in Guyana and Suriname. Small in extent but still significant, the Brazilian states of Rio Grande and Paraiba, Parque del Gran Chaco Kaa-Lya also had below-average FAPAR in 2021. Over Australia, Nullarbor Plain and a zone from Adelaide to Queensland, had low FAPAR. Over Alaska and northeastern Russia, with highest record temperatures during summer, there was below-average photosynthetic activity.

The most noticeable positive anomalies, most likely due to heavy rain linked to La Niña, took place in Botswana and northeastern Namibia, as well as eastern South Sudan. To a lesser extent, further positive anomalies in Africa were seen over the belt of humid savannas in the Sahel, from Liberia, Côte d'Ivoire, Ghana, Togo, and the south of Chad. These positive events were also enhanced by high precipitation totals over these regions (see section 2d4). In South America, positive anomalies occurred over regions such as northwestern Venezuela, the state of Marahnao (Brazil), and Argentina over La Mesopotamia and La Pampa. Southwestern Europe—comprised of Portugal, Spain, France, and around Moldova—had positive anomalies. A large part of northwestern Russia, mainly covered by tundra, also had positive anomalies. A large positive anomaly occurred over New South Wales and southern Queensland in Australia due to heavy precipitation in 2021, and another affected Malaysia.

Figure 2.68 shows the latitudinal anomalies average from 1998 to 2021 compared to the base period 1998–2020. In 2021, the positive behavior extended globally, with the exception of a few locations, highlighting the greenness of the terrestrial surfaces. The Southern Hemisphere (SH) was affected by strong negative anomalies, i.e., below −0.03, from 2002 to 2014, except in 2010–12, for which vegetation had recovered from severe and persistent droughts (Gobron and Belward 2011) and slightly negative anomalies in 2019/20. Fig. 2.69 shows the global and hemispherical anomalies, with more seasonal variability in the SH than in the Northern Hemisphere (NH). Global seasonal anomalies have been positive since 2013, following the NH trend. SH was generally positive but with monthly negative events during its summer period, e.g., 2015/16; 2018/19; 2019/20, and 2020/21. SH data reveal two positive extreme peaks in 2000 and 2017, while the lowest values occurred in 2008/09. The NH experienced fewer extreme negative events, e.g., values below −0.03, compared to the SH. In 2021, only positive FAPAR anomalies were recorded for both SH and NH averages.

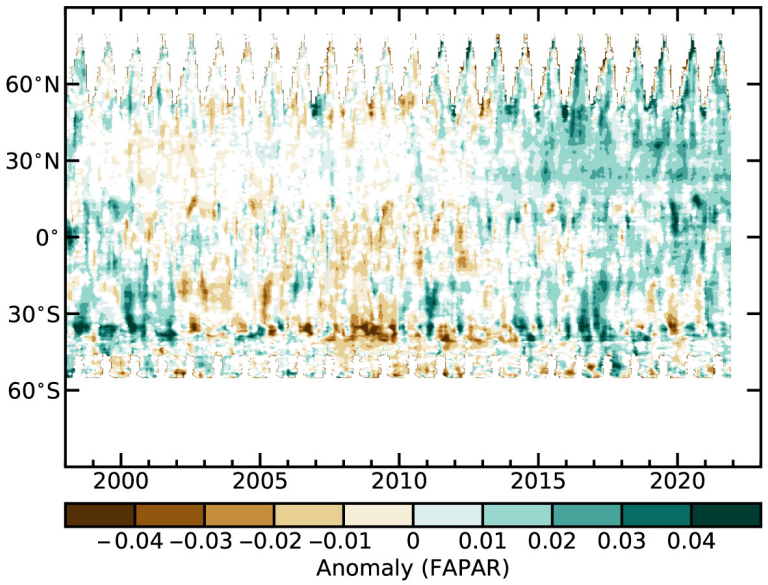

Fig. 2.68. Zonally averaged fraction of absorbed photosynthetically active radiation (FAPAR) anomalies for the period 1998–2021 (1998–2020 base period).

Earth observations are important for monitoring the terrestrial photosynthetic activity worldwide. They are used to infer FAPAR, an essential climate variable (as defined by GCOS [2016]). The 2021 study merged 24 years of global FAPAR monthly products based on three optical sensors from 1998 to 2021 (Gobron et al. 2010; Pinty et al. 2011; Gobron and Robustelli 2013). Uncertainties of each dataset were derived through various means, such as error propagation technique and comparisons against multiple proxies using ground measurements and radiative transfer simulations, that all provide an estimate of the uncertainties and biases. This long-term FAPAR dataset presents an estimated global average uncertainty close to 5%–10% when comparing to ground-based measurements.

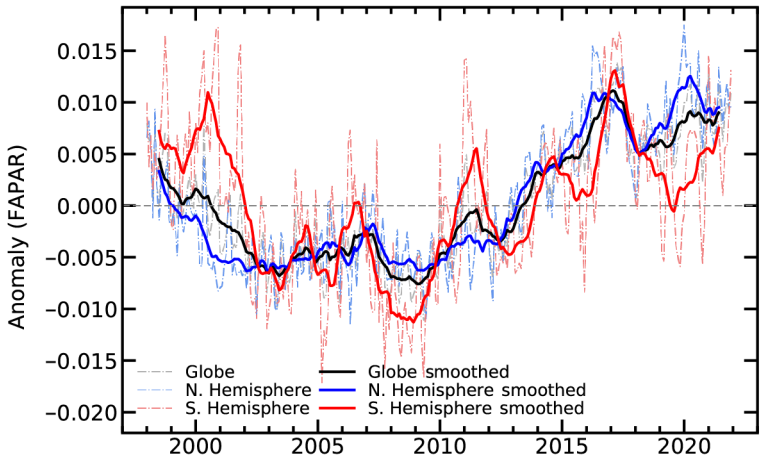

Fig. 2.69. Global (black/gray lines), Northern Hemisphere (blue), and Southern Hemisphere (red) fraction of absorbed photosynthetically active radiation (FAPAR) anomalies for the period 1998–2021 (1998–2020 base period). Dotted lines denote each monthly period; solid lines indicate the 6-month running averaged mean.

3. BIOMASS BURNING—

J. W. Kaiser and G. R. van der Werf

The year 2021 illustrated how two distinct trends that have emerged in global biomass burning over the last decade shaped current pyrogeography: a declining trend in many savanna regions related to agricultural expansion and an increasing trend in many forested regions where climate change has increased the flammability of the landscape. On one hand, 2021 was the fourth-lowest fire year in the Global Fire Assimilation System (GFAS) record (1837 Tg C; 11% below the 2003–20 average; Table 2.12; global map shown in Fig. 2.70), and fire activity in tropical Asia was the lowest since at least 2003. On the other hand, 2021 saw extreme regional fire activity in boreal North America and Siberia, as well as the western United States. After the extreme fires of 2019 and 2020 in the Arctic Circle and southeastern Australia, fire activity in these regions was again near and below average, respectively.

Table 2.12. Annual continental-scale biomass burning budgets in terms of carbon emission (Tg C yr^{-1}). (Source: GFASv1.4.)

Time Period		2003–20	2021	
Quantity Tg C yr^{-1}		Mean value (Range)	Value	Anomaly (%)
Global		2062 (1781–2421)	1837	−225 (−11%)
North America	30°–75°N 190°–330°E	85 (57–114)	114	+28 (+33%)
Central America	13°–30°N 90°–330°E	52 (38–72)	46	−6 (−12%)
South America	13°S–60°N 190°–330°E	368 (242–537)	316	−52 (−14%)
Europe and Mediterranean	30°–75°N 330°–60°E	42 (28–72)	34	−9 (−21%)
N. Hem. Africa	0°–30°N 330°–60°E	421 (308–494)	372	−49 (−12%)
S. Hem. Africa	0°–35°S 330°–60°E	477 (429–532)	476	−1 (0%)
Northern Asia	30°–75°N 60°–190°E	199 (116–436)	256	+57 (+29%)
South-East Asia	10°–30°N 60°–190°E	122 (86–162)	111	−11 (−9%)
Tropical Asia	10°S–10°N 60°–190°E	166 (37–475)	27	−139 (−83%)
Australia	10°–50°S 60°–190°E	129	86	−43 (−34%)
Arctic	67°–90°N 0°–360°E	8 (1–37)	7	−1 (−9%)
Western United States	30°–49°N 230°–260°E	19 (8–42)	37	+18 (+96%)

Global fire emissions are generally dominated by savanna burning. For example, African fire emissions account for roughly half of total fire carbon emissions, and fires here and in many other savanna regions have decreased over the past decade. This trend is partly driven by agricultural expansion into savanna ecosystems and associated fragmentation of the landscape (Andela et al. 2017). The trend continued in 2021, with Africa north of the equator observing emissions 12% below the 2003–20 average and the seven years with the lowest global fire activity in the GFAS record all occurring since 2013; however, emissions were close to average south of the equator in Africa and thus did not contribute to the trend. Fire activity in tropical Asia, including Indonesia, was the lowest on record (Fig. 2.71); fire activity in this region is strongly modulated by precipitation anomalies associated with the El Niño-Southern Oscillation. Environmental protection policies may also have contributed to the low fire activity.

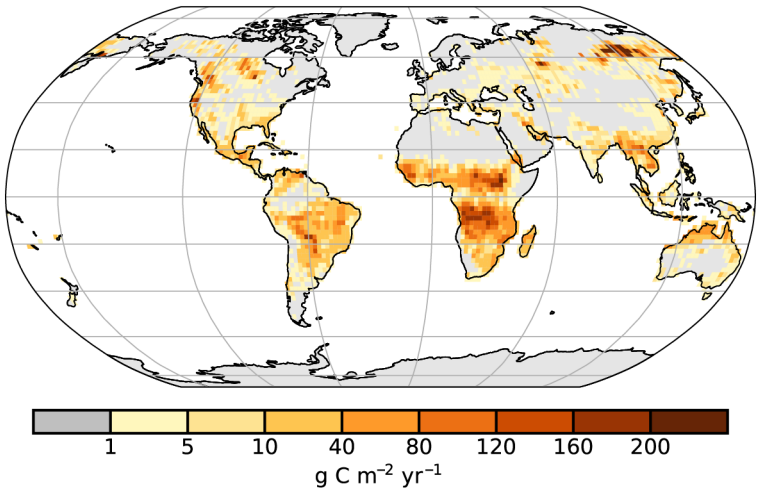

Fig 2.70. Global map of fire activity in 2021 in terms of carbon consumption (g C m^{-2} yr^{-1}). (Source: GFASv1.4.)

At higher latitudes, northern Asia and North America experienced particularly intense fire seasons in 2021, with anomalies of +29% and +33%, respectively. The continental-scale budgets are dominated by boreal fires. Nevertheless, the wildfires in the western United States were second only to those of 2020, consuming twice as much biomass as the long-term average (Fig. 2.71).

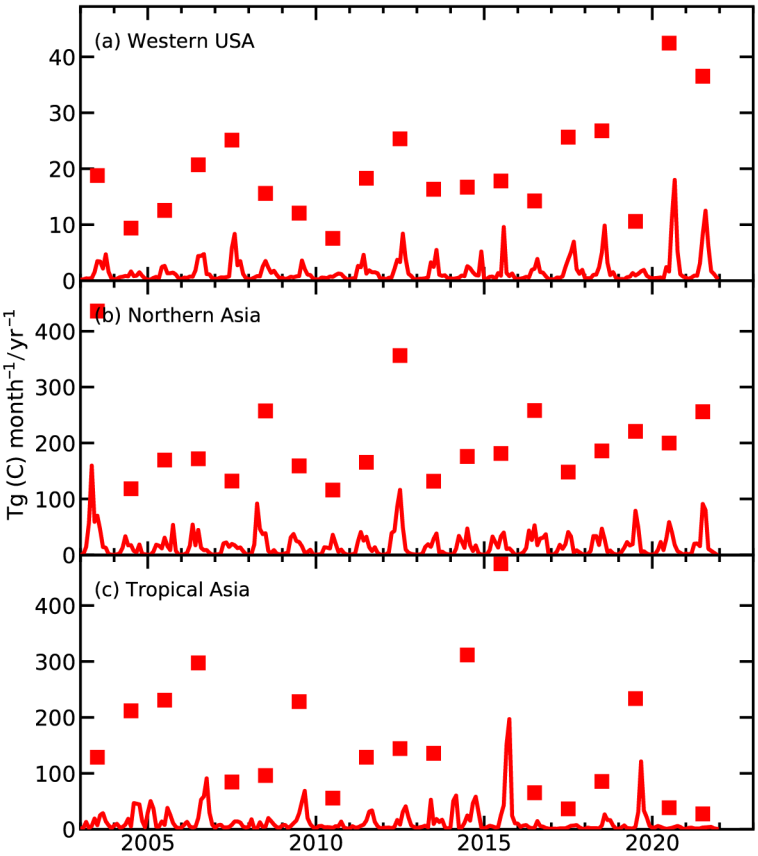

Fig. 2.71. Time series of annual (squares) and monthly (lines) regional fire activity, in terms of carbon consumption for (a) the western United States, (b) northern Asia, and (c) tropical Asia. (Source: GFASv1.4.)

GFAS produces global fire emission estimates in near real-time for the Copernicus Atmosphere Monitoring Service (CAMS; Kaiser et al. 2012). It is based on the MODIS Fire Radiative Power products (Giglio et al. 2016). Here, we use consistent reprocessing with input from MODIS Collection 6 for the entire period of 2003–21. The 14% bias, with respect to Collection 5, has been corrected and the satellite and observation time-specific bias correction factors from Hüser et al. (2018) have been applied for 17 August–2 September 2020 in order to compensate for the outage of observations from MODIS onboard the *Aqua* satellite. The time series in Plate 2.1ae also puts the GFAS time series, which begins in 2003, in the context of GFED4s, which is mostly based on burnt area observation and dates back to 1997 (van der Werf et al. 2017).

4. PHENOLOGY OF PRIMARY PRODUCERS—D. L. Hemming, O. Anneville, Y. Aono, J. Garforth, A. Menzel, J. O'Keefe, T. Park, A. D. Richardson, T. Rutishauser, T. H. Sparks, S. J. Thackeray, A. van Vliet, and Y. Yuan

During 2021, the phenology, of satellite-derived, PhenoCam-derived, terrestrial, and aquatic records, indicate a generally earlier start and longer growing season across the globe relative to the 2000–20 baseline, with the exception of extreme April temperature impacts in Europe. The satellite-derived (MODIS) normalized difference vegetation index (NDVI; Park et al. 2016) across Northern Hemisphere land (NH, > 30°N) revealed earlier mean start of season (SOS_M; –1.8 days) and later end of season (EOS_M, +4.2 days) relative to the baseline (SOS_M = day 135, 15 May and EOS_M = day 283, 10 October; Fig. 2.72). These differences were associated with higher spring (+0.24°C) and autumn (+0.54°C) temperatures from the MERRA-2 reanalysis (Gelaro et al. 2017) and resulted in a 6-day longer growing season in 2021. Regionally, SOS_M occurred earlier across western and

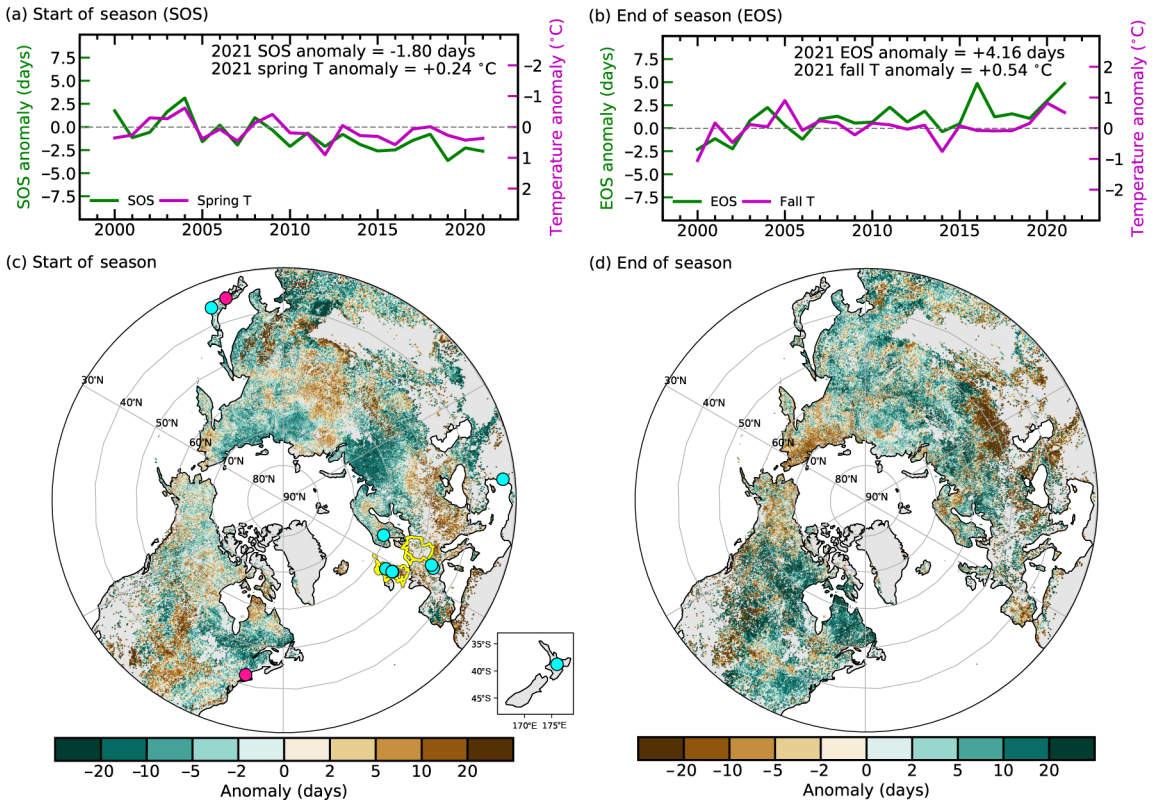

Fig. 2.72. (a) Time series of area-mean anomalies (days relative to 2000–20 baseline) in MODIS NDVI-based vegetation growing season onset (SOSM, green) and MERRA-2 spring (Mar–May, pink) temperature for Northern Hemisphere (> 30°N). (b) Same as (a) but for the end of growing season (EOSM, green) and autumn (Sep–Nov, pink) temperature. Note, temperature scale reversal for panel (a). (c),(d) Spatial pattern of (c) SOSM and (d) EOSM anomalies in 2021 with respect to the baseline. Highlights identify the location of sites shown in Figs. 2.73 and 2.74 and discussed in the text (Country mean phenology data: yellow; site PhenoCam and phenology observations: magenta; lake phytoplankton: blue).

northeastern Eurasia (EA), and northeastern North America (NA) and later across central EA and NA (Fig. 2.72c). A striking earlier SOS_M (–13 days) over western Russia (35°–75°E, 69°–57°N) was associated with an anomalous spring warm spell (+2.7°C). Most EA and NA regions showed a later EOS_M, whereas earlier EOS_M was observed in southwestern EA. The regions displaying early EOS_M were mostly temperate grass and shrublands, which experienced a drier summer and autumn seasons in 2021 (JRC 2021). Two decades of MODIS record show long-term trends of earlier SOS_M and later EOS_M (SOS_M: –1.74 ± 0.42 days decade^{-1}, $p < 0.001$; EOS_M: 1.93 ± 0.47 days decade^{-1}, $p < 0.001$).

PhenoCam data (Seyednasrollah et al. 2019) help link the coarse resolution of satellite-derived phenology with fine resolution visual observations on organisms and ecosystems (Richardson 2019). PhenoCam-derived estimates (2008–21) of SOS (SOS_{PC}) and EOS (EOS_{PC}) at Harvard Forest, a deciduous forest in Massachusetts (United States), were compared with ground observations of red oak (*Quercus rubra*; SOS_{RO} and EOS_{RO}; Richardson and O'Keefe 2009; O'Keefe 2021), and MODIS (SOS_M and EOS_M) for the associated pixel (Figs. 2.73a,b). SOS_{PC} and EOS_{PC} are strongly correlated with SOS_{RO} (r = 0.90) and EOS_{RO} (r = 0.83), and their timings were similar. Although SOS_{PC} and SOS_M were strongly correlated (r = 0.77), SOS_{PC} was later by 12 ± 3 days (Fig. 2.73b). The correlation between EOS_{PC} and EOS_M was weaker (r = 0.58), and EOS_{PC} was earlier by 47 ± 10 days (Fig. 2.73a). In 2021, SOS_{PC}, SOS_{RO}, and SOS_M were 8, 8, and 4 days earlier and EOS_{PC}, EOS_{RO}, and EOS_M were 13, 6, and 11 days later than in 2020 (Figs. 2.73a,b). EOS_{PC} was the latest in the PhenoCam series. All three Harvard Forest records showed a longer growing season in 2021 than 2020, with the PhenoCam showing the largest change where the earlier SOS_{PC} and later EOS_{PC} yielded a growing season that, at 178 days, was three weeks longer than 2020, and 11 days longer than the 2011–20 mean (167 days). First leaf (SOS_{PO}) and leaf falling/bare tree (EOS_{PO}) dates for pedunculate oak (*Quercus robur*) from Germany (D), the United Kingdom (UK), and the Netherlands (NL) are

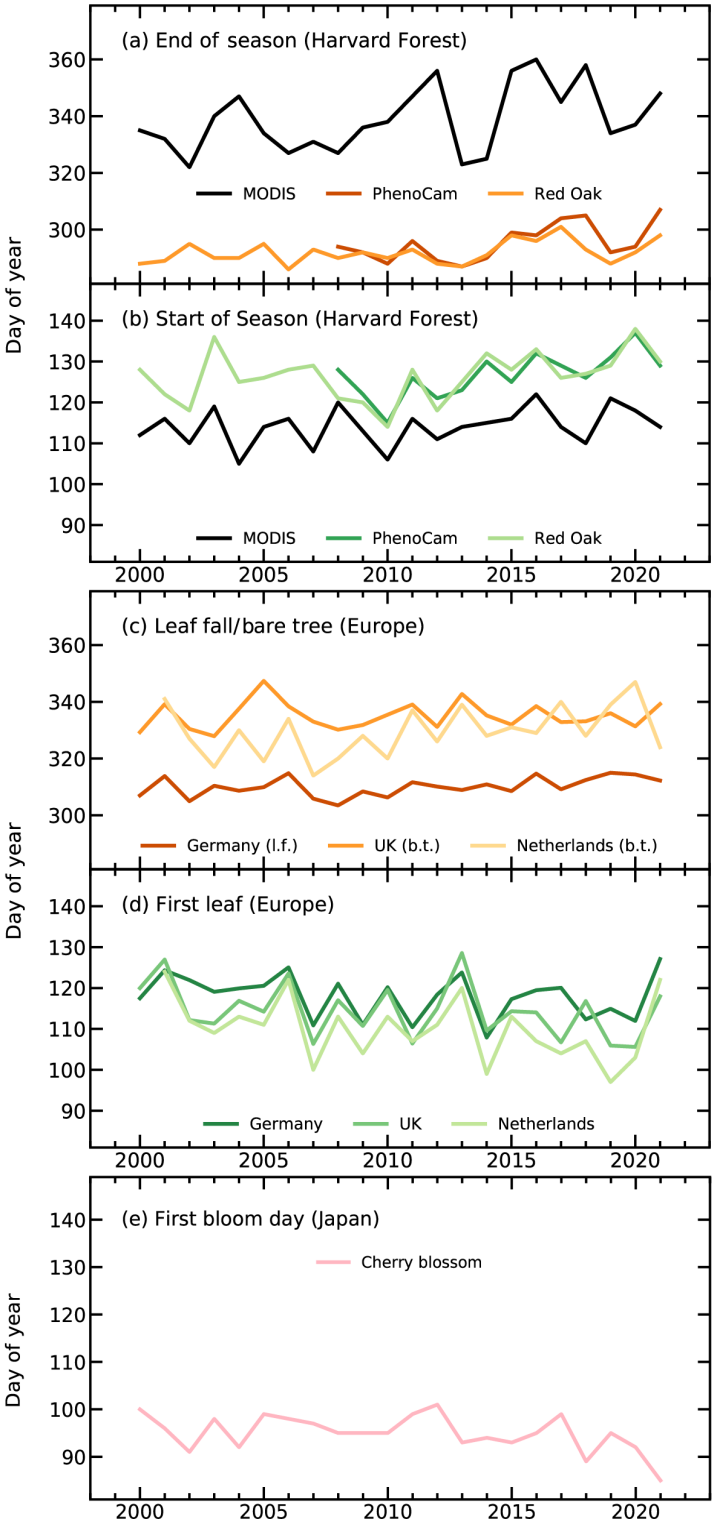

Fig. 2.73. Day of year of spring and autumn vegetation phenology indicators for (a),(b) Harvard Forest, Massachusetts, where (a) start and (b) end of season days are derived from MODIS remote sensing (black), PhenoCam observations and red oak (Quercus rubra) single-tree ground observations (green and orange); (c),(d) Germany, United Kingdom, and the Netherlands, where country-mean first leaf (green) and bare tree or leaf fall (orange) days are derived from ground observations of pedunculate oak (Quercus robur); and (e) Kyoto, Japan, showing first full bloom days for cherry blossom, Prunus jamasakura from ground observations (pink).

presented in Figs. 2.73c,d. The mean SOS_{PO} and EOS_{PO} for the 2000–20 baseline was 27 (D), 24 (UK), and 20 (NL) April, and 5, 30, and 26 November, respectively. Both events were strongly influenced by temperature; in general, it has been shown that SOS_{PO} advances by 4–6 days per °C increase in mean February–April temperature, and EOS_{PO} is delayed 2–4 days per °C increase in September–October temperature (Menzel et al. 2020). April 2021 temperatures were relatively cold in these countries, resulting in SOS_{PO} dates 10 (D), 3 (UK), and 13 (NL) days later than the baseline, while EOSPO dates were mixed; 6 days earlier in NL but 2 and 4 days later in D and UK. The net result was a shorter 2021 oak season in each country (see Kendon et al. 2022).

In Kyoto, Japan, full bloom dates (FBD) for a native cherry tree species, *Prunus jamasakura*, were acquired from historical documents (Aono and Kazui 2008) and updated with current observations. In 2021, the FBD was 26 March (day 85), which was 9.5 days earlier than the 2000–20 baseline mean and the earliest in the entire record, which began in AD 801, breaking the previous earliest date of 27 March in the year 1409.

Monitoring data on lake water concentrations of the photosynthetic pigment chlorophyll-*a* were available to estimate spring phytoplankton phenology in 1 SH and 10 NH lakes (Fig. 2.74). Seasonal timing was quantified for start of season (SOS_L *sensu* Park et al. 2016), day of maximum concentration (DOM_L), and center of gravity (COG_L; Edwards and Richardson 2004). Lake basins showed great interannual variation and mixed phenological behavior in 2021, relative to the 2000–20 baseline. 2021 SOS_L and COG_L were both earlier than the baseline interquartile range in 4 of the 11 lakes and 5 of the 11 for DOM_L. Earlier growth

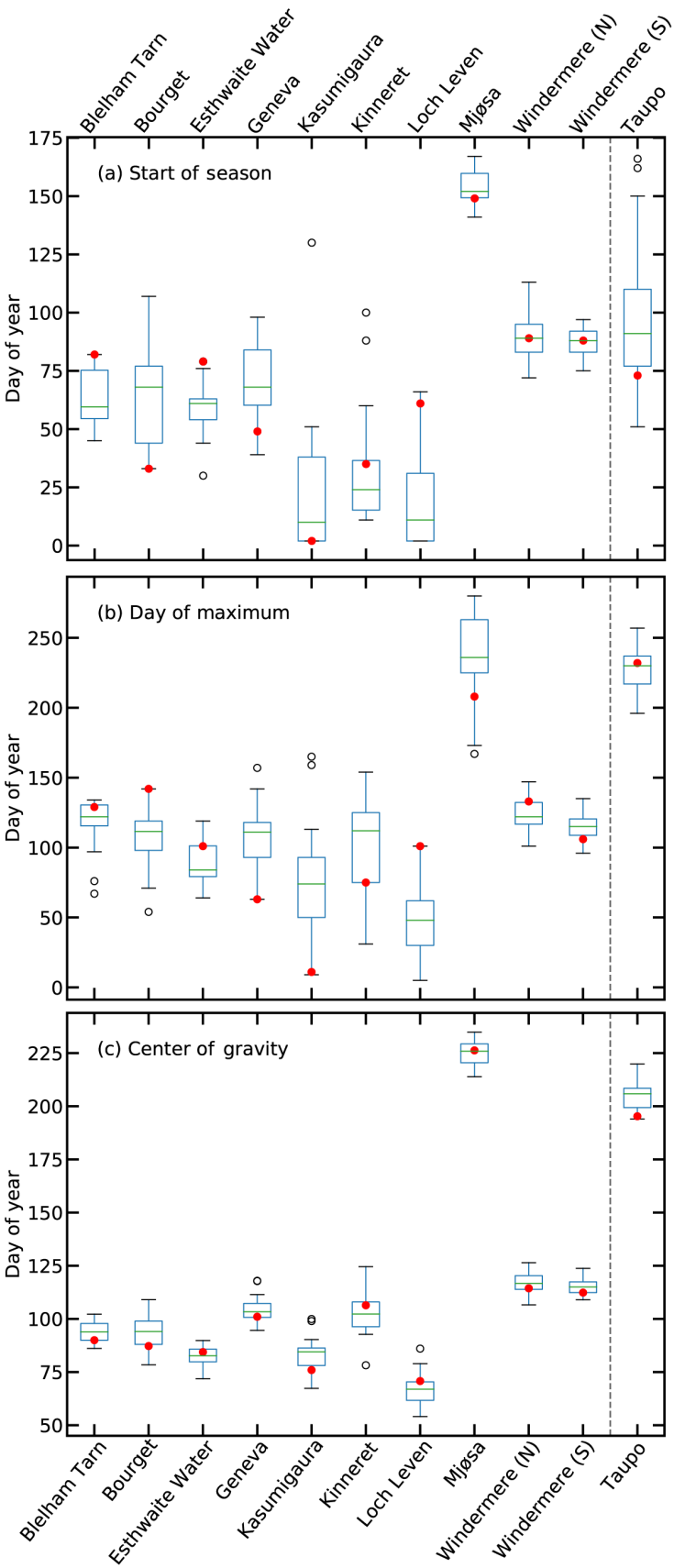

Fig. 2.74. Phenological metrics based on lake chlorophyll-*a* concentrations, as a proxy of phytoplankton biomass: (a) start of season, (b) day of maximum, and (c) center of gravity (a measure of the timing of the peak throughout the growing season). Boxplots show variation during the 2000–20 base period, and red dots show 2021 values. Dashed line identifies Northern Hemisphere (Blelham Tarn in United Kingdom [UK], Bourget in France, Esthwaite Water in UK, Geneva in France/Switzerland, Kasumigaura in Japan, Kinneret in Israel, Loch Leven in UK, Mjøsa in Norway, north and south basins of Windermere in UK) and Southern Hemisphere (Taupo in New Zealand) lakes.

typically occurs in deeper lakes where thermal stratification is an important trigger of spring phytoplankton growth (Sommer et al. 1986).

5. VEGETATION OPTICAL DEPTH—W. Dorigo, R. M. Zotta, R. van der Schalie, W. Preimesberger, L. Moesinger, and R. A. M. de Jeu

Vegetation optical depth (VOD) is a parameter describing the interaction of microwave radiance with vegetation. It is closely related to vegetation above-ground biomass (Mialon et al. 2020), leaf area index (Vreugdenhil et al. 2017), gross primary production (Teubner et al. 2019; Wild et al. 2022), and canopy water content (Konings et al. 2017). Thus, it is a valuable indicator of ecosystem health, agricultural drought, and crop status (Crocetti et al. 2020; Moesinger et al. 2022).

In 2021, VOD anomaly patterns largely resembled those of 2020 (Dorigo et al. 2021). Widespread patterns of negative VOD anomalies occurred in large parts of Russia, Central Asia, and Mongolia. For some of these predominantly rain-fed agricultural areas, below-average cereal production was reported by the UN Food and Agricultural Organization. Clear below-average VOD values were also detected in western Africa, Angola, and Namibia, the southwestern tip of Africa, Mozambique, and southern Madagascar, which were already observed in 2020 and persisted throughout 2021 (Plate 2.1ag). In Madagascar, ongoing droughts have reportedly led to crop failure, according to UN reports. Although some parts of Australia show lower-than-usual VOD, many areas, particularly in the east, shifted from a negative state in 2020 (Dorigo et al. 2021) to a positive one in 2021, as predominately wet conditions have prevailed following a major drought in 2017–19 (see section 7h4). The most evident region with above-average VOD was centered around Botswana and Namibia in southeastern Africa. Compared to 2020, VOD anomalies in this region became more positive and covered a larger area. Above-average rainfall amounts that are commonly associated with La Niña in this region (see section 7e) may have been responsible for this high VOD. Farther north, Uganda and South Sudan, in particular, had above-average VOD, likely related to heavy precipitation and flooding (see section 7e). Other areas of above-average VOD include parts of the Parana basin in South America, the Tigris floodplain in the Middle East, and the Indian subcontinent.

In the Southern Hemisphere, there was a clear connection between interannual variability in precipitation and vegetation activity and variations in ENSO and other climate modes (Fig. 2.75; Miralles et al. 2014; Martens et al. 2018). La Niña conditions prevailed in 2021, and several VOD anomalies coincided with rainfall anomaly patterns typically associated with this phase, including positive VOD anomalies in northeastern Brazil, southern Africa, the northern Sahel region, eastern Australia, and India. However, for VOD, the relationship with climate modes is generally less straightforward than for moisture supply, since VOD anomalies are also affected by drivers such as temperature, radiation, CO_2 fertilization, weather extremes, lagged effects, and land management (e.g., irrigation, fertilization, logging; Gonsamo et al. 2021; Reichstein et al. 2013).

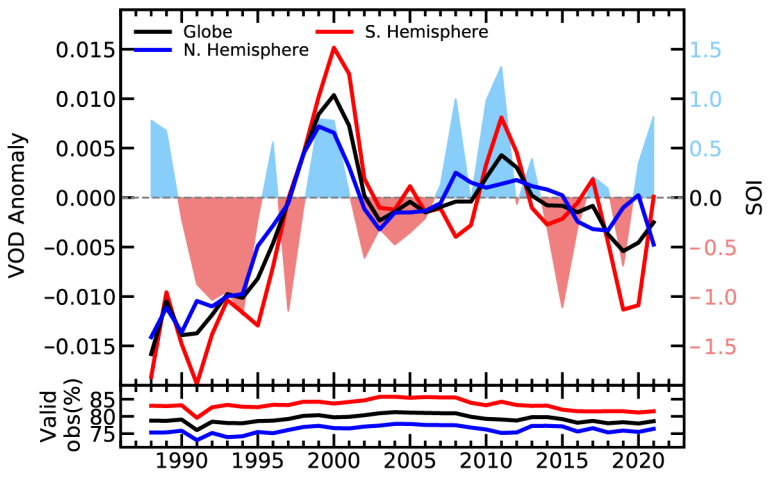

Fig. 2.75. Yearly Ku-band VOD anomalies computed from the 1991–2020 climatology and their agreement with the Southern Oscillation Index (SOI). SOI tracks the state of the El Niño Southern Oscillation, with values > 0.7 indicating La Niña and values < −0.7 indicating El Niño episodes (Source: VODCA, http://www.bom.gov.au/climate/enso/soi/.) The bottom plot shows the percentage of land pixels providing valid data for each year.

Several anomalies observed in 2021 are consistent with patterns of long-term change (Fig. 2.76). For instance,

the below-average vegetation activity in northern Mongolia and Brazil and Bolivia coincide with long-term negative trends related to land degradation and deforestation, respectively (Song et al. 2018). Above-average VOD in several regions can be linked to long-term trends in precipitation (Sahel; Dong and Sutton 2015), intensification of agricultural production (India, China), and reforestation (northeastern China; Song et al. 2018). To differentiate interannual variability from long-term change, one would need to detrend the data first (Moesinger et al. 2022). An alternative view is provided by the difference in VOD between the years 2021 and 2020 (Appendix Fig. A2.14), which reveals, for example, that although Kenya in 2021 had above-average vegetation activity, it was below that of 2020.

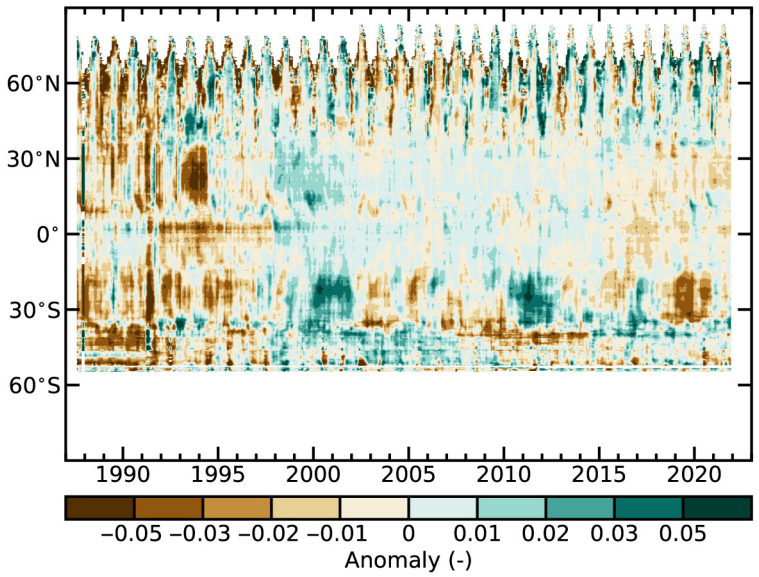

Fig. 2.76. Time–latitude diagram of VOD anomalies (1991–2020 base period). Data are masked where no retrieval is possible or where the quality is not assured and flagged due to frozen soil, radio frequency interference, etc. (Source: VODCA.)

The VOD anomalies were computed from the VOD Climate Archive (VODCA; Moesinger et al. 2020). VODCA blends VOD observations retrieved with the Land Parameter Retrieval Model (Meesters et al. 2005; van der Schalie et al. 2017) from several space-borne radiometers, including SSM/I, TRMM, Windsat, AMSR-E, and AMSR2, into a harmonized long-term dataset. VODCA contains individual datasets for Ku-band (covering the period 1987–2021), X-band (1997–2021), and C-band (2002–21) at 0.25° spatial and daily temporal resolutions. Here, we used the VODCA Ku-band dataset, the longest available record, to compute anomalies from the long-term (1991–2020) climatology. Despite its theoretically higher sensitivity to the upper canopy, intra and interannual dynamics of Ku-band observations strongly agree with those of X-band and C-band (Moesinger et al. 2022). VOD cannot be retrieved over frozen or snow-covered areas for which they are masked in winter (Appendix Fig. A2.13).

Acknowledgments

2.a.1 Introduction

Freya Aldred, Robert Dunn, and Kate Willett were supported by the Met Office Hadley Centre Climate Programme funded by BEIS. We thank John Kennedy, David Parker, and Katrina McNeill for their detailed comments when developing this chapter. We thank the BAMS Editor and the seven anonymous reviewers whose detailed comments improved the contents and presentation of this chapter. We also thank Atsushi Goto and Fumi Sezaki (JMA), Julien Nicolas (ECMWF), and Mike Bosilovich (NASA) for their help in providing the reanalysis data used in this chapter.

2.b.2 Lake Surface Temperature

Lake surface water temperatures from satellite data have been generated within the GloboLakes project funded by the UK National Environment Research Council (NE/J023345/2), with extensions funded by the EU Copernicus Climate Change Service (C3S) programme.

Part of the in situ measurements used to validate the LSWT dataset have been kindly shared by Eugene Silow (Irkutsk State University, Russia), Merja Pulkkanen (SYKE, Helsinki, Finland), Antii Raike (SYKE, Helsinki, Finland), Eric Leibensperger (Department of Physics and Astronomy, Ithaca College, Ithaca, U.S.A.), Alo Laas (Estonian University of Life Sciences, Tartu, Estonia), Michela Rogora (CNR Institute for Water Research, Italy), Martin Dokulil (Austria), Shin-ichiro Matsuzaki (National Institute for Environmental Studies, Japan), Claudia Giardino (CNR IREA, Italy), Curtis DeGasperi (King County Water and Land Resources Division, Department of Natural Resources and Parks, Seattle, Washington), Martin Schmid (Eawag, Switzerland), Don Pierson (Uppsala University, Sweden).

2.b.3 Night Marine Air Temperatures

R. Junod was supported by the U.S. Department of Energy (DE-SC0019296).

2.b.4 Land and Marine temperature extremes

Robert Dunn was supported by the Met Office Hadley Centre Climate Programme funded by BEIS.

2.b.5 Lower Tropospheric Temperature

Work performed by Stephen Po-Chedley at Lawrence Livermore National Laboratory (LLNL) was supported by the Regional and Global Model Analysis Program of the Office of Science at the Department of Energy and performed under the auspices of the DOE under Contract DE-AC52-07NA27344.

2.c.1 Permafrost and ALT

The Swiss Permafrost Monitoring Network PERMOS is financially supported by MeteoSwiss in the framework of GCOS Switzerland, the Federal Office for the Environment, and the Swiss Academy of Sciences, and acknowledges the important contribution of its partner institutions and principal investigators. The French Network PermaFRANCE is financially supported by the Observatoire des Sciences de l'Univers Grenoble and the French Research Infrastructure OZCAR. The research on James Ross Island is supported by Czech Antarctic Research Programme and Czech Science Foundation project (22-28659M).

2.c.2 Rock Glacier Velocity

Rock glacier monitoring at Hinteres Langtalkar and Dösen rock glaciers (AT) is supported by the Hohe Tauern National Park Carinthia through its long-term permafrost monitoring program.

Laurichard (FR) survey is supported by CryobsClim "long-term Observation and Experimentation System for Environmental Research" (SOERE/All'envi-OZCAR Research Infrastructure) and the PermaFrance observatory "monitoring the mountain permafrost in the French Alps" as well as French National Research Agency in the framework of the *Investissements d'Avenir* programs: Risk@UGA (ANR-15-IDEX-02) and LabEx OSUG@2020 (ANR10 LABX56).

The Ecrins National Park helps field surveys since the early 2000s.

The Swiss Permafrost Monitoring Network PERMOS is financially supported by MeteoSwiss in the framework of GCOS Switzerland, the Federal Office for the Environment, and the Swiss Academy of Sciences. PERMOS acknowledges the important contribution of the partner institutions and principal investigators.

The time series for Central Asian rock glaciers was compiled with the ESA Permafrost_CCI project (4000123681/18/I-NB).

The time series for the Dry Andes was supported by the Centro de Estudios Avanzados en Zonas Áridas (CEAZA) and the Leading House for the Latin American Region (University of St. Gallen), grant number MOB1829.

2.c.4 Lake Ice Cover

We thank Alexander Mills, Huaxia Yao, Lars Rudstam, Mr. Miyasaka, Ichiro Matsuzaki, Greg Sass, Don Pierson, the Minnesota Department of Natural Resources, North Temperate Lakes Long-Term Ecological Research Network, and citizen scientist contributors from the Community Lake Ice Collaboration for providing ice phenology records for their local lakes each winter.

Funding was provided by Natural Sciences Engineering and Research Council Discovery Grant to S. Sharma.

T. Nõges was supported by the Estonian Environment Agency and Estonian Research Council project PRG709.

2.c.5 NH Snow Cover

This work is funded in part by NOAA's Climate Data Record (CDR) Program at the National Centers for Environmental Information.

2.d.1 Surface Humidity

Kate Willett was supported by the Met Office Hadley Centre Climate Programme funded by BEIS and Defra. Adrian Simmons and David Lavers were supported by the Copernicus Climate Change Service implemented by ECMWF on behalf of the European Commission.

2.d.5 Land Based Precipitation Extremes

Stephen Blenkinsop is supported by the UK Natural Environment Research Council (NERC) funded FUTURE-STORMS project, grant no. NE/R01079X/1.

2.d.6 Cloudiness

Thank you to the following for providing data for this analysis:
Larry Di Girolamo – University of Illinois at Urbana-Champaign, Illinois
Guangyu Zhao – University of Illinois at Urbana-Champaign, Illinois
Sunny Sun-Mack – Science Systems and Applications, Inc., Hampton, Virginia
Martin Stengel – Deutscher Wetterdienst, Offenbach, Germany

2.d.7 Runoff and River Discharge

This work (research) was supported by the National Research Foundation of Korea (NRF) grant Funded by the Korea Government (MSIT) (2021H1D3A2A03097768) and the Japan Society for the Promotion of Science KAKENHI (21H05002) for this contribution.

2.d.8 Groundwater and Terrestrial Water Storage

M. Rodell and D. Wiese were supported by NASA's GRACE-FO Science Team.

They also thank the German Space Operations Center of the German Aerospace Center (DLR) for providing nearly 100% of the raw telemetry data of the twin GRACE satellites.

2.d.9 Soil Moisture

This work was supported by the ESA Climate Change Initiative Soil Moisture project.

2.d.10 Drought

Tim Osborn received funding from UK NERC (NE/S015582/1).

Ian Harris received funding from UK National Centre for Atmospheric Science (NCAS).

The research presented in the drought section was carried out on the High Performance Computing Cluster supported by the Research and Specialist Computing Support service at the University of East Anglia.

2.d.11 Land Evaporation

D. G. Miralles acknowledges support from the European Research Council (ERC) under grant agreement no. 715254 (DRY–2–DRY).

M. F. McCabe is supported by the King Abdullah University of Science and Technology.

2.e.1 Mean Sea Level Pressure and Related Modes of Variability

David Fereday was supported by the Met Office Hadley Centre Climate Programme funded by BEIS.

2.e.2 Surface Winds

C. Azorin-Molina was supported by CSIC-UV-GVA and funded by RTI2018-095749-A-I00, AICO/2021/023, Leonardo-FBBVA and the CSIC Interdisciplinary Thematic Platform PTI-CLIMA. R. J. H. Dunn was supported by the Met Office Hadley Centre Climate Programme funded by BEIS. L. Ricciardulli was supported by NASA Ocean Vector Wind Science Team grant 80HQTR19C0003.

2.e.3 Upper Air Winds

We thank Martin Weissmann and Anne Martin (both University of Vienna) for their support in estimating the impact of Aeolus data on global analyses in the Tropics and Michael Rennie (ECMWF) for provision of data.

Sidebar 2.1 Lightning

The work of M. Füllekrug was sponsored by the Royal Society (UK) grant NMG/R1/180252 and the Natural Environment Research Council (UK) under grants NE/L012669/1 and NE/H024921/1.

E. Williams is supported for studies on global circuit response to climate change from the Physical and Dynamic Meteorology Program at the National Science Foundation on grant no. 6942679.

C. Price was supported in his lightning research by the Israel Science Foundation (ISF) grant 2701/17 and the Ministry of Energy grant no. 220-17-002.

S. Goodman was supported by NASA Grant 80NSSC21K0923 and NASA Contract 80GSFC20C044.

K. Virts is supported in part by the GOES-R Series Science, Demonstration, and Cal/Val Program at Marshall Space Flight Center.

D. Buechler is supported by the NASA MSFC/UAH Cooperative Agreement NNM11AA01A.

The authors wish to thank Peter Thorne at Maynooth University in Ireland and at the European Centre for Medium Range Weather Forecast (ECMWF) for suggesting and initiating this work and for recommending that lightning be made an essential climate variable.

The data used to generate Fig. SB2.1 are available from the NASA Global Hydrometeorology Resource Center DAAC, Huntsville, Alabama.

The data used to generate Fig. SB.2.2 are provided by WWLLN to GHRC as part of GLM cal/val activities.

2.f.1 Earth Radiation Budget

This research has been supported by the NASA CERES project.

The NASA Langley Atmospheric Sciences Data Center processed the instantaneous Single Scanner Footprint (SSF) data used as input to EBAF Ed4.1 and processes the FLASHFlux TISA version 4A.

2.g.4 Stratospheric Ozone

Carlo Arosio, Melanie Coldewey-Egbers, Daan Hubert, Diego Loyola, Viktoria Sofieva, Alexei Rozanov, and Mark Weber are grateful to ESA's Climate Change Initiative Ozone (CCI+) project and to the EU Copernicus Climate Change Service, 312b Lot4 Ozone project for supporting the generation and extension of the GTO-ECV total ozone and SAGE-CCI-OMPS data records.

Stacey M. Frith is supported by the NASA Long Term Measurement of Ozone program WBS 479717.

Lucien Froidevaux's contribution, with the assistance of Ryan Fuller, was performed at the Jet Propulsion Laboratory, California Institute of Technology, under contract with NASA.

Daan Hubert acknowledges the partial support by the EU/ERC Horizon 2020 project GAIA-CLIM.

2.h.1 Albedo

The authors thank Mirko Marioni for his technical support and NASA's Land Processes Distributed Active Archive Center (LP DAAC) for providing access to the remote sensing data.

2.h.2 Terrestrial Vegetation Dynamics

The author thanks Mirko Marioni for his technical support and the providers of the remote sensing dataset needed to perform this research, i.e., the SeaWiFS Project (Code 970.2) and the Goddard Earth Sciences Data and Information Services Center/Distributed Active Archive Center (Code 902) at the Goddard Space Flight Center, Greenbelt, Maryland .

MERIS products were processed at the Grid On Demand facility of European Space Agency (ESA/ESRIN) using JRC software code.

The standard Two-stream Inversion Package (JRC-TIP) datasets were produced on JRC Big Data Analytics Platform (BDAP).

2.h.4 Phenology

Debbie Hemming acknowledges support from the Met Office Hadley Centre Climate Programme funded by BEIS and the Met Office Climate Service on Food, Farming and Natural Environment funded by Defra, and thanks all co-authors for their interesting and helpful contributions and Robert Dunn for his expertise finalizing the figures for this section.

Taejin Park acknowledges support from the NASA Earth Science Directorate (grants NNX16AO34H and 80NSSC18K0173-CMS).

Andrew Richardson acknowledges support from the National Science Foundation through the Macrosystems Biology (award 1702697) and LTER (award 1832210) programs.

John O'Keefe also acknowledges support from the National Science Foundation through the LTER (award 1832210) program.

Nature's Calendar (Woodland Trust) in the UK thanks all its volunteer recorders and support from players of People's Postcode Lottery.

De Natuurkalender (Nature's Calendar) program in the Netherlands thanks all the volunteers and school children in the GLOBE program for their many observations.

Annette Menzel and Ye Yuan acknowledge support from the Bavarian State Ministry of Science and the Arts in the context of the Bavarian Climate Research Network (BayKlif) (BAYSICS project - Bavarian Citizen Science Portal for Climate Research and Science Communication).

Orlane Anneville acknowledges support from INRAE.

Stephen Thackeray thanks Werner Eckert, Heidrun Feuchtmayr, Shin-Ichiro Matsuzaki, Linda May, Ryuichiro Shinohara, Jan-Erik Thrane, Piet Verburg, Tamar Zohary, and all field and lab workers associated with the provision of the lake chlorophyll-a data.

We acknowledge funding from Vassdragsforbundet for Mjøsa med tilløpselver (https://www.vassdragsforbundet.no/om-oss/) and Natural Environment Research Council award number NE/R016429/1 as part of the UK-SCAPE programme delivering National Capability.

Data for Lakes Geneva and Bourget were contributed by The Observatory on LAkes (OLA), © SOERE OLA-IS, AnaEE-France, INRAE of Thonon-les-Bains, CIPEL, CISALB.

2.h.5 Vegetation Optical Depth

W. Dorigo, R.M. Zotta, and L. Moesinger, acknowledge the TU Wien Wissenschaftspreis 2015, a personal grant awarded to W. Dorigo.

We also acknowledge support from the ESA Climate Change Initiative Soil Moisture project.

Appendix 1: Chapter 2 – Acronyms

AAO	Antarctic Oscillation
AATSR	Advanced Along Track Scanning Radiometer
ALEXI	Atmosphere–Land Exchange Inverse
ALT	active layer thickness
AMSRE-E	Advanced Microwave Scanning Radiometer
AO	Arctic Oscillation
AOD	aerosol optical depth
ATSR	Along Track Scanning Radiometer
AVHRR	Advanced Very High Resolution Radiometer
BDC	Brewer-Dobson circulation
BRW	Barrow Atmospheric Baseline Observatory
C3S	Copernicus Climate Change Service
CALIOP	Cloud-Aerosol Lidar with Orthogonal Polarization
CAMS	Copernicus Atmosphere Monitoring Service
CAMSRA	Copernicus Atmosphere Monitoring Service Reanalysis
CCMI	Chemistry Climate Model Initiative
CEI	Climate Extremes Index
CERES	Clouds and the Earth's Radiant Energy System
CFC	chlorofluorocarbon
CH_4	methane
Cl	chlorine
CO	carbon monoxide
CO_2	carbon dioxide
CPT	cold-point tropopause
CRU TS	Climatic Research Unit gridded Time Series
DDM	drainage direction map
DU	Dobson unit
EA	Eurasia
ECV	essential climate variable
EESC	equivalent effective stratospheric chlorine
EESC-A	equivalent effective stratospheric chlorine-Antarctic
EESC-M	equivalent effective stratospheric chlorine-Midlatitude
ENSO	El Niño–Southern Oscillation
EOFs	empirical orthogonal functions
EOS	end of season
ERB	Earth's radiation budget
ESA CCI SM	European Space Agency's Climate Change Initiative for Soil Moisture
ET	evapotranspiration
ETCCDI	WMO Expert Team in Climate Change Detection and Indices
FAPAR	Fraction of Absorbed Photosynthetically Active Radiation
FF	fossil fuel
GCOS	Global Climate Observing System
GFAS	Global Fire Assimilation System
GFED	Global Fire Emissions Database
GGGRN	NOAA's Global Greenhouse Gas Reference Network
GHCN	Global Historical Climatology Network

GHCNDEX	Global Historical Climatology Network-Daily database
GIN-P	Global Terrestrial Network for Permafrost
GLEAM	Global Land Evaporation Amsterdam Model
GMST	global mean surface temperature
GNSS	Global Navigation Satellite System
GPCC	Global Precipitation Climatology Centre
GPCP	Global Precipitation Climatology Project
GPS-RO	Global Positioning System-Radio Occultation
GRACE	Gravity Recovery and Climate Experiment
GRACE-FO	Gravity Recovery and Climate Experiment - Follow On
GTN-P	Global Terrestrial Network for Permafrost
HFCF	hydrochlorofluorocarbon
HFC	hydrofluorocarbon
HIRS	High Resolution Infra Red Radiation Sounder
HWF	heat wave frequency
HWM	heat wave magnitude
IOD	Indian Ocean dipole
IPA	International Permafrost Association
ITCZ	Intertropical Convergence Zone
LLGHG	long-lived greenhouse gases
LSA-SAF	Land Surface Analysis Satellite Applications Facility
LSWT	lake surface water temperature
LTT	lower tropospheric temperature
LWL	lake water level
MACC	Monitoring Atmospheric Composition and Climate
MAT	marine air temperature
MBL	marine boundary layer
MHW	marine heatwave
MLO	Mauna Loa, Hawaii
MLS	Microwave Limb Sounder
MODIS	Moderate Resolution Imaging Spectroradiometer
MOPITT	Measurement of Pollution in the Troposphere
MSU/AMSU	Microwave Sounding Unit/Advanced Microwave Sounding Unit
N_2O	nitrous oxide
NA	North America
NAO	North Atlantic Oscillation
NDVI	normalized difference vegetation index
NH	Northern Hemisphere
NMAT	night marine air temperature
O_3	ozone
ODGI	Ozone Depleting Gas Index
ODGI-A	Ozone Depleting Gas Index-Antarctic
ODGI-M	Ozone Depleting Gas Index-Midlatitude
ODS	ozone-depleting substances
OH	hydroxyl radical
OLR	outgoing longwave radiation
OMI	Ozone Monitoring Instrument
PDO	Pacific Decadal Oscillation
PSC	polar stratospheric cloud
QBO	quasi-biennial oscillation

QTP	Qinghai-Tibetan Plateau
RFaci	radiative forcing resulting from aerosol–cloud interactions
RFari	radiative forcing resulting from aerosol–radiation
RGK	rock glacier kinematics
RH	relative humidity
RO	radio occultation
RSW	reflected shortwave
SAM	Southern Annular Mode
SAR	Synthetic Aperture Radar
SCE	snow cover extent
scPDSI	self-calibrating Palmer Drought Severity Index
SH	Southern Hemisphere
SLSTR	Sea and Land Surface Temperature Radiometer
SOI	Southern Oscillation Index
SORCE	Solar Radiation and Climate Experiment
SOS	start of season
SPO	South Pole Observatory
SSM/I	Special Sensor Microwave/Imager
SSMIS	Special Sensor Microwave Imager/Sounder
SST	sea surface temperature
SSU	Stratospheric Sounding Unit
SW	shortwave
TCWV	total column water vapor
TIR	thermal infrared
TLS	lower stratospheric temperature
TOA	top of the atmosphere
TSI	total solar irradiance
TSIS-1	Total Solar and Spectral Irradiance Sensor-1
TTL	tropical tropopause layer
TTT	tropical tropospheric temperature
TWS	terrestrial water storage
UTH	upper tropospheric (relative) humidity
UV	ultraviolet
VOC	volatile organic compound
VOD	vegetation optical depth
VODCA	vegetation optical depth Climate Archive
WGMS	World Glacier Monitoring Service
WMO	World Meteorological Organization
WV	water vapor

Appendix 2: Supplemental Material

2.b.1 Surface Temperature

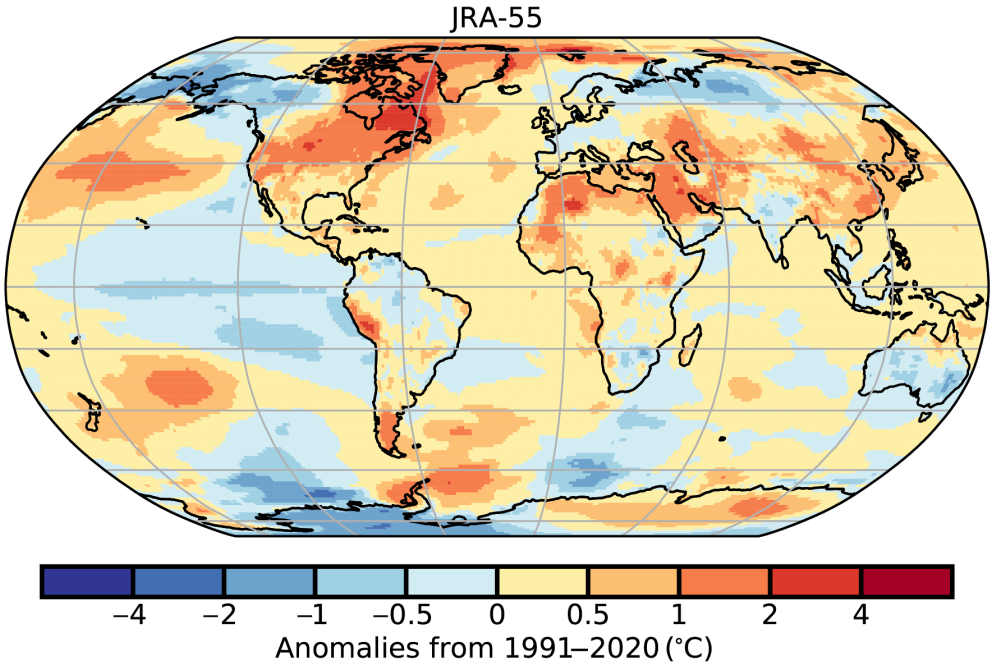

Fig. A2.1. JRA-55 2-m surface temperature anomalies (°C; 1991–2020 base period).

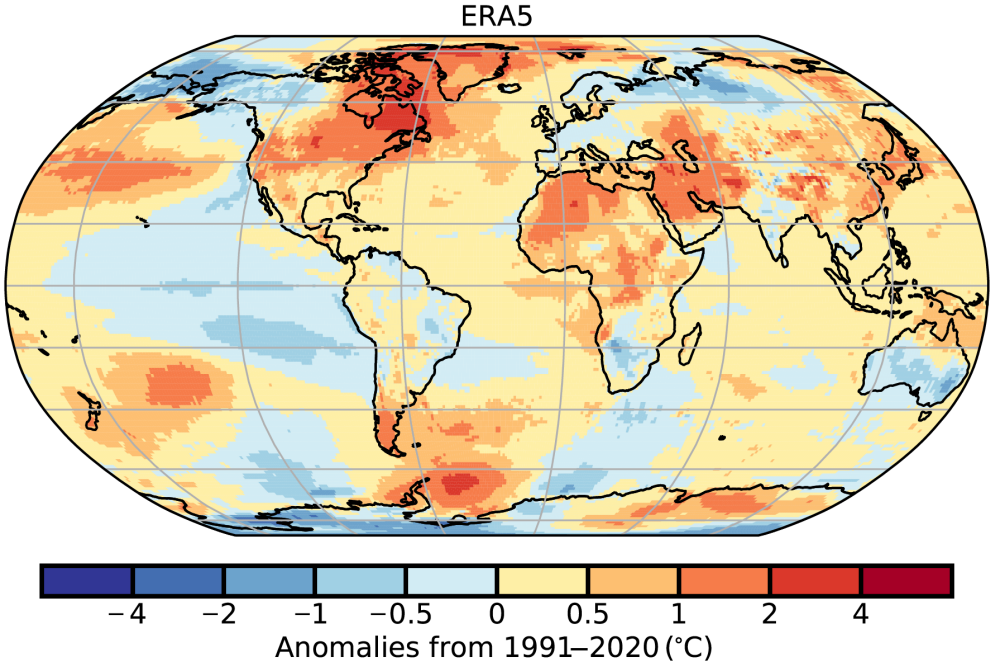

Fig. A2.2. ERA5 2-m surface temperature anomalies (°C; 1991–2020 base period).

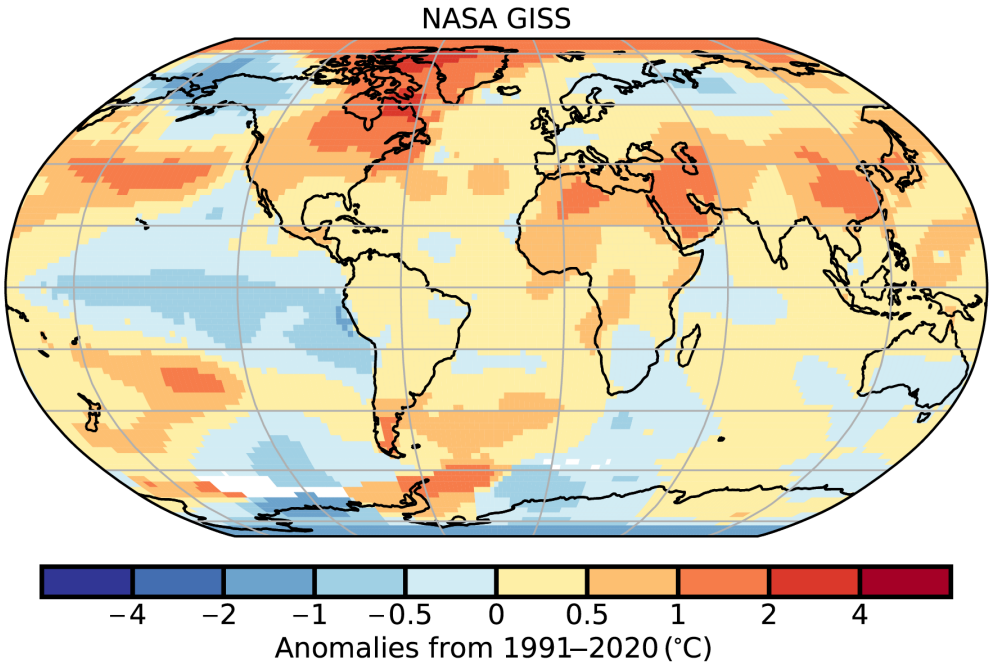

Fig. A2.3. NASA surface temperature anomalies (°C; 1991–2020 base period).

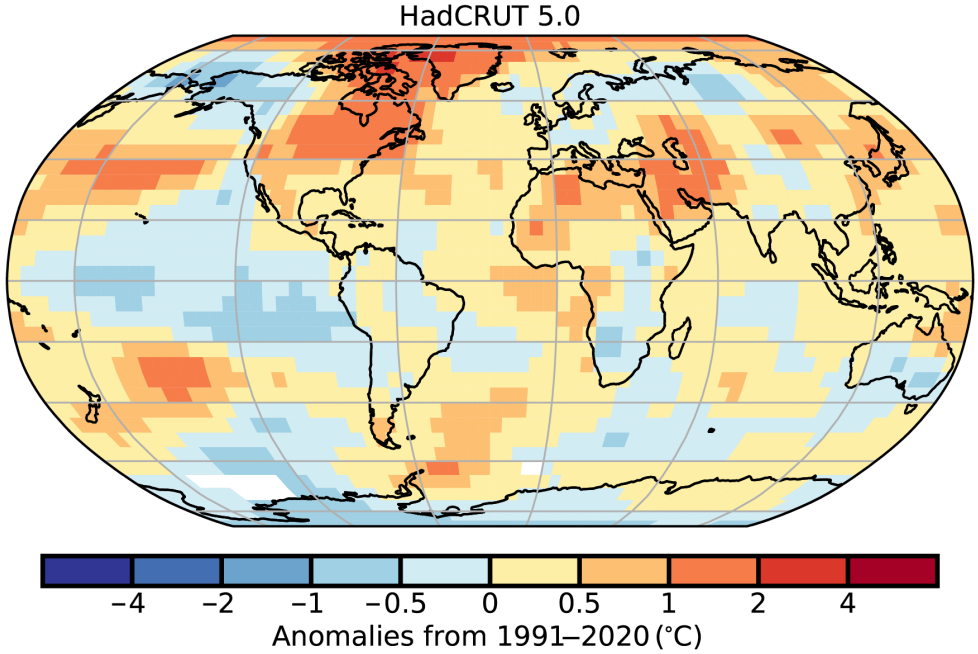

Fig. A2.4. HadCRUT5 surface temperature anomalies (°C; 1991–2020 base period).

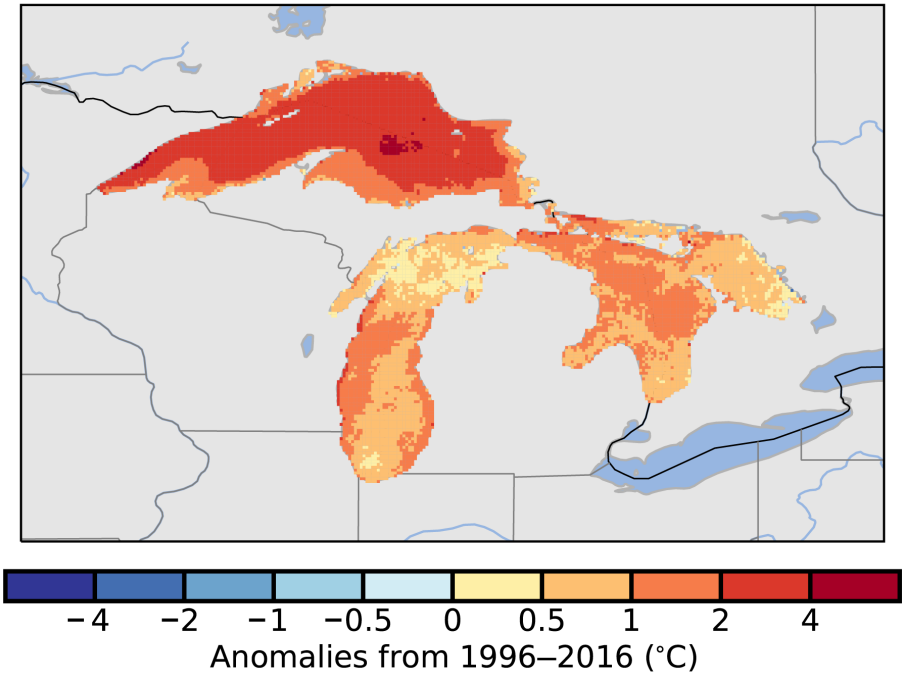

Fig. A2.5. Spatial distribution of the 2021 LSWT anomalies (°C) for Lake Superior, Huron, and Michigan in North America (1996–2016 base period).

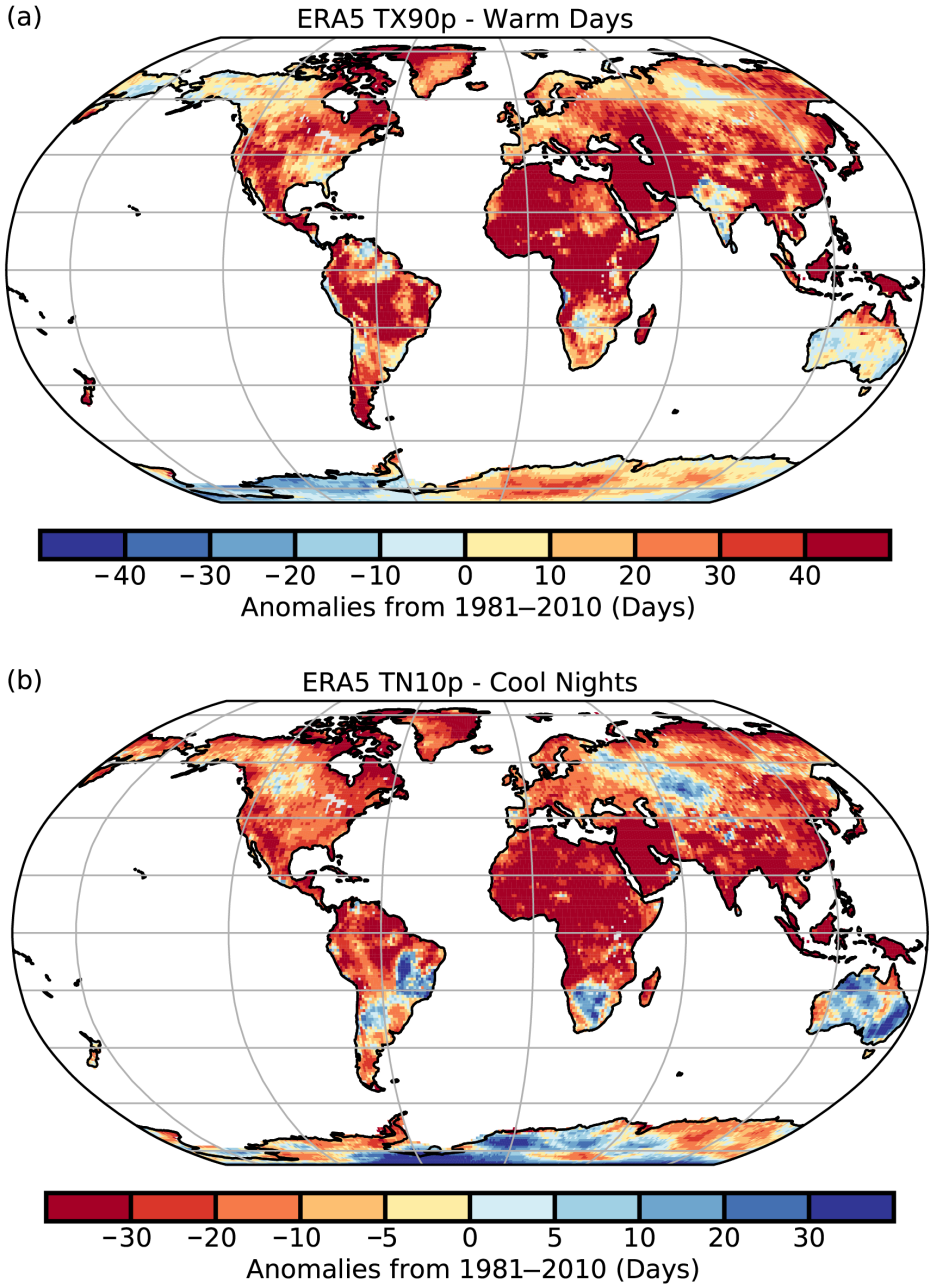

Fig. A2.6. Anomalies of (a) TX90p and (b) TN10p from ERA5 (1981–2010 base period).

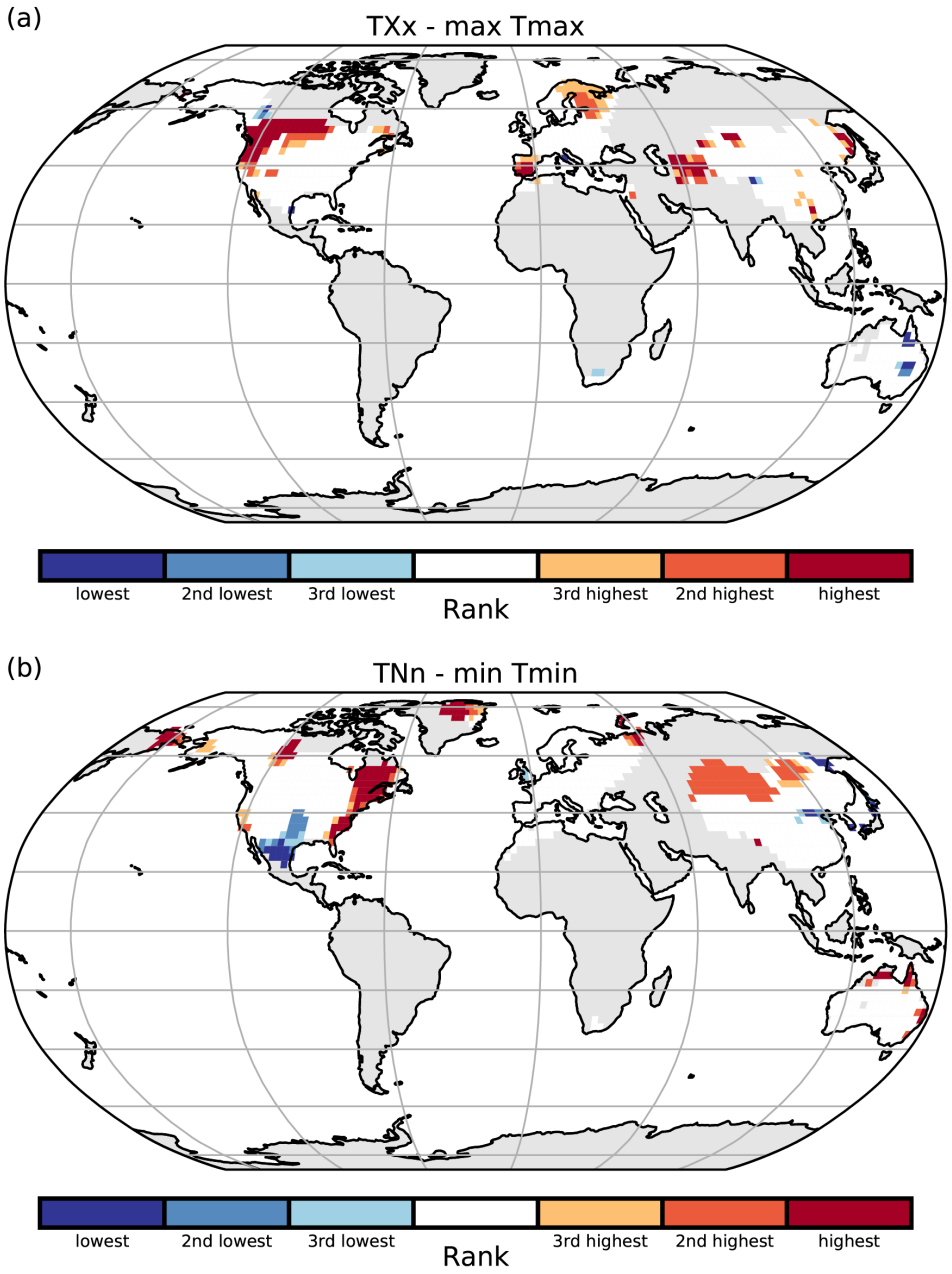

Fig. A2.7. Rank plots highlighting locations where the highest maximum temperature (TXx) and lowest minimum temperature (TNn) in 2021 were among the highest or lowest three on record.

Appendix Table 2.1. Selected extreme temperatures in 2021 relevant to the events discussed in the text. Additional records are presented in the WMO State of the Global Climate in 2021 (WMO 2022).

Location	Country	Date	Value	Notes
Clot del Tuc de la Llança	Spain	6 Jan	–34.1	National minimum record, coldest since station records began in 1956
Houston	Texas, USA	16 Feb	–11	Coldest since 1989
Dallas	Texas, USA	16 Feb	–18.9	Coldest since 1930
Strasbourg	France	31 Mar	26.3	March maximum record
Rheinau-Memprechtshofen	Germany	31 Mar	27.2	National March maximum record
Orléans	France	6 Apr	–5.4	April minimum record
Chalon-sur-Saône	France	7 Apr	–5.4	April minimum record
Orange	France	8 Apr	–3.2	April minimum record
Nova vas na Blokah	Slovenia	7 Apr	–20.6	April minimum record
Moscow	Russia	23 Jun	34.8	June maximum record
Yerevan	Armenia	24 Jun	41.1	June maximum record
Baku	Azerbaijan	26 Jun	40.5	June maximum record
Lytton	British Columbia, Canada	29 Jun	49.6	National record (by 4.6°C)
Utsjoki- Kevo	Lapland, Finland	5 Jul	33.6	Highest maximum since 1914
Death Valley	California, USA	9 Jul	54.4	Equal to hottest maximum temperature since at least 1930s.
Esashi	Iwate Prefecture, Japan	19 Jul	37.3	Equal to station record
Cizre	Turkey	20 Jul	49.1	National maximum record
Tbilisi	Georgia	20 Jul	40.6	National maximum record
Castlederg	Northern Ireland	21 Jul	31.3	Maximum record
Rafha	Saudi Arabia	24 Jul	50.6	—
Dammam	Saudi Arabia	31 Jul	50.4	Equal maximum record (set 2020)
Kairouan	Tunisia	2 Aug	50.3	National maximum record
Syracuse	Italy	11 Aug	48.8	Provisional European maximum record
Montoro	Cordoba, Spain	14 Aug	47.4	National maximum record
Makrakomi Ftiotida	Greece	2 Aug	46.3	National maximum record

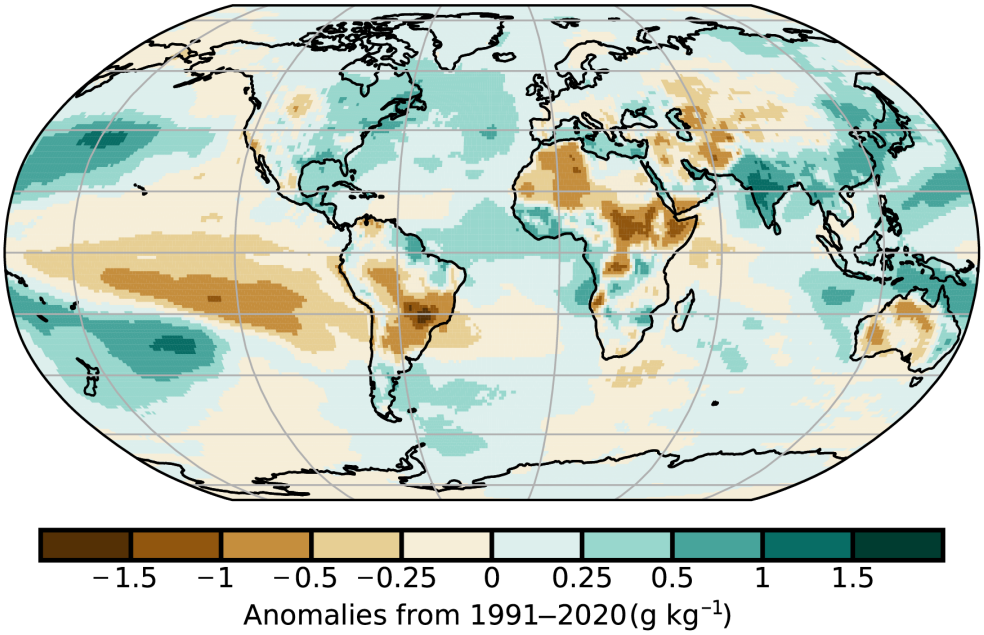

Fig. A2.8. ERA5 surface specific humidity annual average anomalies (g kg^{-1}) for 2021 (1991–2020 base period).

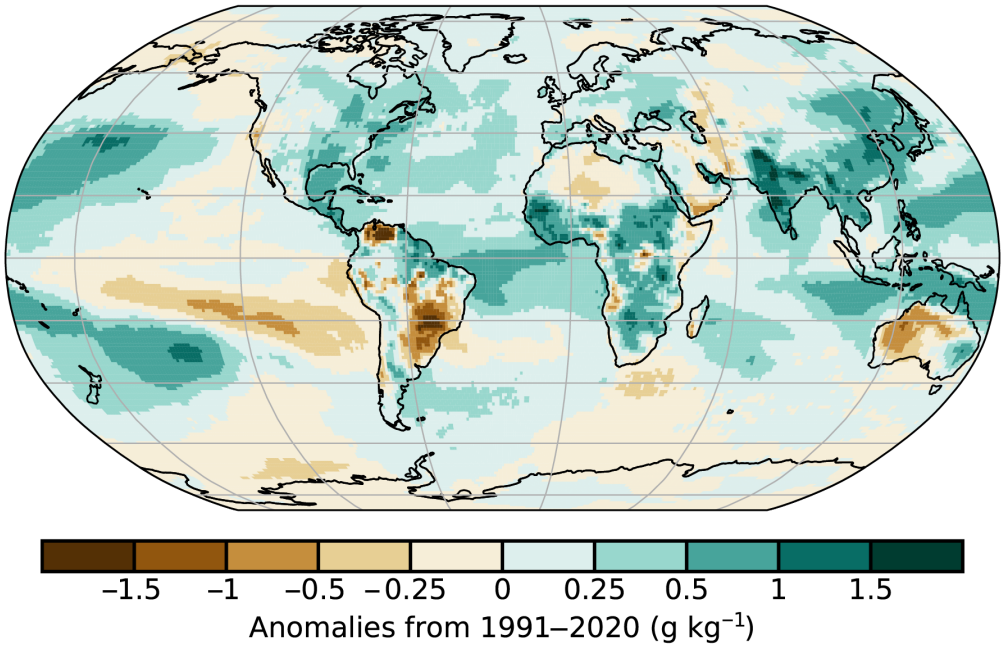

Fig. A2.9. MERRA2 surface specific humidity annual average anomalies (g kg^{-1}) for 2021 (1991–2020 base period).

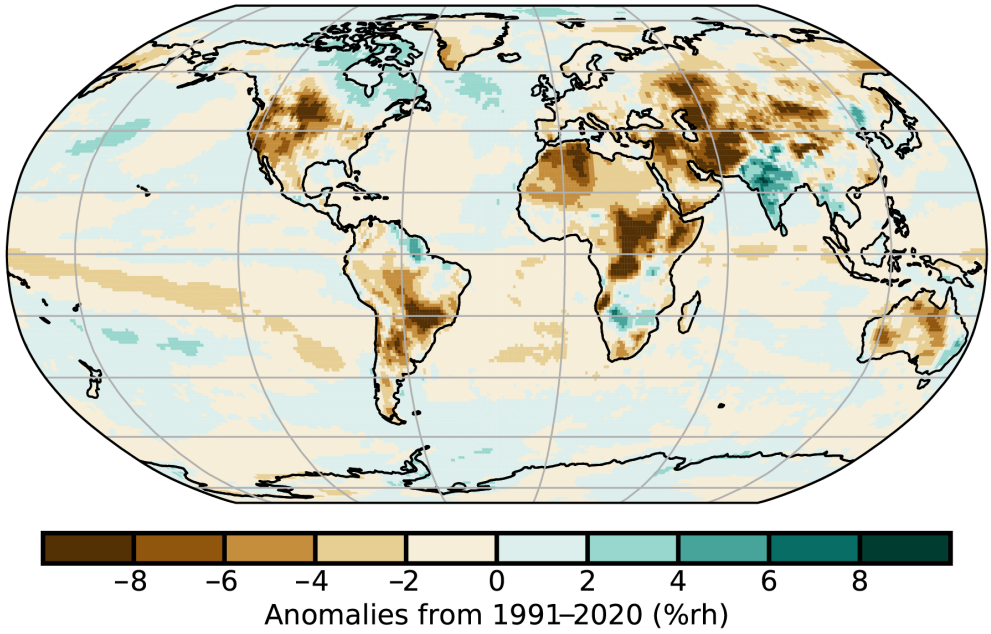

Fig. A2.10. ERA5 surface relative humidity annual average anomalies (%rh) for 2021 (1991–2020 base period).

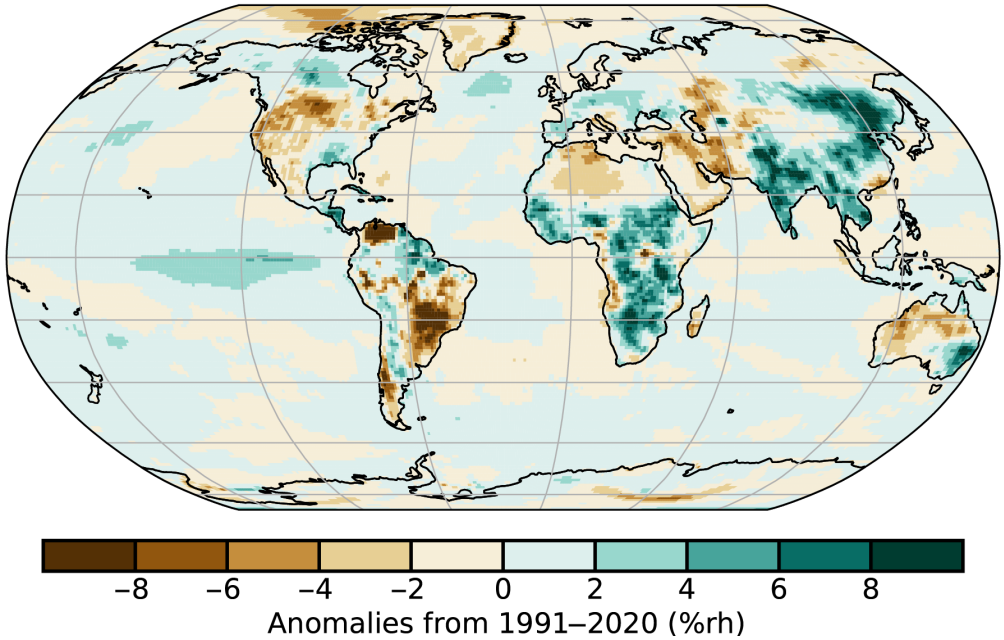

Fig. A2.11. MERRA2 surface relative humidity annual average anomalies (%rh) for 2021 (1991–2020 base period).

Appendix Table 2.2. Selected extreme precipitation events in 2021. The value column shows the recorded amount and accumulation period. Events are listed in the order referred to in the text. Events noted as records are for the location listed unless otherwise stated.

Location	Country	Date	Value	Notes
Paso Robles Airport, California	United States	25 Oct	39 mm (24-h)	Record 24-h total for October
Abbotsford	Canada	14 Nov	100.4 mm (24-h)	Record 24-h total
New York City	United States	1 Sep	80 mm (1-h)	Hurricane Ida set record 1-h total, breaking record of 49 mm set by Henri earlier in the month
Newark, New Jersey	United States	1 Sep	213.6 mm (24-h)	Record 24-h total
Wipperfurth-Gardenau	Germany	14–15 Jul	162.4 mm (24-h)	Record 24-h total
Gävle	Sweden	17–18 Aug	161.6 mm (24-h)	Record 24-h total
Kindee Bridge, New South Wales	Australia	20 Mar	283.4 mm (24-h)	Record 24-h total for March
Samuel Hill Aero, Queensland	Australia	10 Nov	340.8 mm (24-h)	Record 24-h total for November (> 3 times previous record)
Newbicup, Western Australia	Australia	12 Apr	74.0 mm (24-h)	Record 24-h total for April
Zhengzhou, Henan Province	China	20 Jul	201.9 mm (1-h)	Typhoon In-fa. 1-h total reported as national record for mainland China
Taiyuan, Shanxi Province	China	2–7 Oct	185.5 mm (12-h)	Regional record 12-h total for October
Beira	Mozambique	23 Jan	250 mm (24-h)	Close to regional monthly average rainfall

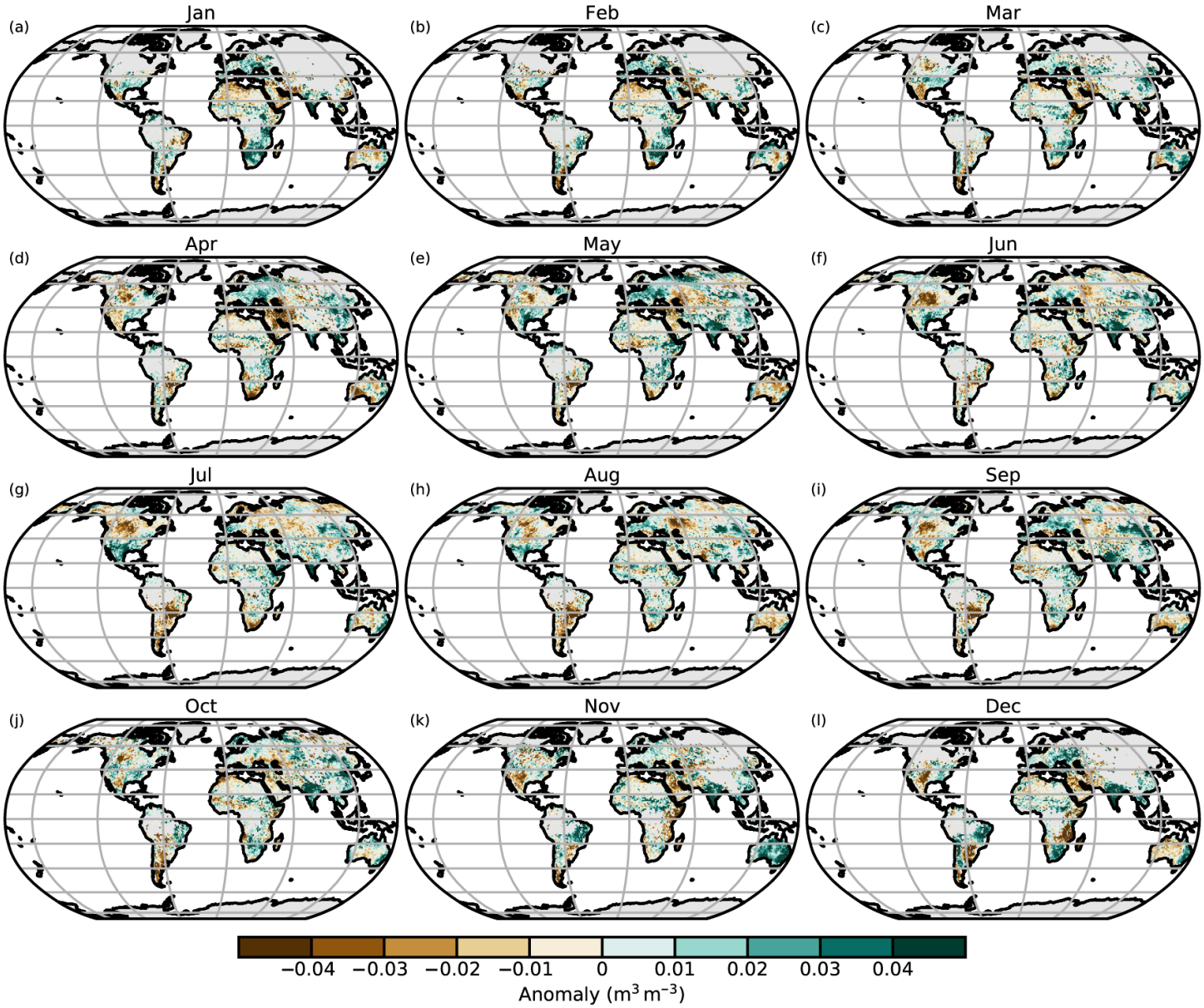

Fig. A2.12. ESA CCI soil moisture monthly average soil moisture anomalies ($m^3\ m^{-3}$) for 2021 (1991–2020 base period). Data are masked where no retrieval is possible or where the quality is not assured and flagged due to dense vegetation, frozen soil, radio frequency interference, etc.

2.h.5 Vegetation Optical Depth

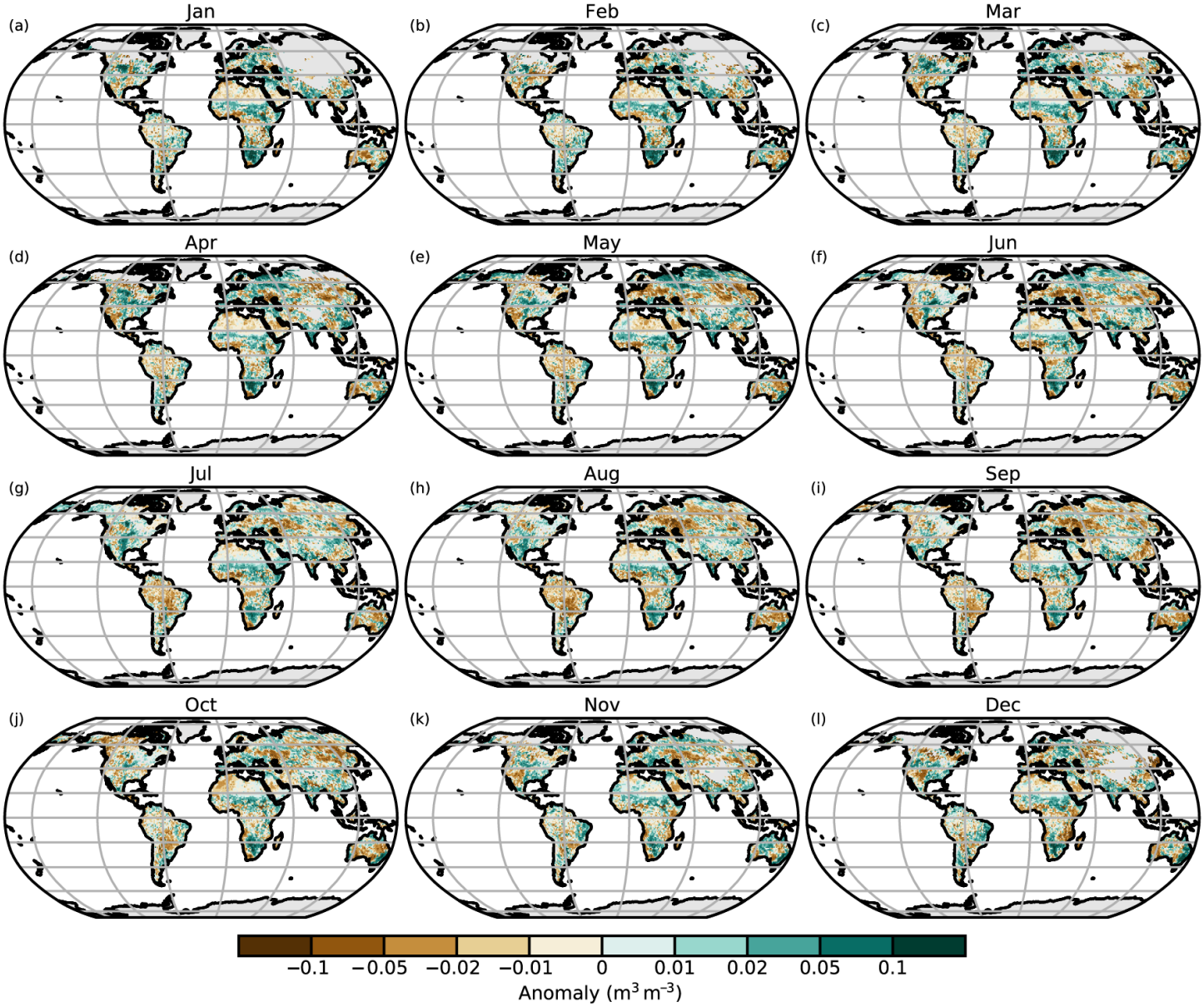

Fig. A2.13. (a–l) VODCA monthly Ku-band VOD anomalies ($m^3\ m^{-3}$) for 2021 (1991–2020 base period).

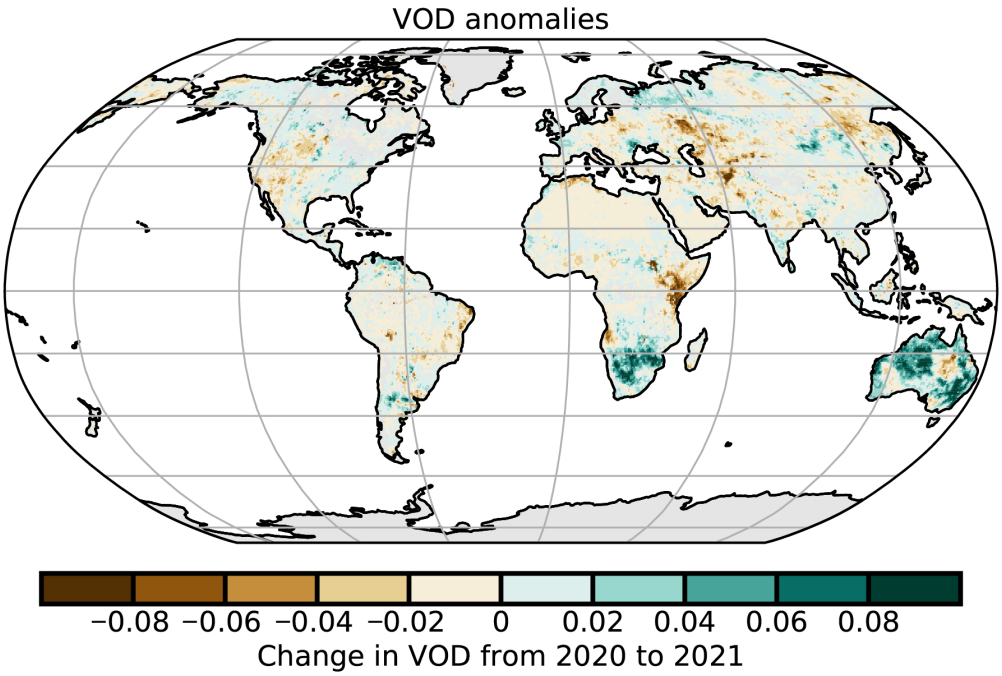

Fig. A2.14. Difference in average Ku-band VOD between the years 2021 and 2020. Brown/green colors indicate areas where VOD in 2021 was lower/higher than in 2020. (Source: VODCA.)

References

Adler, R., and Coauthors, 2018: The global Precipitation Climatology Project (GPCP) monthly analysis (new version 2.3) and a review of 2017 global precipitation. *Atmosphere*, **9**, 138, https://doi.org/10.3390/atmos9040138.

Aich, V., R. Holzworth, S. Goodman, Y. Kuleshov, C. Price, and E. Williams, 2018: Lightning: A new essential climate variable. *Eos*, **99**, https://doi.org/10.1029/2018EO104583.

Alden, C. B., J. B. Miller, and J. W. C. White, 2010: Can bottom-up ocean CO_2 fluxes be reconciled with atmospheric ^{13}C observations? *Tellus*, **62B**, 369–388, https://doi.org/10.1111/j.1600-0889.2010.00481.x.

Anabalón, A., and A. Sharma, 2017: On the divergence of potential and actual evapotranspiration trends: An assessment across alternate global datasets. *Earth's Future*, **5**, 905–917, https://doi.org/10.1002/2016EF000499.

Andela, N., and Coauthors, 2017: A human-driven decline in global burned area. *Science*, **356**, 1356–1362, https://doi.org/10.1126/science.aal4108.

Anyamba, E., E. Williams, J. Süsskind, A. Fraser-Smith, and M. Füllekrug, 2000: The manisfestation of the Madden–Julian oscillation in global deep convection and in the Schumann resonance intensity. *J. Atmos. Sci.*, **57**, 1029–1044, https://doi.org/10.1175/1520-0469(2000)057<1029:TMOTMJ>2.0.CO;2.

Aono, Y., and K. Kazui, 2008: Phenological data series of cherry tree flowering in Kyoto, Japan, and its application to reconstruction of springtime temperatures since the 9th century. *Int. J. Climatol.*, **28**, 905–914, https://doi.org/10.1002/joc.1594.

Archer, D., and V. Brovkin, 2008: The millennial atmospheric lifetime of anthropogenic CO2. *Climatic Change*, **90**, 283–297, https://doi.org/10.1007/s10584-008-9413-1.

Archibald, A. T., and Coauthors, 2020: Tropospheric Ozone Assessment Report: A critical review of changes in the tropospheric ozone burden and budget from 1850 to 2100. *Elem. Sci. Anthropocene*, **8**, 034, https://doi.org/10.1525/elementa.2020.034.

AMAP, 2021: Arctic Climate Change Update 2021: Key trends and impacts: Summary for Policy-makers. Arctic Monitoring and Assessment Programme, 16 pp., www.amap.no/documents/doc/arctic-climate-change-update-2021-key-trends-and-impacts.-summary-for-policy-makers/3508.

Arguez, A., and Coauthors, 2020: Should we expect each year in the next decade (2019–28) to be ranked among the top 10 warmest years globally? *Bull. Amer. Meteor. Soc.*, **101**, E655–E663, https://doi.org/10.1175/BAMS-D-19-0215.1.

Arosio, C., A. Rozanov, E. Malinina, K.-U. Eichmann, T. von Clarmann, and J. P. Burrows, 2018: Retrieval of ozone profiles from OMPS limb scattering observations. *Atmos. Meas. Tech.*, **11**, 2135–2149, https://doi.org/10.5194/amt-11-2135-2018.

——, ——, ——, M. Weber, and J. P. Burrows, 2019: Merging of ozone profiles from SCIAMACHY, OMPS and SAGE II observations to study stratospheric ozone changes. *Atmos. Meas. Tech.*, **12**, 2423–2444, https://doi.org/10.5194/amt-12-2423-2019.

Augustine, J. A., K. O. Lantz, J.-P. Vernier, and H. Telg, 2020: Mauna Loa clear-sky "apparent" solar transmission [in "State of the Climate in 2019"]. *Bull. Amer. Meteor. Soc.*, **101** (8), S61–S62, https://doi.org/10.1175/BAMS-D-20-0104.1.

——, ——, and ——, 2021: Mauna Loa apparent transmission [in "State of the Climate in 2020"]. *Bull. Amer. Meteor. Soc.*, **102** (8), S82–S83, https://doi.org/10.1175/BAMS-D-21-0098.1.

Azorin-Molina, C., J. Asin, T. R. McVicar, L. Minola, J. I. Lopez-Moreno, S. M. Vicente-Serrano, and D. Chen, 2018: Evaluating anemometer drift: A statistical approach to correct biases in wind speed measurement. *Atmos. Res.*, **203**, 175–188, https://doi.org/10.1016/j.atmosres.2017.12.010.

——, and Coauthors, 2021: A decline of observed daily peak wind gusts with distinct seasonality in Australia, 1941–2016. *J. Climate*, **34**, 3103–3127, https://doi.org/10.1175/JCLI-D-20-0590.1.

Baldwin, M. P., and T. J. Dunkerton, 2001: Stratospheric harbingers of anomalous weather regimes. *Science*, **294**, 581–584, https://doi.org/10.1126/science.1063315.

——, and Coauthors, 2001: The quasi-biennial oscillation. *Rev. Geophys.*, **39**, 179–229, https://doi.org/10.1029/1999RG000073.

Ball, W. T., and Coauthors, 2018: Evidence for a continuous decline in lower stratospheric ozone offsetting ozone layer recovery. *Atmos. Chem. Phys.*, **18**, 1379–1394, https://doi.org/10.5194/acp-18-1379-2018.

——, G. Chiodo, M. Abalos, J. Alsing, and A. Stenke, 2020: Inconsistencies between chemistry–climate models and observed lower stratospheric ozone trends since 1998. *Atmos. Chem. Phys.*, **20**, 9737–9752, https://doi.org/10.5194/acp-20-9737-2020.

Ballantyne, A. P., C. B. Alden, J. B. Miller, P. P. Tans, and J. W. C. White, 2012: Increase in observed net carbon dioxide uptake by land and oceans during the past 50 years. *Nature*, **488**, 70–72, https://doi.org/10.1038/nature11299.

Barichivich, J., T. J. Osborn, I. Harris, G. van der Schrier, and P. D. Jones, 2020: Monitoring global drought using the self-calibrating Palmer Drought Severity Index [in "State of the Climate in 2019"]. *Bull. Amer. Meteor. Soc.*, **101** (8), S59–S60, https://doi.org/10.1175/BAMS-D-20-0104.1.

——, ——, ——, ——, and ——, 2021: Monitoring global drought using the self-calibrating Palmer Drought Severity Index [in "State of the Climate in 2020"]. *Bull. Amer. Meteor. Soc.*, **102** (8), S68–S70, https://doi.org/10.1175/BAMS-D-21-0098.1.

Beck, H. E., and Coauthors, 2019: MSWEP V2 global 3-hourly 0.1° precipitation: Methodology and quantitative assessment. *Bull. Amer. Meteor. Soc.*, **100**, 473–500, https://doi.org/10.1175/BAMS-D-17-0138.1.

——, A. I. J. M. van Dijk, P. R. Larraondo, T. R. McVicar, M. Pan, E. Dutra, and D. G. Miralles. 2022: MSWX: Global 3-hourly 0.1° bias-corrected meteorological data including near real-time updates and forecast ensembles. *Bull. Amer. Meteor. Soc.*, 103, E710–E732, https://doi.org/10.1175/BAMS-D-21-0145.1.

Becker, A., P. Finger, A. Meyer-Christoffer, B. Rudolf, K. Schamm, U. Schneider, and M. Ziese, 2013: A description of the global land-surface precipitation data products of the Global Precipitation Climatology Centre with sample applications including centennial (trend) analysis from 1901–present. *Earth Syst. Sci. Data*, **5**, 71–99, https://doi.org/10.5194/essd-5-71-2013.

Behera, S. K., J. J. Luo, S. Masson, S. A. Rao, H. Sakuma, and T. Yamagata, 2006: A CGCM study on the interaction between IOD and ENSO. *J. Climate*, **19**, 1688–1705, https://doi.org/10.1175/JCLI3797.1.

Bell, B., and Coauthors, 2021: The ERA5 global reanalysis: Preliminary extension to 1950. *Quart. J. Roy. Meteor. Soc.*, **147**, 4186–4227, https://doi.org/10.1002/qj.4174.

Bell, G. D., and M. Chelliah, 2006: Leading tropical modes associated with interannual and multidecadal fluctuations in North Atlantic hurricane activity. *J. Climate*, **19**, 590–612, https://doi.org/10.1175/JCLI3659.1.

Bellouin, N., and Coauthors, 2020: Radiative forcing of climate change from the Copernicus reanalysis of atmospheric composition. *Earth Syst. Sci. Data*, **12**, 1649–1677, https://doi.org/10.5194/essd-12-1649-2020.

Bieniek, P., and Coauthors, 2020: Lightning variability in dynamically downscaled simulations of Alaska's present and future summer climate. *J. Appl. Meteor. Climatol.*, **59**, 1139–1152, https://doi.org/10.1175/JAMC-D-19-0209.1.

Biskaborn, B. K., and Coauthors, 2019: Permafrost is warming at a global scale. *Nat. Commun.*, **10**, 264, https://doi.org/10.1038/s41467-018-08240-4.

Blakeslee, R., and Coauthors, 2020: Three years of the Lightning Imaging Sensor onboard the International Space Station: Expanded global coverage and enhanced applications. *J. Geophys. Res. Atmos.*, **125**, e2020JD032918, https://doi.org/10.1029/2020JD032918.

Bock, O., 2020: Global GNSS Integrated Water Vapour data, 1994-2020. AERIS, accessed 20 February 2022, https://doi.org/10.25326/68.

Bodhaine, B. A., B. G. Mendonca, J. M. Harris, and J. M. Miller, 1981: Seasonal variations in aerosols and atmospheric transmission at Mauna Loa Observatory. *J. Geophys. Res.*, **86**, 7395–7398, https://doi.org/10.1029/JC086iC08p07395.

Bojinski, S., M. Verstraete, T. Peterson, C. Richter, A. Simmons, and M. Zemp, 2014: The concept of essential climate variables in support of climate research, applications, and policy. *Bull. Amer. Meteor. Soc.*, **95**, 1431–1443, https://doi.org/10.1175/BAMS-D-13-00047.1.

Brohan, P., J. J. Kennedy, I. Harris, S. F. B. Tett, and P. D. Jones, 2006: Uncertainty estimates in regional and global observed temperature changes: A new data set from 1850. *J. Geophys. Res.*, **111**, D12106, https://doi.org/10.1029/2005JD006548.

Brooks, C., 1925: *The Distribution of Thunderstorms over the Globe*. Geophysical Memoirs, No. 24, H. M. Stationery Office, 164 pp.

Brown, J. R., and Coauthors, 2020: South Pacific Convergence Zone dynamics, variability and impacts in a changing climate. *Nat. Rev. Earth Environ.*, **1**, 530–543, https://doi.org/10.1038/s43017-020-0078-2.

Brutsaert, W., 2017: Global land surface evaporation trend during the past half century: Corroboration by Clausius-Clapeyron scaling. *Adv. Water Resour.*, **106**, 3–5, https://doi.org/10.1016/j.advwatres.2016.08.014.

Buchholz, R. R., and Coauthors, 2021: Air pollution trends measured from Terra: CO and AOD over industrial, fire-prone, and 22 background regions. *Remote Sens. Environ.*, **256**, 112275, https://doi.org/10.1016/j.rse.2020.112275.

Bureau of Meteorology, 2021a: New South Wales in March 2021: A very wet and cool month with extensive flooding. Accessed 9 February 2022, www.bom.gov.au/climate/current/month/nsw/archive/202103.summary.shtml.

——, 2021b: New South Wales in November 2021: Wettest on record. Accessed 9 February 2022, www.bom.gov.au/climate/current/month/nsw/archive/202111.summary.shtml.

——, 2021c: Queensland in November 2021: Seventh-wettest November; wettest since 2010. Accessed 9 February 2022, www.bom.gov.au/climate/current/month/qld/archive/202111.summary.shtml.

——, 2021d: Western Australia in April 2021: Wet in the west; warm in the south. Accessed 9 February 2022, www.bom.gov.au/climate/current/month/wa/archive/202104.summary.shtml.

——, 2022: Annual climate statement 2021: 2021 coolest year in nearly a decade and wettest since 2016. 1 June 2022, https://media.bom.gov.au/releases/919/2021-coolest-year-in-nearly-a-decade-and-wettest-since-2016/.

Carpenter, L. J., and J. S. Daniel, 2018: Scenarios and information for policy makers. Scientific Assessment of Ozone Depletion: 2018, Global Ozone Research and Monitoring Project Rep. 58, 6.1–6.69, https://ozone.unep.org/sites/default/files/2019-05/SAP-2018-Assessment-report.pdf.

Carrea, L., O. Embury, and C. J. Merchant, 2015: Datasets related to in-land water for limnology and remote sensing applications: Distance-to-land, distance-to-water, water-body identifier and lake-centre co-ordinates. *Geosci. Data J.*, **2**, 83–97, https://doi.org/10.1002/gdj3.32.

——, and Coauthors, 2019: Lake surface temperature [in "State of the Climate in 2018"]. *Bull. Amer. Meteor. Soc.*, **100** (9), S13–S14, https://doi.org/10.1175/2019BAMSStateoftheClimate.1.

——, and Coauthors, 2020: Lake surface temperature [in "State of the Climate in 2019"]. *Bull. Amer. Meteor. Soc.*, **101** (8), S26–S28, https://doi.org/10.1175/BAMS-D-20-0104.1.

——, C. Merchant, B. Calmettes, and J.-F. Cretaux, 2021: Lake surface temperature [in "State of the Climate in 2020"]. *Bull. Amer. Meteor. Soc.*, **102** (8), S28–S31, https://doi.org/10.1175/BAMS-D-21-0098.1.

Cassou, C., 2008: Intraseasonal interaction between the Madden-Julian Oscillation and the North Atlantic Oscillation. *Nature*, **455**, 523–527, https://doi.org/10.1038/nature07286.

Cescatti, A., and Coauthors, 2012: Intercomparison of MODIS albedo retrievals and in situ measurements across the global FLUXNET network. *Remote Sens. Environ.*, **121**, 323–334, https://doi.org/10.1016/j.rse.2012.02.019.

Chang, J., S. Peng, P. Ciais, M. Saunois, S. R. Dangal, M. Herrero, P. Havlík, H. Tian, and P. Bousquet, 2019: Revisiting enteric methane emissions from domestic ruminants and their $\delta^{13}C_{CH4}$ source signature. *Nat. Comms.*, **10** (1), 1–14, https://doi.org/10.1038/s41467-019-11066-3.

Chang, K.-L., M. G. Schultz, X. Lan, A. McClure-Begley, I. Petropavlovskikh, X. Xu, and J. R. Ziemke, 2021: Trend detection of atmospheric time series: Incorporating appropriate uncertainty estimates and handling extreme events. *Elem. Sci. Anthropocene*, **9**, 00035, https://doi.org/10.1525/elementa.2021.00035.

——, and Coauthors, 2022: Impact of the COVID-19 economic downturn on tropospheric ozone trends: An uncertainty weighted data synthesis for quantifying regional anomalies above western North America and Europe, *AGU Adv.*, **3**, e2021AV000542, https://doi.org/10.1029/2021AV000542.

Chen, Y., D. Romps, J. Seeley, S. Veraverbeke, W. Riley, Z. Mekonnen, and J. Randerson, 2021: Future increases in Arctic lightning and fire risk for permafrost carbon. *Nat. Climate Change*, **11**, 404–410, https://doi.org/10.1038/s41558-021-01011-y.

Cheng, L., and Coauthors, 2017: Recent increases in terrestrial carbon uptake at little cost to the water cycle. *Nat. Commun.*, **8**, 110, https://doi.org/10.1038/s41467-017-00114-5.

Chipperfield, M. P., and Coauthors, 2018: On the cause of recent variations in lower stratospheric ozone. *Geophys. Res. Lett.*, **45**, 5718–5726, https://doi.org/10.1029/2018GL078071.

Christian, H., and Coauthors, 2003: Global frequency and distribution of lightning as observed from space by the optical transient detector. *J. Geophys. Res.*, **108**, 4005, https://doi.org/10.1029/2002JD002347.

Christiansen, H. H., G. L. Gilbert, U. Neumann, N. Demidov, M. Guglielmin, K. Isaksen, M. Osuch, and J. Boike, 2021: Ground ice content, drilling methods and equipment and permafrost dynamics in Svalbard 2016–2019 (PermaSval). SESS Report 2020, M. Moreno-Ibáñez et al., Eds., Svalbard Integrated Arctic Earth Observing System, 259–275, https://sios-svalbard.org/SESS_Issue3.

Christy, J. R., R. W. Spencer, W. D. Braswell, and R. Junod, 2018: Examination of space-based bulk atmospheric temperatures for climate research. *Yaogan Xuebao*, **39**, 3580–3607, https://doi.org/10.1080/01431161.2018.1444293.

Chronis, T., S. Goodman, D. Cecil, D. Buechler, F. Robertson, J. Pittman, and R. Blakeslee, 2008: Global lightning activity from the ENSO perspective. *Geophys. Res. Lett.*, **35**, L19804, https://doi.org/10.1029/2008GL034321.

Chung, E.-S., B. Soden, and V. O. John, 2013: Intercalibrating microwave satellite observations for monitoring long-term variations in upper- and midtropospheric water vapor. *J. Atmos. Oceanic Technol.*, **30**, 2303–2319, https://doi.org/10.1175/JTECH-D-13-00001.1.

——, B. J. Soden, X. Huang, L. Shi, and V. O. John, 2016: An assessment of the consistency between satellite measurements of upper tropospheric water vapor. *J. Geophys. Res.*, **121**, 2874–2887, https://doi.org/10.1002/2015JD024496.

Cicoira, A., J. Beutel, J. Faillettaz, and A. Vieli, 2019: Water controls the seasonal rhythm of rock glacier flow. *Earth Planet. Sci. Lett.*, **528**, 115844, https://doi.org/10.1016/j.epsl.2019.115844.

Coddington, O. M., 2017: TSIS Algorithm Theoretical Basis Document. Laboratory for Atmospheres and Space Physcis (LASP) Document 151430 RevA, 108 pp., https://docserver.gesdisc.eosdis.nasa.gov/public/project/TSIS/TSIS_Algorithm_Theoretical_Basis_Document_151430RevA.pdf.

Coldewey-Egbers, M., and Coauthors, 2015: The GOME-type Total Ozone Essential Climate Variable (GTO-ECV) data record from the ESA Climate Change Initiative. *Atmos. Meas. Tech.*, **8**, 3923–3940, https://doi.org/10.5194/amt-8-3923-2015.

——, D. G. Loyola, C. Lerot, and M. Van Roozendael, 2022: Global, regional and seasonal analysis of total ozone trends derived from the 1995–2020 GTO-ECV climate data record. *Atmos. Chem. Phys.*, **22**, 6861–6878, https://doi.org/10.5194/acp-22-6861-2022.

Colman, R., and B. J. Soden, 2021: Water vapor and lapse rate feedbacks in the climate system. *Rev. Mod. Phys.*, **93**, 045002, https://doi.org/10.1103/RevModPhys.93.045002.

Cooper, M., and R. Holle, 2019: *Reducing Lightning Injuries Worldwide.* Springer, 233 pp., https://doi.org/10.1007/978-3-319-77563-0.

Cooper, O. R., and Coauthors, 2014: Global distribution and trends of tropospheric ozone: An observation-based review. *Elem. Sci. Anthropocene*, **2**, 000029, http://doi.org/10.12952/journal.elementa.000029.

——, and Coauthors, 2020: Multi-decadal surface ozone trends at globally distributed remote locations. *Elem. Sci. Anthropocene*, **8**, 23, https://doi.org/10.1525/elementa.420.

Cornes, R. C., E. C. Kent, D. I. Berry, and J. J. Kennedy, 2020: CLASSnmat: A global night marine air temperature data set, 1880–2019. *Geosci. Data J.*, **7**, 170–184, https://doi.org/10.1002/gdj3.100.

——, D. I. Berry, R. Junod, E. C. Kent, and N. A. Rayner, 2021: Night marine air temperature [in "State of the Climate in 2020"]. *Bull. Amer. Meteor. Soc.*, **102** (8), S39–S41, https://doi.org/10.1175/BAMS-D-21-0098.1.

Cox, P. M., D. Pearson, B. B. Booth, P. Friedlingstein, C. Huntingford, C. D. Jones, and C. M. Luke, 2013: Sensitivity of tropical carbon to climate change constrained by carbon dioxide variability. *Nature*, **494**, 341–344, https://doi.org/10.1038/nature11882.

Crocetti, L., and Coauthors, 2020: Earth Observation for agricultural drought monitoring in the Pannonian Basin (southeastern Europe): Current state and future directions. *Reg. Environ. Change*, **20**, 123, https://doi.org/10.1007/s10113-020-01710-w.

Cusicanqui, D., A. Rabatel, C. Vincent, X. Bodin, E. Thibert, and B. Francou, 2021: Interpretation of volume and flux changes of the Laurichard Rock Glacier between 1952 and 2019, French Alps. *J. Geophys. Res. Earth Surface*, 126, e2021JF006161, https://doi.org/10.1029/2021JF006161.

Daniel, J. S., S. Solomon, and D. L. Albritton, 1995: On the evaluation of halocarbon radiative forcing and global warming potentials. *J. Geophys. Res.*, **100**, 1271–1285, https://doi.org/10.1029/94JD02516.

Davidson, E. A., 2009: The contribution of manure and fertilizer nitrogen to atmospheric nitrous oxide since 1860. *Nat. Geosci.*, **2**, 659–662, https://doi.org/10.1038/ngeo608.

Davis, S. M., K. H. Rosenlof, D. F. Hurst, and H. Vömel, 2021: Stratospheric water vapor [in "State of the Climate in 2020"]. *Bull. Amer. Meteor. Soc.*, **102** (8), S95–S98, https://doi.org/10.1175/BAMS-D-21-0098.1.

Dee, D. P., and Coauthors, 2011: The ERA-Interim reanalysis: Configuration and performance of the data assimilation system. *Quart. J. Roy. Meteor. Soc.*, **137**, 553–597, https://doi.org/10.1002/qj.828.

Deeter, M. N., and Coauthors, 2014: The MOPITT Version 6 product: Algorithm enhancements and validation. *Atmos. Meas. Tech.*, **7**, 3623–3632, https://doi.org/10.5194/amt-7-3623-2014.

——, D. P. Edwards, G. L. Francis, J. C. Gille, S. Martínez-Alonso, H. M. Worden, and C. Sweeney, 2017: A climate-scale satellite record for carbon monoxide: the MOPITT Version 7 product. *Atmos. Meas. Tech.*, **10**, 2533–2555, https://doi.org/10.5194/amt-10-2533-2017.

——, and Coauthors, 2019: Radiance-based retrieval bias mitigation for the MOPITT instrument: The version 8 product. *Atmos. Meas. Tech.*, **12**, 4561–4580, https://doi.org/10.5194/amt-12-4561-2019.

Del Genio, A., M. Yao, and J. Jonas, 2007: Will moist convection be stronger in a warmer climate? *Geophys. Res. Lett.*, **34**, L16703, https://doi.org/10.1029/2007GL030525.

Delaloye, R., and Coauthors, 2008: Recent interannual variations of rock glacier creep in the European Alps. *Proc. of the 9th Int. Conf. on Permafrost*, Fairbanks, AK, University of Alaska Fairbanks, 343–348.

——, C. Lambiel, and I. Gärtner-Roer, 2010: Overview of rock glacier kinematics research in the Swiss Alps. *Geogr. Helv.*, **65**, 135–145, https://doi.org/10.5194/gh-65-135-2010.

De Mazière, M., and Coauthors, 2018: The Network for the Detection of Atmospheric Composition Change (NDACC): History, status and perspectives. *Atmos. Chem. Phys.*, **18**, 4935–4964, https://doi.org/10.5194/acp-18-4935-2018.

Deng, K., C. Azorin-Molina, L. Minola, G. Zhang, and D. Chen, 2021: Global near-surface wind speed changes over the last decades revealed by reanalyses and CMIP6 model simulations. *J. Climate*, **34**, 2219–2234, https://doi.org/10.1175/JCLI-D-20-0310.1.

——, ——, S. Yang, C. Hu, G. Zhang, L. Minola, and D. Chen, 2022: Changes of Southern Hemisphere westerlies in the future warming climate. *Atmos. Res.*, **270**, 106040, https://doi.org/10.1016/j.atmosres.2022.106040.

Dessler, A. E., M. R. Schoeberl, T. Wang, S. M. Davis, K. H. Rosenlof, and J. P. Vernier, 2014: Variations of stratospheric water vapor over the past three decades. *J. Geophys. Res. Atmos.*, **119**, 12 588–12 598, https://doi.org/10.1002/2014JD021712.

Dewitte, S., D. Crommelynck, and A. Joukof, 2004: Total solar irradiance observations from DIARAD/VIRGO. *J. Geophys. Res.*, **109**, A02102, https://doi.org/10.1029/2002JA009694.

Di Girolamo, L., A. Menzies, G. Zhao, K. Mueller, C. Moroney, and D. J. Diner, 2010: Multi-angle imaging SpectroRadiometer level 3 cloud fraction by altitude algorithm theoretical basis document. JPL Publ., D-62358, 23 pp., https://eospso.nasa.gov/sites/default/files/atbd/MISR_CFBA_ATBD.pdf.

DiGangi, E. A., M. Stock, and J. Lapierre, 2022: Thunder hours: How old methods offer new insights into thunderstorm climatology. *Bull. Amer. Meteor. Soc.*, **103**, E548–E569, https://doi.org/10.1175/BAMS-D-20-0198.1.

Dlugokencky, E. J., L. P. Steele, P. M. Lang, and K. A. Masarie, 1994: The growth rate and distribution of atmospheric methane. *J. Geophys. Res. Atmos.*, **99**(D8), 17 021–17 043, https://doi.org/10.1029/94JD01245.

——, S. Houweling, L. Bruhwiler, K. A. Masarie, P. M. Lang, J. B. Miller, and P. P. Tans, 2003: Atmospheric methane levels off: Temporary pause or a new steady-state? *Geophys. Res. Lett.*, **30**, 1992, https://doi.org/10.1029/2003GL018126.

Döll, P., and B. Lehner, 2002: Validation of a new global 30-min drainage direction map. *J. Hydrol.*, **258**, 214–231, https://doi.org/10.1016/S0022-1694(01)00565-0.

Donat, M., L. Alexander, H. Yang, I. Durre, R. Vose, and J. Caesar, 2013: Global land based datasets for monitoring climatic extremes. *Bull. Amer. Meteor. Soc.*, **94**, 997–1006, https://doi.org/10.1175/BAMS-D-12-00109.1.

Dong, B., and R. Sutton, 2015: Dominant role of greenhouse-gas forcing in the recovery of Sahel rainfall. *Nat. Climate Change*, **5**, 757–760, https://doi.org/10.1038/nclimate2664.

Dorigo, W. A., and Coauthors, 2017: ESA CCI Soil Moisture for improved Earth system understanding: State-of-the art and future directions. *Remote Sens. Environ.*, **203**, 185–215, https://doi.org/10.1016/j.rse.2017.07.001.

——, L. Moesinger, R. van der Schalie, R. M. Zotta, T. Scanlon, and R. A. M. de Jeu, 2021: Long-term monitoring of vegetation state through passive microwave satellites [in "State of the Climate in 2020"]. *Bull. Amer. Meteor. Soc.*, **102** (8), S110–S112, https://doi.org/10.1175/BAMS-D-21-0098.1.

Dunn, R. J. H., 2019: HadISD version 3: Monthly updates. Hadley Centre Technical Note 103, 10 pp., www.metoffice.gov.uk/research/library-and-archive/publications/science/climate-science-technical-notes.

——, and C. P. Morice, 2022: On the effect of reference periods on trends in percentile-based extreme temperature indices. *Environ. Res. Lett.*, **17**, 034026, https://doi.org/10.1088/1748-9326/ac52c8.

——, K. M. Willett, P. W. Thorne, E. V. Woolley, I. Durre, A. Dai, D. E. Parker, and R. S. Vose, 2012: HadISD: A quality-controlled global synoptic report database for selected variables at long-term stations from 1973–2011. *Climate Past*, **8**, 1649–1679, https://doi.org/10.5194/cp-8-1649-2012.

——, K. M. Willett, D. E. Parker, and L. Mitchell, 2016: Expanding HadISD: Quality-controlled, sub-daily station data from 1931. *Geosci. Instrum. Methods Data Syst.*, **5**, 473–491, https://doi.org/10.5194/gi-5-473-2016.

——, and Coauthors, 2020: Development of an updated global land in-situ-based dataset of temperature and precipitation extremes: HadEX3. *J. Geophys. Res. Atmos.*, **125**, e2019JD032263, https://doi.org/10.1029/2019JD032263.

Dussaillant, I., and Coauthors, 2019: Two decades of glacier mass loss along the Andes. *Nat. Geosci.*, **12**, 802–808, https://doi.org/10.1038/s41561-019-0432-5.

Edwards, M., and A. Richardson, 2004: Impact of climate change on marine pelagic phenology and trophic mismatch. *Nature*, **430**, 881–884, https://doi.org/10.1038/nature02808.

Ellis, H. T., and R. F. Pueschel, 1971: Solar radiation: Absence of air pollution trends at Mauna Loa. *Science*, **172**, 845–846, https://doi.org/10.1126/science.172.3985.845.

Else, H., 2021: Climate change implicated in Germany's deadly floods. *Nature*, https://doi.org/10.1038/d41586-021-02330-y.

Engel, A., and M. Rigby, 2018: Update on ozone-depleting substances (ODSs) and other gases of interest to the Montreal protocol. Scientific Assessment of Ozone Depletion: 2018, Global Ozone Research and Monitoring Project Rep. 58, 1.1–1.66, https://ozone.unep.org/sites/default/files/2019-05/SAP-2018-Assessment-report.pdf.

Eriksen, H. Ø., L. Rouyet, T. R. Lauknes, I. Berthling, K. Isaksen, H. Hindberg, Y. Larsen, and G. D. Corner, 2018: Recent acceleration of a rock glacier complex, Ádjet, Norway, documented by 62 years of remote sensing observations. *Geophys. Res. Lett.*, **45**, 8314–8323, https://doi.org/10.1029/2018GL077605.

Espinoza, J.-C., J. A. Marengo, J. Schongart, and J. C. Jimenez, 2022: The new historical flood of 2021 in the Amazon River compared to major floods of the 21st century: Atmospheric features in the context of the intensification of floods. *Wea. Climate Extremes*, **35**, 100406, https://doi.org/10.1016/j.wace.2021.100406.

Estilow, T. W., A. H. Young, and D. A. Robinson, 2015: A long-term Northern Hemisphere snow cover extent data record for climate studies and monitoring. *Earth Syst. Sci. Data*, **7**, 137–142, https://doi.org/10.5194/essd-7-137-2015.

Etheridge, D. M., L. P. Steele, R. L. Langenfelds, R. J. Francey, J. M. Barnola, and V. I. Morgan, 1996: Natural and anthropogenic changes in atmospheric CO_2 over the last 1000 years from air in Antarctic ice and firn. *J. Geophys. Res.*, **101**, 4115–4128, https://doi.org/10.1029/95JD03410.

Etzelmüller, B., and Coauthors, 2020: Twenty years of European mountain permafrost dynamics – The PACE legacy. *Environ. Res. Lett.*, **15**, 104070, https://doi.org/10.1088/1748-9326/abae9d.

Finney, D., 2021: Lightning threatens permafrost. *Nat. Climate Change*, **11**, 379–380, https://doi.org/10.1038/s41558-021-01016-7.

Fioletov, V. E., G. E. Bodeker, A. J. Miller, R. D. McPeters, and R. Stolarski, 2002: Global and zonal total ozone variations estimated from ground-based and satellite measurements: 1964–2000. *J. Geophys. Res.*, **107**, 4647, https://doi.org/10.1029/2001JD001350.

——, and Coauthors, 2008: The performance of the ground-based total ozone network assessed using satellite data. *J. Geophys. Res.*, **113**, D14313, https://doi.org/10.1029/2008JD009809.

Fleming, Z. L., and Coauthors, 2018: Tropospheric Ozone Assessment Report: Present-day ozone distribution and trends relevant to human health. *Elem. Sci. Anthropocene*, **6**, 12, https://doi.org/10.1525/elementa.273.

Flemming, J., and A. Inness, 2018: Carbon monoxide [in "State of the Climate in 2017"]. *Bull. Amer. Meteor. Soc.*, **99** (8), S59–S61, https://doi.org/10.1175/2018BAMSStateoftheClimate.1.

——, and Coauthors, 2017: The CAMS interim reanalysis of carbon monoxide, ozone and aerosol for 2003–2015. *Atmos. Chem. Phys.*, **17**, 1945–1983, https://doi.org/10.5194/acp-17-1945-2017.

Frauenfelder, R., W. Haeberli, and M. Hoelzle, 2003: Rock glacier occurrence and related terrain parameters in a study area of the Eastern Swiss Alps. *Permafrost: Proceedings of the 8th International Conference on Permafrost*, M. Phillips, S. M. Springman, and L. U. Arenson, Eds., A. A. Balkema, 253–258.

Free, M., D. J. Seidel, J. K. Angel, J. Lanzante, I. Durre, and T. C. Peterson, 2005: Radiosonde Atmospheric Temperature Products for Assessing Climate (RATPAC): A new dataset of large-area anomaly time series. *J. Geophys. Res.*, **110**, D22101, https://doi.org/10.1029/2005JD006169.

Friedlingstein, P., and Coauthors, 2022: Global carbon budget 2021. *Earth Syst. Sci. Data*, **14**, 1917–2005, https://doi.org/10.5194/essd-14-1917-2022.

Frith, S. M., N. A. Kramarova, R. S. Stolarski, R. D. McPeters, P. K. Bhartia, and G. J. Labow, 2014: Recent changes in total column ozone based on the SBUV Version 8.6 Merged Ozone Data Set. *J. Geophys. Res. Atmos.*, **119**, 9735–9751, https://doi.org/10.1002/2014JD021889.

——, R. S. Stolarski, N. A. Kramarova, and R. D. McPeters, 2017: Estimating uncertainties in the SBUV Version 8.6 merged profile ozone data set. *Atmos. Chem. Phys.*, **17**, 14695–14707, https://doi.org/10.5194/acp-17-14695-2017.

Garane, K., and Coauthors, 2018: Quality assessment of the Ozone_cci Climate Research Data Package (release 2017): 1. Ground-based validation of total ozone column data products. *Atmos. Meas. Tech.*, **11**, 1385–1402, https://doi.org/10.5194/amt-11-1385-2018.

Garcia, H. E., and Coauthors 2019: World Ocean Atlas 2018: Product documentation. NOAA, 20 pp., www.ncei.noaa.gov/sites/default/files/2020-04/woa18documentation.pdf.

Garfinkel, C. I., and Coauthors, 2021: Influence of the El Niño–Southern Oscillation on entry stratospheric water vapor in coupled chemistry–ocean CCMI and CMIP6 models. *Atmos. Chem. Phys.*, **21**, 3725–3740, https://doi.org/10.5194/acp-21-3725-2021.

Gaubert, B., and Coauthors, 2017: Chemical feedback from decreasing carbon monoxide emissions. *Geophys. Res. Lett.*, **44**, 9985–9995, https://doi.org/10.1002/2017GL074987.

Gaudel, A., and Coauthors, 2018: Tropospheric Ozone Assessment Report: Present-day distribution and trends of tropospheric ozone relevant to climate and global atmospheric chemistry model evaluation. *Elem. Sci. Anthropocene*, 6, 39, https://doi.org/10.1525/elementa.291.

——, and Coauthors, 2020: Aircraft observations since the 1990s reveal increases of tropospheric ozone at multiple locations across the Northern Hemisphere. *Sci. Adv.*, **6**, eaba8272, https://doi.org/10.1126/sciadv.aba8272.

GCOS, 2016: The Global Observing System for Climate: Implementation needs. Tech. Rep. GCOS-200, World Meteorological Organization, 315 pp., https://library.wmo.int/doc_num.php?explnum_id=3417.

Gelaro, R., and Coauthors, 2017: The Modern-Era Retrospective Analysis for Research and Applications, version 2 (MERRA-2). *J. Climate*, **30**, 5419–5454, https://doi.org/10.1175/JCLI-D-16-0758.1.

Getirana, A., S. Kumar, M. Girotto, and M. Rodell, 2017: Rivers and floodplains as key components of global terrestrial water storage variability. *Geophys. Res. Lett.*, **44**, 10359–10368, https://doi.org/10.1002/2017GL074684.

Giglio, L., W. Schroeder, and C. O. Justice, 2016: The Collection 6 MODIS active fire detection algorithm and fire products. *Remote Sens. Environ.*, **178**, 31–41, https://doi.org/10.1016/j.rse.2016.02.054.

GISTEMP Team, 2022: GISS Surface Temperature Analysis (GISTEMP v4). NASA Goddard Institute for Space Studies, accessed 15 February 2022, https://data.giss.nasa.gov/gistemp/.

Gobron, N., and A. S. Belward, 2011: Fraction of Absorbed Photosynthetically Active Radiation (FAPAR) [in "State of the Climate in 2010"]. *Bull. Amer. Meteor. Soc.*, **92** (6), S72, https://doi.org/10.1175/1520-0477-92.6.S1.

——, and M. Robustelli, 2013: Monitoring the state of the global terrestrial surfaces. *Proc. 2013 ESA Living Planet Symp.*, Edinburgh, United Kingdom, European Space Agency, JRC84937, https://publications.jrc.ec.europa.eu/repository/handle/JRC84937.

——, A. S. Belward, B. Pinty, and W. Knorr, 2010: Monitoring biosphere vegetation 1998-2009. *Geophys. Res. Lett.*, **37**, L15402, https://doi.org/10.1029/2010GL043870.

Godin-Beekmann, S., and Coauthors, 2022: Updated trends of the stratospheric ozone vertical distribution in the 60°S–60°N latitude range based on the LOTUS regression model *Atmos. Chem. Phys.*, https://doi.org/10.5194/acp-2022-137, in press.

Gonsamo, A., and Coauthors, 2021: Greening drylands despite warming consistent with carbon dioxide fertilization effect. *Global Change Biol.*, **27** (14), 3336–3349, https://doi.org/10.1111/gcb.15658.

Goodman, S. J., and H. Christian, 1993: Global observations of lightning. *Atlas of Satellite Observations Related to Global Change*, R. Gurney, J. Foster, and C. Parkinson, Eds., Cambridge University Press, 191–222.

——, D. E. Buechler, K. Knupp, K. Driscoll, and E. W. McCaul, 2000: The 1997–98 El Nino event and related wintertime lightning variations in the southeastern United States. *Geophys. Res. Lett.*, **27**, 541–544, https://doi.org/10.1029/1999GL010808.

Gordillo-Vázquez, F. J., F. J. Pérez-Invernón, H. Huntrieser, and A. K. Smith, 2019: Comparison of six lightning parameterizations in CAM5 and the impact on global atmospheric chemistry. *Earth Space Sci.*, **6**, 2317–2346, https://doi.org/10.1029/2019EA000873.

Grandt, C., 1992: Thunderstorm monitoring in South Africa and Europe by means of very low frequency sferics. *J. Geophys. Res.*, **97**, 18215–18226, https://doi.org/10.1029/92JD01623.

Granier, C., and Coauthors, 2011: Evolution of anthropogenic and biomass burning emissions of air pollutants at global and regional scales during the 1980–2010 period. *Climatic Change*, **109**, 163–190, https://doi.org/10.1007/s10584-011-0154-1.

Grant, L., and Coauthors, 2021: Attribution of global lake systems change to anthropogenic forcing. *Nat. Geosci.*, **14**, 849–854, https://doi.org/10.1038/s41561-021-00833-x.

Griffiths, P. T., and Coauthors, 2021: Tropospheric ozone in CMIP6 simulations. *Atmos. Chem. Phys.*, 21, 4187–4218, https://doi.org/10.5194/acp-21-4187-2021.

Gruber, A., W. A. Dorigo, W. Crow, and W. Wagner, 2017: Triple collocation-based merging of satellite soil moisture retrievals. I*EEE Trans. Geosci. Remote Sens.*, **55**, 6780–6792, https://doi.org/10.1109/TGRS.2017.2734070.

——, T. Scanlon, R. van der Schalie, W. Wagner, and W. Dorigo, 2019: Evolution of the ESA CCI Soil Moisture climate data records and their underlying merging methodology. *Earth Syst. Sci. Data*, **11**, 717–739, https://doi.org/10.5194/essd-11-717-2019.

Gui, K., and Coauthors, 2022: Record-breaking dust loading during two mega dust storm events over northern China in March 2021: aerosol optical and radiative properties and meteorological drivers. *Atmos. Chem. Phys.*, 22, 7905–7932, https://doi.org/10.5194/acp-22-7905-2022.

Gulev, S. K., and Coauthors, 2021: Changing state of the climate system. *Climate Change 2021: The Physical Science Basis*, V. Masson-Delmotte et al., Eds., Cambridge University Press, 287–422, https://doi.org/10.1017/9781009157896.004.

Haberkorn, A., R. Kenner, J. Noetzli, and M. Phillips, 2021: Changes in ground temperature and dynamics in mountain permafrost in the Swiss Alps. *Front. Earth Sci.*, **9**, 626686, https://doi.org/10.3389/feart.2021.626686.

Haimberger, L., C. Tavolato, and S. Sperka, 2012: Homogenization of the global radiosonde temperature dataset through combined comparison with reanalysis background series and neighboring stations. *J. Climate*, **25**, 8108–8131, https://doi.org/10.1175/JCLI-D-11-00668.1.

Hansen, J., R. Ruedy, M. Sato, and K. Lo, 2010: Global surface temperature change. *Rev. Geophys.*, **48**, RG4004, https://doi.org/10.1029/2010RG000345.

Harel, M., and C. Price, 2020: Thunder trends over Africa. *J. Climate*, **33**, 2741–2755, https://doi.org/10.1175/JCLI-D-18-0781.1.

Harris, I., T. J. Osborn, P. D. Jones, and D. H. Lister, 2020: Version 4 of the CRU TS monthly high-resolution gridded multivariate climate dataset. *Sci. Data*, **7**, 109, https://doi.org/10.1038/s41597-020-0453-3.

Heidinger, A. K., M. J. Foster, A. Walther, and X. Zhao, 2013: The Pathfinder Atmospheres–Extended AVHRR Climate Dataset. *Bull. Amer. Meteor. Soc.*, **95**, 909–922, https://doi.org/10.1175/BAMS-D-12-00246.1.

Hersbach, H., and Coauthors, 2020: The ERA5 global reanalysis. *Quart. J. Roy. Meteor. Soc.*, **146**, 1999–2049, https://doi.org/10.1002/qj.3803.

Ho, S.-P., X. Zhou, Y.-H. Kuo, D. Hunt, and J.-H. Wang, 2010a: Global evaluation of radiosonde water vapor systematic biases using GPS radio occultation from COSMIC and ECMWF analysis. *Remote Sens.*, **2**, 1320–1330, https://doi.org/10.3390/rs2051320.

——, Y.-H. Kuo, W. Schreiner, and X. Zhou, 2010b: Using SI-traceable global positioning system radio occultation measurements for climate monitoring [in "State of the Climate in 2009"]. *Bull. Amer. Meteor. Soc.*, **91** (7), S36–S37, https://doi.org/10.1175/BAMS-91-7-StateoftheClimate.

——, and Coauthors, 2020a: The COSMIC/FORMOSAT-3 radio occultation mission after 12 years: Accomplishments, remaining challenges, and potential impacts of COSMIC-2. *Bull. Amer. Meteor. Soc.*, **101**, E1107–E1136, https://doi.org/10.1175/BAMS-D-18-0290.1.

——, and Coauthors, 2020b: Initial assessment of the COSMIC-2/FORMOSAT-7 neutral atmosphere data quality in NESDIS/STAR using in situ and satellite data. *Remote Sens.*, **12**, 4099, https://doi.org/10.3390/rs12244099

Hobday, A. J., and Coauthors, 2016: A hierarchical approach to defining marine heatwaves. *Prog. Oceanogr.*, **141**, 227–238, https://doi.org/10.1016/j.pocean.2015.12.014.

——, and Coauthors, 2018: Categorizing and naming marine heatwaves. *Oceanography*, **31**, 162–173, https://doi.org/10.5670/oceanog.2018.205.

Hock, R., and Coauthors, 2019: High mountain areas. *IPCC Special Report on the Ocean and Cryosphere in a Changing Climate*, H.-O. Pörtner, Eds., IPCC, 131–202, www.ipcc.ch/srocc/.

Hofmann, D. J., and S. A. Montzka, 2009: Recovery of the Ozone Layer: The Ozone Depleting Gas Index. *Eos, Trans. Amer. Geophys. Union*, **90**, 1–2, https://doi.org/10.1029/2009EO010001.

——, J. H. Butler, E. J. Dlugokencky, J. W. Elkins, K. Masarie, S. A. Montzka, and P. Tans, 2006: The role of carbon dioxide in climate forcing from 1979 to 2004: Introduction of the annual greenhouse gas index. *Tellus*, **58B**, 614–619, https://doi.org/10.1111/j.1600-0889.2006.00201.x.

Holle, R., 2016: A recent summary of national-scale lightning fatality studies. *Wea. Climate Soc.*, **8**, 35–42, https://doi.org/10.1175/WCAS-D-15-0032.1.

——, R. Lopez, and C. Zimmermann, 1999: Updated recommendations for lightning safety–1998. *Bull. Amer. Meteor. Soc.*, **80**, 2035–2041, https://doi.org/10.1175/1520-0477(1999)080<2035:URFLS>2.0.CO;2.

Holzworth, R. H., M. P. McCarthy, J. B. Brundell, A. R. Jacobson, and C. J. Rodger, 2019: Global distribution of superbolts. *J. Geophys. Res. Atmos.*, **124**, 9996–10 005, https://doi.org/10.1029/2019JD030975.

——, J. B. Brundell, M. P. McCarthy, A. R. Jacobson, C. J. Rodger, and T. S. Anderson, 2021: Lightning in the Arctic. *Geophys. Res. Lett.*, **48**, e2020GL091366, https://doi.org/10.1029/2020GL091366.

Hrbáček, F., and Coauthors, 2021: Active layer monitoring in Antarctica: An overview of results from 2006 to 2015. *Polar Geogr.*, **44**, 217–231, https://doi.org/10.1080/1088937X.2017.1420105.

Hu, L., and Coauthors, 2019: Enhanced North American carbon uptake associated with El Niño. *Sci. Adv.*, **5**, eaaw0076, https://doi.org/10.1126/sciadv.aaw0076.

Huang, B., C. Liu, V. Banzon, E. Freeman, G. Graham, B. Hankins, T. Smith, and H.-M. Zhang. 2021: Improvements of the Daily Optimum Interpolation Sea Surface Temperature (DOISST) version 2.1. *J. Climate*, **34**, 2923–2939, https://doi.org/10.1175/JCLI-D-20-0166.1.

Huang, C.-Y., W.-H. Teng, S.-P. Ho, and Y. H. Kuo, 2013: Global variation of COSMIC precipitable water over land: Comparisons with ground-based GPS measurements and NCEP reanalyses. *Geophys. Res. Lett.*, **40**, 5327–5331, https://doi.org/10.1002/grl.50885.

Hugonnet, R., and Coauthors, 2021: Accelerated global glacier mass loss in the early twenty-first century. *Nature*, **592**, 726–731, https://doi.org/10.1038/s41586-021-03436-z.

Humphrey, V., J. Zscheischler, P. Ciais, L. Gudmundsson, S. Sitch, and S. I. Seneviratne, 2018: Sensitivity of atmospheric CO_2 growth rate to observed changes in terrestrial water storage. *Nature*, **560**, 628–631, https://doi.org/10.1038/s41586-018-0424-4.

Hurst, D. F., and Coauthors, 2016: Recent divergences in stratospheric water vapor measurements by frost point hygrometers and the Aura Microwave Limb Sounder. *Atmos. Meas. Tech.*, **9**, 4447–4457, https://doi.org/10.5194/amt-9-4447-2016.

Hüser, I., B. Gehrke, and J. W. Kaiser, 2018: Methodology to correct biases in individual satellite FRP products. CAMS Rep. CAMS44-2016SC3-D44.3.3.1-2018-20187, ECMWF, Reading, United Kingdom. 20 pp.

IMD, 2022: Statement on Climate of India during 2021. Climate Research and Services, India Meteorological Department, Ministry of Earth Sciences, Government of India, 9 pp., https://mausam.imd.gov.in/Forecast/marquee_data/Annual%20Statement%20on%20Climate%20of%20India%202021%20in%20English.pdf.

Ingram, W., 2010: A very simple model for the water vapour feedback on climate change. *Quart. J. Roy. Meteor. Soc.*, **136**, 30–40, https://doi.org/10.1002/qj.546.

Inness, A., and Coauthors, 2013: The MACC reanalysis: An 8-year data set of atmospheric composition. *Atmos. Chem. Phys.*, **13**, 4073–4109, https://doi.org/10.5194/acp-13-4073-2013.

——, A. Benedetti, J. Flemming, V. Huijnen, J. W. Kaiser, M. Parrington, and S. Remy, 2015: The ENSO signal in atmospheric composition fields: Emission-driven versus dynamically induced changes. *Atmos. Chem. Phys.*, **15**, 9083–9097, https://doi.org/10.5194/acp-15-9083-2015.

——, and Coauthors, 2019: The CAMS reanalysis of atmospheric composition. *Atmos. Chem. Phys.*, **19**, 3515–3556, https://doi.org/10.5194/acp-19-3515-2019.

IPCC, 2013: *Climate Change 2013: The Physical Science Basis*. Cambridge University Press, 1535 pp., https://doi.org/10.1017/CBO9781107415324.

——, 2021: Summary for policymakers. *Climate Change 2021: The Physical Science Basis*. V. Masson-Delmotte et al., Eds., Cambridge University Press, 3–32, https://doi.org/10.1017/9781009157896.001.

John, V. O., G. Holl, R. P. Allan, S. A. Buehler, D. E. Parker, and B. J. Soden, 2011: Clear-sky biases in satellite infra-red estimates of upper tropospheric humidity and its trends. *J. Geophys. Res.*, **116**, D14108, https://doi.org/10.1029/2010JD015355.

Joint Research Centre, 2021: Drought in southern Urals and Turan Depression October 2021. GDO Analytical Rep., 21 pp., https://edo.jrc.ec.europa.eu/documents/news/GDODroughtNews202110_Southern_Urals_and_Turan_Depression.pdf.

Junghänel, T. and Coauthors, 2021: Hydro-klimatologische Einordnung der Stark- und Dauerniederschläge in Teilen Deutschland sim Zusammenhang mit dem Tiefdruckgebiet "Bernd" vom 12. bis 19. Juli 2021 (in German). DWD, 16 pp., www.dwd.de/DE/leistungen/besondereereignisse/niederschlag/20210721_bericht_starkniederschlaege_tief_bernd.pdf?__blob=publicationFile&v=10.

Junod, R. A., and J. R. Christy, 2020: A new compilation of globally gridded nighttime marine air temperatures: The UAHNMATv1 dataset. *Int. J. Climatol.*, **40**, 2609–2623, https://doi.org/10.1002/joc.6354.

Kääb, A., R. Frauenfelder, and I. Roer, 2007: On the response of rockglacier creep to surface temperature increase. *Global Planet. Change*, **56**, 172–187, https://doi.org/10.1016/j.gloplacha.2006.07.005.

——, T. Strozzi, T. Bolch, R. Caduff, H. Trefall, M. Stoffel, and A. Kokarev, 2021: Inventory and changes of rock glacier creep speeds in Ile Alatau and Kungöy Ala-Too, northern Tien Shan, since the 1950s. *Cryosphere*, **15**, 927–949, https://doi.org/10.5194/tc-15-927-2021.

Kaiser, J. W., and Coauthors, 2012: Biomass burning emissions estimated with a global fire assimilation system based on observed fire radiative power. *Biogeosciences*, **9**, 527–554, https://doi.org/10.5194/bg-9-527-2012.

Kaplan, A., 2011: Patterns and indices of climate variability [in "State of the Climate in 2010"]. *Bull. Amer. Meteor. Soc.*, **92** (6), S20–S25, https://doi.org/10.1175/1520-0477-92.6.S1.

Karlsson, K.-G., and Coauthors, 2017: CLARA-A2: The second edition of the CM SAF cloud and radiation data record from 34 years of global AVHRR data. *Atmos. Chem. Phys.*, **17**, 5809–5828, https://doi.org/10.5194/ACP-17-5809-2017.

——, and Coauthors, 2020: CLARA-A2.1: CM SAF CLoud, Albedo and Surface RAdiation Dataset from AVHRR Data - Edition 2.1. Satellite Application Facility on Climate Monitoring, accessed 23 February 2022, https://doi.org/10.5676/EUM_SAF_CM/CLARA_AVHRR/V002_01.

——, and Coauthors, 2021: ICDR AVHRR - Based on CLARA-A2 Methods. Satellite Application Facility on Climate Monitoring, accessed 23 February 2022, https://wui.cmsaf.eu/safira/action/viewICDRDetails?acronym=CLARA_AVHRR_V002_ICDR.

Karpechko, A. Y., and A. C. Maycock, 2018: Stratospheric ozone changes and climate. Scientific Assessment of Ozone Depletion: 2018, Global Ozone Research and Monitoring Project Rep. 58, 5.1–5.50, https://ozone.unep.org/sites/default/files/2019-05/SAP-2018-Assessment-report.pdf.

Keeling, C. D., and R. Revelle, 1985: Effects of El-Nino Southern Oscillation on the atmospheric content of carbon-dioxide. *Meteoritics*, **20**, 437–450.

Kellerer-Pirklbauer, A., and V. Kaufmann, 2012: About the relationship between rock glacier velocity and climate parameters in central Austria. *Aust. J. Earth Sci.*, **105** (2), 94–112.

——, and Coauthors, 2018: Interannual variability of rock glacier flow velocities in the European Alps. *5th European Conf. on Permafrost*, Chamonix, France. Laboratoire EDYTEM, 615–616, https://hal.archives-ouvertes.fr/hal-01816115/.

Kendon, M., M. McCarthy, S. Jevrejeva, A. Matthews, T. Sparks, and J. Garforth, 2022: State of the UK Climate 2021. *Int. J. Climatol.*, **42** (S1), 1–80, https://doi.org/10.1002/joc.7787.

Kennedy, J. J., N. A. Rayner, C. P. Atkinson, and R. E. Killick, 2019: An ensemble data set of sea surface temperature change from 1850: The Met Office Hadley Centre HadSST.4.0.0.0 data set. *J. Geophys. Res. Atmos.*, **124**, 7719–7763, https://doi.org/10.1029/2018JD029867.

Kent, G. S., E. R. Williams, P. Wang, M. P. McCormick, and K. M. Skeens, 1995: Surface temperature-related variations in tropical cirrus clouds as measured by SAGE II. *J. Climate*, **8**, 2577–2594, https://doi.org/10.1175/1520-0442(1995)008%3C2577:STRVIT%3E2.0.CO;2.

Kim, H., 2020: River discharge and runoff [in "State of the Climate in 2019"]. *Bull. Amer. Meteor.*, **101** (8), S53–S55, https://doi.org/10.1175/BAMS-D-20-0104.1.

——, and D. Tokuda, 2021: River discharge and runoff [in "State of the Climate in 2020"]. *Bull. Amer. Meteor. Soc.*, **102** (8), S63–S65, https://doi.org/10.1175/BAMS-D-21-0098.1.

——, P. J.-F. Yeh, T. Oki, and S. Kanae, 2009: Role of rivers in the seasonal variations of terrestrial water storage over global basins. *Geophys. Res. Lett.*, **36**, L17402, https://doi.org/10.1029/2009GL039006.

Kitagawa, N., 1989: Long-term variations in thunder-day frequencies in Japan. *J. Geophys. Res.*, **94**, 13 183–13 189, https://doi.org/10.1029/JD094iD11p13183.

Klein Tank, A. M. G., and Coauthors, 2002: Daily dataset of 20th-century surface air temperature and precipitation series for the European Climate Assessment. *Int. J. Climatol.*, **22**, 1441–1453, https://doi.org/10.1002/joc.773.

Ko, M. K., P. A. Newman, S. Reimann, and S. E. Strahan, 2013: Recommended values for steady-state atmospheric lifetimes and their uncertainties. Lifetimes of Stratospheric Ozone-Depleting Substances, Their Replacements, and Related Species, M. K. W. Ko et al., Eds., SPARC Rep. 6, WCRP-15-2013, 6-1–6-21, www.sparc-climate.org/publications/sparc-reports/sparc-report-no-6/.

Kobayashi, S., and Coauthors, 2015: The JRA-55 Reanalysis: General specifications and basic characteristics. *J. Meteor. Soc. Japan*, **93**, 5–48, https://doi.org/10.2151/jmsj.2015-001.

Konings, A. G., Y. Yu, L. Xu, Y. Yang, D. S. Schimel, and S. S. Saatchi, 2017: Active microwave observations of diurnal and seasonal variations of canopy water content across the humid African tropical forests. *Geophys. Res. Lett.*, **44**, 2290–2299, https://doi.org/10.1002/2016GL072388.

Kopp, G., and J. L. Lean, 2011: A new, lower value of total solar irradiance: evidence and climate significance. *Geophys. Res. Lett.*, **38**, L01706, https://doi.org/10.1029/2010GL045777.

Kratz, D. P., P. W. Stackhouse Jr., S. K. Gupta, A. C. Wilber, P. Sawaengphokhai, and G. R. McGarragh, 2014: The Fast Longwave and Shortwave Flux (FLASHFlux) data product: Single scanner footprint fluxes. *J. Appl. Meteor. Climatol.*, **53**, 1059–1079, https://doi.org/10.1175/JAMC-D-13-061.1.

Lan, X., and Coauthors, 2021: Improved constraints on global methane emissions and sinks using $\delta^{13}C\text{-}CH_4$. *Global Biogeochem. Cycles*, **35**, e2021GB007000, https://doi.org/10.1029/2021GB007000.

Landerer, F. W., and Coauthors, 2020: Extending the global mass change data record: GRACE Follow-On instrument and science data performance. *Geophys. Res. Lett.*, **47**, e2020GL088306, https://doi.org/10.1029/2020GL088306.

Lassey, K. R., D. M. Etheridge, D. C. Lowe, A. M. Smith, and D. F. Ferretti, 2007: Centennial evolution of the atmospheric methane budget: What do the carbon isotopes tell us? *Atmos. Chem. Phys.*, **7**, 2119–2139, https://doi.org/10.5194/acp-7-2119-2007.

Laughner, J. L., and Coauthors, 2021: Societal shifts due to COVID-19 reveal large-scale complexities and feedbacks between atmospheric chemistry and climate change. *Proc. Natl. Acad. Sci. USA*, **118**, e2109481118, https://doi.org/10.1073/pnas.2109481118.

Lavigne, T., C. Liu, and N. Liu, 2019: How does the trend in thunder days relate to the variation of lightning flash density? *J. Geophys. Res. Atmos.*, **124**, 4955–4974, https://doi.org/10.1029/2018JD029920.

Lawrence, Z. D., J. Perlwitz, A. H. Butler, G. L. Manney, P. A. Newman, S. H. Lee, and E. R. Nash, 2020: The remarkably strong arctic stratospheric polar vortex of winter 2020: Links to record-breaking arctic oscillation and ozone loss. *J. Geophys. Res. Atmos.*, **125**, e2020JD033271, https://doi.org/10.1029/2020JD033271.

Lee, D. Y., M. R. Petersen, and W. Lin, 2019: The southern annular mode and southern ocean surface westerly winds in E3SM. *Earth Space Sci.*, **6**, 2624–2643, https://doi.org/10.1029/2019EA000663.

Lee, H.-T., and NOAA CDR Program, 2011: NOAA Climate Data Record (CDR) of Monthly Outgoing Longwave Radiation (OLR), version 2.2-1. Subset: March 2000–December 2021, NOAA National Climatic Data Center, accessed 6 January 2022, https://doi.org/10.7289/V5222RQP.

Lee, S. H., 2021: The January 2021 sudden stratospheric warming. *Weather*, **76**, 135–136, https://doi.org/10.1002/wea.3966.

Lenssen, N. J. L., G. A. Schmidt, J. E. Hansen, M. J. Menne, A. Persin, R. Ruedy, and D. Zyss, 2019: Improvements in the GISTEMP uncertainty model. *J. Geophys. Res. Atmos.*, **124**, 6307–6326, https://doi.org/10.1029/2018JD029522.

Levy, R. C., S. Mattoo, L. A. Munchak, L. A. Rember, A. M. Sayer, F. Patadia, and N. C. Hsu, 2013: The Collection 6 MODIS aerosol products over land and ocean. *Atmos. Meas. Tech.*, **6**, 2989–3034, https://doi.org/10.5194/amt-6-2989-2013.

Li, M., and Coauthors, 2017: Anthropogenic emission inventories in China: A review. *Nat. Sci. Rev.*, **4**, 834–866, https://doi.org/10.1093/nsr/nwx150.

Li, W., S. Zhao, Y. Chen, L. Wang, W. Hou, Y. Jiang, X. Zou, and S. Shi, 2022: State of China's climate in 2021. *Atmos. Ocean. Sci. Lett.*, **15**, 100211, https://doi.org/10.1016/j.aosl.2022.100211.

Lieb, G. K., and A. Kellerer-Pirklbauer, 2021: Sammelbericht über die Gletschermessungen des Österreichischen Alpenvereins im Jahr 2020. Letzter Bericht: Bergauf 2/2020, Jg. 75 (145), S. 6–15, www.alpenverein.at/portal_wAssets/docs/service/presse/2021/gletscherbericht/Alpenverein_Bergauf-2-21_Gletscherbericht.pdf.

Liu, Y., and Coauthors, 2021: Lightning enhancement in moist convection with smoke-laden air advected from Australian wildfires. *Geophys. Res. Lett.*, **48**, e2020GL092355, https://doi.org/10.1029/2020GL092355.

Livesey, N. J., and Coauthors, 2021: Investigation and amelioration of long-term instrumental drifts in water vapor and nitrous oxide measurements from the Aura Microwave Limb Sounder (MLS) and their implications for studies of variability and trends. *Atmos. Chem. Phys.*, **21**, 15 409–15 430, https://doi.org/10.5194/acp-21-15409-2021.

Lockwood, J. and Coauthors, 2022: Predictability of winter 2020/21: Influence of a mid-winter sudden stratospheric warming. *Atmos. Sci. Lett.*, in press, https://doi.org/10.1002/ASL.1126.

Loeb, N. G., B. A. Wielicki, D. R. Doelling, G. L. Smith, D. F. Keyes, S. Kato, N. Manalo-Smith, and T. Wong, 2009: Toward optimal closure of the Earth's top-of-atmosphere radiation budget. *J. Climate*, **22**, 748–766, https://doi.org/10.1175/2008JCLI2637.1.

——, S. Kato, W. Su, T. Wong, F. Rose, D. R. Doelling, and J. Norris, 2012: Advances in understanding top-of-atmosphere radiation variability from satellite observations. *Surv. Geophys.*, **33**, 359–385, https://doi.org/10.1007/s10712-012-9175-1.

——, and Coauthors, 2018a: Clouds and the Earth's Radiant Energy System (CERES) Energy Balanced and Filled (EBAF) top-of-atmosphere (TOA) Edition-4.0 data product. *J. Climate*, **31**, 895–918, https://doi.org/10.1175/JCLI-D-17-0208.1.

——, T. J. Thorsen, J. R. Norris, H. Wang, and W. Su, 2018b: Changes in Earth's energy budget during and after the "pause" in global warming: An observational perspective. *Climate*, **6**, 62, https://doi.org/10.3390/cli6030062.

——, G. C. Johnson, T. J. Thorsen, J. M. Lyman, F. G. Rose, and S. Kato, 2021: Satellite and ocean data reveal marked increase in Earth's heating rate. *Geophys. Res. Lett.*, **48**, e2021GL093047, https://doi.org/10.1029/2021GL093047.

Lu, Q., J. Rao, Z. Liang, D. Guo, J. Luo, S. Liu, C. Wang, and T. Wang, 2021: The sudden stratospheric warming in January 2021. *Environ. Res. Lett.*, **16**, 084029, https://doi.org/10.1088/1748-9326/ac12f4.

Lu, X., and Coauthors, 2019: Surface and tropospheric ozone trends in the Southern Hemisphere since 1990: Possible linkages to poleward expansion of the Hadley circulation. *Sci. Bull.*, **64**, 400–409, https://doi.org/10.1016/j.scib.2018.12.021.

MacCallum, S. N., and C. J. Merchant, 2012: Surface water temperature observations of large lakes by optimal estimation. *Can. J. Rem. Sens.*, **38**, 25–45, https://doi.org/10.5589/m12-010.

MacFarling Meure, C., D. Etheridge, C. Trudinger, P. Steele, R. Langenfelds, T. van Ommen, A. Smith, and J. Elkins, 2006: Law Dome CO_2, CH_4 and N_2O ice core records extended to 2000 years BP. *Geophys. Res. Lett.*, **33**, L14810, https://doi.org/10.1029/2006GL026152.

Madden, R. A., and P. R. Julian, 1971: Detection of a 40–50 day oscillation in the zonal wind in the tropical Pacific. *J. Atmos. Sci.*, **28**, 702–708, https://doi.org/10.1175/1520-0469(1971)028<0702:DOADOI>2.0.CO;2.

Magnin, F., P. Deline, L. Ravanel, J. Noetzli, and P. Pogliotti, 2015: Thermal characteristics of permafrost in the steep alpine rock walls of the Aiguille du Midi (Mont Blanc Massif, 3842 m asl). *Cryosphere*, **9**, 109–121, https://doi.org/10.5194/tc-9-109-2015.

Magnusson, L., A. Simmons, S. Harrigan, and F. Pappenberger, 2021: Extreme rain in Germany and Belgium in July 2021. *ECMWF Newsletter*, No. 169, ECMWF, Reading, United Kingdom, www.ecmwf.int/en/newsletter/169/news/extreme-rain-germany-and-belgium-july-2021.

Martens, B., and Coauthors, 2017: GLEAM v3: Satellite-based land evaporation and root-zone soil moisture. *Geosci. Model Dev.*, **10**, 1903–1925, https://doi.org/10.5194/gmd-10-1903-2017.

——, W. Waegeman, W. A. Dorigo, N. E. C. Verhoest, and D. G. Miralles, 2018: Terrestrial evaporation response to modes of climate variability. *npj Climate Atmos. Sci.*, **1**, 43, https://doi.org/10.1038/s41612-018-0053-5.

Martin, A., M. Weissmann, O. Reitebuch, M. Rennie, A. Geiß, and A. Cress, 2021: Validation of Aeolus winds using radiosonde observations and numerical weather prediction model equivalents. *Atmos. Meas. Tech.*, **14**, 2167–2183, https://doi.org/10.5194/amt-14-2167-2021.

McVicar, T. R., and Coauthors, 2012: Global review and synthesis of trends in observed terrestrial near-surface wind speeds: Implications for evaporation. *J. Hydrol.*, **416–417**, 182–205, https://doi.org/10.1016/j.jhydrol.2011.10.024.

Mears, C. A., and F. J. Wentz, 2016: Sensitivity of satellite-derived tropospheric temperature trends to the diurnal cycle adjustment. *J. Climate*, **29**, 3629–3646, https://doi.org/10.1175/JCLI-D-15-0744.1.

——, D. K. Smith, L. Ricciardulli, J. Wang, H. Huelsing, and F. J. Wentz, 2018: Construction and uncertainty estimation of a satellite-derived total precipitable water data record over the world's oceans. *Earth Space Sci.*, **5**, 197–210, https://doi.org/10.1002/2018EA000363.

Meesters, A. G. C. A., R. A. M. De Jeu, and M. Owe, 2005: Analytical derivation of the vegetation optical depth from the microwave polarization difference index. *IEEE Trans. Geosci. Remote Sens.*, **2**, 121–123, https://doi.org/10.1109/LGRS.2005.843983.

Meng, L., J. Liu, D. W. Tarasick, W. J. Randel, A. K. Steiner, H. Wilhelmsen, L. Wang, and L. Haimberger, 2021: Continuous rise of the tropopause in the Northern Hemisphere over 1980–2020. *Sci. Adv.*, **7**, eabi8065, https://doi.org/10.1126/sciadv.abi8065.

Menne, M. J., I. Durre, R. S. Vose, B. E. Gleason, and T. G. Houston, 2012: An overview of the Global Historical Climatology Network-Daily database. *J. Atmos. Oceanic Technol.*, **29**, 897–910, https://doi.org/10.1175/JTECH-D-11-00103.1.

Menzel, A., Y. Yuan, M. Matiu, T. H. Sparks, H. Scheifinger, R. Gehrig, and N. Estrella, 2020: Climate change fingerprints in recent European plant phenology. *Global Change Biol.*, **26**, 2599–2612, https://doi.org/10.1111/gcb.15000.

MeteoSwiss, 2022: Klimabulletin Jahr 2021. MeteoSwiss, 13 pp., www.meteoschweiz.admin.ch/home/service-und-publikationen/publikationen.subpage.html/de/data/publications/2022/1/klimabulletin-jahr-2021.html.

Mialon, A., N. Rodriguez-Fernandez, M. Santoro, S. Saatchi, S. Mermoz, E. Bousquet, and Y. Kerr, 2020: Evaluation of the sensitivity of SMOS L-VOD to forest above-ground biomass at global scale. *Remote Sens.*, **12**, 1450, https://doi.org/10.3390/rs12091450.

Miller, B. R., and Coauthors, 2010: HFC-23 (CHF_3) emission trend response to HCFC-22 ($CHClF_2$) production and recent HFC-23 emission abatement measures. *Atmos. Chem. Phys.*, 10, 7875–7890, https://doi.org/10.5194/acp-10-7875-2010.

Mills, G., and Coauthors, 2018: Tropospheric Ozone Assessment Report: Present-day tropospheric ozone distribution and trends relevant to vegetation. *Elem. Sci. Anthropocene*, **6**, 47, https://doi.org/10.1525/elementa.302.

Minnis, P., and Coauthors, 2008: Cloud detection in nonpolar regions for CERES using TRMM VIRS and Terra and Aqua MODIS data. *IEEE Trans. Geosci. Remote Sens.*, **46**, 3857–3884, https://doi.org/10.1109/TGRS.2008.2001351.

Minola, L., H. Reese, H. W. Lai, C. Azorin-Molina, J. A. Guijarro, S. W. Son, and D. Chen, 2022: Wind stilling-reversal across Sweden: The impact of land-use and large-scale atmospheric circulation changes. *Int. J. Climatol.*, 42, 1049–1071, https://doi.org/10.1002/joc.7289.

Miralles, D. G., T. R. H. Holmes, R. A. M. De Jeu, J. H. Gash, A. G. C. A. Meesters, and A. J. Dolman, 2011: Global land-surface evaporation estimated from satellite-based observations. *Hydrol. Earth Syst. Sci.*, **15**, 453–469, https://doi.org/10.5194/hess-15-453-2011.

——, and Coauthors, 2014: El Niño–La Niña cycle and recent trends in continental evaporation. *Nat. Climate Change*, **4**, 122–126, https://doi.org/10.1038/nclimate2068.

Miyazaki, K., K. Bowman, T. Sekiya, M. Takigawa, J. L. Neu, K. Sudo, G. Osterman, and H. Eskes, 2021: Global tropospheric ozone responses to reduced NOx emissions linked to the COVID-19 worldwide lockdowns. *Sci. Adv.*, **7**, eabf7460, https://doi.org/10.1126/sciadv.abf7460.

Moesinger, L., W. Dorigo, R. de Jeu, R. van der Schalie, T. Scanlon, I. Teubner, and M. Forkel, 2020: The global long-term microwave Vegetation Optical Depth Climate Archive (VODCA). *Earth Syst. Sci. Data*, **12**, 177–196, https://doi.org/10.5194/essd-12-177-2020.

——, R.-M. Zotta, R. van der Schalie, T. Scanlon, R. de Jeu, and W. Dorigo, 2022: Monitoring vegetation condition using microwave remote sensing: The Standardized Vegetation Optical Depth Index SVODI. *Biogeosci. Discuss.*, https://doi.org/10.5194/bg-2021-360.

Mollaret, C., C. Hilbich, C. Pellet, A. Flores-Orozco, R. Delaloye, and C. Hauck, 2019: Mountain permafrost degradation documented through a network of permanent electrical resistivity tomography sites. *Cryosphere*, **13**, 2557–2578, https://doi.org/10.5194/tc-13-2557-2019.

Montzka, S. A., J. H. Butlerrichard, C. Myers T. M. Thompson, T. H. Swanson, A. D. Clarke, L. T. Lock, and J. W. Elkins, 1996: Decline in the tropospheric abundance of halogen from halocarbons: Implications for stratospheric ozone depletion. *Science*, **272**, 1318–1322, https://doi.org/10.1126/science.272.5266.1318.

——, and Coauthors, 2011: Ozone-depleting substances (ODSs) and related chemicals. Scientific Assessment of Ozone Depletion: 2010, Global Ozone Research and Monitoring Project Rep.. 52, World Meteorological Organization, Ch. 1, https://tsapps.nist.gov/publication/get_pdf.cfm?pub_id=909747.

——, and Coauthors, 2018: An unexpected and persistent increase in global emissions of ozone-depleting CFC-11. *Nature*, **557**, 413–417, https://doi.org/10.1038/s41586-018-0106-2.

——, and Coauthors, 2021: A decline in global CFC-11 emissions during 2018–2019. *Nature*, **590**, 428–432, https://doi.org/10.1038/s41586-021-03260-5.

Morice, C. P., and Coauthors, 2021: An updated assessment of near-surface temperature change from 1850: The HadCRUT5 data set. *J. Geophys. Res. Atmos.*, **126**, e2019JD032361, https://doi.org/10.1029/2019JD032361.

Mote, P. W., and Coauthors, 1996: An atmospheric tape recorder: The imprint of tropical tropopause temperatures on stratospheric water vapor. *J. Geophys. Res. Atmos.*, **101**(D2), 3989–4006, https://doi.org/10.1029/95JD03422.

Mühle, J., and Coauthors, 2010: Perfluorocarbons in the global atmosphere: tetrafluoromethane, hexafluoroethane, and octafluoropropane. *Atmos. Chem. Phys.*, **10**, 5145–5164, https://doi.org/10.5194/acp-10-5145-2010.

Myhre, G., and Coauthors, 2013: Anthropogenic and natural radiative forcing. *Climate Change 2013: The Physical Science Basis*, T. F. Stocker et al., Eds., Cambridge University Press, 659–740.

Naumann, G., and Coauthors, 2021: The 2019–2021 extreme drought episode in La Plata Basin. EUR 30833 EN, Publications Office of the European Union, 44 pp., https://doi.org/10.2760/773.

Nédélec, P., and Coauthors, 2015: Instrumentation on commercial aircraft for monitoring the atmospheric composition on a global scale: the IAGOS system, technical overview of ozone and carbon monoxide measurements. *Tellus*, **67B**, 27791, https://doi.org/10.3402/tellusb.v67.27791.

Newchurch, M. J., E. S. Yang, D. M. Cunnold, G. C. Reinsel, J. M. Zawodny, and J. M. Russell III, 2003: Evidence for slowdown in stratospheric ozone loss: First stage of ozone recovery. *J. Geophys. Res.*, **108**, 4507, https://doi.org/10.1029/2003JD003471.

Newman, P. A., J. S. Daniel, D. W. Waugh, and E. R. Nash, 2007: A new formulation of equivalent effective stratospheric chlorine (EESC). *Atmos. Chem. Phys.*, **7**, 4537–4552, https://doi.org/10.5194/acp-7-4537-2007.

Nisbet, E. G., and Coauthors, 2019. Very strong atmospheric methane growth in the 4 years 2014–2017: Implications for the Paris Agreement. *Global Biogeochem. Cycles*, **33** (3), 318–342, https://doi.org/10.1029/2018GB006009.

NIWA, 2022: New Zealand's warmest year on record. 11 January, NIWA, https://niwa.co.nz/climate/summaries/annual-climate-summary-2021.

NOAA, 2021a: October 2021 was the sixth warmest on record for US. 8 November, accessed 9 February 22, www.noaa.gov/news/october-2021-was-sixth-warmest-on-record-for-us#:~:text=The%20U.S.%20precipitation%20total%20for,Louisiana%20saw%20its%20fourth%20wettest.

——, 2021b: National climate report - August 2021. Accessed 14 February 2022, www.ncdc.noaa.gov/sotc/national/202108.

——, 2021c: Global climate report - April 2021. Accessed 14 February 2022, www.ncdc.noaa.gov/sotc/global/202104.

——, 2021d: Assessing the global climate in August 2021. 14 September, www.ncei.noaa.gov/news/global-climate-202108.

——, 2022a: U.S. Climate Extremes Index (CEI): Definition. Accessed 20 June 2022, www.ncdc.noaa.gov/extremes/cei/definition.

——, 2022b: U.S. Climate Extremes Index (CEI): Graph. Accessed 7 February 2022, www.ncdc.noaa.gov/extremes/cei/graph/us/01-12/4.

——, 2022c: State of the Climate: Monthly global climate report for annual 2021. Accessed 9 February 2022, www.ncei.noaa.gov/access/monitoring/monthly-report/global/202113.

——, 2022d: Assessing the global climate in 2021. 13 January, www.ncei.noaa.gov/news/global-climate-202112.

——, 2022e: State of the Climate: Monthly national climate report for annual 2021. Accessed 9 February 2022, www.ncdc.noaa.gov/sotc/national/202113.

Noetzli, J., and Coauthors, 2018: Permafrost thermal state [in "State of the Climate in 2017"]. *Bull. Amer. Meteor. Soc.*, **99** (8), S20–S22, https://doi.org/10.1175/2018BAMSStateoftheClimate.1.

——, H. H. Christiansen, K. Isaksen, S. Smith, L. Zhao, and D. A. Streletskiy, 2021a: Permafrost thermal state [in "State of the Climate in 2019"]. *Bull. Amer. Meteor. Soc.*, 101 (8), S34–S36, https://doi.org/10.1175/BAMS-D-20-0104.1.

——, and Coauthors, 2021b: Best practice for measuring permafrost temperature in boreholes based on the experience in the Swiss Alps. *Front. Earth Sci.*, **9**, 607875, https://doi.org/10.3389/feart.2021.607875.

O'Keefe, J., 2021: Phenology of woody species at Harvard Forest since 1990 ver 32. Environmental Data Initiative, accessed 10 February 2022, https://doi.org/10.6073/pasta/6b0a6e266e06ab52148af3e5cd942159.

O'Reilly, C. M., and Coauthors, 2015: Rapid and highly variable warming of lake surface waters around the globe. *Geophys. Res. Lett.*, **42**, 10773–10781, https://doi.org/10.1002/2015GL066235.

Orimoloye, I. R., J. A. Belle, Y. M. Orimoloye, A. O. Olusola, and O. O. Ololade, 2022: Drought: A common environmental disaster. *Atmosphere*, **13**, 111, https://doi.org/10.3390/atmos13010111.

Osborn, T. J., P. D. Jones, D. H. Lister, C. P. Morice, I. R. Simpson, J. P. Winn, E. Hogan, and I. C. Harris, 2021: Land surface air temperature variations across the globe updated to 2019: The CRUTEM5 dataset. *J. Geophys. Res. Atmos.*, **126**, e2019JD032352, https://doi.org/10.1029/2019JD032352

Park, T., and Coauthors, 2016: Changes in growing season duration and productivity of northern vegetation inferred from long-term remote sensing data. *Environ. Res. Lett.*, **11**, 084001, https://doi.org/10.1088/1748-9326/11/8/084001.

Pascolini-Campbell, M., J. T. Reager, H. A. Chandanpurkar, and M. A. Rodell, 2021: 10 per cent increase in global land evapotranspiration from 2003 to 2019. *Nature*, **593**, 543–547, https://doi.org/10.1038/s41586-021-03503-5.

Pellet, C., X. Bodin, R. Delaloye, V. Kaufmann, J. Noetzli, E. Thibert, and A. Kellerer-Pirklbauer, 2021: Rock glacier kinematics [in "State of the Climate in 2020"]. *Bull. Amer. Meteor. Soc.*, **102** (8), S44–S45, https://doi.org/10.1175/BAMS-D-21-0098.1.

Pelto, M., P. Panday, T. Matthews, J. Maurer, and L. B. Perry, 2021: Observations of winter ablation on glaciers in the Mount Everest region in 2020–2021. *Remote Sens.*, **13**, 2692, https://doi.org/10.3390/rs13142692.

——, M. Dryak, J. Pelto, T. Matthews, and L. B. Perry, 2022: Contribution of glacier runoff during heat waves in the Nooksack River basin USA. *Water*, **14**, 1145, https://doi.org/10.3390/w14071145.

PERMOS, 2019: Permafrost in Switzerland 2014/2015 to 2017/2018. Glaciological Report Permafrost No. 16–19, J. Noetzli, C. Pellet, and B. Staub, Eds., Cryospheric Commission of the Swiss Academy of Sciences, 104 pp., https://doi.org/10.13093/permos-rep-2019-16-19.

——, 2022. Swiss Permafrost Bulletin 2021. J. Noetzli and C. Pellet, Eds., Swiss Permafrost Monitoring Network, 22 pp., https://doi.org/10.13093/permos-bull-2022.

Petersen, W. A., and S. A. Rutledge, 1998: On the relationship between cloud-to-ground lightning and convective rainfall. *J. Geophys. Res.*, **103**, 14 025–14 040, https://doi.org/10.1029/97JD02064.

Peterson, M. J., and Coauthors, 2022: New WMO certified megaflash lightning extremes for flash distance and duration recorded from space. *Bull. Amer. Meteor. Soc.*, 103, 257–261, https://doi.org/10.1175/BAMS-D-21-0254.1.

Petrenko, V., and Coauthors, 2013: A 60 yr record of atmospheric carbon monoxide reconstructed from Greenland firn air. *Atmos. Chem. Phys.*, **13**, 7567–7585, https://doi.org/10.5194/acp-13-7567-2013.

Philip, S. Y., and Coauthors, 2021: Rapid attribution analysis of the extraordinary heatwave on the Pacific Coast of the US and Canada June 2021. *Earth Syst. Dyn. Discuss.*, https://doi.org/10.5194/esd-2021-90.

Piepgrass, M., E. Krider, and C. Moore, 1982: Lightning and surface rainfall during Florida thunderstorms. *J. Geophys. Res.*, **87**, 11 193–11 201, https://doi.org/10.1029/JC087iC13p11193.

Pinto, O., Jr., K. P. Naccarato, and I. R. C. A. Pinto, 2013: Thunderstorm incidence in southeastern Brazil estimated from different data sources. *Ann. Geophys.*, **31**, 1213–1219, https://doi.org/10.5194/angeo-31-1213-2013.

Pinty, B., and Coauthors, 2011: Exploiting the MODIS albedos with the Two-stream Inversion Package (JRC-TIP): 2. Fractions of transmitted and absorbed fluxes in the vegetation and soil layers. *J. Geophys. Res.*, **116**, D09106, https://doi.org/10.1029/2010JD015373.

Pisoft, P., and Coauthors, 2021: Stratospheric contraction caused by increasing greenhouse gases. *Environ. Res. Lett.*, **16**, 064038, https://doi.org/10.1088/1748-9326/abfe2b.

Platnick, S., 2022: Cloud Issues (06_L2). NASA Atmosphere Discipline Team Imager Products, accessed 14 February 2022, https://atmosphere-imager.gsfc.nasa.gov/issues/cloud.

——, and Coauthors, 2015: MODIS Atmosphere L3 Monthly Product. NASA MODIS Adaptive Processing System, Goddard Space Flight Center, accessed 11 February 2022, https://doi.org/10.5067/MODIS/MYD08_M3.061.

Po-Chedley, S., T. J. Thorsen, and Q. Fu, 2015: Removing diurnal cycle contamination in satellite-derived tropospheric temperatures: Understanding tropical tropospheric trend discrepancies. *J. Climate*, **28**, 2274–2290, https://doi.org/10.1175/JCLI-D-13-00767.1.

——, J. R. Christy, L. Haimberger, and C. A. Mears, 2021: Tropospheric temperature [in "State of the Climate in 2020"]. *Bull. Amer. Meteor. Soc.*, **102** (8), S34–S37, https://doi.org/10.1175/BAMS-D-21-0098.1.

Pogliotti, P., M. Guglielmin, E. Cremonese, U. M. di Cella, G. Filippa, C. Pellet, and C. Hauck, 2015: Warming permafrost and active layer variability at Cime Bianche, Western European Alps. *Cryosphere*, **9**, 647–661, https://doi.org/10.5194/tc-9-647-2015.

Popp, T., and Coauthors, 2016: Development, production and evaluation of aerosol climate data records from European satellite observations (Aerosol_cci). *Remote Sens.*, **8**, 421, https://doi.org/10.3390/rs8050421.

Potocki, M., and Coauthors, 2022: Mt. Everest's highest glacier is a sentinel for accelerating ice loss. *npj Climate Atmos. Sci.*, **5**, 7, https://doi.org/10.1038/s41612-022-00230-0.

Prather, M. J., C. D. Holmes, and J. Hsu, 2012: Reactive greenhouse gas scenarios: Systematic exploration of uncertainties and the role of atmospheric chemistry. *Geophys. Res. Lett.*, 39, L09803, https://doi.org/10.1029/2012GL051440.

Price, C., 1993: Global surface temperature and the atmospheric electric circuit. *Geophys. Res. Lett.*, **20**, 1363–1366, https://doi.org/10.1029/93GL01774.

——, and D. Rind, 1993: What determines the cloud-to-ground lightning fraction in thunderstorms. *Geophys. Res. Lett.*, **20**, 463–466, https://doi.org/10.1029/93GL00226.

——, and M. Asfur, 2006: Can lightning observations be used as an indicator of upper-tropospheric water vapor variability? *Bull. Amer. Meteor. Soc.*, **87**, 291–298, https://doi.org/10.1175/BAMS-87-3-291.

——, J. Penner, and M. Prather, 1997: NO_x from lightning: 1. Global distribution based on lightning physics. *J. Geophys. Res.*, **102**, 5929–5941, https://doi.org/10.1029/96JD03504.

Ramon, J., L. Lledó, V. Torralba, A. Soret, and F. J. Doblas-Reyes, 2019: What global reanalysis best represents near-surface winds? *Quart. J. Roy. Meteor. Soc.*, **145**, 3236–3251, https://doi.org/10.1002/qj.3616.

Randel, W. J., and J. B. Cobb, 1994: Coherent variations of monthly mean total ozone and lower stratospheric temperature. *J. Geophys. Res.*, **99**, 5433–5447, https://doi.org/10.1029/93JD03454.

Rao, J., C. I. Garfinkel, H. Chen, and I. P. White, 2019: The 2019 New Year stratospheric sudden warming and its real-time predictions in multiple S2S models. *J. Geophys. Res. Atmos.*, **124**, 11 155–112174, https://doi.org/10.1029/2019JD030826.

Ravishankara, A. R., J. S. Daniel, and R. W. Portmann, 2009: Nitrous oxide (N_2O): The dominant ozone-depleting substance emitted in the 21st century. *Science*, **326**, 123–125, https://doi.org/10.1126/science.1176985.

Ray, E. A., F. L. Moore, J. W. Elkins, K. H. Rosenlof, J. C. Laube, T. Röckmann, D. R. Marsh, and A. E. Andrews, 2017: Quantification of the SF6 lifetime based on mesospheric loss measured in the stratospheric polar vortex. *J. Geophys. Res. Atmos.*, **122**, 4626– 4638, https://doi.org/10.1002/2016JD026198.

Reichstein, M., and Coauthors, 2013: Climate extremes and the carbon cycle. *Nature*, **500**, 287–295, https://doi.org/10.1038/nature12350.

Reid, K. J., T. A. O'Brien, A. D. King, and T. P. Lane, 2021: Extreme water vapor transport during the march 2021 Sydney floods in the context of climate projections. *Geophys. Res. Lett.*, **48**, e2021GL095335, https://doi.org/10.1029/2021GL095335.

Rennie, M. P., L. Isaksen, F. Weiler, J. de Kloe, T. Kanitz, and O. Reitebuch, 2021: The impact of Aeolus wind retrievals on ECMWF global weather forecasts. *Quart. J. Roy. Meteor. Soc.*, **147**, 3555–3586, https://doi.org/10.1002/qj.4142.

RGIK, 2021: Towards standard guidelines for inventorying rock glaciers: Baseline concepts (version 4.2.1). IPA Action Group Rock glacier inventories and kinematics, 13 pp., https://bigweb.unifr.ch/Science/Geosciences/Geomorphology/Pub/Website/IPA/Guidelines/V4/210801_Baseline_Concepts_Inventorying_Rock_Glaciers_V4.2.1.pdf.

——, 2022: Rock Glacier Velocity as an associated parameter of ECV Permafrost: Baseline concepts (version 3.1). IPA Action Group Rock glacier inventories and kinematics, 12 pp., https://bigweb.unifr.ch/Science/Geosciences/Geomorphology/Pub/Website/IPA/RGV/RockGlacierVelocity_V3.1.pdf.

Ricciardulli, L., and F. J. Wentz, 2015: A scatterometer geophysical model function for climate-quality winds: QuikSCAT Ku-2011. *J. Atmos. Oceanic Technol.*, **32**, 1829–1846, https://doi.org/10.1175/JTECH-D-15-0008.1.

——, and A. Manaster, 2021: Intercalibration of ASCAT scatterometer winds from MetOp-A, -B, and -C, for a stable climate data record. *Remote Sens.*, **13**, 3678, https://doi.org/10.3390/rs13183678.

Richardson, A. D., 2019: Tracking seasonal rhythms of plants in diverse ecosystems with digital camera imagery. *New Phytol.*, **222**, 1742–1750, https://doi.org/10.1111/nph.15591.

——, and J. O'Keefe, 2009: Phenological differences between understory and overstory. *Phenology of Ecosystem Processes*, A. Noormets, Eds., Springer, 87–117, https://doi.org/10.1007/978-1-4419-0026-5_4.

Rieger, L. A., W. J. Randel, A. E. Bourassa, and S. Solomon, 2021: Stratospheric temperature and ozone anomalies associated with the 2020 Australian New Year fires. *Geophys. Res. Lett.*, **48**, e2021GL095898, https://doi.org/10.1029/2021GL095898.

Rigby, M., and Coauthors, 2019: Increase in CFC-11 emissions from eastern China based on atmospheric observations. *Nature*, **569**, 546–550, https://doi.org/10.1038/s41586-019-1193-4.

Rodell, M., J. S. Famiglietti, D. N. Wiese, J. T. Reager, H. K. Beaudoing, and M.-H. Lo, 2018: Emerging trends in global freshwater availability. *Nature*, **557**, 651–659, https://doi.org/10.1038/s41586-018-0123-1.

Roderick, M. L., L. D. Rotstayn, G. D. Farquhar, and M. T. Hobbins, 2007: On the attribution of changing pan evaporation. *Geophys. Res. Lett.*, **34**, L17403, https://doi.org/10.1029/2007GL031166.

Rohde, R. A., and Z. Hausfather, 2020: The Berkeley Earth land/ocean temperature record. *Earth Syst. Sci. Data*, **12**, 3469–3479, https://doi.org/10.5194/essd-12-3469-2020.

Romps, D. M., J. T. Seeley, D. Vollaro, and J. Molinari, 2014: Projected increase in lightning strikes in the United States due to global warming. *Science*, **346**, 851–854, https://doi.org/10.1126/science.1259100.

Rosenfeld, D., U. Lohmann, G. B. Raga, C. D. O'Dowd, M. Kulmata, A. Reissell, and M. O. Andreae, 2008: Flood or drought: How do aerosols affect precipitation? *Science*, **321**, 1309–1313, https://doi.org/10.1126/science.1160606.

Rudlosky, S., and K. Virts, 2021: Dual geostationary lightning mapper observations. *Mon. Wea. Rev.*, **149**, 979–998, https://doi.org/10.1175/MWR-D-20-0242.1.

——, S. Goodman, K. Calhoun, C. Schultz, A. Back, B. Kuligowski, S. Stevenson, and C. Gravelle, 2020: Geostationary Lightning Mapper value assessment. NOAA Tech. Rep. NESDIS 153, 46 pp., https://doi.org/10.25923/2616-3v73.

Ryley, T., S. Baumeister, and L. Coulter, 2020: Climate change influences on aviation: A literature review. *Transp. Policy*, **92**, 55–64, https://doi.org/10.1016/j.tranpol.2020.04.010.

Safaei Pirooz, A. A., R. G. Flay, L. Minola, C. Azorin-Molina, and D. Chen, 2020: Effects of sensor response and moving average filter duration on maximum wind gust measurements. *J. Wind Eng. Ind. Aerodyn.*, **206**, 104354, https://doi.org/10.1016/j.jweia.2020.104354.

Said, R. K., U. S. Inan, and K. L. Cummins, 2010: Long-range lightning geolocation using a VLF radio atmospheric waveform bank. *J. Geophys. Res.*, **115**, D23108, https://doi.org/10.1029/2010JD013863.

Sánchez-Lugo, A., C. Morice, J. P. Nicolas, and A. Argüez, 2021: Global surface temperature [in "State of the Climate in 2020"]. *Bull. Amer. Meteor. Soc.*, **102** (8), S26–S28, https://doi.org/10.1175/BAMS-D-21-0098.1.

Santer, B. D., and Coauthors, 2008: Consistency of modelled and observed temperature trends in the tropical troposphere. *Int. J. Climatol.*, **28**, 1703–1722, https://doi.org/10.1002/joc.1756.

——, and Coauthors, 2021: Using climate model simulations to constrain observations. *J. Climate*, **34**, 6281–6301, https://doi.org/10.1175/JCLI-D-20-0768.1.

Satheesh, S. K., S. Suresh Babu, B. Padmakumari, G. Pandithurai, and V. K. Soni, 2017: Variability of atmospheric aerosols over India. *Observed Climate Variability and Change over the Indian Region*, M. N. Rajeevan and S. Nayak, Eds., Springer, 221–248, https://doi.org/10.1007/978-981-10-2531-0_13.

Sátori, G., V. Mushtak, and E. Williams, 2009: Schumann resonance signatures of global lightning activity. *Lightning: Principles, Instruments and Applications: Review of Modern Lightning Research*, H.-D Betz, U. Schumann, and P. Laroche, Eds., Springer, 347–386, https://doi.org/10.1007/978-1-4020-9079-0_16.

Saunois, M., and Coauthors, 2020: The global methane budget 2000–2017. *Earth Syst. Sci. Data*, **12**, 1561–1623, https://doi.org/10.5194/essd-12-1561-2020.

Scaife, A. A., and Coauthors, 2014: Skilful long range prediction of European and North American winters. *Geophys. Res. Lett.*, **41**, 2514–2519, https://doi.org/10.1002/2014GL059637.

Schaaf, C. B., and Coauthors, 2002: First operational BRDF, albedo nadir reflectance products from MODIS. *Remote Sens. Environ.*, **83**, 135–148, https://doi.org/10.1016/S0034-4257(02)00091-3.

Schaefer, H., and Coauthors, 2016; A 21st-century shift from fossil-fuel to biogenic methane emissions indicated by 13CH4. *Science*, **352** (6281), 80–84, https://doi/10.1126/science.aad2705.

Schamm, K., M. Ziese, A. Becker, P. Finger, A. Meyer-Christoffer, B. Rudolf, and U. Schneider, 2013: GPCC First Guess Daily Product at 1.0°: Near Real-Time First Guess Daily Land-Surface Precipitation from Rain-Gauges Based on SYNOP Data. Global Precipitation Climatology Centre, accessed 18 January 2021, https://doi.org/10.5676/DWD_GPCC/FG_D_100.

Schneider, U., A. Becker, P. Finger, R. Elke, and M. Ziese, 2020: GPCC Monitoring Product: Near Real-Time Monthly Land-Surface Precipitation from Rain-Gauges based on SYNOP and CLIMAT Data, Global Precipitation Climatology Centre Global Precipitation Climatology Centre, accessed 7 February 2022, https://doi.org/10.5676/DWD_GPCC/MP_M_V2020_100.

Schumann, U., and H. Huntrieser, 2007: The global lightning-induced nitrogen oxides source. *Atmos. Chem. Phys.*, **7**, 3823–3907, https://doi.org/10.5194/acp-7-3823-2007.

Schwietzke, S., and Coauthors, 2016: Upward revision of global fossil fuel methane emissions based on isotope database. *Nature*, **538**, 88–91, https://doi.org/10.1038/nature19797.

Seneviratne, S. I., T. Corti, E. L. Davin, M. Hirschi, E. B. Jaeger, I. Lehner, B. Orlowsky, and A. J. Teuling, 2010: Investigating soil moisture–climate interactions in a changing climate: A review. *Earth-Sci. Rev.*, **99**, 125–161, https://doi.org/10.1016/j.earscirev.2010.02.004.

Seyednasrollah, B., A. M. Young, K. Hufkens, T. Milliman, M. A. Friedl, S. Frolking, and A. D. Richardson, 2019: Tracking vegetation phenology across diverse biomes using Version 2.0 of the PhenoCam Dataset. *Sci. Data*, **6**, 261, https://doi.org/10.1038/s41597-019-0270-8.

Sharma, S., and R. I. Woolway, 2021: Lake ice [in "State of the Climate in 2020"]. *Bull. Amer. Meteor. Soc.*, **102** (8), S48–S51, https://doi.org/10.1175/BAMS-D-21-0098.1.

——, and Coauthors, 2021: Loss of ice cover, shifting phenology, and more extreme events in Northern Hemisphere lakes. *J. Geophys. Res. Biogeosci.*, **126**, e2021JG006348, https://doi.org/10.1029/2021JG006348.

Shi, L., and J. J. Bates, 2011: Three decades of intersatellite-calibrated high-resolution infrared radiation sounder upper tropospheric water vapor. *J. Geophys. Res.*, **116**, D04108, https://doi.org/10.1029/2010JD014847.

Simmons, A. J., P. Berrisford, D. P. Dee, H. Hersbach, S. Hirahara, and J. N. Thepaut, 2017: A reassessment of temperature variations and trends from global reanalyses and monthly surface climatological datasets. *Quart. J. Roy. Meteor. Soc.*, **143**, 101–119, https://doi.org/10.1002/qj.2949.

——, and Coauthors, 2021: Low frequency variability and trends in surface air temperature and humidity from ERA5 and other datasets. ECMWF Tech. Memo. 881, 97 pp., https://doi.org/10.21957/ly5vbtbfd.

Sindelarova, K., and Coauthors, 2014: Global data set of biogenic VOC emissions calculated by the MEGAN model over the last 30 years. *Atmos. Chem. Phys.*, **14**, 9317–9341, https://doi.org/10.5194/acp-14-9317-2014.

SMHI, 2021: August 2021 - Rainy month with torrential rain over Gävle. 15 November, accessed 9 February 2022, www.smhi.se/klimat/klimatet-da-och-nu/manadens-vader-och-vatten-sverige/manadens-vader-i-sverige/augusti-2021-meteorologi-1.173428#:~:text=Augustiv%C3%A4dret%20blev%20en%20skarp%20kontrast,kraftigt%20regn%20och%20lokala%20%C3%B6versv%C3%A4mningar.

Smith, S. L., H. B. O'Neill, K. Isaksen, J. Noetzli, and V. E. Romanovsky, 2022: The changing thermal state of permafrost. *Nat. Rev. Earth Environ.*, **3**, 10–23, https://doi.org/10.1038/s43017-021-00240-1.

Sofieva, V. F., and Coauthors, 2021: Measurement report: regional trends of stratospheric ozone evaluated using the MErged GRIdded Dataset of Ozone Profiles (MEGRIDOP). *Atmos. Chem. Phys.*, **21**, 6707–6720, https://doi.org/10.5194/acp-21-6707-2021.

Sommer, U., Z. M. Gliwicz, W. Lampert, and A. Duncan, 1986: The PEG-model of seasonal succession of planktonic events in fresh waters. *Arch. Hydrobiol.*, **106** (4), 433–471.

Song, X.-P., M. C. Hansen, S. V. Stehman, P. V. Potapov, A. Tyukavina, E. F. Vermote, and J. R. Townshend, 2018: Global land change from 1982 to 2016. *Nature*, **560**, 639–643, https://doi.org/10.1038/s41586-018-0411-9.

SPARC/IO3C/GAW, 2019: SPARC/IO3C/GAW report on long-term ozone trends and uncertainties in the stratosphere. I. Petropavlovskikh et al., Eds., SPARC Rep. 9, WCRP-17/2018, GAW Rep. 241, 99 pp., https://doi.org/10.17874/f899e57a20b.

Spencer, R. W., J. R. Christy, and W. D. Braswell, 2017: UAH Version 6 global satellite temperature products: Methodology and results. *Asia-Pac. J. Atmos. Sci.*, **53**, 121–130, https://doi.org/10.1007/s13143-017-0010-y.

Stackhouse, P. W., T. Wong, D. P. Kratz, P. Sawaengphokhai, A. C. Wiber, S. K. Gupta, and N. G. Loeb, 2016: Earth radiation budget at top-of-atmosphere [in "State of the Climate in 2015"]. *Bull. Amer. Meteor. Soc.*, **97** (8), S41–S43, https://doi.org/10.1175/2016BAMSStateoftheClimate.1.

Staub, B., C. Lambiel, and R. Delaloye, 2016: Rock glacier creep as a thermally-driven phenomenon: A decade of inter-annual observation from the Swiss Alps. XI Int. Conf. on Permafrost, Potsdam, Germany, Alfred Wegener Institute Helmholtz Center for Polar and Marine Research, 96–97, https://doi.org/10.2312/GFZ.LIS.2016.001.

Stein, O., M. G. Schultz, I. Bouarar, H. Clark, V. Huijnen, A. Gaudel, M. George, and C. Clerbaux, 2014: On the wintertime low bias of Northern Hemisphere carbon monoxide found in global model simulations. *Atmos. Chem. Phys.*, **14**, 9295–9316, https://doi.org/10.5194/acp-14-9295-2014.

Steinbrecht, W., and Coauthors, 2017: An update on ozone profile trends for the period 2000 to 2016. *Atmos. Chem. Phys.*, **17**, 10675–10690, https://doi.org/10.5194/acp-17-10675-2017.

——, and Coauthors, 2021: COVID-19 crisis reduces free tropospheric ozone across the Northern Hemisphere. *Geophys. Res. Lett.*, **48**, e2020GL091987, https://doi.org/10.1029/2020GL091987.

Steiner, A. K., and Coauthors, 2020: Observed temperature changes in the troposphere and stratosphere from 1979 to 2018. *J. Climate*, **33**, 8165–8194, https://doi.org/10.1175/JCLI-D-19-0998.1.

Stocker, M., F. Ladstädter, and A. K. Steiner, 2021: Observing the climate impact of large wildfires on stratospheric temperature. *Sci. Rep.*, **11**, 22994, https://doi.org/10.1038/s41598-021-02335-7.

Stolz, D., S. Rutledge, and J. Pierce, 2015: Simultaneous influences of thermodynamics and aerosols on deep convection and lightning in the tropics. *J. Geophys. Res. Atmos.*, **120**, 6207–6231, https://doi.org/10.1002/2014JD023033.

Streletskiy, D., J. Noetzli, S. L. Smith, G. Vieira, P. Schoeneich, F. Hrbacek, and A. M. Irrgang, 2021: Strategy and Implementation Plan 2021–2024 for the Global Terrestrial Network for Permafrost (GTN-P). International Permafrost Association, 44 pp., https://doi.org/10.5281/ZENODO.6075468.

Stroeve, J., J. E. Box, Z. Wang, C. Schaaf, and A. Barrett, 2013: Re-evaluation of MODIS MCD43 Greenland albedo accuracy and trends. *Remote Sens. Environ.*, **138**, 199–214, https://doi.org/10.1016/j.rse.2013.07.023.

Susskind, J., G. Molnar, L. Iredell, and N. G. Loeb, 2012: Interannual variability of outgoing longwave radiation as observed by AIRS and CERES. *J. Geophys. Res.*, **117**, D23107, https://doi.org/10.1029/2012JD017997.

Szeląg, M. E., V. F. Sofieva, D. Degenstein, C. Roth, S. Davis, and L. Froidevaux, 2020: Seasonal stratospheric ozone trends over 2000–2018 derived from several merged data sets. *Atmos. Chem. Phys.*, **20**, 7035–7047, https://doi.org/10.5194/acp-20-7035-2020.

Szopa, S., and Coauthors, 2021: Short-lived climate forcers. *Climate Change 2021: The Physical Science Basis*, V. Masson-Delmotte et al., Eds., Cambridge University Press, 817–922, https://doi.org/10.1017/9781009157896.008.

Tapley, B. D., S. Bettadpur, J. C. Ries, P. F. Thompson, and M. M. Watkins, 2004: GRACE measurements of mass variability in the Earth system. *Science*, **305**, 503–505, https://doi.org/10.1126/science.1099192.

Tarasick, D. W., and Coauthors, 2019: Tropospheric Ozone Assessment Report: Tropospheric ozone from 1877 to 2016, observed levels, trends and uncertainties. *Elem. Sci. Anthropocene*, **7**, 39, https://doi.org/10.1525/elementa.376.

Teng, W.-H., C.-Y. Huang, S.-P. Ho, Y.-H. Kuo, and X.-J. Zhou, 2013: Characteristics of global precipitable water in ENSO events revealed by COSMIC measurements. *J. Geophys. Res. Atmos.*, **118**, 8411–8425, https://doi.org/10.1002/jgrd.50371.

Teubner, I. E., and Coauthors, 2019: A carbon sink-driven approach to estimate gross primary production from microwave satellite observations. *Remote Sens. Environ.*, **229**, 100–113, https://doi.org/10.1016/j.rse.2019.04.022.

Thompson, R. L., and Coauthors, 2019: Acceleration of global N_2O emissions seenfrom two decades of atmospheric inversion. *Nat. Climate Change*, **9**, 993–998, https://doi.org/10.1038/s41558-019-0613-7.

Thornton, J. A., K. S. Virts, R. H. Holzworth, and T. P. Mitchell, 2017: Lightning enhancement over major oceanic shipping lanes. *Geophys. Res. Lett.*, **44**, 9102–9111, https://doi.org/10.1002/2017GL074982.

Torralba, V., F. J. Doblas-Reyes, and N. Gonzalez-Reviriegol, 2017: Uncertainty in recent near-surface wind speed trends: A global reanalysis intercomparison. *Environ. Res. Lett.*, **12**, 114019, https://doi.org/10.1088/1748-9326/aa8a58.

Trepte, Q. Z., P. Minnis, C. R. Trepte, S. Sun-Mack, and R. Brown, 2010: Improved cloud detection in CERES Edition 3 algorithm and comparison with the CALIPSO Vertical Feature Mask. *13th Conf. on Atmospheric Radiation and Cloud Physics*, Portland, OR, Amer. Meteor. Soc., JP1.32, https://ams.confex.com/ams/13CldPhy13AtRad/webprogram/Paper171785.html.

UN Environment Programme, 2021: Global Methane Assessment: Benefits and Costs of Mitigating Methane Emissions. United Nations Environment Programme and Climate and Clean Air Coalition Rep., 172 pp., www.unep.org/resources/report/global-methane-assessment-benefits-and-costs-mitigating-methane-emissions.

van der A, R. J., M. A. F. Allaart, and H. J. Eskes, 2015: Extended and refined multi sensor reanalysis of total ozone for the period 1970–2012. *Atmos. Meas. Tech.*, **8**, 3021–3035,, https://doi.org/10.5194/amt-8-3021-2015.

van der Schalie, R., and Coauthors, 2017: The merging of radiative transfer-based surface soil moisture data from SMOS and AMSR-E. *Remote Sens. Environ.*, **189**, 180–193, https://doi.org/10.1016/j.rse.2016.11.026.

——, and Coauthors, 2021: Soil moisture [in "State of the Climate in 2020"]. *Bull. Amer. Meteor. Soc.*, **102** (8), S67–S68, https://doi.org/10.1175/BAMS-D-21-0098.1.

van der Schrier, G., J. Barichivich, K. R. Briffa, and P. D. Jones, 2013: A scPDSI-based global dataset of dry and wet spells for 1901-2009. *J. Geophys. Res. Atmos.*, **118**, 4025–4048, https://doi.org/10.1002/jgrd.50355.

van der Werf, G. R., and Coauthors, 2017: Global fire emissions estimates during 1997–2016. *Earth Syst. Sci. Data*, **9**, 697–720, https://doi.org/10.5194/essd-9-697-2017.

van Dijk, A. I. J. M., and Coauthors, 2015: Rainfall interception and the coupled surface water and energy balance. *Agric. For. Meteor.*, **214–215**, 402–415, https://doi.org/10.1016/j.agrformet.2015.09.006.

Virts, K. S., and S. J. Goodman, 2020: Prolific lightning and thunderstorm Initiation over the lake Victoria basin in East Africa. *Mon. Wea. Rev.*, **148**, 1971–1985, https://doi.org/10.1175/MWR-D-19-0260.1.

——, J. M. Wallace, M. L. Hutchins, and R. H. Holzworth, 2013: Highlights of a new ground-based, hourly global lightning climatology. *Bull. Amer. Meteor. Soc.*, 94, 1381–1391, https://doi.org/10.1175/BAMS-D-12-00082.1.

Vivero, S., X. Bodin, D. Farías-Barahona, S. MacDonell, N. Schaffer, B. A. Robson, and C. Lambiel, 2021: Combination of aerial, satellite, and UAV photogrammetry for quantifying rock glacier kinematics in the Dry Andes of Chile (30°S) since the 1950s. *Front. Remote Sens.*, **2**, 784015, https://doi.org/10.3389/frsen.2021.784015.

Vreugdenhil, M., S. Hahn, T. Melzer, B. Bauer-Marschallinger, C. Reimer, W. Dorigo, and W. Wagner, 2017: Assessing vegetation dynamics over mainland Australia with Metop ASCAT. *IEEE J. Sel. Top. Appl. Earth Obs. Remote Sens.*, **10**, 2240–2248, https://doi.org/10.1109/JSTARS.2016.2618838.

Wagner, W., and Coauthors, 2013: The ASCAT Soil Moisture Product: A review of its specifications, validation results, and emerging applications. *Meteor. Z.*, **22**, 5–33, https://doi.org/10.1127/0941-2948/2013/0399.

Wang, Q., Z. Li, J. Guo, C. Zhao, and M. Cribb, 2018: The climate impact of aerosols on the lightning flash rate: Is it detectable from long-term measurements? *Atmos. Chem. Phys.*, **18**, 12 797–12 816, https://doi.org/10.5194/acp-18-12797-2018.

Wang, X., and Coauthors, 2021: High-resolution mapping of ice cover changes in over 33,000 lakes across the North Temperate Zone. *Geophys. Res. Lett.*, **48**, e2021GL095614, https://doi.org/10.1029/2021GL095614.

Wargan, K., C. Orbe, S. Pawson, J. R. Ziemke, L. D. Oman, M. A. Olsen, L. Coy, and K. E. Knowland, 2018: Recent decline in extratropical lower stratospheric ozone attributed to circulation changes. *Geophys. Res. Lett.*, **45**, 5166–5176, https://doi.org/10.1029/2018GL077406.

Weatherhead, E. C., and Coauthors, 1998: Factors affecting the detection of trends: Statistical considerations and applications to environmental data. *J. Geophys. Res.*, **103**, 17 149–17 161, https://doi.org/10.1029/98JD00995.

Weber, M., S. Dikty, J. P. Burrows, H. Garny, M. Dameris, A. Kubin, J. Abalichin, and U. Langematz, 2011: The Brewer-Dobson circulation and total ozone from seasonal to decadal time scales. *Atmos. Chem. Phys.*, **11**, 11 221–11 235, https://doi.org/10.5194/acp-11-11221-2011.

Weber, M., and Coauthors, 2022: Global total ozone recovery trends attributed to ozone-depleting substance (ODS) changes derived from five merged ozone datasets. *Atmos. Chem. Phys.*, 22, 6843–6859, https://doi.org/10.5194/acp-22-6843-2022.

Weir, B., and Coauthors, 2021: Regional impacts of COVID-19 on carbon dioxide detected worldwide from space. *Sci. Adv.*, **7**, eabf9415, https://doi.org/10.1126/sciadv.abf9415.

Wells, N., S. Goddard, and M. J. Hayes, 2004: A self-calibrating palmer drought severity index. *J. Climate*, **17**, 2335–2351, https://doi.org/10.1175/1520-0442(2004)017<2335:ASPDSI>2.0.CO;2.

Wentz, F. J., 1997: A well calibrated ocean algorithm for Special Sensor Microwave/Imager. *J. Geophys. Res.*, **102**, 8703–8718, https://doi.org/10.1029/96JC01751.

——, 2015: A 17-year climate record of environmental parameters derived from the Tropical Rainfall Measuring Mission (TRMM) microwave imager. *J. Climate*, **28**, 6882–6902, https://doi.org/10.1175/JCLI-D-15-0155.1.

——, L. Ricciardulli, K. Hilburn, and C. Mears, 2007: How much more rain will global warming bring? *Science*, **317**, 233–235, https://doi.org/10.1126/science.1140746.

WGMS, 2021: Global Glacier Change Bulletin No. 4 (2018-2019). M. Zemp et al., Eds., ISC(WDS)/IUGG(IACS)/UNEP/UNESCO/WMO, World Glacier Monitoring Service, 278 pp., https://wgms.ch/downloads/WGMS_GGCB_04.pdf.

Wielicki, B. A., B. R. Barkstrom, E. F. Harrison, R. B. Lee III, G. L. Smith, and J. E. Cooper, 1996: Clouds and the Earth's Radiant Energy System (CERES): An Earth observing system experiment. *Bull. Amer. Meteor. Soc.*, **77**, 853–868, https://doi.org/10.1175/1520-0477(1996)077<0853:CATERE>2.0.CO;2.

——, and Coauthors, 1998: Clouds and the Earth's Radiant Energy System (CERES): Algorithm overview. *IEEE Trans. Geosci. Remote Sens.*, **36**, 1127–1141, https://doi.org/10.1109/36.701020.

Wiese, D. N., F. W. Landerer, and M. M. Watkins, 2016: Quantifying and reducing leakage errors in the JPL RL05M GRACE mascon solution. *Water Resour. Res.*, **52**, 7490–7502, https://doi.org/10.1002/2016WR019344.

Wild, B., I. Teubner, L. Moesinger, R. Zotta, M. Forkel, R. van der Schalie, S. Sitch, and W. Dorigo, 2022: VODCA2GPP – A new global, long-term (1988–2020) gross primary production dataset from microwave remote sensing. *Earth Syst. Sci. Data*, **14**, 1063–1085, https://doi.org/10.5194/essd-14-1063-2022.

Willett, K. M., C. N. Williams Jr., R. J. H. Dunn, P. W. Thorne, S. Bell, M. de Podesta, P. D. Jones, and D. E. Parker, 2013: HadISDH: An updated land surface specific humidity product for climate monitoring. *Climate Past*, **9**, 657–677, https://doi.org/10.5194/cp-9-657-2013.

——, R. J. H. Dunn, P. W. Thorne, S. Bell, M. de Podesta, D. E. Parker, P. D. Jones, and C. N. Williams Jr., 2014: HadISDH land surface multi-variable humidity and temperature record for climate monitoring. *Climate Past*, **10**, 1983–2006, https://doi.org/10.5194/cp-10-1983-2014.

——, ——, J. Kennedy, and D. Berry, 2020: Development of the HadISDH marine humidity climate monitoring dataset. *Earth Syst. Sci. Data*, **12**, 2853–2880, https://doi.org/10.5194/essd-12-2853-2020.

Williams, E. R., 1992: The Schumann resonance: A global tropical thermometer, *Science*, **256**, 1184–1187, https://doi.org/10.1126/science.256.5060.1184.

——, 1994: Global circuit response to seasonal variations in global surface air temperature. *Mon. Wea. Rev.*, **122**, 1917–1929, https://doi.org/10.1175/1520-0493(1994)122%3C1917:GCRTSV%3E2.0.CO;2.

——, 2009: The global electrical circuit: A review. *Atmos. Res.*, **91**, 140–152, https://doi.org/10.1016/j.atmosres.2008.05.018.

——, 2020: Lightning and climate change. Fundamentals and Modelling, Vol. 1, *Lightning Interaction with Power Systems*, A. Piantini, Ed., CRC Press, 1–46, https://doi.org/10.1049/PBPO172F_ch1.

——, and S. Stanfield, 2002: The physical origin of the land-ocean contrast in lightning activity. *C. R. Phys.*, **3**, 1277–1292, https://doi.org/10.1016/S1631-0705(02)01407-X.

——, and Coauthors, 2002: Contrasting convective regimes over the Amazon: Implications for cloud electrification. *J. Geophys. Res.*, **107**, 8082, https://doi.org/10.1029/2001JD000380.

——, A. Guha, R. Boldi, H. Christian, and D. Buechler, 2019: Global lightning activity and the hiatus in global warming. *J. Atmos. Sol.-Terr. Phys.*, **189**, 27–34, https://doi.org/10.1016/j.jastp.2019.03.011.

——, and Coauthors, 2021: Evolution of global lightning in the transition from cold to warm phase preceding two super El Niño events. *J. Geophys. Res. Atmos.*, **126**, e2020JD033526, https://doi.org/10.1029/2020JD033526.

WMO, 2018: Scientific assessment of ozone depletion, 2018. Global Ozone Research and Monitoring Project Rep. 58, 588 pp., https://csl.noaa.gov/assessments/ozone/2018.

——, 2019a: Lightning for climate. GCOS-227, 56 pp., https://library.wmo.int/doc_num.php?explnum_id=6262.

——, 2019b: Vision for the WMO Integrated Global Observing System in 2040. WMO-1243, 38 pp., https://library.wmo.int/doc_num.php?explnum_id=10278.

——, 2021a: GAW data: Volume IV-Greenhouse and related gases. WMO WDCGG Data Summary, WDCGG 45, 97 pp. https://gaw.kishou.go.jp/static/publications/summary/sum45/sum45.pdf.

——, 2021b: Provisional report on the state of the global climate 2021. Provisional Rep., 47 pp., accessed 9 February 2022, https://reliefweb.int/sites/reliefweb.int/files/resources/WMO%20Provisional%20Report%20on%20the%20State%20of%20the%20Global%20Climate%202021.pdf.

——, 2022: State of the Global Climate 2021. WMO-1290, 54 pp., https://library.wmo.int/doc_num.php?explnum_id=11178.

Wohland, J., N.-E. Omrani, D. Witthaut, and N.-S. Keenlyside, 2019: Inconsistent wind speed trends in current twentieth century reanalyses. *J. Geophys. Res. Atmos.*, **124**, 1931–1940, https://doi.org/10.1029/2018JD030083.

Wood, K. M., P. J. Klotzbach, J. M. Collins, L.-P. Caron, R. E. Truchelut, and C. J. Schreck, 2020: Factors affecting the 2019 Atlantic hurricane season and the role of the Indian Ocean Dipole. *Geophys. Res. Lett.*, **47**, e2020GL087781, https://doi.org/10.1029/2020GL087781.

Woolway, R. I., and C. J. Merchant, 2018: Intralake heterogeneity of thermal responses to climate change: A study of large Northern Hemisphere lakes. *J. Geophys. Res. Atmos.*, **123**, 3087–3098, https://doi.org/10.1002/2017JD027661.

——, and Coauthors, 2017: Lake surface temperature [in "State of the Climate in 2016"]. *Bull. Amer. Meteor. Soc.*, **98** (8), S13–S14, https://doi.org/10.1175/2017BAMSStateoftheClimate.1.

——, and Coauthors, 2018: Lake surface temperature [in "State of the Climate in 2017"]. *Bull. Amer. Meteor. Soc.*, **99** (8), S13–S15, https://doi.org/10.1175/2018BAMSStateoftheClimate.1.

Worden, H. M., and Coauthors, 2013: Decadal record of satellite carbon monoxide observations. *Atmos. Chem. Phys.*, **13**, 837–850, https://doi.org/10.5194/acp-13-837-2013.

Yamazaki, D., S. Kanae, H. Kim, and T. Oki, 2011: A physically based description of floodplain inundation dynamics in a global river routing model. *Water Resour. Res.*, **47**, W04501, https://doi.org/10.1029/2010WR009726.

Yeh, S.-W., and Coauthors, 2018: ENSO atmospheric teleconnections and their response to greenhouse gas forcing. *Rev. Geophys.*, **56**, 185– 206, https://doi.org/10.1002/2017RG000568

Yin, Y., F. Chevallier, P. Ciais, G. Broquet, A. Fortems-Cheiney, I. Pison, and M. Saunois, 2015: Decadal trends in global CO emissions as seen by MOPITT. *Atmos. Chem. Phys.*, **15**, 13 433–13 451, https://doi.org/10.5194/acp-15-13433-2015.

Yosef, Y., E. Aguilar, and P. Alpert, 2021: Is it possible to fit extreme climate change indices together seamlessly in the era of accelerated warming? *Int. J. Climatol.*, **41** (S1), E952–E963, https://doi.org/10.1002/joc.6740.

Young, I., and A. Ribal, 2019: Multiplatform evaluation of global trends in wind speed and wave height. *Science*, **364**, 548–552, https://doi.org/10.1126/science.aav9527.

Yu, B., X. Zhang, G. Li, and W. Yu, 2022: Interhemispheric asymmetry of climate change projections of boreal winter surface winds in CanESM5 large ensemble simulations. *Climatic Change*, **170**, 23, https://doi.org/10.1007/s10584-022-03313-2.

Yu, P., and Coauthors, 2021: Persistent stratospheric warming due to 2019–2020 Australian wildfire smoke. *Geophys. Res. Lett.*, **48**, e2021GL092609, https://doi.org/10.1029/2021GL092609.

Yulaeva, E., and J. M. Wallace, 1994: The signature of ENSO in global temperature and precipitation fields derived from the microwave sounding unit. *J. Climate*, **7**, 1719–1736, https://doi.org/10.1175/1520-0442(1994)007<1719:TSOEIG>2.0.CO;2.

Zeng, Z., and Coauthors, 2019: A reversal in global terrestrial stilling and its implications for wind energy production. *Nat. Climate Change*, **9**, 979–985, https://doi.org/10.1038/s41558-019-0622-6.

Zha, J., and Coauthors, 2021: Projected changes in global terrestrial near-surface wind speed in 1.5° C–4.0° C global warming levels. *Environ. Res. Lett.*, **16**, 114016, https://doi.org/10.1088/1748-9326/ac2fdd.

Zhang, G., and Coauthors, 2021: Uneven warming likely contributed to declining near-surface wind speeds in northern China between 1961 and 2016. *J. Geophys. Res. Atmos.*, **126**, e2020JD033637, https://doi.org/10.1029/2020JD033637.

Zhang, H.-M., and Coauthors, 2019: Updated temperature data give a sharper view of climate trends. *Eos*, **100**, https://doi.org/10.1029/2019EO128229.

Zhang, X., L. Alexander, G. C. Hegerl, P. Jones, A. Klein Tank, T. C. Peterson, B. Trewin, and F. W. Zwiers, 2011: Indices for monitoring changes in extremes based on daily temperature and precipitation data. *Wiley Interdiscip. Rev.: Climate Change*, **2**, 851–870, https://doi.org/10.1002/wcc.147.

Zhang, Y., J. M. Wallace, and D. S. Battisti, 1997: ENSO-like interdecadal variability: 1900-93. *J. Climate*, **10**, 1004–1020, https://doi.org/10.1175/1520-0442(1997)010<1004:ELIV>2.0.CO;2.

Zhang, Y.-Q., and Coauthors, 2016: Multi-decadal trends in global terrestrial evapotranspiration and its components. *Sci. Rep.*, **5**, 19124, https://doi.org/10.1038/srep19124.

Zhang, Y., O. R. Cooper, A. Gaudel, A. M. Thompson, P. Nédélec, S.-Y. Ogino, and J. J. West, 2016: Tropospheric ozone change from 1980 to 2010 dominated by equatorward redistribution of emissions. *Nat. Geosci.*, **9**, 875–879, https://doi.org/10.1038/ngeo2827.

——, and Coauthors, 2021: Contributions of world regions to the global tropospheric ozone burden change from 1980 to 2010. *Geophys. Res. Lett.*, **48**, e2020GL089184, https://doi.org/10.1029/2020GL089184.

Zhao, L., and Coauthors, 2020: Changing climate and the permafrost environment on the Qinghai–Tibet (Xizang) Plateau. *Permafrost Periglacial Processes*, **31**, 396–405, https://doi.org/10.1002/ppp.2056.

——, and Coauthors, 2021: A synthesis dataset of permafrost thermal state for the Qinghai–Tibet (Xizang) Plateau, China. *Earth Syst. Sci. Data*, **13**, 4207–4218, https://doi.org/10.5194/essd-13-4207-2021.

Zhou, L., and Coauthors, 2021: A continuous decline of global seasonal wind speed range over land since 1980. *J. Climate*, **34**, 9443–9461, https://doi.org/10.1175/JCLI-D-21-0112.1.

Ziemke, J. R., and Coauthors, 2019: Trends in global tropospheric ozone inferred from a composite record of TOMS/OMI/MLS/OMPS satellite measurements and the MERRA-2 GMI simulation. *Atmos. Chem. Phys.*, **19**, 3257–3269, https://doi.org/10.5194/acp-19-3257-2019.

Zipser, E. J., D. J. Cecil, C. Liu, S. W. Nesbitt, and D. P. Yorty, 2006: Where are the most intense thunderstorms on Earth? *Bull. Amer. Meteor. Soc.*, **87**, 1057–1072, https://doi.org/10.1175/BAMS-87-8-1057.

Zou, C.-Z., and W. Wang, 2011: Intersatellite calibration of AMSU-A observations for weather and climate applications. *J. Geophys. Res.*, **116**, D23113, https://doi.org/10.1029/2011JD016205.

——, H. Xu, X. Hao, and Q. Fu, 2021: Post-millennium atmospheric temperature trends observed from satellites in stable orbits. *Geophys. Res. Lett.*, **48**, e2021GL093291, https://doi.org/10.1029/2021GL093291.